5-2023

Al-Ce-Mn Solidification Phase Selection and Solid-State Phase Transformations

Kevin Dean Sisco
ksisco@vols.utk.edu

To the Graduate Council:

I am submitting herewith a dissertation written by Kevin Dean Sisco entitled "Al-Ce-Mn Solidification Phase Selection and Solid-State Phase Transformations." I have examined the final electronic copy of this dissertation for form and content and recommend that it be accepted in partial fulfillment of the requirements for the degree of Doctor of Philosophy, with a major in Materials Science and Engineering.

Sudarsanam S. Babu, Major Professor

We have read this dissertation and recommend its acceptance:

Alex Plotkowski, Amit Shyam, Eric Lass

Accepted for the Council:

Dixie L. Thompson

Vice Provost and Dean of the Graduate School

(Original signatures are on file with official student records.)

Al-Ce-Mn Solidification Phase Selection and Solid-State Phase Transformations

A Dissertation Presented for

Doctor of Philosophy

Degree

The University of Tennessee, Knoxville

Kevin Dean Sisco

May 2023

Acknowledgements

I would like to acknowledge all the people that supported my growth and education as I worked towards attaining my PhD. I would like to thank Suresh Babu for taking me on as my primary advisor and continually challenging me to improve. I would like to thank Alex Plotkowski for indulging my variety of investigations into Al alloys.

I would like to thank the University of Tennessee for being a home to me for eight years, where countless amounts of knowledge were absorbed. I would like to thank Oak Ridge National lab for allowing me to take advantage of their facilities so that I could be a productive researcher.

I would like to thank everyone I worked with in the multiple additive manufacturing processes, from defect detection to microstructure control: Dr. Larry Allard, Dr. Ying Yang, Dr. Sumit Bahl, Dr. Amit Shyam, Dr. Donovan Leonard, Andrés Márquez Rossy, Dr. Claudia Rawn, Dr. Kurt Sickafus, and Dr. Eric Lass.

Finally, I would like to thank the students that helped me in my academic journey: Michael Pagan, Michael Haines, Sabina Kumar, Steven Eilertson, Alex Pawlowski, Serena Beauchamp, Amy Godfrey, Caitlyn Hensley, Vanshika Singh, and so many more.

A significant amount of work was performed at the Manufacturing Demonstration Facility of the Oak Ridge National Laboratory.

Abstract

The design of Al alloys has become an important topic in Additive Manufacturing (AM). The adoption of Al alloys to AM has been difficult because traditional alloys are prone to processing related defects such as solidification cracking. The Al-10Si-Mg alloy was initially adopted because of its resistance to solidification cracking. However, the Al-10Si-Mg alloy has reduced tensile properties especially at high temperatures, where the silicon phase coarsens readily. Therefore, efforts have been made to design new Al alloys that can take advantage of the AM processing. The goal of new alloys is to optimize based on rapid solidification conditions, while being less prone to processing related defects. The Al-Ce, and higher order Al-Ce-X, systems have been adopted because of the low solubility and diffusivity of Ce through FCC Al. The challenge is metastable phases form as a function of the unique processing conditions. Metastable phases have been observed to have unique phase transformations during heat treatment. The goal is to understand the above observations.

In this work, an Al-10Ce-8Mn (wt.%) alloy is used to understand the metastable phase $Al_{20}Mn_2Ce$. The $Al_{20}Mn_2Ce$ phase, surrounded by FCC Al has different decomposition pathways (at 400°C) depending on its thermal history within a single weld track. Initially, the research focuses on an AM Al-Ce-Mn part that demonstrates the change in decomposition pathways based upon the local solidification conditions, e.g., primary $Al_{20}Mn_2Ce$ to eutectic (between FCC Al and $Al_{20}Mn_2Ce$) solidification. Following the AM parts, weld tracks are preformed to understand the role of solidification conditions that can lead to each decomposition pathway observed in the Al-Ce-Mn system. The interface response function model is used to understand phase selection as a function of solidification conditions. The overall goal of this work is to demonstrate how a single metastable phase in a weld track, specifically $Al_{20}Mn_2Ce$, may be manipulated by local solidification conditions, and how that affects the subsequent phase decomposition. The impact of this work is to understand the role of solidification conditions on the solid-state phase transformation to give insight into how the mechanical properties of a particular alloy can be controlled.

Table of Contents

List of Tables

List of Figures

Chapter 1. Introduction

Metal Additive Manufacturing (AM) is an advanced manufacturing technique that has been adopted in industrial applications for its ability to create complex parts and unique microstructures thereby expanding the design and performance space for selected parts. The automotive and aerospace industries are early adopters of the AM technology. BMW, an automotive manufacturer, has used metal AM to create lightweight components from aluminum alloys that combine multiple parts into a single part allowing for the reduction in design complexity and assembly of a vehicle [1]. General Motors (GM) has adopted AM to usher in a "made to order" strategy for high-end vehicles that uses metal and polymer AM to make personalized customizations [2,3]. GM also uses AM machines to produce job specific tools to make a safer and more efficient work environment [4]. However, AM relevance is far beyond its capability to make unique and lightweight geometries. For example, NASA has designed AM specific materials, such as GRX-810 [5] with unique structural and thermal properties. The GRX-810 alloy is difficult to produce through conventional methods including casting and forging. Additional examples related to adopting AM pertain to tooling and part production such as those pursued by Boeing [6], Ford [7], and Airbus [8]. As AM becomes increasingly prevalent in industry, it is beneficial to understand how it can be leveraged to improve current part designs and their performance.

The challenges in AM, specifically laser powder bed fusion (L-PBF), are the unique processing conditions that are applied to a material. L-PBF essentially is a collection of micro welds (more information in Section 2.1.1) that contain an order of magnitude change in solidification conditions (solidification velocity and thermal gradient which will be explained in a later section) across each weld. The weld tracks also cause repeated thermal cycling to the deposited material which can influence the final part properties. In the current work, aluminum (Al) alloys are investigated because of their potential to lightweight structures and replace Ti-6Al-4V at intermediate temperature (< 400°C) [9]. One of the challenges with aluminum alloy adoption is the high temperatures in a L-PBF weld tracks which can depletes key strengthening elements such as Zn (907°C) and Mg (1091°C), that have low boiling points compared to Al (2470°C) [10,11]. On top of the unique processing conditions, conventional high strength Al alloys are

difficult to adopt because of the propensity for the formation of solidification cracking. The difficulty in processing traditional high strength aluminum e.g., 7xxx alloys, has led to the exploration of new systems that are resistant to processing related defects, have high strength, and are usable at high temperatures.

In a review of AM of aluminum alloys, Michi *et al.* [12] highlights various new alloys that can be used for low- and high-temperature structural applications. A specific target for new high temperature aluminum alloys is to maintain properties above 200°C to compete with the specific strength of Ti-6Al-4V alloys, because traditional Al alloys have difficulty retaining strength above 200°C. The degradation of strength at high temperatures is commonly attributed to coarsening and dissolution of secondary strengthening precipitates. Therefore, targeted alloy design towards AM has been investigating new Al alloys [13–15].

The overall design goal for a new alloy for AM would be to have an alloy that is not prone to processing-related defects in AM (such as solidification cracking or porosity), is easy to process, and is able to operate up to 400°C. With these criteria, high intermetallic content alloys near the eutectic point are of interest because of their ability to reduce the propensity for solidification cracking. The formation of a eutectic microstructure can reduce the freezing range of an alloy which can result in a reduction of the propensity to solidification crack, as discussed by Sindo Kou [16].

New alloys could ideally take advantage of the high solidification rates (liquid solid interface velocity m/s) observed in AM by refining the eutectic spacings [17], which has been previously observed in an Al-Ni alloy. The Al-Ce system appears to fit some of these criteria. The interest in the system is the low diffusivity of Ce (~$1x10^{18}$ m^2/s at 400°C) and its low solubility (<$1x10^{-5}$ at.% at room temperature) in the FCC Al Matrix which might limit the microstructural degradation, which can include coarsening and phase transformations [18,19]. The challenge with taking advantage of the high intermetallic content alloys is highlighted by Plotkowski *et al.* [20], where a binary Al-Ce alloy was evaluated for use in AM. The experiments explored a single weld track, where a variety of solidification microstructures are observed. The change in solidification microstructures can cause localized changes in properties, which might not be desirable in a final part. A specific example of the unique solidification microstructure in AM

was examined in an Al-Ce-Mg system. In the Al-Ce-Mg system, the formation of the metastable $Al_{13}CeMg_6$ phase has been observed in both a near eutectic and hyper eutectic Al-Ce-Mg alloy after production in AM [21]. The metastable phase subsequently decomposes to FCC Al with Mg in solid solution and $Al_{11}Ce_3$ after hot isostatic pressing at elevated temperatures.

The current work examines the spatially heterogeneous microstructure of an Al-10Ce-8Mn (wt.%) alloy. The goal is to understand how the unique solidification conditions across a single weld track of AM impact not only the initial solidification microstructure, but also the change in the microstructure as a function of time and temperature. The focus on the unique solidification conditions can give insight into how the AM process can be used to produce more desirable microstructure. In the current case, high temperature properties can be improved by promoting more stable phases that are resistant to change with time. In this work, the emphasis is placed on the solid-state phase transformations and the possible decomposition pathways observed in the microstructure. The decomposition pathway of a material is how the initial phases change as a function of time and temperature particularly in the solid state. The structure of the dissertation is described briefly as follows:

Chapter 2 examines the motivation and overview of AM powder bed fusion processes, solidification phase selection models, and solid-state phase transformations. A review of aluminum alloys in additive manufacturing and the justification for investigating Al-Ce-X alloys is discussed. General comments on alloy design are located within the discussion of defects in AM.

Chapter 3 focuses on the heterogeneous phase transformations observed across individual weld tracks in an AM Al-Ce-Mn alloy. The initial phase presence observed in the microstructure is characterized by X-ray diffraction (XRD). Scanning electron microscopy (SEM) is used to show a localized bimodal microstructure. The thermally exposed microstructure is examined as a function of time and temperature to determine how the observed solid-state phase transformations occur. The $Al_{51}Mn_7Ce_4$ phase is identified as a new phase resulting from the decomposition of a eutectic solidification structure based on $Al_{20}Mn_2Ce$ and FCC Al.

Chapter 4 examines the relationship of phase selection to local solidification conditions in the Al-Ce-Mn system by varying the processing conditions of weld tracks over Al-Ce-Mn alloy disks. Seven weld tracks confirmed the critical transition points for the primary solidification of $Al_{10}Mn_2Ce$, to the primary solidification of $Al_{20}Mn_2Ce$, and finally the onset of eutectic solidification between $Al_{20}Mn_2Ce$ and FCC Al. These weld tracks were thermally exposed to evaluate the phase transformation pathways and to compare with previous results for Al-Ce-Mn alloys.

Chapter 5 discusses the ability to predict phase selection using the interface response functions (IRF). The interface response function is investigated by manipulating the original binary derivation to model the ternary Al-Ce-Mn system. The ability to implement Aziz's solute trapping model for intermetallic compounds is discussed. The IRF is calibrated to the weld tracks from Chapter 4. This process can predict phase selection based upon solidification conditions to be encountered in future experiments.

Chapter 6 summarizes the observed results during these experiments. The agreement between the experiments and modeled data is discussed. Future work is proposed for both the Al-Ce-Mn system, as well as a general adaptation of the IRF methodology for the primary solidification of intermetallic compounds, under rapid cooling conditions.

Chapter 2. Background and Literature Review

Chapter 2 introduces additive manufacturing, microstructure control, modeling of solidification, solid state phase transformations, background on the Al-Ce-Mn system, and the scientific and technical approach used in the current work. During the discussion of AM, general comments are made about alloy design for Aluminum AM.

2.1 Introduction to Additive Manufacturing and Microstructure Control

Additive manufacturing (AM) is the layer wise buildup of three-dimensional parts using two dimensional cross sections. AM has been adopted across a variety of materials such as plastics, ceramics, and metals [22,23]. The manufacturing of each of these materials uses different ideas for joining methodology. The current work focuses only on the metal AM of parts.

Metal AM can be broken up into two types: solidification and solid-state processes [24]. The solid-state processes, such as ultrasonic and friction stir AM use plastic deformation to join materials to make a solid part [25–28]. Alternatively, solidification processes use a heat source that locally melts material. The ISO standards for metal AM are laid out in Figure 2.1. In Figure 2.1, the state of fusion, material feedstock, material distribution, basic AM principle, source of fusion, and finally process category is discussed for a variety of metal additive processes. In the following sections and chapters, the focus is on melted state metal AM using a metal powder feedstock that can use localized solidification conditions.

2.1.1 Additive Manufacturing using Metal Powder

Metal powder in AM is largely used in two types of systems, powder bed fusion (PBF), and directed energy deposition (DED). The two technologies will be discussed in depth later in this section. A key difference between PBF and DED is how material is provided to the weld track. In PBF, a bed of powder is raked over a two-dimensional cross section, and then melted along a specified pathway. In DED, the material is directly added to a molten weld track, removing the need for powder spreading. There are additional systems that take advantage of metal powder but are not considered because they are out of the current scope of work.

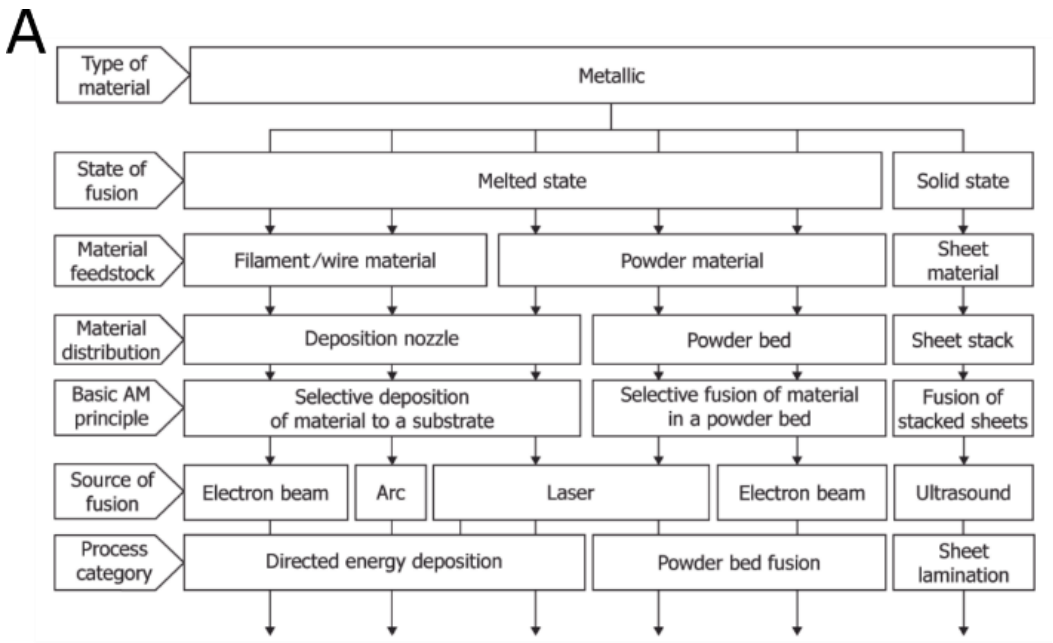

Figure 2.1 The ISO standard flowchart that describes the current methods of metal AM [29].

Powder bed fusion (PBF) consists of two main types, electron beam (EBM) and Laser Powder Bed Fusion (L-PBF) [24]. The building process of L-PBF and EBM is very similar. To start a typical build, a build plate of similar material to the powder is inserted in the machine. There are also instances where preexisting parts are used as a base material for repair [30] . Then, a powder layer, is raked over the build plate which is then selectively melted using a predetermined scan path. The process is repeated for as many layers as required until a full part exists. The excess powder around the part is typically recycled [31–33]. An example of L-PBF layout is shown in Figure 2.2A, and an example of an EBM layout is shown in Figure 2.2B.

There are a few key differences between the two approaches. The EBM machine uses an electron beam source; therefore, it requires a vacuum chamber. The L-PBF machines use a laser source, and the build chamber is typically filled with an inert gas (such as argon or nitrogen). The preheat temperature of the material in each machine is different. An EBM system can preheat the top layer using the electron beam source, while L-PBF typically preheats its builds using a heater in the bottom of the base plate. The preheating of the top layer in EBM can allow individual layers to be preheated to a targeted temperature [34]. The ability to control the localized preheat of the material, allows the control of the local solidification conditions in a part. The local solidification conditions refers to the solidification velocity and thermal gradient. The solidification velocity is the rate at which the liquid/solidus interface moves typically described as (m/s). The thermal gradient describes the direction and magnitude of temperature changes around a part, typically described as (K/m). These solidification conditions influence the solidification microstructure. A specific example of how solidification conditions play a role on the resultant microstructure is the columnar to equiaxed transition of grain structures in Ni superalloys. The transition between microstructures has been experimentally shown to be sensitive to the solidification velocity and thermal gradient of the built material [35].

In contrast to the layer wise preheating observed in EBM, L-PBF systems are limited because the preheating is typically controlled by a heater in the base of the build plate. The result is that a localized preheat is more difficult to control (at the current state of L-PBF) and in general, the preheat temperature is not as high (<200 °C provided by GE [36]).

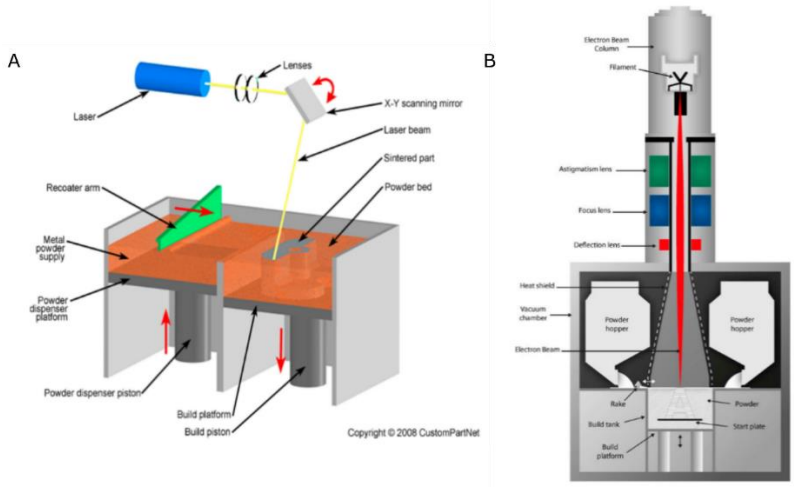

Figure 2.2 Schematic of L-PBF System [37], *(B) Schematic of EBM system* [38]

Another difference between the systems is the rate of material deposition. The rate of deposition in EBM is ~60 cm^3/hr and L-PBF is ~5-20 cm^3/hr [24]. Although these values for L-PBF were reported for single laser systems, and there have been significant advancement in machine design, where the usage of multiple lasers has been adopted to improve processing speed [39,40]. GE reports a using a Concept Laser X Line 2000R the Al-10Si-Mg alloy can be produced at a rate of 28.2 cm^3/hr using a 2 laser system [41].

The directed energy deposition (DED) process differs from PBF machines by applying material directly to a weld track. DED machines typically follow the layer wise printing strategy discussed above. DED process is similar to fusion welding. An example layout of a powder fed DED system is shown in Figure 2.3 which gives an example of a coaxially powder fed DED system where the material is blow from powder nozzles onto the molten weld track.

There are two main types of feedstocks for DED: wire and powder. The current case examines powder fed DED machines to have a more direct comparison to powder bed fusion processes. One of the key differences between DED and PBF is the heat source velocity. In powder bed fusion, specifically in Al alloys the speed of the heat source is generally >600 mm/s [14,21,42]. In DED of aluminum alloys, the heat source moves significantly slower where it is generally less than 100 mm/s. In a LENS® system, which is a commercially available powder fed DED system, an Al 5xxx series runs at a scan speed of 21 mm/s [43]. The differences in velocity can dramatically change the solidification conditions, by limiting the maximum solidification velocity in a material, which is at a maximum the heat source velocity. The change in solidification conditions can lead to different microstructure selection. The limitation of slower heat source velocity is typically coupled with a larger heat source size to avoid defect creation in parts. The increased heat source size has the benefit of an increased deposition rate up to 230 cm^3/hr [24]. The improvement in deposition rate may also be coupled with a decrease in part resolution. The reduction in part resolution may require additional machining to create finished parts. The DED machines are specifically mentioned because the slower scan speed of the laser can be useful when attempting to control the selection of the microstructure, which will be discussed in future sections.

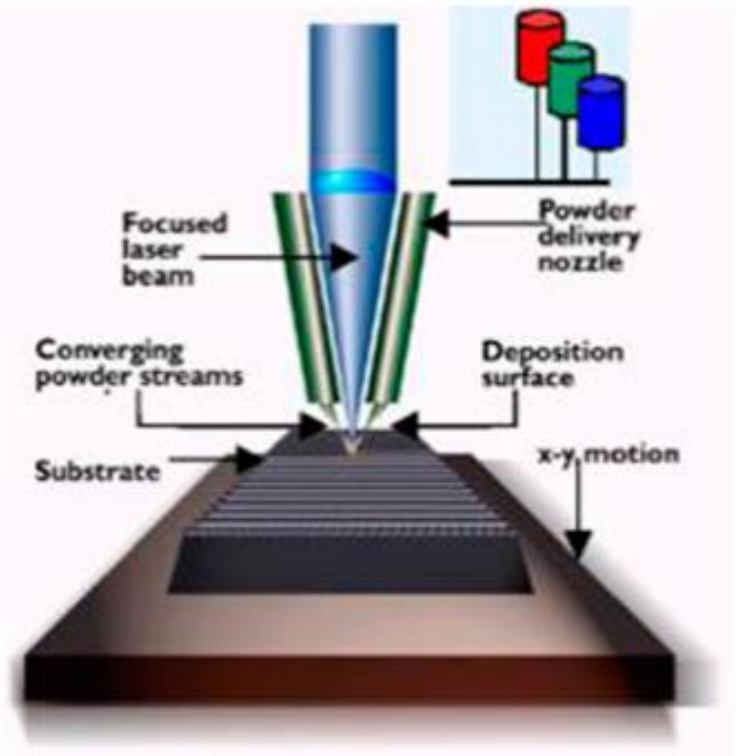

Figure 2.3 Coaxially fed powder DED system [44].

2.1.2 Residual Stress in Additively Manufactured Parts

Residual stress in a body (of a part) are stresses that are unnecessary to maintain equilibrium between a body and its environment [45]. Residual stress is known in traditional processes and welding to influence the mechanical properties of parts, particularly fatigue. In steels, surface processing is used to improve the fatigue life of components. Landgraf *et al.* [46] showed that different surface processes on spring steel, such as induction hardening, shot peening and strain peening, influence the fatigue life of components. Landgraf's work shows that an increase in residual stress at the surface of a sample can increase the fatigue life of the component [46]. In some cases, the fatigue life doubled depending on surface treatment.

In additive manufacturing, Chen et al. [47] describes residual stress in AM by three key mechanisms: (1) The temperature gradient mechanism, (2) the cool-down phase mechanism, and (3) the solid-state phase transformation mechanism [47,48]. The solid-state phase transformation mechanism is not discussed here.

First, the temperature gradient mechanism is when a material is rapidly heated to form a weld track. As a molten pool forms, the material surrounding the molten pool is heated. The expansion of the heated material is limited by the surrounding material due to the gradient in temperature that is experienced. As the metal can more easily yield at high temperatures, the thermal stress can become plastic strain. When the heat source is removed and the material cools, additional strain is needed to compensate for the plastic strain formed by the weld track [48].

The second is the cool down phase mechanism. This mechanism is attributed to the layer wise processing seen in AM. As the deposited layer shrinks due to the cooling process, the shrinkage is limited by the previously deposited layer. This leads to a balancing of forces between layers. The stress will continue to accrue in the interior of a part to balance with the stresses distributed at the surface for each built layer [49].

The effect of thermally induced residual stress has been observed in an Al-10Si-Mg alloy using two experiments (preheated and not preheated) in L-PBF by Buchbinder *et al.* [50]. The example in Figure 2.4 shows two cases using the same geometry. The first shown on the left is printed without a preheated build plate and shows deflection after being removed from the build plate.

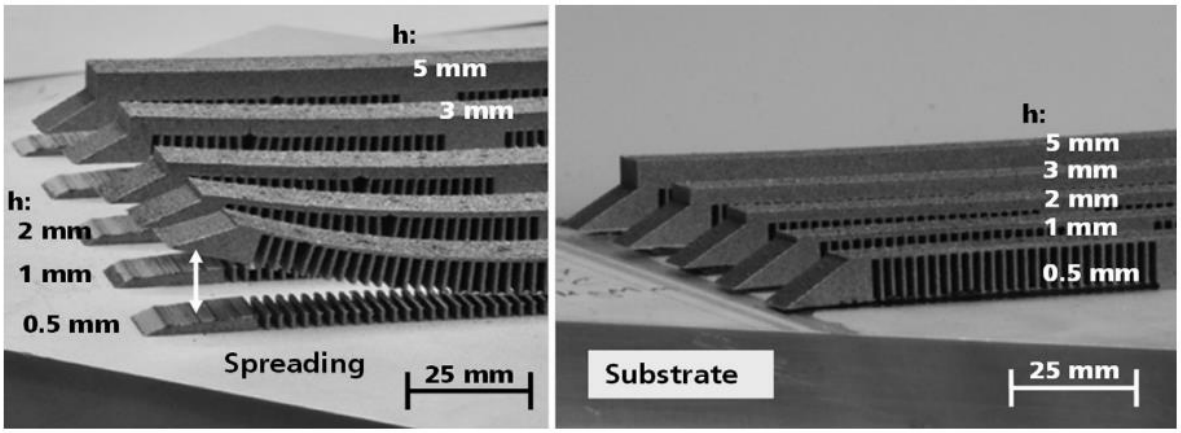

Figure 2.4 Shows two examples of L-PBF produced Al-10Si-Mg. The left image is an experiment that shows an Al-10Si-Mg part produced without a preheated build plate, which results in residual stresses that curl the part upwards when detached from the base. The right image is an experiment that shows the Al-10Si-Mg built in L-PBF on a preheated build plate, where the residual stress appears to be minimized during processing [50].

The second build shown on the right is printed with a 200°C preheat that does not show any deflection after being cut from the baseplate. The change in deflection is likely the result of a reduction in residual stress in the parts.

In AM, the residual stress observed after processing a Ti-6Al-4V part in L-PBF AM, has been shown to influence the yield strength of a part after production [51]. The different processing conditions were achieved by varying the layer thickness and input power and laser velocity of the system. The residual stress was externally measured using strain gauges and a drilled hole in the center of a 30x30x10 cube.

2.1.3 Defects in Laser Powder Bed Fusion

In AM, there are a variety of common defects that are observed. The general focus of the defects discussed here are in the reference frame of powder bed fusion processes. The typical defects in L-PBF are delamination, cracking, swelling, and porosity. These processing defects are related to the input processing conditions and can have various implications on a final part. It is important to understand the defects possible in AM, so that alloy compositions can be chosen that attempt to minimize the possibility of processing related defects. Each of these defects are briefly discussed as follows.

Delamination

Delamination occurs when a part splits across an individual layer. An example of layer delamination and cracking is shown for M2 tool steels produced by L-PBF[52]. In the current example, delamination is attributed to the separation of adjacent layers within parts due to incomplete melting between layers. Delamination defects are macroscopic and cannot be repaired by post-processing methods. In the example with H2 tool steel, as seen in Figure 2.5, the delamination was attributed to thermal stresses. The delamination observed in Figure 2.5 was avoided in different builds by preheating the build plate to reduce the stress [52].

Solidification Cracking

Solidification cracking is observed as a function of material and processing condition in Al alloys.

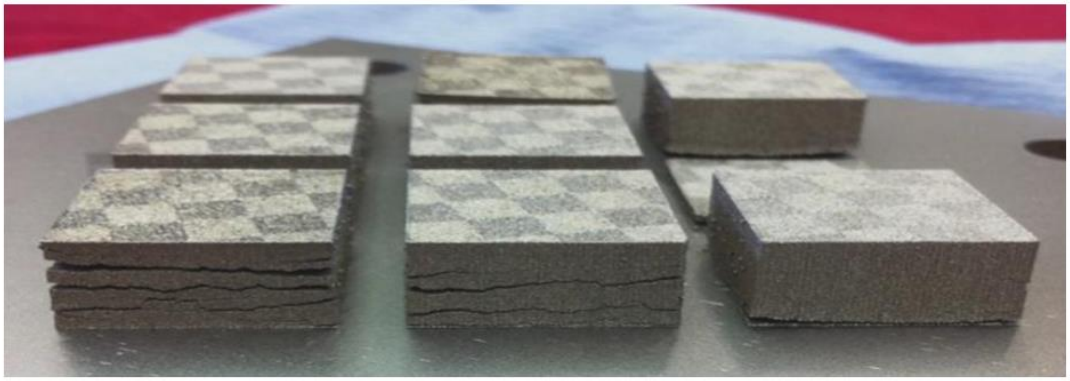

Figure 2.5 Delamination observed for M2 High Speed Steel (HSS) which is a type of Tool Steel produced by L-PBF. The cracking observed in these parts is attributed to thermal stresses. [52]

Solidification cracking can occur because of a lack of liquid feeding to the mushy zone of the material. A schematic from Rappaz *et al.* [53] is shown in Figure 2.6, describes the mechanism, where liquid has to flow in-between dendrites to compensate for the shrinkage due to solidification. However, the primary driving mechanism is the tensile stress at the dendrite root and not the hydrostatic depression due to shrinkage. If the liquid flow cannot compensate for the deformation that results from the tensile stress, a solidification crack can form.

In traditional welding, solidification cracking is avoided using a variety of methods. A common approach is to use Al-Si as a filler between materials because of its low viscosity and large quantity of eutectic microstructure [54]. The low viscosity can help the Al-Si flow in between dendrites into the mushy zone to help compensate for the shrinkage due to solidification. Another benefit of the Al-Si system is that it can solidify as a eutectic which can assist in eliminating solidification cracking because it removes the mushy zones between dendrites. Eutectic solidification is a coupled solidification front between FCC Al and Si in the case of an Al-Si alloy, wherein there are no dendrite roots because of the coupled solidification. The Al-Si alloy is also desirable because of its low freezing range, or the difference in temperature between the liquidus and solidus temperatures of the material, which has been shown to reduce the propensity of solidification cracking [16].

However, in L-PBF, the subsequent layers are not combined with a filler material, but a combination of weld tracks of the same material stacked atop each other. Therefore, it is important to have a base material that can be resistance to solidification cracking. Altiparmak *et al.* [11] discusses how traditional Al alloys have been observed to experience solidification cracking in AM, as seen in Figure 2.7. Figure 2.7 shows a variety of commercial aluminum alloys that were produced using L-PBF. The results of these experiments show that the processing windows were limited by the existence of solidification cracking. Altiparmak *et al*. also noted that the defects observed in AM appeared to act as nucleation sites for the formation of solidification cracking defects. A common approach to avoid solidification cracking is to promote the formation of eutectic growth. The coupled solidification of two phases is resistant to solidification cracking because of the possibility to eliminate deep mushy-zones by reducing the freezing range of the material [54].

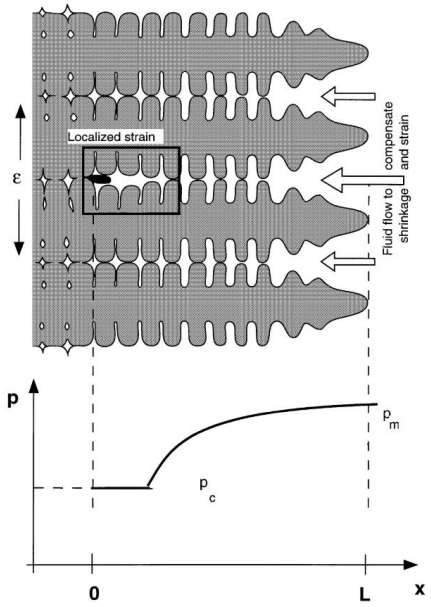

Figure 2.6 shows a schematic for the formation of a solidification crack between columnar dendrites because of a localized strain at the root of a dendrite tip. The plot at the bottom of the figure represents the pressure in the interdendritic liquid. Provided by Rappaz et al. [53]

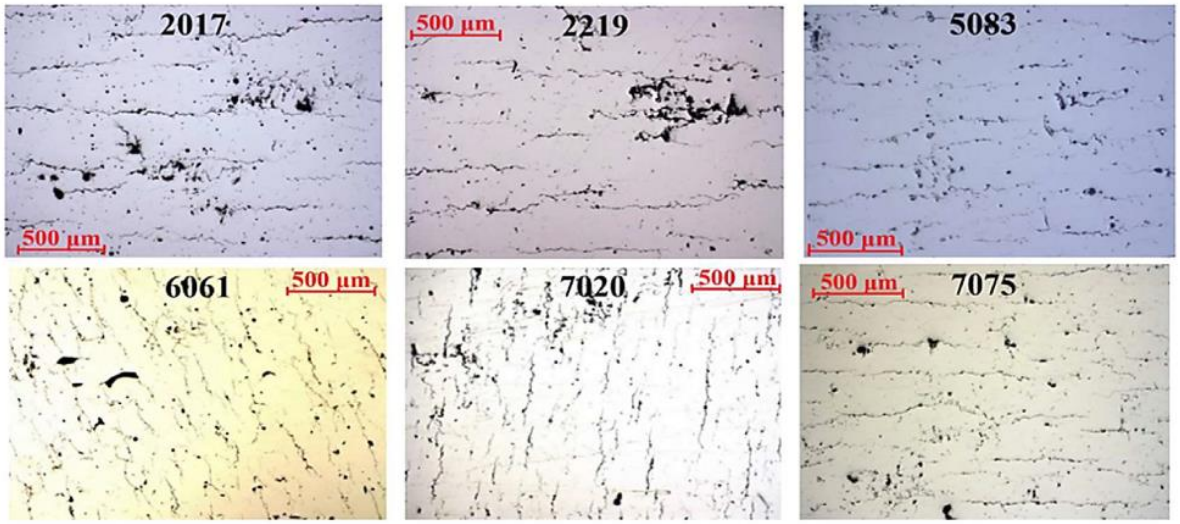

Figure 2.7 is a series SEM images of common Al alloys that after processing with L-PBF contained solidification cracking. [11]

Sindo Kou [55] additionally explains that solidification cracking can be caused by deep liquid channels in-between columnar grains. A strategy for reducing solidification cracking can be done by reducing the distance for feeding to occur. The criterion developed by Sindo Kou examines the solidification pathway predicted from thermodynamic calculations, where the slope near the terminal solidification is used to quantify the susceptibility to solidification cracking. If this slope is minimized, i.e., there is a smaller solidification range near terminal solidification, the alloy will be less susceptible to solidification cracking. To quantify this, Sindo Kou developed a hot-tearing susceptibility index defined by

$$C_{kou} = \frac{1}{\Delta f_s} \int_{0.87}^{0.94} \left| \frac{\partial T}{\partial \left(f_s^{\frac{1}{2}} \right)} \right| df_s \qquad (1)$$

Where T is temperature, f_s is the solid fraction predicted from Scheil Solidification results. The 0.87 and 0.94 is the solid fraction range of interest during solidification of Al-Cu alloys. The solidification region of interest is notable different for each alloy system. The index calculates, for an Al-Cu alloy, the susceptibility of hot cracking based on the composition of the alloy, which agreed with previous literature. The key advantage of the methodology is that the hot cracking criteria of alloys can be targeted from previously defined thermodynamics of a system.

Swelling

Swelling defects are when the material expands above the expected plane of powder distribution. Swelling defects are typically can be caused by high surface tension in the weld track and is directly related to the weld track geometry [24]. Swelling defects are typically avoided by tuning processing parameters as they can lead to increased defect formation in parts. Swelling is caused by the shape of the weld pool and changing the processing conditions will change the weld pool shape. In traditional welding, swelling is commonly referred to as humping. In a paper by Grazke et al. [56] on classical welding it is suggested that to avoid humping (swelling) the width to length ratio of a weld pool must be maximized. In literature, it has been shown that the detection and classification of swelling defects can lead to reduced mechanical properties by propagating

defects in material. Swelling is detectable using optical camera in AM. Scime *et al.* [57,58] implemented a software solution for the in-situ detection of swelled regions of a part. Swelling is a function of part geometry and processing parameters and can be mitigated in build planning.

Keyhole Porosity

Keyhole porosity is formed when localized evaporation of metal in the keyhole front wall results in a perturbation on the rear wall of the keyhole. The formation of keyhole porosity is well described in literature, specifically with regards to traditional welding [59–61]. A schematic of keyhole porosity formation is shown by Matsunawa *et al.* [59] in Figure 2.8.

The general concept from welding is applied to AM, where a variety of modeling and experimental results attempt to capture in-situ keyhole formation and have more in-depth explanations on how and why keyhole porosity form [62,63]. Keyhole porosity is avoided in AM by decreasing the overall energy input to reduce the material vaporization. In certain Al alloys, alloy elements such as Zn and Mg have low boiling points compared to Al. The difference in boiling points can lead to selective vaporization during processing. The vaporization of these elements can change the material composition away from the desired range after processing. The change in composition can in turn affect the final mechanical properties. The vaporization of Zn and Mg can be mitigated by manipulating the process parameters in the material.

In a simple cylindrical geometry, a reduction in local preheating in an Al-Ce-Mg alloy by manipulating the infill scan strategy of a part was used to reduce the amount of keyhole porosity. The two scan strategies investigated were a traditional and a skip raster. During processing, the traditional raster resulted in a 1.78 wt.% drop in Mg from atomized powder to manufacturing AM part. The skip raster resulted in a 0.77 wt.% drop in Mg from atomized powder to manufactured AM part [21]. The Mg vaporization was correlated with a decrease in porosity was rationalized by discussing the decrease in local preheating by subsequent passes of the laser. In the skip raster, there is a hatch spacing skip between each laser pass allowing for local cooling before the laser returns and finishes a layer, which experimentally resulted in less porosity and more Mg retention.

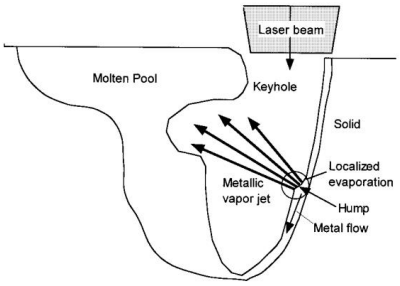

Figure 2.8 is a schematic of the localized evaporation of metal in the keyhole front wall, and its effect on the perturbation of the keyhole rear wall and a weld track [59].

Lack of Fusion Porosity

In AM lack of fusion porosity is the result of incomplete melting over a series of weld tracks. Foster *et al.* [64] drew a schematic for lack of fusion porosity wherein overlapping weld tracks do not completely combine, resulting in un-melted powder particles being trapped between the weld track and the substrate, as seen in Figure 2.9C. Figure 2.9 examines three possible scenarios that can occur in producing PBF parts.

The first in Figure 2.9A, represents an idealized scenario wherein the weld track shape and the hatch spacing (the spacing between consecutive passes of the heat source) have sufficient overlap to reduce the amount of surface roughness seen at the top surface of the part and ensure that no powder particles are trapped on continuing layers. The second scenario, in Figure 2.9B, is where the weld track shape creates large surface roughness where the subsequent layers can form lack of fusion porosity because of the continued need to have deep remelting into the material. The final scenario, in Figure 2.9C, examines a case where the weld track shape and hatch spacings do not melt enough material in a layer, which leave behind un-melted powder particles, resulting in lack of fusion porosity. Without proper weld track shape and hatch spacing, the propensity to form lack of fusion porosity increases.

Gas Porosity

Gas porosity in AM parts can occur due to various reasons. Gas pores may form inside the powder feedstock and get trapped in the AM part during subsequent remelting [65]. The defects are generally spherical and can range from 5 to 20 μm. [66]. Gas porosity is also attributed to the lack of liquid feeding, where in the mushy zone, a combination of hydrostatic pressure depression, and the segregation of gaseous solutes contribute to the formation of gas porosity. The depression in hydrostatic pressure is associated with the liquid being suctioned away from the porous dendritic region due to shrinkage. Rappaz *et al.* [53] implies that solidification cracking and gas porosity are driven by a similar mechanism, but solidification cracking only occurs when there is an external shear or tensile stress is present. For gas porosity, it can occur when the hydrostatic pressure drops below a threshold that allows for a “bubble” to form in the liquid at the root of a dendrite.

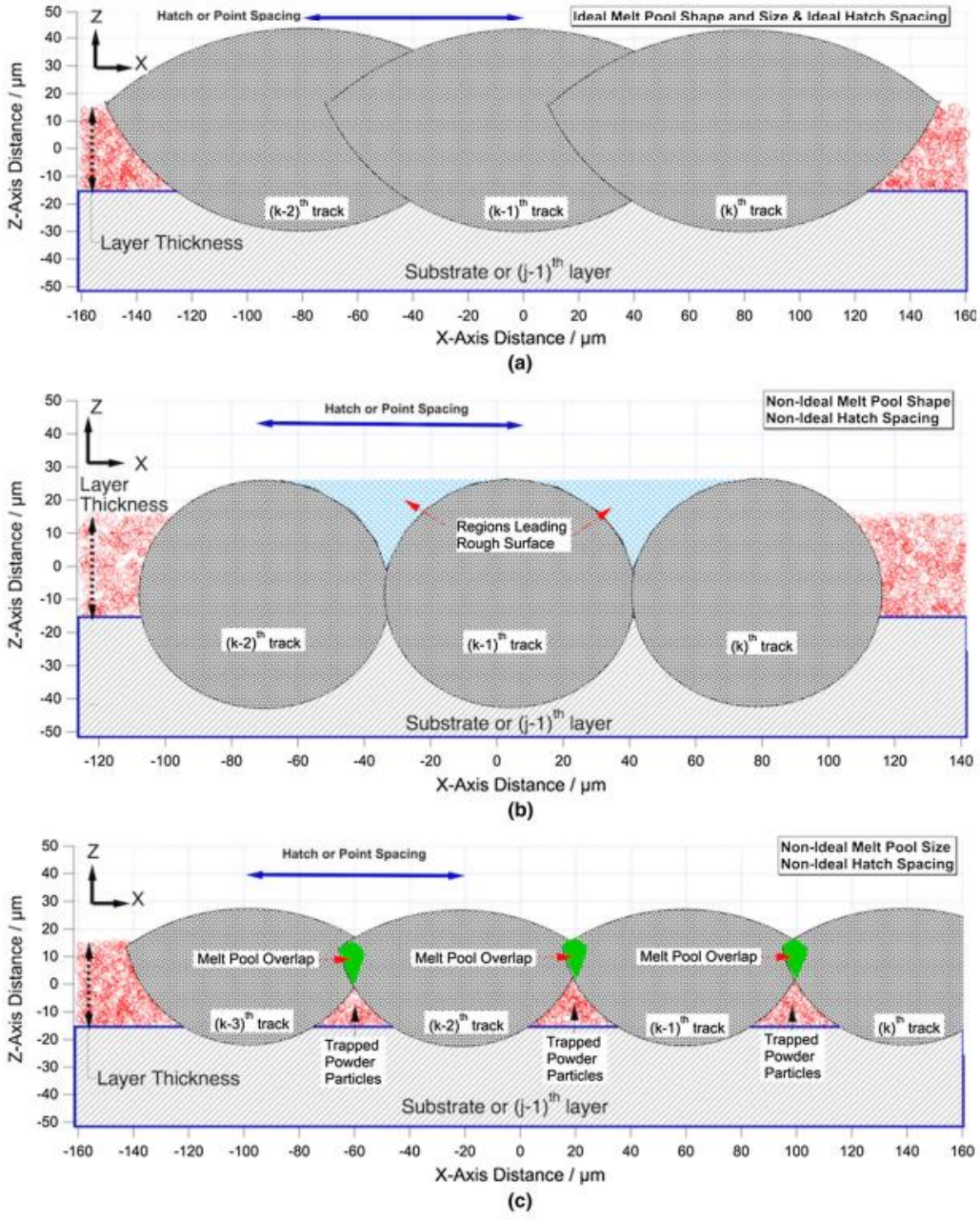

Figure 2.9 A schematic illustration from Foster et al [64], *where (A) shows an ideal overlap of molten beads leading to the reduction in surface roughness and complete melting, (B) shows an example of a collection of weld track beads contain large separation which leads to surface roughness, and (C) is where the weld tracks have a minimized overlap which lead to regions of trapped powder known as lack of fusion porosity.*

2.1.4 Microstructure Control in Welding and Additive Manufacturing

Now that the defects of AM are described, it is important to consider solidification conditions. Therefore, before discussion about the ability to control the microstructure in AM, it is important to understand a single weld tracks microstructure. An example of varying microstructure is presented by Rappaz *et al.* [67] wherein, the grain orientation changed as a function of solidification conditions, laser direction, and orientation of a single crystal base material in a Fe-Ni-Cr alloy. The goal of the work is to separate the extent to which epitaxially growth and preferred growth direction complete with the direction of the thermal gradient.

The change in orientation of the grains is attributed to the localized solidification conditions that exist across the weld track. Essentially, based on the solidification conditions, the easiest crystal direction for epitaxial growth to occur is selected. Epitaxial growth occurs when the growth of a new crystal is dependent on the orientation of the previous crystal orientation. In Figure 2.10 the grain orientation of a weld track is shown. The change in orientations of the grains is a result of different dendrite tip growth direction with respect to the single crystal base material as a function of the localized solidification conditions. The change in local solidification conditions directly refers to V (m/s), the velocity of the liquid/solid interface, and the thermal gradient G (k/m), which vary with location along the melt pool surface. Rappaz et al. demonstrated that the growth velocity of a particular crystallographic direction, $\overrightarrow{v_{hkl}}$ is shown by the relationship.

$$|\vec{v}_{hkl}| = |\overrightarrow{v_b}| \frac{\cos(\theta)}{\cos(\psi)} \qquad (2)$$

Where, θ is the angle between the normal to the weld pool surface (the thermal gradient direction) $\vec{n}$ and the velocity of the heat source $\overrightarrow{v_b}$, and ψ is the angle between $\vec{n}$ and the [h k l] of the dendrite growth direction. The example from Rappaz et al. demonstrates the ability to locally manipulate the microstructure from a weld track by changing the solidification velocity and thermal gradient present during processing. Eq. (2), is indeed independent of crystal orientation as described in a later section.

In electron beam AM (EBM), the control of grain orientation has been shown by a variety of authors from modeling to experimentation [35,68,69].

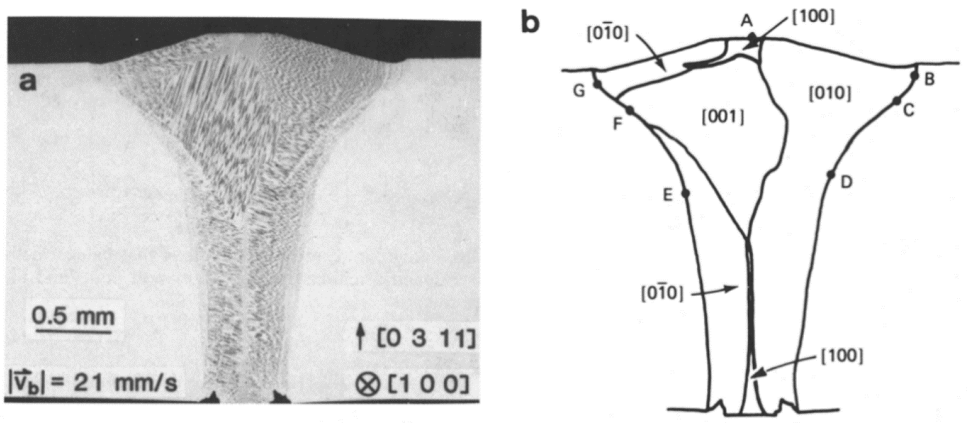

Figure 2.10 (A) Cross section of weld track perpendicular to the travel direction made along the [100] orientation of the base material on the laser travel direction of [0 3 11]. (B) is a schematic of the dendritic pattern shown which demonstrates the change in grain orientation as a function of location. Rappaz et al. [67]

One of the initial experiments in EBM is performed by Körner *et al.* [70]. In the experiment, they demonstrated the ability to tailor the grain structure of IN718 during EBM processing by manipulating the scan strategy of the system. The change in scan strategy manipulates the solidification velocity and thermal gradient across a build. Then, in a single part, Dehoff *et al.* [71] controlled the transition from columnar to equiaxed microstructure as a function of processing parameters in IN718 as seen in Figure 2.11. Dehoff *et al.* leverage the change from a line scan to a spot melt strategy to change the orientation of the grain structure. The DOE lettering was printed as a 2D cross-section throughout a 3D cuboid to explore the capability of grain structure control. Since the work from Dehoff *et al.* there has been continued interest in controlling the grain structure in Nickel superalloys for EBM systems. In a continuation of Dehoff efforts, Haines *et al.* [35] evaluated the columnar to equiaxed transition in nickel-based superalloys by manipulating the compositions and solidification conditions in an EBM process.

More recently, a near single crystal part has been fabricated using the Haynes 282 and Nimonic 105 alloys, by Fernandez-Zelaia et. al. [72]. The control over grain structures can be implemented in the EBM system because of its flexibility it has in controlling the preheat, and therefore thermal gradient and solidification velocity of a material. The creation of single crystal Nimonic 105 is shown in Figure 2.12. In the study, an evaluation of processing parameters is used to determine what will work best for the formation of single crystal material. The manipulation in process parameters will ultimately result in a change in solidification velocity and thermal gradient by manipulating the input conditions of the system. In contrast, L-PBF systems have a limited ability to control the grain structure because of the inability to create a controlled high temperature localized preheat to control the thermal gradient in the material.

The concept of microstructure control has been previously reported in welding. Gill *et al.* [73,74] achieved microstructure control by remelting different Al-Cu alloy with a CO_2 laser to create weld tracks. In the experiments, the primary phase selection in the Al-Cu system was manipulated by three key solidification parameters: solidification velocity (V), thermal gradient (G), and alloy composition. The changes in the solidification mode is understood using the interface response function (IRF).

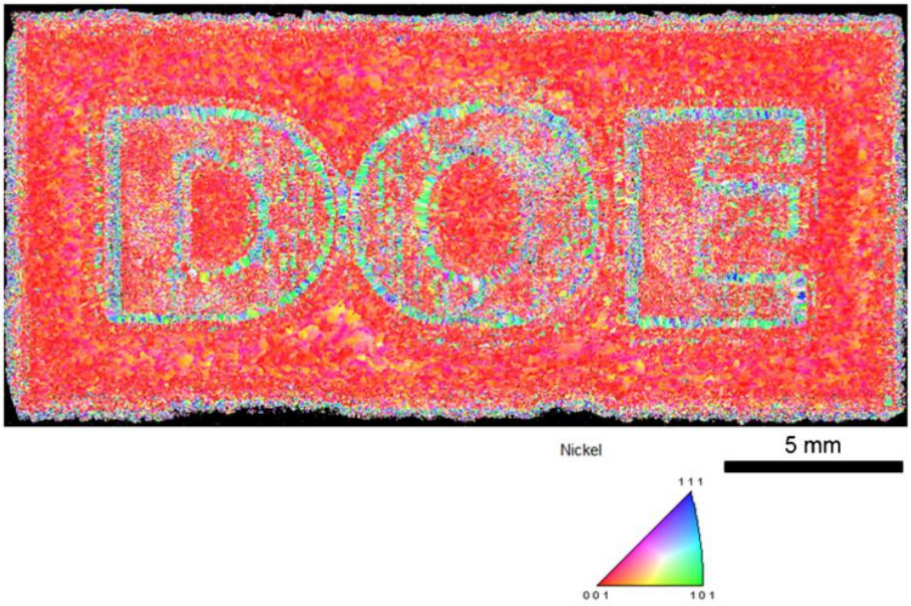

Figure 2.11 The orientation map of a cross section from an EBM build obtained using EBSD. The bulk region demonstrates a columnar solidification grain growth, while the lettering regions demonstrate a more equiaxed microstructure. From Dehoff et al. [71]

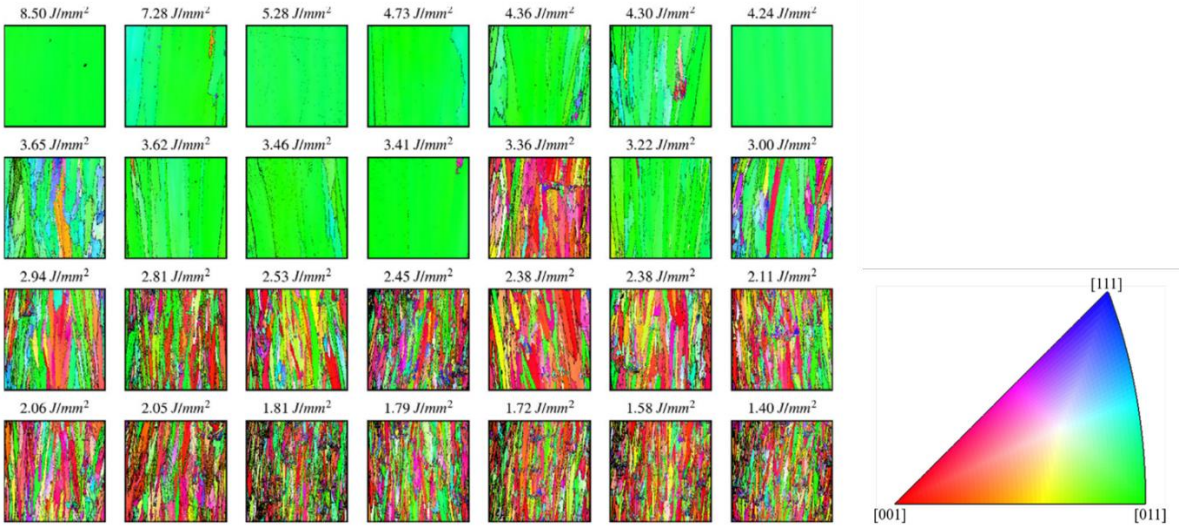

Figure 2.12 Inverse Pole Figures (IPF) are used to show how parameter manipulation can lead to the selection of more single crystal orientations. The build direction is vertical in all images. The plane direction is parallel to the line scan direction. The image demonstrates as a function of processing parameters, the ability to control the grain distribution in the ARCAM process. From Fernandez-Zelaia et al. [72]

The IRF is a collection of models that determines the interface temperature between the solid and liquid phases at set solidification conditions (Planar, Dendritic and Eutectic). Using the IRF for a variety of solidification modes can allow for the determination of the highest interface temperature solidification mode, which should be the stable growth phase at the selected solidification conditions.

Each solidification phase is individually described by a model developed for steady state growth conditions into liquid. Gill *et al.* used the IRF and selected experiments to demonstrate as a function of composition and solidification velocity, the propensity of each solidification state to form at a set thermal gradient $5x10^6$ (m/k), as seen in Figure 2.13.

Additionally, Fukumoto et. al. [75] adapted the IRF to the Fe-Cr-Ni system to understand the transition between austenite and ferrite phase selection based upon a Cr/Ni ratio and the solidification velocity seen in a welded track. Fukumoto implemented a methodology that allowed for the additional elements beyond binary alloys in the IRF model.

The examples by Gill *et al.* and Fukumoto *et al.* are based on work by Kurz and Trivedi that is summarized in "Dendritic Growth" [76]. The work is a combination of methods used to describe three types of solidification microstructures: Dendritic [75,77,78], Eutectic [75,79,80], and Planar [76] as a function of thermal gradient, solidification velocity, and composition. The combination of these three models is known as the IRF. The IRF is used to calculate the undercooling of each solidification phase and postulates that the highest temperature phase will preferentially grow. The dendritic and planar models have developed extensions beyond binary systems, although, the eutectic models for IRF are limited to binary systems. Fukumoto did extend a eutectic model for the Fe-Cr-Ni ternary system, but his solution contained simplifying assumptions that are not generally applicable to all systems. The interface response function will be discussed in more depth in Section 2.2.2.

In AM of SS316L, Godfrey *et al.* [81] demonstrated that there was a change in the primary solidification phase at a melt pool boundary (MPB) and used the IRF as one methodology of rationalization of the primary solidification of austenite instead of the expected ferrite.

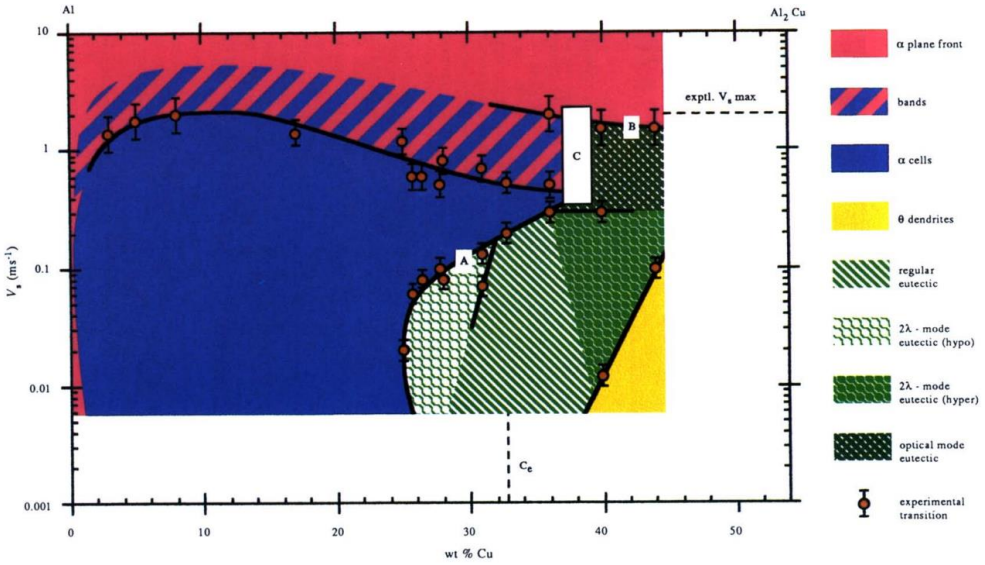

Figure 2.13 Demonstrates the Al-Cu microstructure phase selection map determined by Gill et al. [73,74]. *The map shows the expected primary solidification mode as a function of Cu concentration and solidification velocity at a set thermal gradient in the material. The orange dots represent experimental results targeted at transition points. The colored/patterned regions represent a variety of dendritic or eutectic solidification modes observed in the Al-Cu system.*

The rationalization of phase selection in SS316L was explained by manipulating the diffusivity of elements in the liquid. The reduction in diffusivity of solute elements by an order of magnitude manipulates the IRF to predict the austenite phase as the primary solidification phase at slow solidification velocities.

2.1.5 Aluminum Additive Manufacturing

Czerwinski *et al.* [82] discusses the ability to light weight automotive parts for the production of more sustainable transportation. The light weighting of vehicles can improve the fuel economy where a 100kg of weight reduction will reduce the fuel consumption of a vehicle by 0.3 to 0.5 L/100 km [82]. Czerwinski *et al.* [83] also reports that the corporate average fuel economy for passenger cars must increase by 50% by 2025 mandated by the US Department of Transportation. One way to increase the fuel economy is by replacing large engines with smaller ones. The weight reduction caused by this replacement can increase the fuel economy of vehicles. Additionally, in diesel engines, computer simulations have shown that an increase in 60% power and torque requires an increase in peak temperature on the combustion face of 215°C to 275°C. The combination of a need for engines to run at high temperatures, and materials to keep engines light have opened up room for innovation in the Al alloy design space [83,84].

If AM of aluminum alloys are going to contribute to the improved fuel economy in vehicles, it may be necessary for new alloys to be specifically designed for AM. In AM, the Al-10Si-Mg alloy has been widely adopted because it has a small solidification range resistant to solidification cracking defects [85–91]. However, the alloy demonstrates lower strength than conventional alloys. The Al-10Si-Mg alloy does not retain strength high temperatures [92–94]. Takata *et al.* [95] showed that the tensile strength of an Al-10Si-Mg alloy dropped from 475 MPa to 285 MPa after annealing at 300°C for 2 hours. The drastic reduction in strength at temperature over a short period of time makes Al-10Si-Mg not suitable for high temperature applications (>200°C). Therefore, new compositions are being explored in AM specifically targeted high temperature application [12].

One of the possible alloy design solutions relies on high temperature stable precipitation-based alloys. Typically, in this approach nanoparticle nucleate from the FCC Al matrix is triggered through heat treatment. A variety of work on Scandium containing alloys has been performed in

the L-PBF process because of the nanoparticle coherency with the FCC Al matrix, which can contribute to increased strength [96]. The Sc containing alloys are notable for their formation of a high number density of nano-precipitates during subsequent heat treatment [97–101]. The limitation with Sc based alloys is the high cost associated with alloying.

A different approach relies on intermetallic dispersion strengthened alloys. The basic principle is based on the fact that the strengthening can be achieved by a refined intermetallic network. A common system used for intermetallic dispersion strengthened alloys is Al-Ce [102]. Al-Ce alloys near have notable thermal stability and resistance to solidification cracking in castings [103,104]. The thermal stability, or secondary phases typically $Al_{11}Ce_3$ in the binary system, see reduced particle coarsening compared to more traditional Al alloys. Particle coarsening typically refers to Oswalt Ripening [105].

Oswalt ripening is the phenomenon that attempts to describe the change in the microstructure over time. In solids, small particles will dissolve into the matrix and provide solute for larger particles to continue growth. This occurs because larger particles are more energetically favorable for a system compared to small particles. The reasoning is the Gibbs-Thomson effect which causes the solute in the matrix at the interface of the particles to increase as the radius of the particle decreases. This relationship has been described by Lifshitz-Slyozov-Wagner (LSW) [18,19,106] with the equation assuming the volume diffusion is the rate controlling factor,

$$< \bar{r} >^3 - < r >^3 = \frac{D\gamma X_e}{t}\left[\frac{8V_m(1-X_e)}{9RT(X_P - X_e)^2}\right] \qquad (3)$$

Where $\bar{r}$ (m) is the mean radius with time, r is the initial radius (m), D is the volume diffusivity (m^2/s), γ is the interfacial energy (j/m^2) between the particle and the matrix, X_e is the equilibrium solute (at. %), V_m is the precipitate molar volume (mol/m^3), X_P concentration of solute in the precipitate (at. %), T is temperature (k), and R is the universal gas constant. Using the previous relationship, it is simple to see that for the Al-Ce system, the denominator will be minimized by the high solute in the $Al_{11}Ce_3$ phase ($X_P = 21.4$ at.%), as well as the minimized solute in the matrix ($X_e = <1\text{x}10^{-5}$ at.%). The Oswalt ripening effect is additionally reduced by the relatively low diffusivity ($D \sim 1\text{x}10^{-18}$ m^2/s at 400°C) of Ce observed in FCC Al.

An Al-12Ce (wt.%) alloy was initially evaluated for AM by Plotkowski *et al.* [20] by producing laser tracks over a cast plate. The microstructure near the edge of the weld track was a refined eutectic between FCC Al and $Al_{11}Ce_3$, where the size of $Al_{11}Ce_3$ was refined an order of magnitude to result in the length across lathes at approximately 50-150 nm.

As the solidification velocity of the weld track increased moving toward the center of the weld track, dendritic solidification of FCC Al preferentially formed over the FCC Al and $Al_{11}Ce_3$ eutectic. The change in solidification morphology by Plotkowski *et al.* in the Al-Ce alloy is observed in Figure 2.14. The experimentation by Plotkowski *et al.* confirms the ability of the Al-Ce system to respond to change in the localized solidification conditions. After the work of Plotkowski, Zhou *et al.* [107] investigated an Al-10Ce (wt.%) alloy in L-PBF which it was determined that the Al-Ce alloy could be enhanced with ternary additions. The addition of ternary, or more elements, is discussed because of other work that points to an increase in tensile strength in casting and L-PBF. In the work, an Al-3Ce-7Cu alloy has improved yield strength to the L-PBF Al-10Ce (wt.%) binary, where the yield strengths are reported 222.1 to 274 MPa respectively. Using the Al-Ce system as a base, a variety of Al-Ce-X alloys have been investigated that demonstrate promising mechanical properties.

The Al-Ce-Mg system has been investigated by multiple authors [21,108], where Henderson *et al.* demonstrated the nanoscale particles that form during solidification are resistance to coarsening at 300°C. In the work by Henderson et al., four alloys are compared, AM Al-Ce-Mg, 7075-T6, 2055-T8X, and 2618-T6 which are heat treated at 300°C for 200, 200, 100, and 100 hours respectively. The change in secondary phase diameter is measured along with the hardness as a function of heat treatment is shown in Figure 2.15. In the Al-Ce-Mg alloy, the secondary phase is $Al_{11}Ce_3$. In the other alloys it is a mixture of precipitates. The results of the study by Henderson *et al.* demonstrated that the AM Al-Ce-Mg alloy appears to have more thermal stability and hardness retention after thermal exposure for extended periods.

The Al-Ce-Cu alloy system has also been of recent interest. In the system, two alloys, the Al-4.73Ce-7.78Cu and Al-5.56Ce-7.92Cu-0.82Zr (wt.%) have been investigated, which show an increase in strength with the addition of Zr [109].

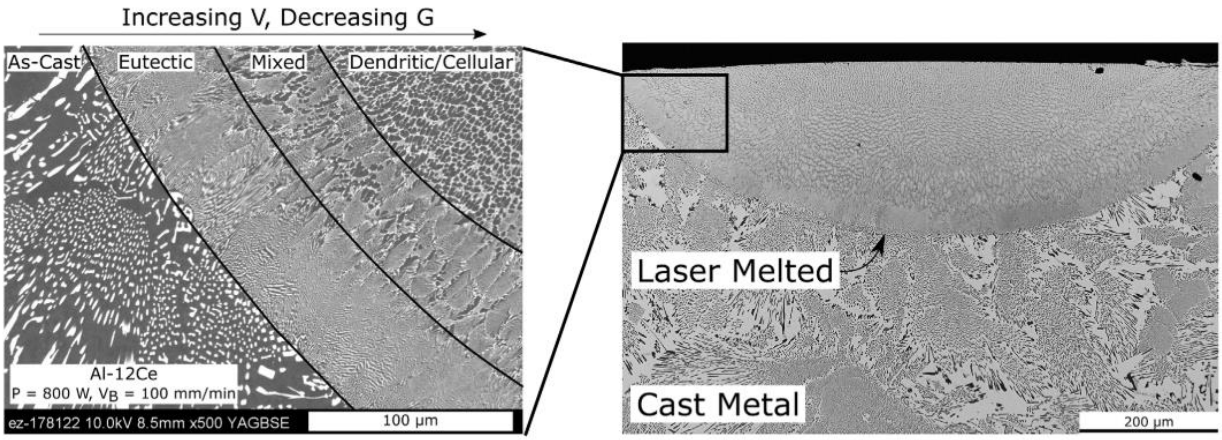

Figure 2.14 Comparison of as-cast and laser remelting using a beam velocity of 100 mm/min in an Al-12Ce (wt.%) binary alloy. Provided by Plotkowski et al. [20]. *In right image an optical micrograph shows a base cast material that on top contains a remelted laser track. The figure shows that the microstructure length scale is refined in the in the weld track as compared to the produced cast material.*

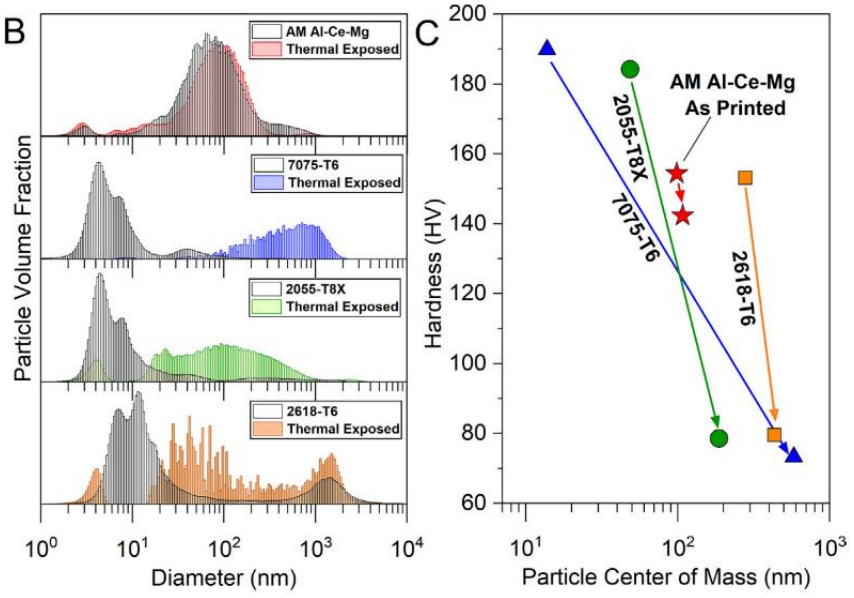

Figure 2.15 shows the change in secondary phase diameter as a function of thermal exposure in three alloys. The particle volume fraction and particle diameter are shown in (B) before and after thermal exposure of 300°C for 100-200 hours. The hardness of the four alloys is also demonstrated in before and after thermal exposure in (C). Taken from Henderson et al. [108]

The intermetallic phase, Al_8Cu_3Ce present from solidification, in both the Al-Ce-Cu and Al-Ce-Cu-Zr alloys, appears to be stabilized with the addition of Zr. In the Zr containing alloy, after 200 hours at 400°C the coarsening was sluggish [110,111]. The effect of this stabilization is seen in Figure 2.16. In Figure 2.16, the alloys were heat treated for 200 hours at a variety of temperatures. In the high temperatures heat treatments of 350 and 400°C, the Al-Cu-Ce alloy appears to have undergone a phase change which increased the rate of coarsening in the system.

Additional alloys in the Al-Ce-Ni family [112,113] have been processed by additive manufacturing. The Al-Ce-Ni-Mn showed improved creep performance with respect to several cast alloys at high temperatures (up to 400°C). Literature has shown Al-Ce-X systems have the potential for promising high temperature properties. However, some of the Al-Ce-X systems have been noted that the initial phase selection and subsequent phase decomposition appears are sensitive to the initial solidification conditions. In the Al-Cu-Ce and Al-Ce-Ni-Mn alloys, there are different metastable solidification phases that form across a single weld track. As these alloys are heat treated, the local response of the microstructure appears to change. This led to a question, how does the initial solidification influence the stability of the microstructure during AM? In the current work, an Al-10Ce-8Mn (wt.%) alloy is used to explain the heterogeneous microstructure produced by AM, which In turn can modify the microstructure evolution during heat treatment.

A summary of relevant alloys, their challenges, and their impact on the AM technology is provided in Table 2.1. It is notable that this list is not all encompassing but covers several of the possible pathways in AM Al alloys design. There are significant amounts of work in the Al-Sc-(X) system that is not listed here, because it follows the same general principal as the Al-Mg-Si-Sc-Zr. These alloys have additional slow diffusing elements to stabilize the system with time and temperature.

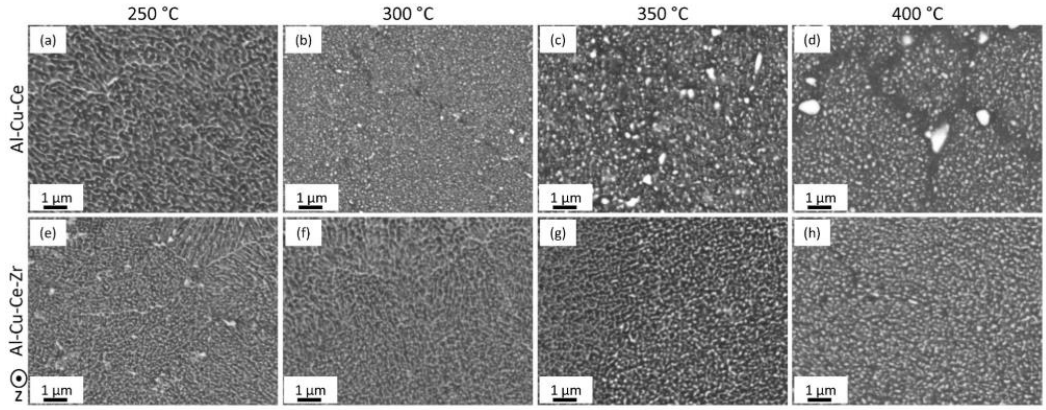

Figure 2.16 SEM images of (a-d) Al-Cu-Ce after heat treatment for 200 hours at a variety of temperatures from 250 to 400°C, and (e-h) Al-Cu-Ce-Zr alloy after heat treatment for 200 hours at a variety of temperatures from 250 to 400°C. Bahl et al. [109]

Table 2.1 Description of some current Al alloys designed for AM.

Alloy	Challenges	Impact
Al-10Si-Mg	Additive Al Base Line	Easily Printable AM Alloy
Al-Ce-Ni-Mn [113]	Highly Heterogeneous Microstructure with several unique metastable phases	Promising HT Properties and Creep Performance
Al-Mg-Si-Sc-Zr [114]	High Cost	Good Performance Through grain refinement and precipitation
Al-Cu-Ce-(Zr)[109]	Phase Selection Controlled by Addition/Removal of Zr	Easy to Process/improve thermal stability over the AlSiMg
Al-Cu-Mn-Zr [115,116]	Different Strengthening mechanisms to conventional counterpart	Adopting Traditional Compositions to AM
Al-Ce-Mg [21]	Vaporization of Mg	New Scan Strategies to reduce keyhole porosity
Al + TiC Nano Particles [117]	Creating Bulk Parts	Initial promising micropillar compression results up to 1000 MPa

2.2 Process Modeling

In this section, two types of process modeling are discussed. The first is the prediction of a weld pool geometry, which allows for the calculation of solidification conditions such as thermal gradient (G) and solidification velocity (V). The second is the interface response function (IRF). The IRF allows for the prediction of the primary phase at a particular set of solidification conditions (solidification velocity, thermal gradient, and composition) from the liquid. The model can be used to select processing conditions that may lead to preferred phase selection during AM. The goal of this section is to predict the localized solidification conditions (solidification velocity, thermal gradient, and composition), so that the IRF model may be used to rationalize the microstructure evolution.

2.2.1 Weld Track Prediction

In the work, the classical point source Rosenthal model [118,119] is used to determine the local thermal conditions across a weld pool. The Rosenthal model allows for the calculation of the temperature isotherms around a steady state weld track. The Rosenthal model has two key assumptions: (1) thermal conductivity, and thermal diffusivity are independent of temperature, (2) The speed and the heat input of the heat source is constant. The two assumptions are used by Rosenthal to derive heat flow due to a moving heat source from the following differential equation assuming a rectangular coordinate system.

$$\frac{\partial^2 T}{\partial x^2}+\frac{\partial^2 T}{\partial y^2}+\frac{\partial^2 T}{\partial z^2}=\frac{1}{2\alpha}\frac{\partial T}{\partial t} \qquad (4)$$

Where T is temperature, (x, y, z) are spatial coordinates to a fixed origin, α is thermal diffusivity, and t is time. Using the differential equation, and the simplifying assumption that the heated material is infinite, implying $\frac{\partial T}{\partial x}=\frac{\partial T}{\partial y}=\frac{\partial T}{\partial z}=0$ when x, y, z = ∞, for a point source heat source, the classical point source Rosenthal model [118,119] was derived.

$$T(x,R)=T_0+\frac{\eta P}{2\pi k}\left(\frac{1}{R}\right)\exp\left(-\frac{v}{2a}(R+x)\right) \qquad (5)$$

Where, T_0 is the initial temperature, η is the absorption efficiency of the material, P is the input power, k is the thermal conductivity, α is the thermal diffusivity, and the distance to the heat source is defined by,

$$R = \sqrt{x^2 + y^2 + z^2} \quad (6)$$

The thermal gradients are determined in the Rosenthal model by taking the derivative at the temperature isotherm of interest, wherein

$$G = |\nabla T(x, y, z)|_{T=T_L} \quad (7)$$

T_L is the expected liquidus temperature. Using the thermal gradient, the solidification velocity is determined by through the relationship reported by multiple authors [120,121],

$$V_s = \overrightarrow{V_{Laser}} \cdot \vec{n} \quad (8)$$

Where V_s is the solidification velocity, $\overrightarrow{V_{Laser}}$ is the direction of the laser, and $\vec{n}$ is the unit vector normal to the weld track surface determined by the thermal gradient. It is important to note that in the Rosenthal model, the solidification velocity is limited to the laser velocity, as the maximum surface normal is one. The surface of the weld track is approximated by the Rosenthal equation to approximate the solidification conditions.

One of the manipulations to the Rosenthal model is changing the spatial distribution of the heat source. Grong [120] outlines a variety of methods to manipulate the local distribution of heat sources. A commonly adopted heat source is the two-dimensional Gaussian distribution. The issue with the adoption of a Gaussian heat source in the Rosenthal model is the solution is no longer analytical and must be iteratively solved. Therefore, a line heat source is commonly adopted to approximate a Gaussian heat source to have a direct solution for the temperature vs. time.

A second problem for the Rosenthal methodology is its inability to describe the weld crater/weld finger formation, which is demonstrated in Figure 2.17. The classical single point source solution cannot model an abnormal weld pool shape. A common solution to this is to use two discrete point source solutions to model the finger and crater separately. To create the observed crater/finger formation, a second discrete point source is displaced into the plate to achieve the observed finger geometry. The weld track in this case is calibrated using ex-situ measurements.

Moving past the Rosenthal model, in L-PBF process Wei *et al.* [122] outlined modeling efforts to understand the complex conditions. The full complexity is not discussed here, but the five key components of weld pool modeling are (1) the heat transfer, (2) the fluid flow in the weld track, (3) temperature dependent thermophysical properties, (4) the heat source descriptions, and (5) powder packing. To simulate these conditions, several models have been developed to capture the intricacies with the tradeoff of computational cost [123,124]. A list of common open-source software used for modeling the AM process is shown in Table 2.2. The tradeoff between these models is as the complexity of the model is increased, the runtime of the model is increased. Table 2.2 demonstrates a very limited view of the possible models used to understand a weld pool during AM that covers the range of complexity in a weld pool. More information about weld track modeling from classical welding and AM can be found by Grong [120], Dantzig and Rappaz [125], or Wei *et al.* [122].

2.2.2 Interface Response Function Model

The interface response function (IRF) can be used as a criterion for the selection of a particular growth mode during solidification. The IRF is calculated for a given solidification condition (set solidification velocity, thermal gradient, and composition). The IRF models describe planar, dendritic, and eutectic growth during solidification. In the current work, the dendritic growth model is the only implementation because of its relevance to the problem of primary intermetallic phase selection. The eutectic growth model is also relevant, but in its current development stage does not have the ability to consider to the ternary system of interest.

The dendritic IRF model, called the IRF for the remainder of the document, calculates cumulative undercooling determined by five undercooling parameters.

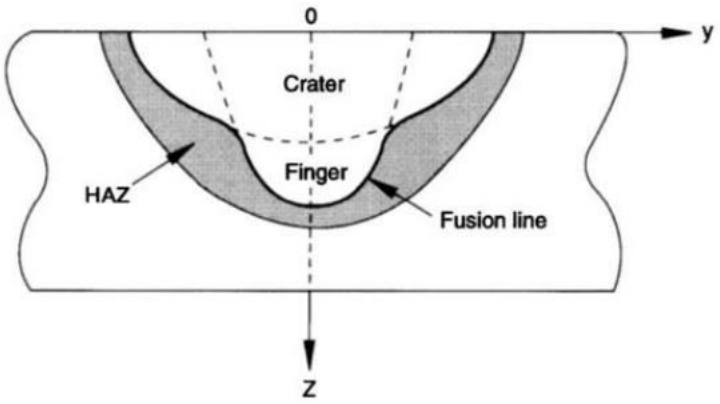

Figure 2.17 Example of a crater/finger weld tack taken from Grong et al. [120]

Table 2.2 Open-source heat transfer solutions to weld track modeling in AM.

Model	Method	Model Scope	Source
3D-Thesis	Semi-Analytical	Conductive Heat Transfer Gaussian Heat Source	[126,127]
Pennsylvania State University	Numerical Solution (Traveling Grid)	Layer wise Powder Additions Conductive Heat Transfer Fluid Flow	[124,128]
Truchas	Finite Volume	Modular Heat Source Conductive Heat Transfer Convective Heat Transfer Radiative Heat Transfer Surface Tension affects Fluid Flow	[129]

$$\Delta T = \Delta T_T + \Delta T_R + \Delta T_C + \Delta T_K + \Delta T_{Cell} \quad (9)$$

These undercoolings are, ΔT_T or the undercooling required to move the latent heat of fusion away from the dendrite, ΔT_R the undercooling due to the Gibbs-Thomson Effect, ΔT_C the constitutional (solutal) undercooling, ΔT_K the undercooling for attachment kinetics from the liquid to the solid, and ΔT_{Cell} is the cellular undercooling at low interface velocities.

In the current investigation, the ΔT_T is ignored because in AM it is assumed there is directional solidification, which implies there are large thermal gradients into the solid phase. The large thermal gradients conduct latent heat away from the solid/liquid interface into the solid phase. Since the heat is conducted away from the solid/liquid interface into the solid and not the liquid, the ΔT_T term is minimized. The result of the previous effect leads to the assumption that the thermal undercooling is approximately zero.

The first two terms described here are the ΔT_R, and ΔT_{Cell}. The ΔT_R term is an undercooling resulting from the capillary effect and is described in the following equation.

$$\Delta T_c = \frac{2\Gamma}{R} \quad (10)$$

Where R is the dendrite tip radius, and Γ is the Gibbs Thomson coefficient described by

$$\Gamma = \frac{\gamma V_m}{\Delta S_m}, \quad (11)$$

where γ is the interfacial energy between the solid and the liquid phases, V_m is the molar volume of the phase, and ΔS_m is the entropy of fusion per mole for the solid phase forming from the liquid. The capillary effect is simply a result of the predicted radius and does not influence the iterative solution on the system. The cellular undercooling at low interface velocities is described by

$$\Delta T_{Cell} = \frac{GD}{V}, \quad (12)$$

where G is the thermal gradient, V is the solidification velocity, and D is the liquid diffusivity of the solute.

The next two undercooling terms, ΔT_C and ΔT_k have more complicated descriptions and are derived by Kurz and Trivedi [76]. To solve these terms, the derivation of the interface response function will be explored, which will provide two key missing variables, the dendrite tip radius, and the composition of the liquid at the dendrite tip.

The current derivation follows the solution described by Kurz and Trivedi [76]. In the derivation of the IRF by Kurz and Trivedi, the Ivantsov solution is used to describe concentration profile across a parabolic dendrite tip, assuming both the diffusion and shape preservation equations are satisfied [76]. The Ivantsov solution describes the tip of a dendrite by defining it as a fixed shape parabola for a set Peclet number growing into the liquid at a steady state. The Peclet number describes the transport of a substance by bulk motion of a fluid (advection) to the rate of the diffusion transport. A schematic of the dendrite tip is seen in Figure 2.18A which demonstrates a parabolic axis away from the dendrite tip.

The differential equation governing the steady state thermal diffusion is ignored because of the assumption that there is directional solidification. The differential equation governing the steady state solute diffusion is defined by

$$\frac{\partial^2 C}{\partial z^2} + \left(\frac{V}{D}\right)\left(\frac{\partial C}{\partial z}\right) = 0 \qquad (13)$$

where C is concentration, V is the solidification velocity, D is solute diffusivity in the liquid, and z is the distance away from the dendrite tip. To solve the steady state solute diffusion relationship, Ivantsov derived a coordinate transformation from a parabolic axis to determine the composition of the liquid at a dendrite tip.

The solution to Eq. (13) is shown in Eq. (14).

$$C_{t,i} - C_{0,i} = C_{t,i}(1 - k_i)Iv(Pe_i) \qquad (14)$$

where $C_{t,i}$ is the composition in the liquid at the dendrite tip (for each element, i), $C_{0.i}$ is the bulk composition of the liquid (for each element, i), k_0^i is the equilibrium partition coefficient.

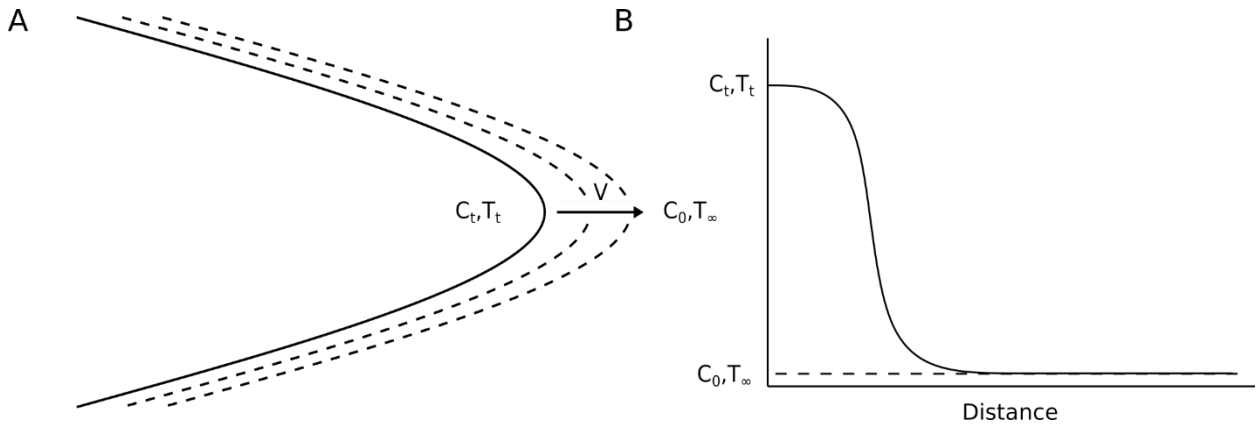

Figure 2.18 Contains two schematics that demonstrates (A) the Ivantsov parabolic coordinate system (B) the composition ahead of the dendrite tip.

(for each element, i), Iv(Pe_i) is defined in Eq. (16), and Pe_i is the Peclet number (for each element, i), which is a dimensionless number defined by Eq. (15)

$$Pe_i = \frac{RV}{2D_i} \tag{15}$$

where R is the dendrite tip radius, V is the solidification velocity, and D_i is the liquid diffusivity of a particular element, where i denotes the element.

The Ivantsov function, or the coordinate transformation, defined for a parabolic geometry is defined by Eq. (16).

$$Iv(Pe_i) = Pe_i * e^{Pe_i} * E_1(Pe_i) \tag{16}$$

$E_1(Pe)$ is the exponential integral function of the Peclet number.

In the current application, the solidification velocity (V) and thermal gradient (G) are fixed, and an iterative solution is used for determining the radius, which subsequently determines the Peclet number.

The radius solution used is estimated from the linear stability analysis of a planar front [125], defined in Eq. (17).

$$R = \left(\frac{\Gamma}{\sigma^*(\sum_0^i m_i G_{c,i}\xi_i - G)}\right)^{\frac{1}{2}} \tag{17}$$

where, σ^* is the dendrite tip selection parameter determined by Kurz and Trivedi as 0.025 [76], m_i is the liquidus slope (for each element, i), in the current case approximated at the initial liquidus composition, G is the thermal gradient of the material into the solid, ξ_i is the deviation from equilibrium also known as the variation for solute as a function of the Peclet number (for each element, i),.

$$\xi_i = \frac{2k_0^i}{\sqrt{1 + \frac{1}{Pe_i^2 \sigma^*}} - 1 + 2k_0^i} \tag{18}$$

and $G_{c,i}$ is the concentration gradient in the liquid ahead of the dendrite tip (for each element, i),

$$G_{C,i} = \frac{\left(C_{t,i} - C_{0,i}\right)V}{D_i \, Iv(Pe_d)} \tag{19}$$

These equations are used by Kurz and Trivedi as well as other authors [76,130].

Once a solution is found that converges on a dendrite tip radius, the undercooling of the system can be determined. In the current example, the solution is defined by the linear approximation from Kurz and Trivedi [76]. The linear approximation defines the liquidus line using the equation $T_t = T_M + mC_t$, where T_t is the dendrite tip temperature, T_m is the pure melt temperature, m is the linear liquidus slope, and C_t is the composition of the liquid at the dendrite tip interface. Using the direct example laid by Kurz and Trivedi, the undercooling of a dendrite tip is defined by

$$\Delta T = \frac{k_0^i \Delta T_0 Iv(Pe_i)}{1 - \left(1 - k_0^i\right) Iv(Pe_i)} + \frac{2\Gamma}{R} + \frac{GD}{V} + \Delta T_K \tag{20}$$

Where the ΔT_C term is replaced as a function of linear approximation and ΔT_K has yet to be defined.

The initial derivation shown above assumes there is no deviation from equilibrium solidification. However, it is well understood that during solidification non-equilibrium effects occur. Kurz and Trivedi acknowledge three non-equilibrium effects (1) the effect of attachment kinetics, (2) the variation in solute partitioning as a function of velocity, and (3) the change in interface

compositions due to thermodynamic constraints. The three non-equilibrium effects will play a role together to determine a non-equilibrium composition of the liquid and dendrite tip.

First is an investigation into the effect of attachment kinetics. Initially, consider that the motion of any solid/liquid interface must have departure from local equilibrium, or the interface will not move. Using this assumption, the driving force required for motion is defined by the reaction rate theory of atomic jumps.

$$V = V_0(1 - e^{-\frac{\Delta G_m}{R_g T}}) \tag{21}$$

where ΔG_m is the free energy required for interface motion, R_g is the gas constant, T is the interface temperature, and V_0 is on the order of the velocity of sound in a solid solution matrix. For intermetallic compounds, V_0 is controlled by bulk liquid diffusion [131], D_l and speed of interface diffusion, V_{DI}. Using the attachment rate kinetics equation, an additional assumption is made that the ΔG_m for the attachment kinetics is proportional to the kinetic undercooling.

$$\Delta G_m = \Delta S_m \Delta T_K \tag{22}$$

where ΔS_m is the entropy of fusion. This assumption allows for the undercooling to be predicted using the relationship.

$$\Delta \mathrm{T_k} = -\frac{R_g T_i}{\Delta S_m} \ln\left(1 - \frac{V}{V_0}\right) \tag{23}$$

The relationship can be simplified for approximant dilute linear systems described by Kurz et al. [76]

$$\Delta \mathrm{T_k} = \frac{V m_i}{V_0\left(1 - k_0^i\right)} \tag{24}$$

where, m_i is the liquidus slope for each element i. The second, non-equilibrium effect to consider is the non-equilibrium partitioning of solute. It has been shown in literature that partition coefficients change as a function of solidification velocity. Aziz *et al.* [132] describes this effect for the solute redistribution that occurs during rapid solidification.

$$k_v^i = \frac{k_0^i + \left(\frac{a_0 V}{D_i}\right)}{1 + \left(\frac{a_0 V}{D_i}\right)} \tag{25}$$

where k_0^i is the equilibrium partition coefficient at the dendrite tip composition, C_t^i, a_0 is of the order of interatomic distance, sometimes referred to as the characteristic diffusion length, and D_i is the liquid diffusivity of an element. Solute trapping occurs when the composition of the solid and liquid phases are the same, or the partition coefficient k_v^i = 1, typically referred to as the T_0 line. A schematic of trapping as a function of solidification velocity is shown in Figure 2.19 The non-equilibrium partition coefficient is incorporated in the model by applying it directly to the diffusion equation solved by the Ivantsov function, as seen in Eq. (27).

The implementation of the Aziz solute trapping model additionally changes the liquidus slope of the system. Kurz and Trivedi acknowledge this by developing a relationship for the change in liquidus slope as a function of partitioning. The velocity dependent liquidus slope is defined by

$$m_i^v = m_i \left(1 + \frac{k_0^i - k_v^i \left[1 - \ln\left(\frac{k_v^i}{k_0^i}\right) \right]}{1 - k_0^i} \right) \tag{26}$$

where the liquidus slope is defined per element with its respective partition coefficients. The third approximation is combined into the kinetic undercooling using the simplification of a dilute system, and the approximation of a non-equilibrium liquidus slope which will manipulate the convergence on a Peclet number.

$$\Delta T = \frac{k_v^i \Delta T_0 Iv(Pe)}{1 - \left(1 - k_v^i\right) Iv(Pe)} + \frac{2\Gamma}{\mathrm{R}} + \frac{GD}{V} + \frac{V}{\mu_k} \tag{27}$$

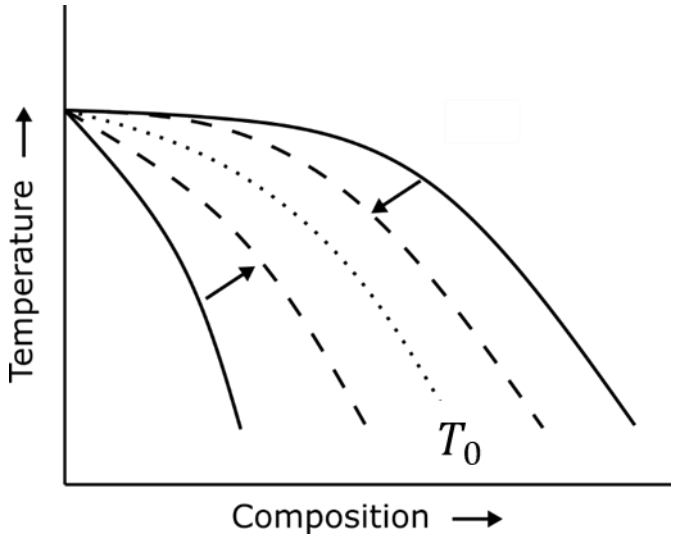

Figure 2.19 Demonstrates the effect of the Aziz solute trapping model.

In Chapter 5, the change in interface compositions due to thermodynamic constraints will be directly solved. The combination of all the previously mentioned parameters lead to the undercooling of a dendrite tip in direction solidification described by

2.3 Solid State Phase Transformations

In this section, an introduction to solid-state phase transformations is described. The goal of this section is to understand the link between solidification and the subsequent decomposition of solidified phases can be understood. In solid state phase transformations, there are two key mechanisms that are relevant, nucleation and growth. These processes occur in order when new precipitates form, being that nucleation of a new particle must occur before the growth of that particle. It is notable that growth can occur on existing particles in the microstructure and is generally considered an easier process because it can occur on preexisting phases in a material that are not inhibited by a nucleation barrier. Nucleation and growth will be discussed in the following sections.

2.3.1 Introduction to Nucleation

The solidification processes provides the initial microstructure in which solid state phase transformations can occur. The microstructure and solute in the matrix is at an initial point from which solid state phase transformations starts. The formation of stable or metastable product phases from the parent microstructure is generally attributed to a reduction in the barrier to nucleation, or the activation energy, [133–136] for a product phase. The activation energy for a precipitate nucleating out of a matrix can be determined as a balance of interfacial energy (γ), volumetric driving force (ΔG_v), and long-range strain energy (ΔG_s). The effects of activation energy are prevalent in all phase transformations and influence the pathways depending on the initial microstructure.

The classical approach to homogeneous nucleation assumes a matrix α that is rich in element A and has a solid solution of element B. A precipitate can form when a clustering of the B atoms initiates the nucleation of a β precipitate. The classical models for nucleation rely on three key variables. The first, is the reduction in volumetric driving force, ΔG_v, for the formation of the β phase from α phase. The driving force can be calculated using the driving force modules within

software based on the CALPHAD approach. The second term is the interfacial energy, γ, associated with the formation of the new interface $\alpha|\beta$. The third term is the misfit strain energy, ΔG_s, which is defined as the strain created by introducing a new particle that produces long-range elastic deformation within the parent matrix. These three terms can be combined to determine the total change in free energy in the system for homogeneous nucleation [105], given in Eq. (28).

$$\Delta G = -V\Delta G_v + A\gamma_{\alpha|\beta} + V\Delta G_s \tag{28}$$

The change in free energy has a critical point above which nucleation can occur and is referred to as the activation barrier. The activation barrier can be described by assuming a shape for a precipitate. Typically, the precipitate is assumed to be a sphere, where the $V = \frac{4}{3}\pi r^3$ and $A = 4\pi r^2$. Using the assumption that the nucleus is a sphere, the critical radius can be determined using $d(\Delta G)/d(r) = 0$, Eq. (29).

$$r^* = \frac{2\gamma}{(\Delta G_v - \Delta G_s)} \tag{29}$$

In the above equation, ΔG_s reduces the net ΔG_v. Using the critical radius, the activation barrier can be determined by combining Eq. (29) and Eq. (28) for Eq. (3).

$$\Delta G^* = \frac{16\pi\gamma^3}{3(\Delta G_v - \Delta G_s)^2} \tag{30}$$

This relation has been expanded to more unique cases such as nucleation at grain boundaries. In Figure 2.20A, a schematic of a newly formed β precipitate at an α grain boundary is shown.

Investigating the homogeneous nucleation of a secondary phase, β, at the grain boundary of a matrix. The total change in free energy in a homogeneous nucleation including the destruction of the original interface results in

$$\Delta G = -V\Delta G_v + A_{\alpha|\beta}\gamma_{\alpha|\beta} - A_{\alpha|\alpha}\gamma_{\alpha|\alpha} + V\Delta G_s \tag{31}$$

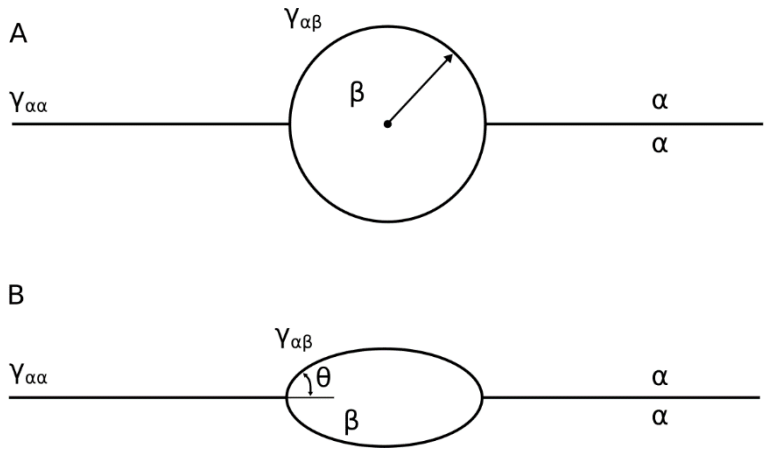

Figure 2.20 Demonstrates two cases of nucleation at a grain boundary where A) demonstrates the homogeneous nucleation of a sphere at a grain boundary, B) demonstrates a heterogeneous nucleation case where the nucleus is defined by spherical caps related to the interfacial energy between phases.

Discussed by Porter and Easterling [105] if you ignore the misfit strain energy, the optimal shape of a nucleus should minimize the surface energy. The result, assuming a spherical basis for the nuclei will be a function of the angle described by the interfacial energies. Therefore, the heterogenous nucleation barrier is described by the equation.

$$\Delta G^*_{het} = \Delta G^*_{hom} S(\theta) \tag{32}$$

where $S(\theta)$ is a shape factor of the nucleus

$$S(\theta) = \frac{1}{2}(2 + \cos\theta)(1 - cos\ \theta)^2 \tag{33}$$

The θ is the optimum angle at which a spherical cap will exists on a grain boundary, described as

$$cos\theta = \frac{\gamma_{\alpha|\alpha}}{2\gamma_{\alpha|\beta}} \tag{34}$$

Using the determined activation energy, the nucleation rate of a phase can be calculated. Discussed by several authors, [105,137,138] the description of nucleation rate can be used to rationalize the rate of nucleation change as a function of increased nucleation sites. Eq. (35) describes the rate of formation of particles at the critical size for stability.

$$N_{hom} = Ce^{-\frac{\Delta G^*}{kT}} \tag{35}$$

In the nucleation rate equation, C encompasses a variety of parameters such as the number of nucleation sites and the attachment rate of atoms, as well as the activation energy for atoms jumping across an interface. The nucleation rate equations have been applied with various authors [139,140]. There are a variety of different applications of the nucleation rate equations which change how the initial parameter C is described [140,141]. The discussion by Lange *et al.* [140] additionally address the relationship between a coherent interface that can occur on one side of a grain boundary during nucleation.

2.3.2 Introduction to Growth

Growth of a precipitate occurs after the nucleation event. The growth of particles is not discussed in detail in the document, but the fundamentals of how growth occurs are important to gaining insight into the phase transformations observed in the Al-Ce-Mn system.

An important concept to growth is the transport of solute across the parent and product phases. Solute transport can occur through a matrix or over all interface types such as coherent, semi-coherent, and incoherent interfaces. In the current work, the diffusion is expected to largely occur over incoherent interfaces because of the phases in the Al-Ce-Mn system. The growth equation in which a general solution for growth rate behind a planar incoherent interface in a binary system is described by Porter and Easterling, derived from Zener's initial approach [105,142], and shown in Eq. (36).

$$v = \frac{D}{C_{Precipitate} - C_{Matrix}} * \frac{dC}{dx} \tag{36}$$

where D is the mass diffusion coefficient of the solute, $C_{Precipitate}$ is the composition of the precipitate, C_{matrix} is the composition of the solute in the matrix, and $\frac{dC}{dx}$ is the concentration gradient near the interface of the phase of interest. The concentration gradient relationship has been simplified in the past by Zener *et al.* [142] to be approximated with a linear profile. The relationship of the growth of a planar interface can be extended to describe the lengthening of a plate or needle precipitate, and the thickening of plate like precipitates through lateral migration using ledge mechanisms. The growth of precipitates is limited to the rate solute can diffuse to the interface, the supersaturation of a matrix, and the chemical potential of the elements in the phases of interest. Therefore, growth is highly dependent on the localized conditions in the material surrounding a precipitate.

In a specific example of the growth of the θ phase in an Al-Cu system. It was observed that grain boundaries and interphase boundaries can accelerate diffusion. The excess solute along grain boundaries, coupled with its increased diffusivity of solute can allow significant increases in the rate of growth [143,144]. In Al-Cu alloys explored by Aaron *et al.* [143], the growth of a θ phase has been observed by a two-step diffusion process where Cu diffuses from the α $(FCC\ Al)$ phase to the $\alpha|\alpha$ grain boundaries. Then, the Cu is transported along the interface boundaries to the growing θ phase. This was hypothesized because the lengthening and thickening rate of θ occurred orders of magnitude quicker than what is possible with measured bulk volume diffusion

of Cu in FCC Al. The result by Aaron was at 300°C, the interface diffusion was 4.02×10^{-10} (m^2/s) and the bulk volume diffusion were calculated as 3.8×10^{-17} (m^2/s). The significance of this result demonstrates that diffusion along interface boundaries can increase the growth rate of precipitates in a system.

There are additional difficulties related to predicting the growth of new phases at pre-existing parent interfaces. One such example is the microsyntactic intergrowth of cementite and χ in steels. Nagakura *et al.* [145] discusses this topic wherein the higher order carbides θ_n-$Fe_{2n+1}C_n$ and χ phases grow simultaneously to relieve elastic strain formation in material. It is observed that to form cementite, higher order caribes θ_n-$Fe_{2n+1}C_n$ and χ gradually transform to cementite (θ-Fe_3C) as a function of tempering. The conclusion to draw from this work is that growth, or nucleation of an inter-boundary phase could assist in the nucleation and growth of new phases.

The overall motivation to understand growth is that just because a phase can nucleate does not mean it will be able to consume the product phase. If a phase fails to continue growth, it is likely that over time the nuclei will be reabsorbed into the surrounding material to provide solute for larger particles that are more stable.

2.3.3 Introduction to Kinetics Modeling Including Nucleation and Growth

The classical approach to describing phase transformations is by the Johnson, Mehl, Avrami, and Kolmogorov referred to as the JMAK model [146–148]. The JMAK model describes the nucleation and growth of a product phase over a random and homogeneous parent phase. A specific example of a modification of the JMAK equation is discussed by Robson *et al.* using Cr-Mo steels. Where a non-equilibrium microstructure, consisting of ferrite (BCC phase) and cementite (M_3C, M represents metallic elements) undergoes a series of solid-state phase transformations, forming a mixture of ferrite with M_2X (X represents C and/or N) and $M_{23}C_6$ carbides [149]. Robinson *et al.* extended the JMAK model by a demonstration that phase transformations can occur in sequences, which allowed for the modeling of simultaneous nucleation and growth of multiple phases. The transformation pathway observed in Cr-Mo steels has been rationalized based on nucleation site density, interfacial energy, and driving force, by using phenomenological theories of overall transformation kinetics [138,149]. The benefit of having the ability to predict the reaction kinetics with the JMAK model (and specifically the

extension by Robinson and Bhadeshia) is the ability to predict the time-temperature-transformation diagram (TTT) which can allow for the reactions during heat treatment to be predicted a priori based on interfacial energies, number densities of nucleation sites and thermodynamic data.

Once the initial solidification microstructure of an alloy is known, then it can be possible to use kinetics modeling to understand how the material will change during heat treatment. The ability to link solidification microstructure to the solid-state phase transformations can be invaluable to understanding the longevity of a microstructure that can influence initial design decision of a part. Though, the current work only looks at the initial steps to approach the complete understanding of the Al-Ce-Mn material.

2.4 Background on the Al-Ce-Mn System

In this section, a background of previous work on the Al-Ce-Mn system will be explored to give a baseline of understanding for the continued work in this dissertation. The focus of the current work is to investigate the solidification phase selection and subsequent solid-state decomposition of the solidified phases.

2.4.1 Phase Selection During Solidification in Al-Ce-Mn System

In casting of the Al-9.0Ce-6.2Mn (wt. %) system, Yang *et al.* [150] observed solidification of the metastable $Al_{20}Mn_2Ce$ phase over the equilibrium $Al_{10}Mn_2Ce$ phase. Yang's calculations showed that differences in solid-liquid interfacial energy, 0.166 and 0.321 (j/m^2) respectively, result in a competition between homogenous nucleation of the two intermetallic phases as a function of undercooling in the liquid, and the $Al_{20}Mn_2Ce$ phase preferentially nucleates when the undercooling is high. In laser additive manufacturing, higher undercoolings (> 100 °C) compared to that of casting are indeed expected due to large solidification velocity values, i.e., reaching up to 1 m/s. Yang *et al.* also demonstrated that in the casting microstructure, the $Al_{20}Mn_2Ce$ phase decomposes into $Al_{10}Mn_2Ce$, at 350, 400 and 450° C for a variety of heat treatment times. In Figure 2.21, the initial and heat-treated microstructure of a cast Al-Ce-Mn alloy by Yang *et al.* is shown.

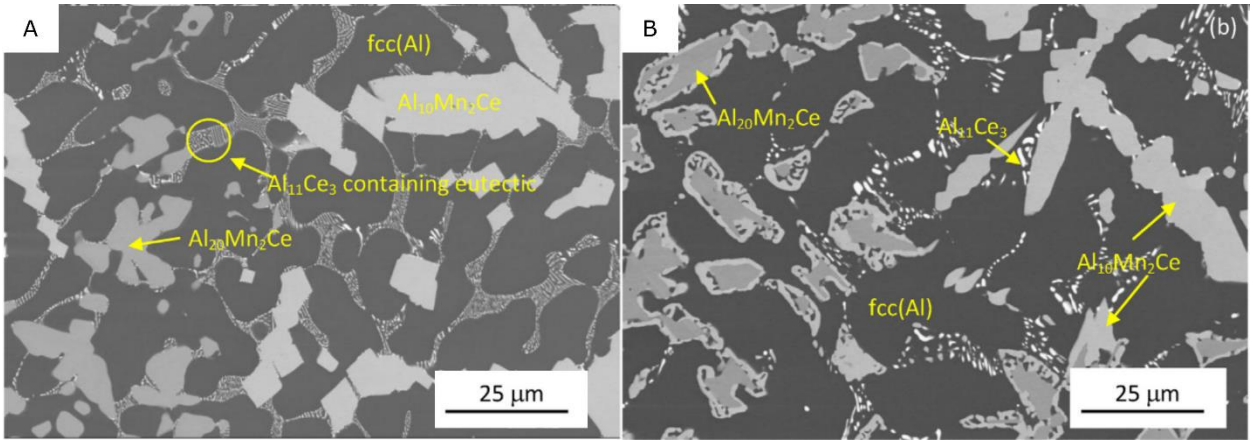

Figure 2.21 SEM BSE provided by Yang et al. [150], *where (A) is an as-cast Al-Ce-Mn alloy that demonstrates four phases, FCC Al, $Al_{10}Mn_2Ce$, $Al_{20}Mn_2Ce$, and $Al_{11}Ce_3$. (B) is a heat treated at 400°C for 100 hours Al-Ce-Mn casting that demonstrates the $Al_{20}Mn_2Ce$ decomposing into $Al_{10}Mn_2Ce$.*

In additive manufacturing of Al-Ce-Mn, Plotkowski *et al.* [151] observed the suppression of the $Al_{10}Mn_2Ce$ phase and a mix of non-equilibrium primary $Al_{20}Mn_2Ce$ particles at the weld track boundary where the solidification velocity is low and thermal gradient is high, and the onset of eutectic solidification including FCC Al and $Al_{20}Mn_2Ce$ near the center of the weld track where the solidification velocity is high, and the thermal gradient is low. These two regions of microstructure, while containing the same phases, FCC Al, $Al_{11}Ce_3$, and $Al_{20}Mn_2Ce$, decomposed into two different microstructures at temperature from (300-450°C), which will be explored in Chapter 3.

Other studies have also reported interesting microstructural features and phase transformations in the Al-Ce-Mn system for cooling conditions between the extremes of casting and AM [152–155]. Coury *et al.* investigated the Al-Ce-Mn system in three different studies. The first, was an investigation into the quasicrystal formation in the Al-Ce-Mn system using melt spun casting [153]. In this study phase equilibrium was investigated at various alloy compositions, and a key discussion point about quasicrystal formation was clarified, wherein the addition of Ce to an Al-Ce-Mn system stabilizes the $Al_{20}Mn_2Ce$ phase.

The observation by Coury *et al.* disproved the theory by Inoue *et al.* [155,156] that proposed in melt spun castings, an increase in Ce is theorized to favor an increase in quasicrystal formation. The second study was targeting properties by manipulating alloy composition and heat treatments of cast Al-Ce-Mn alloys [152]. In this study, multiple compositions were selected to manipulate the amount of $Al_{20}Mn_2Ce$ phase present in the microstructure with two alloys Al-6Mn-2Ce and Al-6Mn-4Ce (at. %). Targeted heat treatments were additionally used to demonstrate the variability in compressive mechanical properties that are possible. The Al-6Mn-2Ce (at. %) alloy demonstrated a significant drop in ultimate tensile strength after a heat treatment at 350°C after 15 hours. The alloy Al-6Mn-4Ce (at. %) mechanical properties appear to be stable or only have a slight drop in mechanical properties using similar heat treatments. In Figure 2.22, the compression properties of each alloy are demonstrated before and after heat treatment. Coury rationalized the change in mechanical properties by investigating how the microstructure changes during the heat treatment.

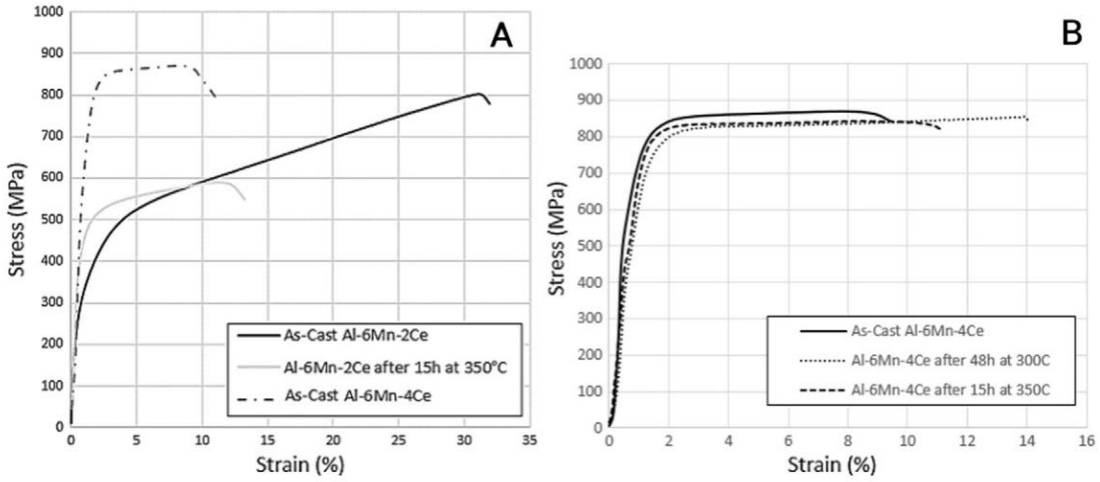

Figure 2.22 Compressive Stress Curves provided by Coury et al. [152] *that demonstrate the variability in stress-strain response as a function of alloy composition and heat treatment.*

The initial high strength of the alloys is attributed to a correlation with the fine distribution of the $Al_{20}Mn_2Ce$ particles. The Al-6Mn-4Ce alloy was insensitive to heat treatment which is likely why the properties remained similar. The increase in yield strength of the Al-6Mn-2Ce alloy was attributed to the precipitation of the Al_6Mn precipitate in the matrix.

The third, was investigating the complex phase transformations observed in the Al-Ce-Mn system [154]. The investigations performed by Coury *et al.* are generally performed on multiple alloys far from the Al-rich corner of the Al-Ce-Mn system produced by arc melting. In this study Coury demonstrated that the Al_8Mn_4Ce and $Al_{10}Mn_2Ce$ were related in that ratio of Al to Mn, wherein the structure changed from I4/mmm to P4/nmm with increasing aluminum content from 4 to 2 in the composition $Al_{12-x}Mn_xCe$. It was demonstrated that across an interface with increasing Mn an Antiphase boundary forms and the structures transition from P4/nmm to I4/mmm. Coury et al. theorized that the structure change is a result of similar atom positions within each structure, but small displacements that reduce the symmetry. Additionally, Gordillo *et al.* [157] investigated solid-state phase transformations in an Al-9Ce-9Mn (wt.%) alloy processed as extruded and canned billets in a 4500-ton press preheated to 310 °C. The as-fabricated samples contained five phases, as determined by XRD: (35.93 wt.%) FCC Al, (40.40 wt.%) $Al_{20}Mn_2Ce$, (20.50 wt.%), Al_6Mn, (1.44 wt.%) $Al_{12}Mn$, and (1.72 wt.%) $Al_{11}Ce_3$. These samples were heat treated at 350 °C for 96 h. The heat-treated sample contained five phases: (~11.09 wt.%) FCC Al, (~1.10 wt.%), $Al_{20}Mn_2Ce$, (~2.1 wt. %), Al_6Mn, (~68.74 wt.%) $Al_{12}Mn$, and (~16.96 wt.%) $Al_{11}Ce_3$.

The notable difference here is the change in decomposition pathway from what was observed by Yang *et al.* [150]. In the cast experiments by Yang the $Al_{20}Mn_2Ce$ decomposed into FCC Al and $Al_{10}Mn_2Ce$. In the Gordillo experiments, the $Al_{20}Mn_2Ce$ and FCC Al decomposed into $Al_{12}Mn$ and $Al_{11}Ce_3$. The primary difference between the two experimental sets are the solidification conditions of each system, where Yang *et al.* used casting material that contained $Al_{10}Mn_2Ce$ after solidification, and Gordillo *et al.* initially used atomized powder that did not contain $Al_{10}Mn_2Ce$ after solidification. The initial solidification state appears from their work to play a role in the decomposition of the $Al_{20}Mn_2Ce$ phase.

Given the unexplained and spatially varying phase transformations observed in AM Al-Ce-Mn, this work seeks to characterize the phase evolution as a function of initial microstructural features. The overarching goal is to understand the range of initial metastable conditions produced by different processing routes and to classify the subsequent types of solid-state phase transformations within the system.

2.5 Scientific and Technical Approach

2.5.1 Problem Statement

The current focus on the Al-Ce-X systems has led to the observation in literature that the FCC Al is no longer the primary solidification phase. The Al-Ce-Mn system contains various primary intermetallic solidification phases because of changing solidification conditions. In the AM part, the decomposition pathways (the decomposition of the initial phases present during solidification to different phases as a function of time and temperature) initially appear to be a function of the solidification microstructure. The goal of the current work is to address how the $Al_{20}Mn_2Ce$ phase the formed during solidification is decomposing during heat treatments, and the role of solidification on the observed decomposition pathways.

The question is how the non-homogeneous microstructure plays a role in the decomposition pathway of the material. In the Al-Ce-Mn system it has been well documented in literature that the processing method, or the thermal history (during material processing of the solidification or solid state) of a material appears to control the decomposition of the $Al_{20}Mn_2Ce$ phase. For example, in Yang *et al.* the casting of an Al-9Ce-6.2 Mn alloy resulted in the formation of the $Al_{10}Mn_2Ce$, $Al_{20}Mn_2Ce$, $Al_{11}Ce_3$, and FCC Al in the initial microstructure. The $Al_{20}Mn_2Ce$ phase was observed to decompose into $Al_{10}Mn_2Ce$ after heat treatment at 400°C. In the work by Gordillo *et al.* by consolidating atomized powder, the initial microstructure of $Al_{20}Mn_2Ce$, Al_6Mn, $Al_{11}Ce_3$, and FCC Al did not observe the formation of $Al_{10}Mn_2Ce$ in the microstructure after heat treatment at 400°C. The problem for this work is to combine and examine previous literature and new experimental data to explain the mechanism by which the $Al_{20}Mn_2Ce$ decomposition pathway during thermal exposure changes as a function of thermal history.

2.5.2 Study Hypothesis

The current research hypothesizes that the initial microstructure defined by the prevailing solidification conditions of an Al-10-Ce-8Mn (wt.%) alloy will alter the subsequent solid state decomposition pathway during heat treatment. Multiple microstructures can evolve from regions defined by a wide range of solidification parameters i.e., thermal gradient, liquid-solid interface velocity and number of cycles in the liquid + solid phase regions. Therefore, this study focuses on the relationship between solidification conditions and the subsequent decomposition of phases at 400 °C. The L-PBF and laser remelting tracks experiments used in this work targeted order of magnitude changes to the solidification velocity and are used as a methodology to reveal how the solidification and solid-state microstructures change as a function of process parameters and heat treatments.

The FCC Al phase can exists as a range of composition, which has been reported in literature [158]. The Aziz relationship describes the mechanism in which a phase can change its partitioning of solute as a function of its solidification velocity. In the published literature, the composition of stoichiometric intermetallic phases is considered to be invariant even at high liquid-solid interface velocities. However, based on our results to be presented later, the current research explores the idea of the $Al_{20}Mn_2Ce$ phase as solid solution. It is hypothesized that in the production of Al-Ce-Mn alloys, the localized compositions of the $Al_{20}Mn_2Ce$, and FCC Al phases will vary as a function of its thermal gradient, liquid-solid interface velocity and subsequent thermal history.

The variance in composition of both phases is expected to change the chemical potential of each element in the system for localized regions within the system. The change in composition of each phase will likely play a role in the observed solid state phase transformations. It appears that FCC Al and $Al_{20}Mn_2Ce$ act cooperatively in the decomposition of the initial microstructure. It is hypothesized in this work that the changing compositions of each parent phase (i.e., FCC Al and $Al_{20}Mn_2Ce$) will modify the driving force for the nucleation of the product phases. The change in driving force will manipulate the selected decomposition phases.

Finally, we also hypothesized that the FCC Al may be acting as an intermediary phase for the exchange and source of alloying elements during the decomposition of the $Al_{20}Mn_2Ce$ phase into

the Al_6Mn, $Al_{12}Mn$, $Al_{11}Ce_3$, and $Al_{51}Mn_7Ce_4$ phases dependent on its initial condition. Interestingly, these situations are expected to modify the trajectory of the decomposition of parent phases, based on multiple constraints that include local reduction of molar free energy and/or minimization the interfacial energy between parent phases, through the nucleation and growth of the new product phase between them.

Chapter 3. Additively Manufactured Al-Ce-Mn Parts

A version of this chapter was originally published by Kevin D. Sisco, Alex Plotkowski, Ying Yang, Larry Allard, Chris Fancher, Claudia Rawn, Jonathan D. Poplawsky, Ryan Dehoff, and S.S. Babu:

Kevin D. Sisco, Alex Plotkowski, Ying Yang, Larry Allard, Chris Fancher, Claudia Rawn, Jonathan D. Poplawsky, Ryan Dehoff, S.S. Babu, Heterogeneous phase transformation pathways in additively manufactured Al-Ce-Mn alloys, Journal of Alloys and Compounds, Volume 938, 2023, 168490, ISSN 0925-8388, https://doi.org/10.1016/j.jallcom.2022.168490.

No major content in the article was changed, some wording was clarified to fit into the larger work as well as removing the article introduction from the journal, and adding a preface to the article that puts it in the scope of the current document.

Kevin D. Sisco – Authored the manuscript as well as did the majority of data analysis.

Alex Plotkowski – Edited and provided key feedback on research direction.

Ying Yang – Assisted in CALPHAD phase description and modeling.

Larry Allard – STEM data collection and assisted with STEM data analysis.

Chris Fancher – Assisted with Synchrotron proposals and XRD data analysis.

Claudia Rawn- Assisted with phase I.D. and XRD data analysis.

Jonathan D. Poplawsky – Assisted with Atom Probe Tomography and Quantification

Ryan Dehoff – Project management and funding

Suresh Babu – Editing and key discussion on mechanisms of phase transformations in the text.

The first question that needs to be addressed is how the Al-Ce-Mn alloy responds to AM. To achieve this goal, AM samples will be produced to observe the solidification phase selection and solid-state phase decomposition as a function of AM processing.

There are six parts to the description of this chapter: The experimental setup, the initial microstructure characterization, the final heat treatment characterization, the identification of the $Al_{51}Mn_7Ce_4$ phase, the stepped heat treatment characterization, the discussion on theories of nucleation of new phases, and a summarization of results.

The main questions in Chapter 3 are

- What phases are present after the initial solidification?
- What are the compositions of the phases (FCC Al and $Al_{20}Mn_2Ce$) resulting from different solidification conditions?
- How does the $Al_{20}Mn_2Ce$ phase decompose in each solidification region, and what phases result from the decomposition?
- Why does the primary solidification region of $Al_{20}Mn_2Ce$ decompose into a different set of phases than the eutectic solidification region of $Al_{20}Mn_2Ce$ + FCC Al

3.1 Experimentation, Characterization, and Modeling

In this section the experimental details, characterization methods, and modeling descriptions

3.1.1 Materials and Manufacturing

An Al-10Ce-8Mn (wt.%) [or Al-2.2Ce-4.5Mn (at. %)], alloy was produced by melting and mixing of raw materials in a 250 kg SiC crucible using an argon cover gas. Cast ingots were nitrogen gas atomized to produce powders. The powder was sieved for a 20-63 μm size distribution. AM was performed using a Concept Laser M2 laser powder bed fusion (L-PBF) system. A more detailed description of the alloy production and composition can be found by Plotkowski *et al.* [151]. There is notably slight Si contamination in the alloy as measured by inductively coupled plasma. The silicon content is measured to be less than 0.1 wt.%. AM samples were heat treated in air at 400 °C for up to 1000 h. The heat-treated samples were air cooled to room temperature.

3.1.2 Synchrotron X-ray Diffraction

High resolution X-ray diffraction patterns were collected from samples with different heat treatment conditions at Argonne National Laboratory (ANL) at the Advanced Photon Source (APS) 11-BM high resolution powder diffraction beamline through the rapid-access mail-in program. Bulk AM samples were made into filings by filing with a diamond file. Efforts were made during the filing to reduce the amount of cold work by this process, the main goal of these measurements are only relevant for the phase identification. Data were collected between 0.5° and 50° 2θ. A calibrated wavelength of λ = 0.457927 Å was used. The sample filings were loaded in 1mm diameter Kapton tubes. Additional details about 11-BM can be found from Wang *et al.* [159].

3.1.3 Crystal structure Analysis

Measured diffraction data were analyzed by Rietveld analysis with the GSAS-II software package [160] to extract phase fractions and to refine crystallographic parameters associated with the $Al_{51}Mn_7Ce_4$ phase. The $Al_{51}Mn_7Ce_4$ phase identified here was modeled after the $Al_{50.26}Mo_7Ce_{3.662}$ phase reported by Thiede *et al.* [161] and was assumed to be stoichiometric. The $Al_{51}Mn_7Ce_4$ phase was adopted because it matched well to the diffraction peaks at high d-spacing (low 2θ) and exhibited good agreement between crystal projections and STEM atomic resolution images, seen in section 3.2.3. The crystal structure of the $Al_{51}Mn_7Ce_4$ phase was obtained by fitting the powder diffraction data from a sample that was annealed at 400 °C for 1000 h. Calculated diffraction patterns used crystal structures for $Al_{11}Ce_3$ and $Al_{20}Mn_2Ce$ adopted from Gordillo *et al.* [157] and crystal structures of FCC Al, Al_6Mn, and $Al_{12}Mn$ were taken from the Inorganic Crystal Structure Database (ICSD) [162].

To perform the Rietveld analysis, the instrument parameters were kept constant, and provided by APS 11-BM. The zero of the system was calibrated to the diamond contamination peak, as the diamond lattice parameter is unlikely to change. The system zero is the offset from the center of the beam, which can shift diffraction peaks. The sample parameters were kept constant and at default settings for a Debye-Scherrer setup, except the histogram scale factor which varied with each sample. The background for each sample was fit with a Chebyshev-1 polynomial between 5 and 9 coefficients depending on the best fit. The key parameters for each phase were μ-strain

(micro-strain), domain size, and phase fractions. The atomic locations and U_{iso} were also refined for each phase. The results were found to be different for each of the phases and measurement. Evaluation of the μ-strain and domain size were difficult to delineate because of the diamond filing method used for making the powders. However, the filing step was necessary to eliminate strong texture in the AM microstructure which would have affected the accuracy of phase fraction determination.

3.1.4 Scanning Electron Microscopy

Samples were cross-sectioned perpendicular to the build direction from 15 mm diameter cylinders. The samples were ground to remove any surface effect from sectioning with 4000 grit SiC grinding pad. The samples were then polished to 3 μm and then finally to a 1 μm finish with a diamond slurry. Then the samples were ion milled using a Hitachi ArBlade at a voltage of 5 Kv and a current of 2.5 nA for 15 minutes using the maximum eccentricity. Scanning electron microscopy (SEM) images were collected from two microscopes, the Zeiss Crossbeam 550, using a Zeiss aBSD[1] detector, and the Zeiss Gemini 450 using a Zeiss BSD detector. An accelerating voltage of 5 kV current of 3 nano-amperes (nA) were used for all images. The spatial resolution was varied for each image.

3.1.5 Scanning Transmission Electron Microscopy

The microstructure at the atomic level was characterized in the as-fabricated and heat-treated states by aberration-corrected scanning transmission electron microscopy (AC-STEM) using a JEOL 2200FS STEM/TEM instrument operated at 200 kV and equipped with a CEOS GmbH corrector for the probe-forming lenses. Images were recorded from electron-transparent regions in 3 mm disks that were prepared by standard grinding methods, and electropolishing using a Struers A/S TenuPol dual-jet electro-polisher. Electrolyte composition, polishing conditions and other handling details generally followed procedures described by Unlü *et al.* [163]. The electropolishing samples were taken from a plane parallel to the build surface. The resolution in high-angle annular dark-field (HAADF) images is at the sub-Å level; details on typical imaging onditions are given by Roy *et al.* [164]. STEM imaging was performed by Larry Allard at ORNL

[1] Commercial acronym for backscattered electron imaging detector

3.1.6 Atom Probe Tomography

Atom probe tomography (APT) specimens were fabricated with a Thermo Fisher Nova 200 dual beam scanning electron microscope (SEM)/focused ion beam (FIB) instrument using the method described by Thompson *et al.* [165]. Site specific extraction was performed by first imaging a sample with an SEM and then specifically FIB extracting the desired location. The $Al_{20}Mn_2Ce$ and FCC Al are distinguishable in SEM. The APT experiments were run using a CAMECA LEAP 4000XHR in voltage mode with a 70 K base temperature, a 30% pulse fraction, a 0.5% detection rate, and a 200 kHz pulse repetition rate. The APT results were reconstructed using the voltage evolution method. The mass spectrum is reported in the appendix. The error presented in the APT data is the standard error [166]. The samples were taken from cross sections perpendicular to the build direction. The samples were initially prepped before FIB using the same preparation outline for the SEM samples. APT was performed by Jonathan Poplawsky at ORNL.

3.1.7 Thermodynamic calculations

The CALPHAD approach was implemented using PANDAT® [167]. Calculation of driving forces was performed as specified by the documentation using the thermodynamic database for Al rich Al-Ce-Mn systems developed by Yang *et al.* [150]. The driving forces for nucleation of various new phases, including $Al_{11}Ce_3$, from the initial microstructure was calculated using parallel tangent concept [168]. The driving force was calculated by assuming that the overall system contains two parent (*i.e.*, FCC and $Al_{20}Mn_2Ce$) phases which are in thermodynamic equilibrium with each other. The effect of the initial microstructure on driving force was implemented by changing the supersaturation of alloying elements in FCC Al and maintaining the stoichiometry of $Al_{20}Mn_2Ce$. Such calculations will also modify the equilibrium concentration of FCC. For example, increasing the Mn concentration in FCC changes the equilibrium quantity of Ce in FCC.

3.2 Results

3.2.1 As Fabricated Microstructures

Synchrotron X-ray diffraction (XRD) was used to determine the weight percentage of each phase in the as-fabricated Al-Ce-Mn samples. Figure 3.1 shows XRD data for the as fabricated microstructures with identifying peaks for FCC Al, $Al_{11}Ce_3$, and $Al_{20}Mn_2Ce$ phases. The peak at $2\theta \sim 13°$ was attributed to diamond contamination during sample preparation.

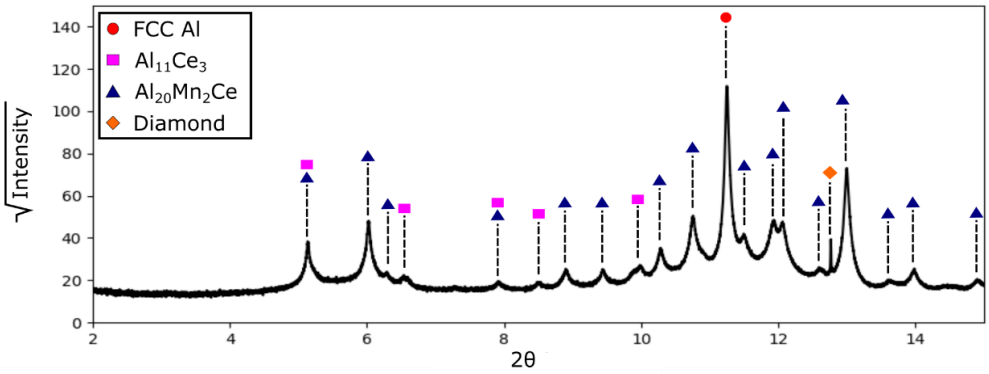

Figure 3.1. X-ray diffraction data of as-fabricated Al-Ce-Mn alloy. The diffraction peaks from different phases are labelled.

The weight percentages determined from Rietveld analysis of the diffraction data were FCC Al (49.6 $\pm$0.06 wt.%), $Al_{20}Mn_2Ce$ (47.5$\pm$0.03 wt.%), and $Al_{11}Ce_3$ (2.9$\pm$0.01 wt.%). The bulk XRD results are in good agreement with the phase formation during solidification predicted by CALPHAD models by Yang *et al.* [150], assuming the suppression of the $Al_{10}Mn_2Ce$ phase. In Figure 3.2A, a liquidus diagram of the Al-Ce-Mn system shows the first phase to form from liquid will be $Al_{20}Mn_2Ce$. The Scheil solidification diagram (Figure 3.2B) calculated with the bulk alloy composition predicts that a majority fraction of phases in the solidified microstructure will be FCC and $Al_{20}Mn_2Ce$ and minority phase will be $Al_{11}Ce_3$.

The Shiel solidification diagram suggests the following solidification pathway as the liquid cools: (1) Primary $Al_{20}Mn_2Ce$ formation from liquid, (2) eutectic solidification of FCC Al and $Al_{20}Mn_2Ce$ and (3) completion of solidification with terminal eutectic FCC Al and $Al_{11}Ce_3$ formation.

The bulk XRD spectrum characterizes the phase fraction in the as-fabricated microstructure, but not their spatial distribution. Therefore, detailed morphological characterization was performed using SEM. The SEM images (Figure 3.3) reveal multiple solidification microstructures distributed heterogeneously within the sample. Figure 3.3A shows a stitched image of a weld track in which three distinct regions can be observed (Figure 3.3B-D): a primary $Al_{20}Mn_2Ce$ solidification region at the melt pool boundary, a fine-eutectic, and a coarse-eutectic structure in the bulk of the weld track. For brevity, the melt pool region and eutectic structure regions will be referred to as MPB and ES.

The MPB region highlighted in Figure 3.3B has three phases. The phases were delineated based on SEM-BSE Z-contrast (regions containing higher atomic numbers (*i.e.*, Ce) appear as brighter), which is sensitive to elemental concentration. The three phases identified through bulk XRD could therefore be identified using the SEM-BSE contrast ($Al_{11}Ce_3$ appears brightest, FCC Al darkest, and $Al_{20}Mn_2Ce$ between). In the MPB region, $Al_{20}Mn_2Ce^{MPB}$ particles solidified first from the melt with a rosette morphology, consistent with previous observations by Gordillo *et al.* and Yang *et al.* [150,157]. Primary solidification was followed by a eutectic reaction forming FCC Al and $Al_{20}Mn_2Ce$.

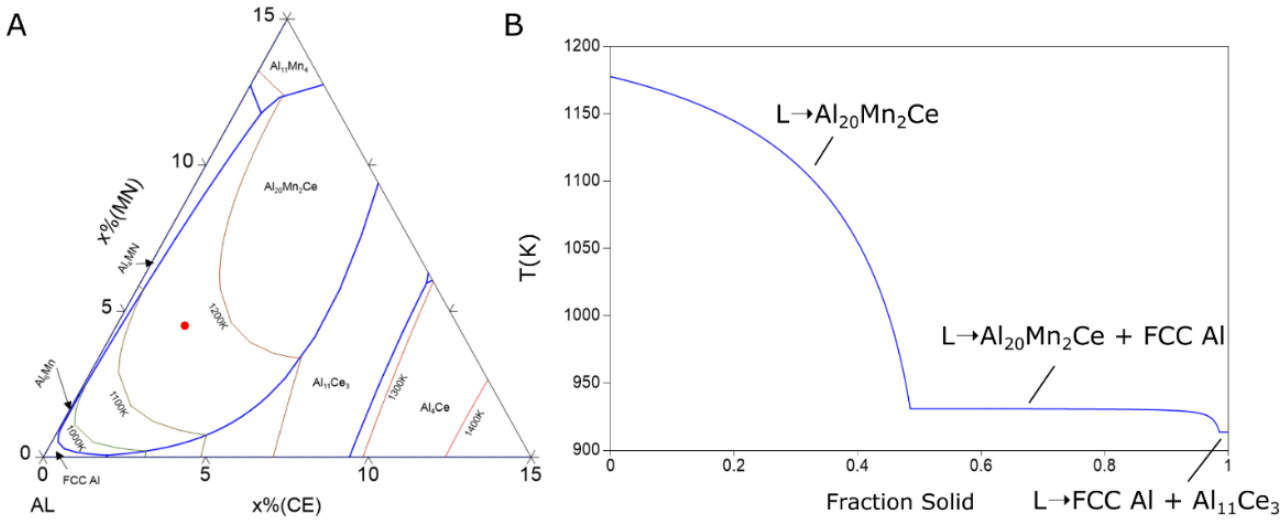

Figure 3.2 (A) Liquidus Projection of the Al-Ce-Mn ternary system which demonstrates the bulk composition with a red dot. (B) Shiel Solidification Simulation of an Al-10Ce-8Mn (wt.%) Alloy

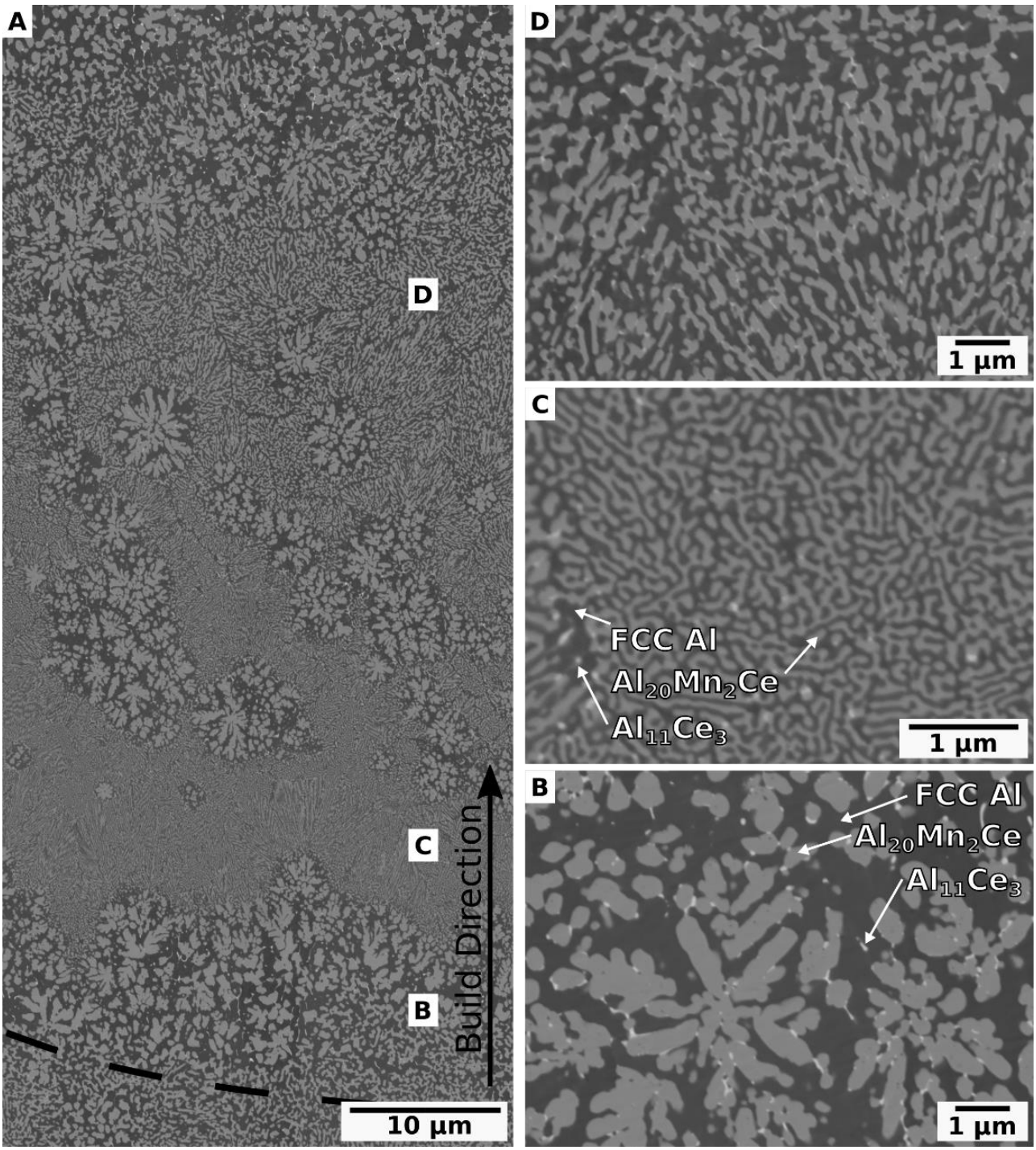

Figure 3.3. SEM (BSE) micrographs of differing microstructural regions in the additively manufactured Al-Ce-Mn system A) microstructure across the depth of a weld track, B) $Al_{20}Mn_2Ce$ solidification region at the Melt Pool Boundary, C) fine eutectic region, D) coarse eutectic region.

The FCC Al and $Al_{20}Mn_2Ce^{MPB}$ phases in the MPB region were on the length scale of mm (< 3 μm). The $Al_{11}Ce_3$ was elongated in the MPB region and generally less than 100 nm in width, and forms in the terminal eutectic with FCC Al.

There are two ES regions in the microstructure. The first region is the fine eutectic FCC Al + $Al_{20}Mn_2Ce^{ES}$ (Figure 3.3C) which was found near the center of the weld track where the liquid-solid interface velocity (R) is expected to be high. Second is the coarse eutectic, typically found in the overlapping region of stacked weld track, referred to as the remelted zone. The existence of the coarse eutectic in the i^{th} layer was attributed to the remelting and solidification caused by deposition in the $(i+1)^{th}$ layer during the laser powder bed fusion process. Here, the fine and coarse eutectic regions are considered to follow the same solid-state transformation pathway. Our results (presented in section 3.2) showed that the length scale of the eutectic microstructure did not impact the microstructure evolution during heat treatment. Therefore, the two regions will be consolidated and identified as the eutectic solidification (ES) region. The eutectic solidification region contained three phases: FCC Al, $Al_{11}Ce_3$, and $Al_{20}Mn_2Ce^{ES}$. In the ES region, the $Al_{11}Ce_3$ phase preferentially solidified near the boundary between eutectic colonies, especially in the fine eutectic. The eutectic spacing between FCC Al and $Al_{20}Mn_2Ce$ was 100-300 nm. The $Al_{11}Ce_3$ in the ES region was <100 nm in width, with varying lengths.

In Figure 3.3A, primary solidification of $Al_{20}Mn_2Ce$ was also found in the eutectic region. The presence of primary $Al_{20}Mn_2Ce$ in the interior of the weld track could result from a variety of factors. Primary nucleation of $Al_{20}Mn_2Ce$ in the liquid may compete with the eutectic solidification front for complex thermal fields. Liquid advection in the weld track driven by Marangoni effects might generate fluctuations in the local temperature or composition. A second possibility is that $Al_{20}Mn_2Ce$ particles originate from partial remelting of powder particles or previously deposited material, which may then be advected within the liquid. Nevertheless, results show that this $Al_{20}Mn_2Ce$ decomposes along the same pathway as the MPB region during subsequent heat treatment and will therefore be considered similarly.

The change in morphology of $Al_{20}Mn_2Ce$ between the MPB (rosette) and ES (lamellar) regions corresponded with changes in the composition as measured using APT. The relevant mass spectroscopy for identifying the elements from APT data are provided in Appendix A.

Table 3.1 shows the measured compositions of the $Al_{20}Mn_2Ce$ phase for each region of the microstructure. In the MPB region, the Ce concentration is lower than the stoichiometric value. Furthermore, the $Al_{20}Mn_2Ce^{MPB}$ phase has a higher Mn concentration than the stoichiometric condition.

Interestingly, the $Al_{20}Mn_2Ce^{ES}$ phase from the ES region shows a higher than stoichiometric Ce content and has a higher Mn concentration. The composition of FCC Al in the MPB region was measured as 0.227 ± 0.005 (at. % Mn) separately from previous measurements. The composition of FCC Al in the ES region was measured between 0.468-1.651 (at. % Mn).

The APT data was further analyzed at the interface between FCC Al and $Al_{20}Mn_2Ce^{ES}$ as shown in Figure 3.4. The results confirm that the $Al_{20}Mn_2Ce^{ES}$ particle maintains the non-equilibrium concentration as a function of depth into the intermetallic. At the interface of the two phases, FCC Al and $Al_{20}Mn_2Ce^{ES}$, excess impurity Si atoms were observed. Similar concentration versus depth analysis could not be obtained from the MPB region due to difficulties in APT sample ruptures at the interface region between FCC and $Al_{20}Mn_2Ce^{MPB}$ particles.

The APT data shows that the $Al_{20}Mn_2Ce$ phase solidified in a non-equilibrium state and behaves as a solid solution for high solidification rates in AM. The APT results show that the naming convention of stoichiometric $Al_{20}Mn_2Ce$ may not be valid, for consistency we will use the $Al_{20}Mn_2Ce^{MPB}$ to describe the solid-solution phase at the MPB region, and $Al_{20}Mn_2Ce^{ES}$ to describe the solid solution in the ES region.

3.2.2 Heat Treated Microstructure

Figure 3.5 shows synchrotron diffraction data used to determine the phase content following heat treatment of the as-fabricated material at 400 °C for 1000 h. Prominent peaks above the normalized intensity of 15% of each phase are identified, as well as low angle peaks of the $Al_{51}Mn_7Ce_4$ phase.

The x-ray diffraction data indicates a greater number of phases in the heat-treated state than the as-fabricated state. In addition to the three phases in the as-fabricated state (FCC Al, $Al_{20}Mn_2Ce$, and $Al_{11}Ce_3$), three additional phases (Al_6Mn, $Al_{12}Mn$, and $Al_{51}Mn_7Ce_4$) were identified in the heat-treated samples.

Table 3.1. APT measurements of the $Al_{20}Mn_2Ce$ phase composition from different solidification conditions.

	Stoichiometric $Al_{20}Mn_2Ce$	ES region $Al_{20}Mn_2Ce^{ES}$	MPB region $Al_{20}Mn_2Ce^{MPB}$
Al (at. %)	86.96	83.75 – 84.77	86.22 – 86.28
Mn (at. %)	8.69	9.55 – 10.30	10.52 - 10.81
Ce (at. %)	4.34	5.13 - 5.62	2.84 - 3.19

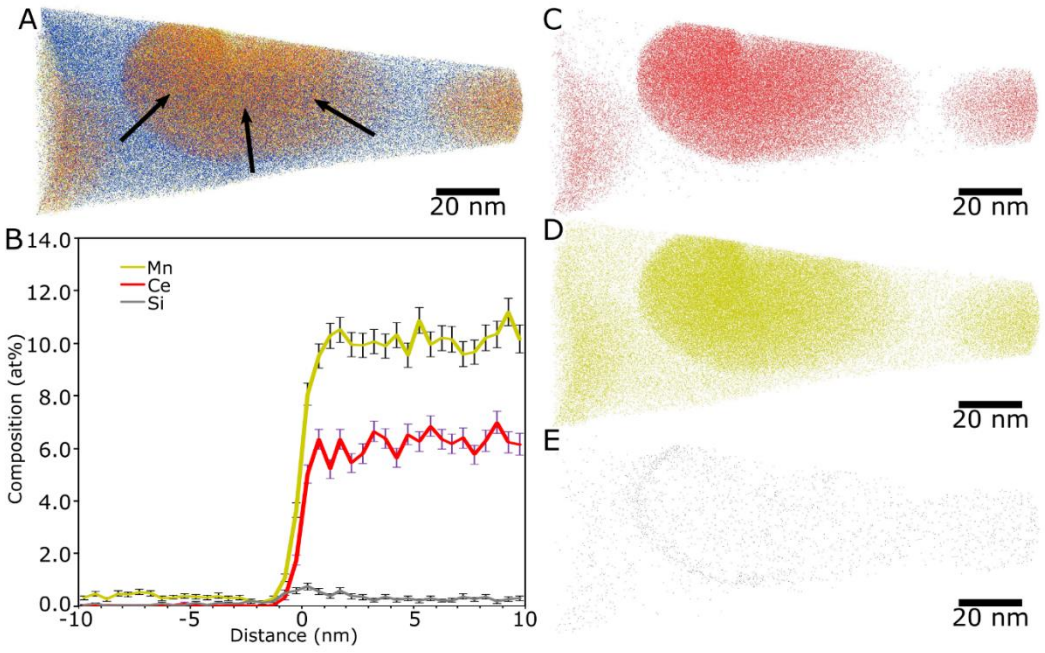

Figure 3.4. Atom Probe measurement across a eutectic interface. Atom map of all elements (Al, Ce, Mn, and Si) in (A), (B) distribution of Mn, Ce and Si across the phase interface, (C) Ce atomic map, (D) Mn atomic map, and (E) Si atomic map. The sample for this data was extracted from the ES region.

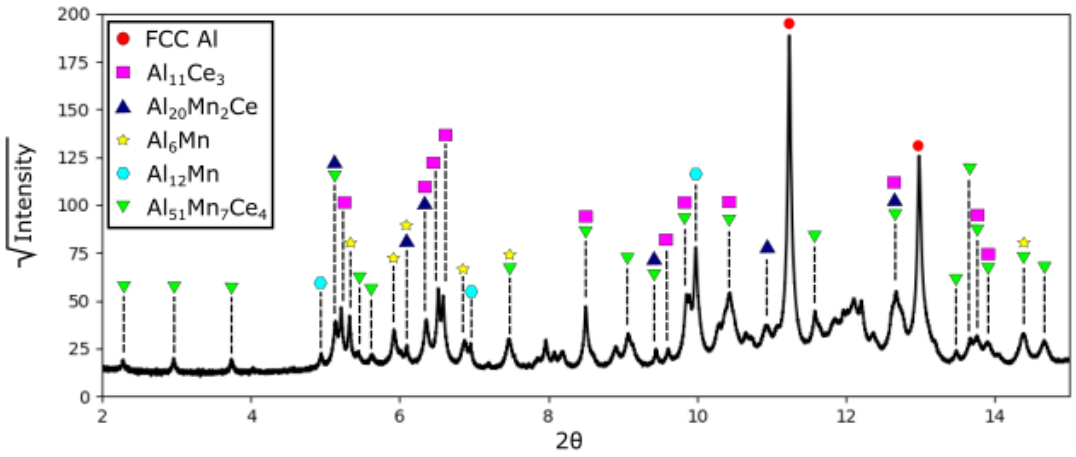

Figure 3.5. X-ray diffraction data of a heat-treated sample at 400 °C for 1000 h, prominent peaks are identified. The phases identified using Rietveld analysis are also labelled.

$Al_{51}Mn_7Ce_4$ was previously unknown, and its identification is discussed in the next section. Refined phase fraction determined from the x-ray diffraction data were FCC Al 50.9±0.04 wt.%, $A_{20}Mn_2Ce$ 1.4±0.02 wt.%, $Al_{11}Ce_3$ 8.2±0.01 wt.%, Al_6Mn 17.3±0.04 wt.%, $Al_{12}Mn$ 5.5±0.04 wt.%, and $Al_{51}Mn_7Ce_4$ 16.7±0.03 wt.%. Additionally, the FCC Al lattice parameter increased from the as-processed condition value after heat treatment. The increase in lattice parameter was attributed to Mn diffusing out of solid solution in the FCC matrix and into the new Mn rich precipitates [169].

The spatial distribution of phases in the heat-treated microstructure is shown in Figure 3.6 by SEM-BSE imaging, revealing two distinct regions. The bottom region in Figure 3.6A shows the MPB with higher magnification in Figure 3.6B. Phases identified from XRD were delineated using Z-contrast from SEM-BSE images. With this method, the Al_6Mn and $Al_{12}Mn$ are not distinguishable from each other. Therefore, from darkest to lightest contrast the phases are FCC Al > Al-Mn binary Phases > $Al_{11}Ce_3$.

Figure 3.6C shows higher magnification of the heat-treated ES region. The two prominent phases, FCC Al and $Al_{51}Mn_7Ce_4$, are identified in the ES region again based on Z-contrast. In Figure 3.6A, a region circled in red within the ES region also contains both $Al_{11}Ce_3$ and Al-Mn binary phases. The decomposition in this region differs from its surroundings likely because of the presence of a primary $Al_{20}Mn_2Ce$ particle in the as-fabricated microstructure. Additionally, interspersed $Al_{11}Ce_3$ particles in the decomposed ES region are likely from the $Al_{11}Ce_3$ that existed at eutectic colony boundaries. Since $Al_{11}Ce_3$ is an equilibrium phase at 400° C, it is not expected to decompose.

3.2.3 Identifying the $Al_{51}Mn_7Ce_4$ Phase

The $Al_{51}Mn_7Ce_4$ phase was identified using two different techniques: X-ray diffraction and STEM HAADF images. The $Al_{51}Mn_7Ce_4$ crystal structure was identified using a literature search for systems that contain $Al_{20}TM_2RE$ compounds, where the TM stands for transition metals and RE stands for rare earth elements. From this search, it was found that within the Al-Mo-La system, the $Al_{50.26}Mo_7La_{3.662}$ phase [161] shares similarities with that of $Al_{20}Mn_2Ce$. The $Al_{50.26}Mo_7La_{3.662}$ phase has a similar diffraction pattern to the that from the Al-Ce-Mn samples. This observation suggests similar lattice symmetry. Therefore, $Al_{51}Mn_7Ce_4$, a phase with the

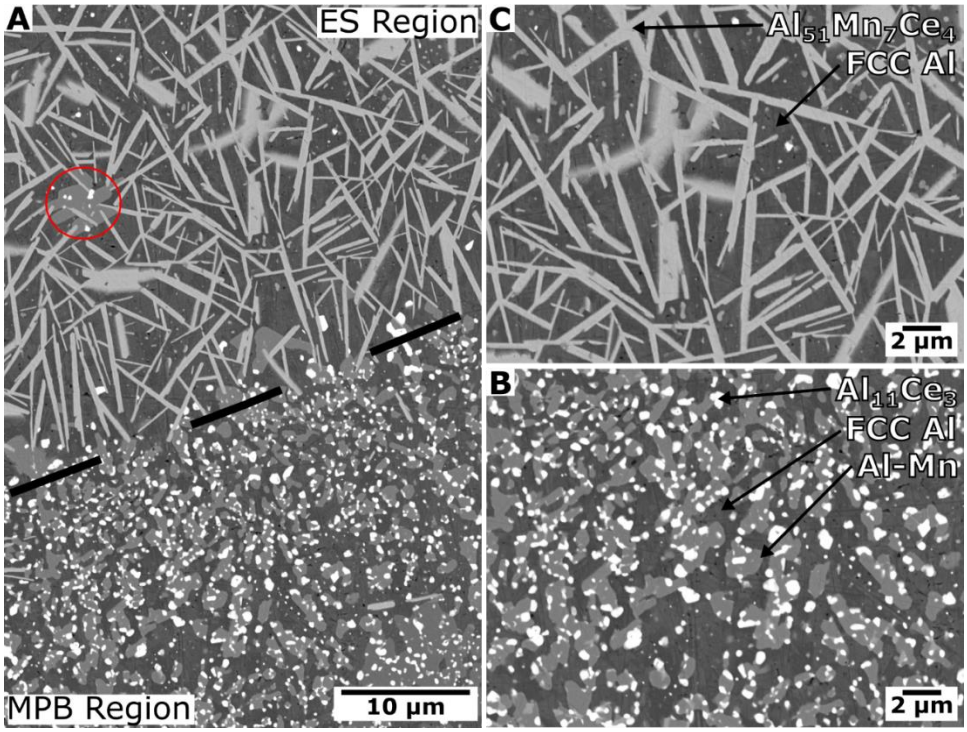

Figure 3.6. SEM (BSE) micrographs of differing microstructural regions in the additively manufactured Al-Ce-Mn system after heat treatment at 400 °C for 1000 h: A) microstructure across a weld track, B) final decomposition of the typical MPB region, C) final decomposition of a typical ES region.

same crystal structure as $Al_{50.26}Mo_7La_{3.662}$, was hypothesized as a candidate for the unidentified Al-Ce-Mn intermetallic. By adjusting the lattice parameter in the model crystal structure, the theoretical diffraction pattern for $Al_{51}Mn_7Ce_4$ was matched to experimental data. In Figure 3.5 the diffraction peaks, specifically at low 2θ angles between 2° and 4°, match well and give a high degree of confidence of the proposed crystal structure of $Al_{51}Mn_7Ce_4$.

Figure 3.7 shows atomic resolution STEM HAADF of the $Al_{51}Mn_7Ce_4$ phase. The STEM HAADF images highlight the location of the Ce atoms in the crystal structure due to their high atomic number.

In Figure 3.7A-B, the observed atomic planes are compared against theoretical HAADF images simulated using the MacTempas Software for the same zone-axes in the proposed crystal structure [170]. Additionally, crystallographic projections from Crystal Maker® are overlayed onto the images, showing good agreement between the crystal model and the measured data. The Crystal Maker® projections are also shown in Figure 3.7D-E for clarity. The $Al_{51}Mn_7Ce_4$ crystal structure was further refined to using the X-ray diffraction data from samples heat treated at 400 °C for 1000 h. The $Al_{51}Mn_7Ce_4$ structure was determined to be a $P\bar{3}m1$ (Space Group 161) structure with lattice parameters a = 10.21$\pm$0.006, c =11.49 $\pm$0.005 Å. A full exhaustive search of all possible structures was not performed, the $Al_{51}Mn_7Ce_4$ phase is proposed here because it has good agreement with two independent experimental methods.

3.2.4 Overview of Phase Transformation Pathways

The heat treatments of as-fabricated AM samples were performed at 400 °C for various times up to 1000 hrs. The phase fractions were then measured using X-ray diffraction and are summarized graphically in Figure 3.8A, with FCC Al being the balance in each case. Errors bars are not shown because the estimated standard deviation is less than 0.1 wt.% for all phases. The as-fabricated sample included FCC Al (49.6$\pm$0.06) wt.%, $Al_{20}Mn_2Ce$ (47.5$\pm$0.03 wt.%), and $Al_{11}Ce_3$ (2.9$\pm$0.01 wt.%). The $Al_{11}Ce_3$ fraction increased with heat treatment time, which correlated with the decomposition of the $Al_{20}Mn_2Ce$, the fraction of which decreases substantially with time. The phase fractions measured with XRD are consistent with observations from SEM BSE (see appendix).

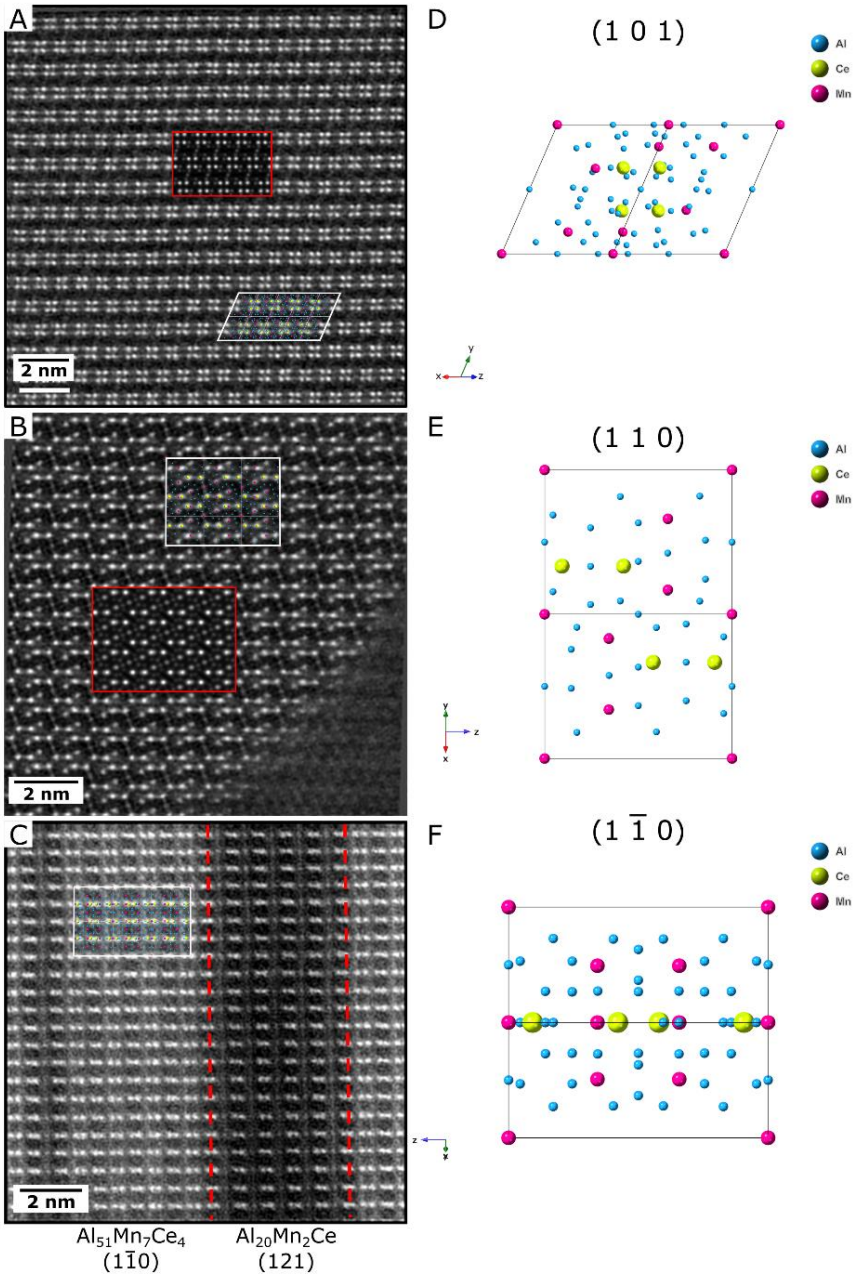

Figure 3.7 (A) STEM HAADF showing the (101) plane of the $Al_{51}Mn_7Ce_4$ phase with simulated and Crystal Maker® inset. (B) STEM HAADF showing the (110) plane of the Al51Mn7Ce4 phase with simulated and Crystal Maker Inset. (C) STEM HAADF showing the Al51Mn7Ce4 (11 $\bar{0}$) phase with a Crystal Maker inset and the $Al_{20}Mn_2Ce$ (121) phase. (D-E) demonstrate the Crystal Maker® projections of the $Al_{51}Mn_7Ce_4$ phase of one unit cell for the (101), (110), and (1-10) planes respectively.

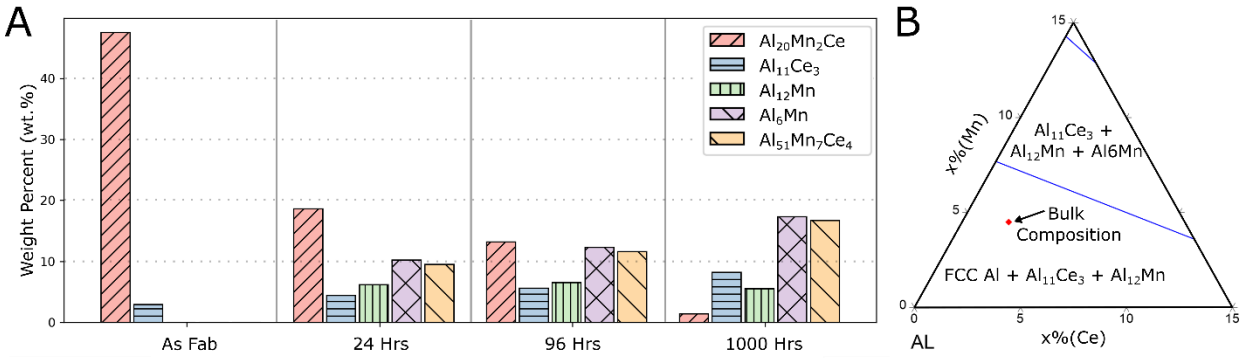

Figure 3.8. (A) is the calculated phase fractions for Al-Ce-Mn samples after heat treatment at 400 °C for 0, 24, 96, and 1000 h using computational models for refinement of X-ray diffraction data. (B) is the isothermal section at 400°C for the Al-Ce-Mn system

The predicted equilibrium phase fractions are FCC Al (27.5 %), $Al_{12}Mn$ (55.4 %), and $Al_{11}Ce_3$ (17.1 %). Compared to the experimental data there is a notable difference in both the types and quantities of phases present. The Gibbs phase rule dictates that a ternary system at constant temperature and pressure can exhibit a maximum of three phases at equilibrium, yet six phases were found experimentally. The three equilibrium phases predicted by the phase diagram for the nominal composition are FCC Al, $Al_{11}Ce_3$ and $Al_{12}Mn$, and do not include $Al_{20}Mn_2Ce$, Al_6Mn, or $Al_{51}Mn_7Ce_4$. These results suggest that even at 1000 hours at 400°C, the system does not evolve to a global equilibrium. However, we also observe that each solidification microstructure region follows a different decomposition pathway and cannot rule out a local equilibrium in between each phase.

Based on the above results, the phase transformation paths are examined for each spatial location within the weld track. Figure 3.9 summarizes the microstructural changes in the MPB and ES regions for the as-fabricated state and several heat-treatment times at 400°C up to 1000 h. The red lines delineate the boundary between MPB and ES region. In the top region Figure 3.9A-E, the decomposition of the ES region results in a sectioned plate morphology, whereas the MPB region results in a globular structure. The initial decay of the $Al_{20}Mn_2Ce$ phase in the ES region corresponds with the formation of $Al_{51}Mn_7Ce_4$ plates. In the MPB region, the decay of $Al_{20}Mn_2Ce$ is coupled with the nucleation and growth of three phases, $Al_{11}Ce_3$, A_6Mn and $A_{12}Mn$. In both cases, decomposition of $Al_{20}Mn_2Ce$ occurs at its interface with FCC Al.

3.3 Discussion

The stability of microstructural regions from the MPB and ES regions exhibit intriguing features which appear to depend on their initial conditions in the as-fabricated solidification microstructure. Both regions contain the same initial phases (FCC Al, $Al_{20}Mn_2Ce$, and $Al_{11}Ce_3$) each follows a different decomposition pathway upon aging at 400°C. The key measured difference in the as-fabricated microstructure is the measured compositions of FCC Al and $Al_{20}Mn_2Ce$. In the discussion, the decomposition pathways are rationalized using a thermodynamic approach.

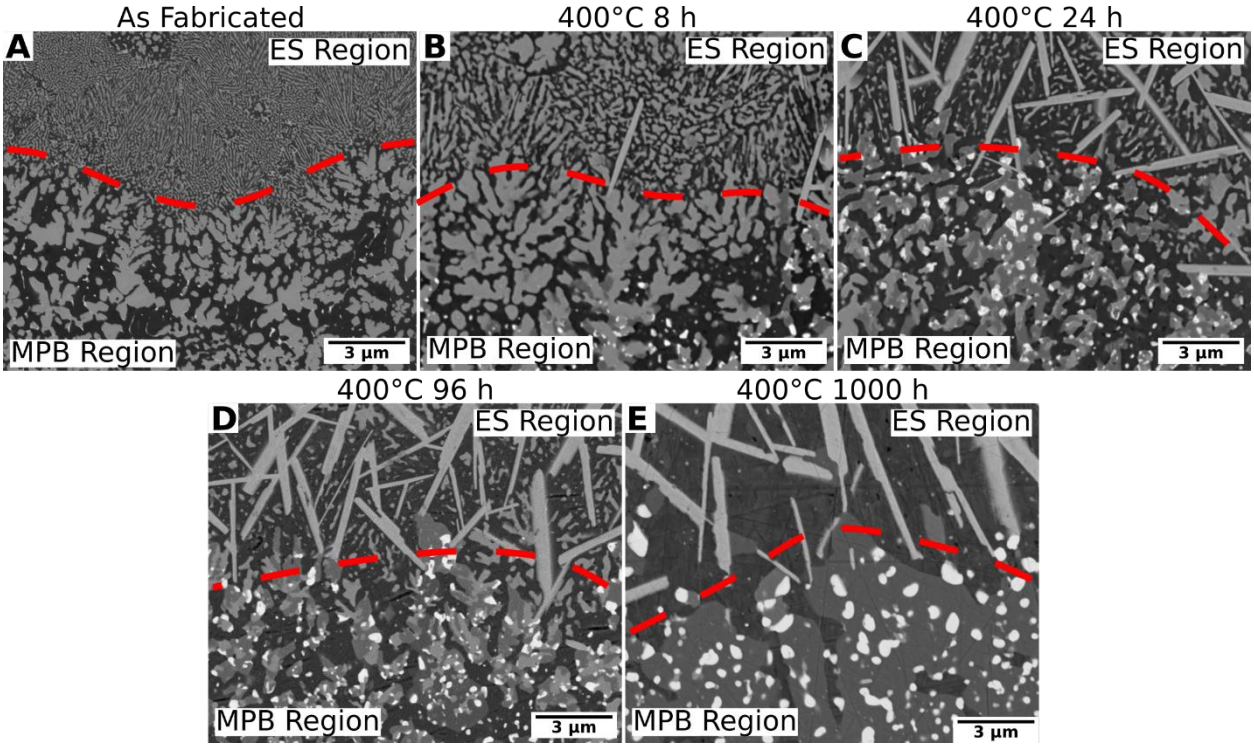

Figure 3.9. Varied heat treatment times at 400 °C with the interface between the MPB and ES indicated A) as fabricated, B) after 8 h, C) after 24 h, D) after 96 h, E) after 1000 h.

3.3.1 Local versus Global Equilibrium

Two questions must be addressed to rationalize the experimental results: (1) does the long-range diffusion of solute play a role in the observed phase transformations, and (2) how does the local composition of FCC Al and $Al_{20}Mn_2Ce$ affect the driving force for local phase transformations.

The role of long-range diffusion of solute in the microstructure: The as-fabricated microstructure contains two distinct regions distributed on the length scale of the weld track (~100s μm). To evaluate the subsequent solid-state transformations, the extent of diffusional interactions between the regions is first evaluated.

The diffusion distance, δ_i, in FCC Al may be estimated as:

$$\delta_i \sim \sqrt{4D_i\Delta t}, \tag{37}$$

where i is either Ce or Mn, the diffusivity is evaluated using the Arrhenius relationship $D_i = D_0 \exp\left(-\frac{Q}{RT}\right)$, and Δt is the diffusion time.

Using diffusivity data from Du *et al.* [171] and Cai *et al.* [172], the estimated diffusion distance after 1000 hours at 400°C is 274.5 nm and 352.9 nm for Ce and Mn, respectively. As these length scales are small compared to the heterogeneous distribution of the solidification microstructure on the scale of the weld track, the solid-state transformations within each region may reasonably be treated independently.

The effect of local phase composition on driving force: To evaluate the effect of phase composition on the decomposition pathways, we first summarize the initial microstructural features: (1) The microstructure in both regions contain FCC Al and $Al_{20}Mn_2Ce$ phases, (2) The compositions of $Al_{20}Mn_2Ce$ and FCC Al are different in the MPB and ES regions, (3) The $Al_{20}Mn_2Ce^{MPB}$ phase appears in the MPB as a primary intermetallic that forms from the liquid, and (4) In the center of the melt track, $Al_{20}Mn_2Ce^{ES}$ and FCC Al form as a lamellar eutectic.

A product phase that forms at the interface of two parent phases (FCC Al and $Al_{20}Mn_2Ce$) requires elemental contribution from both parent phases. At 400°C, we assume local equilibrium

at the FCC Al and $Al_{20}Mn_2Ce$ interface defined by the following two relationships for chemical potentials of each element μ_i, where $i = Al, Ce, Mn$:

$$\mu_i^{FCC\ Al\ (MPB)} = \mu_i^{Al_{19.92}Mn_{2.42}Ce_{0.67}{}^{MPB}}, \text{ and}$$

$$\mu_i^{FCC\ Al\ (ES)} = \mu_i^{Al_{19.62}Mn_{2.2}Ce_{1.18}{}^{ES}}.$$

These equations define the equilibrium tangent plane between the FCC Al and $Al_{20}Mn_2Ce$ free energy surfaces based on their measured compositions indicated with superscripts for each region. For these calculations, the Gibbs free energy of $Al_{19.92}Mn_{2.42}Ce_{0.67}{}^{MPB}$ was assumed equal to that of $Al_{20}Mn_2Ce$ determined by Yang *et al.* [150], but the location of the intermetallic was moved to the measured composition. The Ce content in FCC Al was dependent on the equilibrium tangent plane defined between FCC Al at a set Mn content and the $Al_{20}Mn_2Ce$ phase. The ES region was treated in the same way using the local compositions. The goal of these calculations was to determine the reduction in free energy (the driving force) for various product phases to form from the FCC Al and $Al_{20}Mn_2Ce$ parent phases.

The driving forces were calculated for each measured condition in Table 3.2. Each phase observed following heat treatment at 400°C was considered. Because it is not included in the thermodynamic database, the Gibbs free energy for $Al_{51}Mn_7Ce_4$ was defined at 400°C as -46,250 j/mol at the stoichiometric composition. The selection of this value is somewhat arbitrary and will affect the magnitude of the driving force, but we adopt it here to interrogate the trends with respect to the chemistry of the phases in each microstructural region.

The bolded text are the phases experimentally observed to nucleate in each region. In the MPB region, the Al_6Mn phase has the largest driving force for nucleation. This calculation is consistent with experimental observations (Figure 3.9).

In the ES region (at both measured Mn compositions), $Al_{51}Mn_7Ce_4$ phase has the second largest driving force for nucleation, being surpassed by the $Al_{10}Mn_2Ce$ and Al_6Mn phases. Since the $Al_{51}Mn_7Ce_4$ is observed to nucleate, the structure is investigated more in section 4.3 which demonstrates a possible orientation relationship which could reduce the barrier of nucleation by reducing the penalty of nucleation attributed to interfacial energy. The reduction in the barrier of

Table 3.2 Calculated Driving Forces for the MPB and ES localized equilibrium states.

Phase Name	MPB (FCC Al 0.227 at. % Mn)	ES (FCC Al 0.468 at. % Mn)	ES (FCC Al 1.651 at. % Mn)
$Al_{11}Ce_3$ (j/mol)	-16,164.98	3,120.3	257.48
$Al_{12}Mn$ (j/mol)	984.59	1,292.52	1,816.37
Al_6Mn (j/mol)	**1,800.11**	2374.68	3,419.37
$Al_{51}Mn_7Ce_4$ (j/mol)	-1,978.91	**2786.59**	**2749.64**
$Al_{10}Mn_2Ce$ (j/mol)	-2,676.15	4,876.842	4,996.68

nucleation is likely a key reason as to why the $Al_{51}Mn_7Ce_4$ phase is selected over the $Al_{10}Mn_2Ce$ and Al_6Mn phase. Another possible reasoning is that the free energy surface of $Al_{20}Mn_2Ce$ and $Al_{51}Mn_7Ce_4$ are complex and can result in different possible local compositions of FCC Al. In the current case, an approximation is used for the $Al_{20}Mn_2Ce$ phase, but more information is needed to establish a full understanding of the free energy curves.

The above formalism shows that the phase decomposition pathways in our experiment can be rationalized based on the barriers for nucleation. The high driving forces of the $Al_{51}Mn_7Ce_4$ and $Al_{10}Mn_2Ce$ compared to the other phases indicates that the phase is very sensitive to local compositional conditions that manipulate the equilibrium tangent plane.

3.3.2 Melt Pool Boundary Decomposition Pathway

In the MPB region, Al_6Mn is not the only phase observed from the decomposition of $Al_{19.92}Mn_{2.42}Ce_{0.67}^{MPB}$. After heat treatment at 400°C for 1000 hours, the final microstructure contained FCC Al, $Al_{12}Mn$, Al_6Mn, and $Al_{11}Ce_3$. The question is how the decomposition of the initial local microstructure of FCC Al (0.227 at. %) Mn + $Al_{19.92}Mn_{2.42}Ce_{0.67}^{MPB}$ leads to these four-phases. From the thermodynamic results in Table 3.2, Al_6Mn has the highest driving force to nucleate from the decomposition of the initial microstructure containing FCC and $Al_{19.92}Mn_{2.42}Ce_{0.67}^{MPB}$ phase. Initial nucleation of Al_6Mn could locally deplete the Mn in FCC Al at the interface of $Al_{20}Mn_2Ce$. The local depletion of Mn could contribute to the nucleation of $Al_{11}Ce_3$ by increasing the relative Ce fraction present near the interface. The increase in Ce likely makes a favorable driving force for $Al_{11}Ce_3$ to form.

The formation of $Al_{12}Mn$ is complicated by uncertainty in the nucleation site. We hypothesize that Al_6Mn forms at the interface between FCC Al and $Al_{19.92}Mn_{2.42}Ce_{0.67}^{MPB}$. In a similar case, Gordillo et al [157] demonstrated that, in a Al-9Mn-9Ce (wt.%) alloy, Al_6Mn decomposed into $Al_{12}Mn$ after its initial formation from the decomposition of $Al_{20}Mn_2Ce$. A similar decomposition pathway is observed here, where $Al_{12}Mn$ (wt. %) formation appears to stagnate between 96- and 1000-hour heat treatment at 400°C. More work is needed to understand the local interactions that lead to the formation of Al_6Mn or $Al_{12}Mn$ in the current system.

3.3.3 Eutectic Decomposition Pathway

The interface between $Al_{19.62}Mn_{2.2}Ce_{1.18}^{ES}$ and $Al_{51}Mn_7Ce_4$ were characterized with STEM. Figure 3.10 shows crystallographic matching at this interface after heat treatment at 400°C for 200 hours. The flat interface along with the good matching between structures may indicate that the interface between the intermetallic is at least semi-coherent. A favorable interface between these two phases will tend to reduce the activation energy required for the nucleation of $Al_{51}Mn_7Ce_4$. The enrichment of Si at the interface (Figure 3.4) may also affect the interfacial energy between the $Al_{20}Mn_2Ce$ and FCC-Al phase during eutectic growth. Therefore, in the ES region, we hypothesize that the local FCC Al and $Al_{20}Mn_2Ce$ compositions formed during solidification and the favorable interface between $Al_{51}Mn_7Ce_4$ and $Al_{20}Mn_2Ce$ favor nucleation of $Al_{51}Mn_7Ce_4$. Overall, the nucleation of $Al_{51}Mn_7Ce_4$ appears to be sensitive to the characteristics of FCC Al and $Al_{19.62}Mn_{2.2}Ce_{1.18}^{ES}$.

3.3.4 Relationship to Solidification Conditions

Since our results show initial solidification microstructure plays a critical role on subsequent decomposition during heat treatment, further analysis was performed on other solidification microstructures. The Al-Ce-Mn system has been explored for a variety of compositions and processing techniques [150,151,154,156]. The range of solidification conditions provided by different techniques have produced several solidification modes and morphologies. Yang *et al.* [150] concluded that the formation of the equilibrium $Al_{10}Mn_2Ce$ phase could be suppressed from the liquid with sufficient undercooling which gives rise to the formation of metastable $Al_{20}Mn_2Ce$. Alternatively, gas atomized power taken before AM from Plotkowski *et al.* [151], shows three phases (FCC Al, $Al_{20}Mn_2Ce$, and $Al_{11}Ce_3$) with no indication of $Al_{10}Mn_2Ce$.

These observations from the literature may be contextualized with the present results as shown in Figure 3.11. The casting microstructure from Ying *et al.* is representative of the lower solidification cooling rate. Gas atomization generally has a high cooling rate compared to casting, but slower than laser additive manufacturing. In our results, the melt pool boundary solidifies more slowly than the weld track interior.

From the combination of these results, we may hypothesize that the equilibrium $Al_{10}Mn_2Ce$ phase forms only on slow cooling rates but is easily suppressed as faster solidification tends to

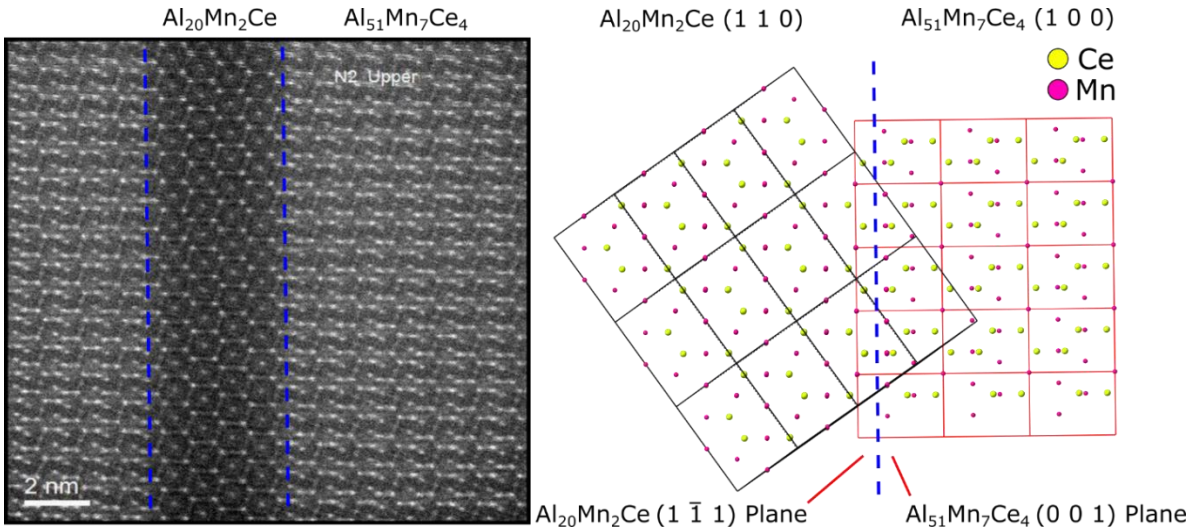

Figure 3.10 (A) HAADF STEM image of an interface between $Al_{20}Mn_2Ce$ and $Al_{51}Mn_7Ce_4$. (B) Projections of the $Al_{20}Mn_2Ce$ ($\mathbf{1\bar{1}1}$) and $Al_{51}Mn_7Ce_4$ (100) drawn using Crystal Maker® illustrating the matching with interface between the two phases.

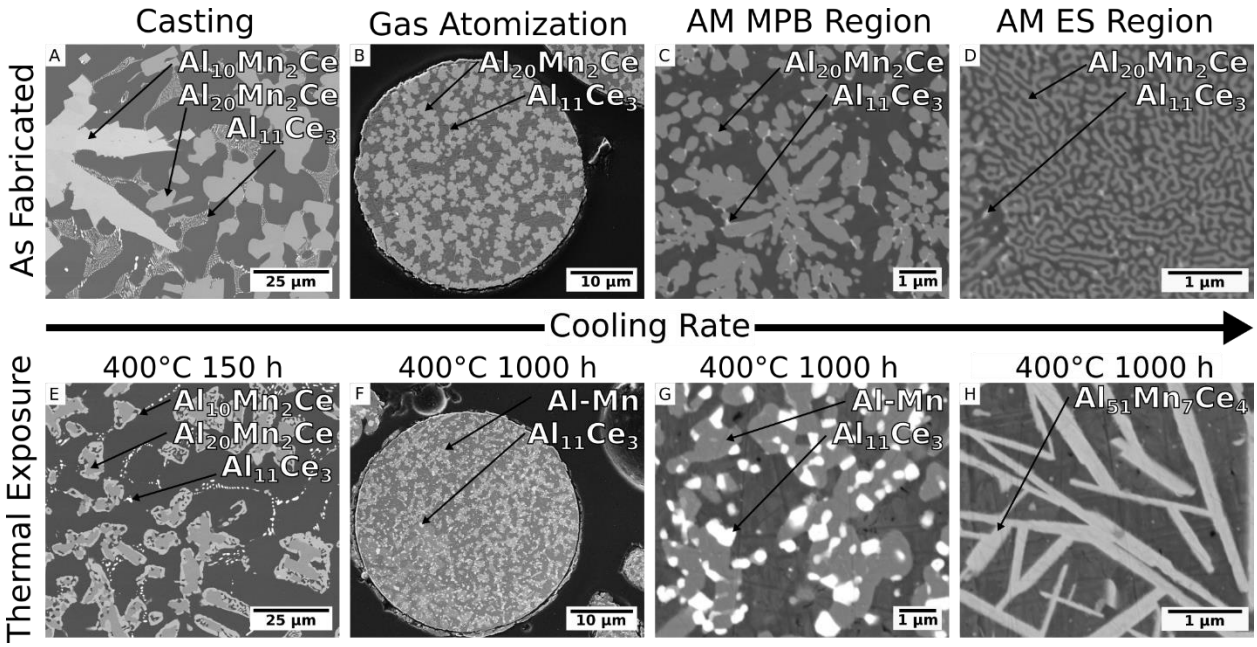

Figure 3.11. Changing microstructure in the Al-Ce-Mn system as a function of cooling rate and subseqent heat treatment.

increase the solid-liquid interface undercooling. At this point, primary $Al_{20}Mn_2Ce$ tends to form from the liquid. Further increase in solidification rate leads to reduction in the size of the $Al_{20}Mn_2Ce$ particles, and possibly changes in composition away from strict stoichiometry. At even faster solidification rates, primarily $Al_{20}Mn_2Ce$ solidification is suppressed in favor of eutectic solidification consisting of $Al_{20}Mn_2Ce$ and FCC Al, likely with far-from-equilibrium compositions.

These differences lead to corresponding variations in the solid-state decomposition $Al_{20}Mn_2Ce$. In the heat-treated casting microstructure (Figure 3.11E), $Al_{20}Mn_2Ce$ decomposes into the equilibrium $Al_{10}Mn_2Ce$ phase, likely because some amount of $Al_{10}Mn_2Ce$ exists in the solidification microstructure and may therefore increase its phase fraction through growth without overcoming the need for new nucleation. In the heat-treated powder particle (Figure 3.11F) $Al_{20}Mn_2Ce$ decomposes into the $Al_{11}Ce_3$, Al_6Mn, and $Al_{12}Mn$. In the heat treated MPB region, Figure 3.11G, the $Al_{20}Mn_2Ce$ phase decomposes into $Al_{11}Ce_3$, Al_6Mn, and $Al_{12}Mn$. In the heat-treated ES region, Figure 3.11H, the $Al_{20}Mn_2Ce$ phase decomposes into the $Al_{51}Mn_7Ce_4$ phase.

We may rationalize which decomposition pathway is selected from the starting solidification conditions by further examining the equilibrium free energy tangents at specific local compositions representative of each process. For this purpose, the composition of the as-cast and as-atomized microstructure was assumed to follow a Scheil solidification path resulting in 0.7762 at. % Mn in FCC Al, using the weighted average composition of FCC Al. The $Al_{20}Mn_2Ce$ composition was taken as stoichiometric in the casting, and $Al_{19.62}Mn_{2.42}Ce_{0.67}$[MPB], the same as the MPB region, for the atomized powder. The driving force calculations for these and the AM conditions were performed the same as Section 4.1 with results given in Table 3.3.

For the cast case, the driving forces for decomposition of stoichiometric $Al_{20}Mn_2Ce$ favors the formation of $Al_{10}Mn_2Ce$. In the atomized powder, Al_6Mn has the highest driving force for nucleation. In both cases, $Al_{51}Mn_7Ce_4$ does not have a reduction in free energy to form from $Al_{20}Mn_2Ce$.

Table 3.3 Calculated Driving Forces for the MPB and ES localized equilibrium states.

Phase Name	Approximate Casting Conditions	Approximate Powder Conditions
$Al_{11}Ce_3$ (j/mol)	-2547.54	-11,312.22
$Al_{12}Mn$ (j/mol)	521.45	519.57
Al_6Mn (j/mol)	932.69	**929.18**
$Al_{10}Mn_2Ce$ (j/mol)	**1269.75**	-2710.15
$Al_{51}Mn_7Ce_4$ (j/mol)	-68.72	-1880.13

The negative driving force means that the reduced interfacial energy between phases will be of no consequence. This observation follows the same rationalization discussed in Section 4.2 and has the same decomposition pathway as the MPB in the AM samples.

3.4 Conclusions

The phase transformation pathways in the Al-10Ce-8Mn (wt. %) system produced by L-PBF AM coupled with post-process heat treatment at 400°C were studied. In the as-fabricated condition, two distinct microstructural regions were observed: (1) the primary intermetallic solidification region near the melt pool boundary (MPB), containing $Al_{19.92}Mn_{2.42}Ce_{0.67}$[MPB] intermetallic phase, at the edge of the weld track with high thermal gradient and low liquid-solid interface velocity. (2) the eutectic solidification (ES) region, consisting of lamellar FCC Al and $Al_{19.62}Mn_{2.2}Ce_{1.18}$[ES] structure, at the center of the weld track. The $Al_{20}Mn_2Ce$ compounds in both regions were found to be non-stoichiometric. The microstructures in these two regions followed different decomposition pathways upon heat treatment. The MPB region decomposed into the FCC Al, Al_6Mn, $Al_{12}Mn$, and $Al_{11}Ce_3$. The ES region decomposed into FCC Al and a newly identified phase $Al_{51}Mn_7Ce_4$ with space group, $P\bar{3}m1$ (Space Group 161) a = 10.21$\pm$0.006, c =11.49$\pm$0.005 Å. The local compositions in each region were treated independently and a driving force for nucleation of each product phase was estimated using computational thermodynamics. The localized compositions of FCC Al and $Al_{20}Mn_2Ce$ in each solidification region were found to strongly influence the selection of specific decomposition pathways. Chapter 3 has previously been published.

Chapter 4. Confirmation of Microstructure Decomposition Pathways using Single Pass Laser Track Experiments

In Chapter 3, the additively manufactured (AM) Al-10Ce-8Mn (wt. %) alloy samples showed two initial solidification modes, primary $Al_{20}Mn_2Ce$ and a eutectic between FCC Al and $Al_{20}Mn_2Ce$. These two solidification modes were rationalized with the spatial variations of thermal gradient (G) and liquid-solid interface velocity (V). On heat treatment, the primary $Al_{20}Mn_2Ce$ decomposed into $Al_{11}Ce_3$, Al_6Mn, and $Al_{12}Mn$. In contrast, with the similar heat treatment, the eutectic $Al_{20}Mn_2Ce$ decomposed into $Al_{51}Mn_7Ce_4$. In both the cases, the FCC Al matrix likely supplied Mn to aid the above decomposition pathways.

It is noteworthy that our interpretation of AM microstructure does have uncertainties related to repeated heating and cooling thermal cycles. Therefore, in this chapter we attempt to address the following questions:

- Where are the transition points between solidification phase selection from $Al_{10}Mn_2Ce$, $Al_{20}Mn_2Ce$, and a eutectic between FCC Al and $Al_{20}Mn_2Ce$?
- What decomposition pathway does the $Al_{20}Mn_2Ce$ phase follow under different solidification conditions?

The first question is addressed by laser track experiments with different processing conditions, which in turn changes the thermal gradient and solidification velocity in a controlled fashion. Specifically, the change in solidification velocity is targeted by increasing the laser velocity from 1 to 83 mm/s. The second question is addressed by heat treating the weld tracks at 400°C for 96 hours to observe the decomposition pathways of the solidified microstructure.

4.1 Experimental Setup

Multiple weld track experiments were performed on an Okuma MU-8000V Laser Ex. The results are obtained from an extensive number of experiments to minimize keyhole porosity while ensuring a large enough weld track to analyze the results. The selected parameters are discussed in section 4.1.1.

4.1.1 Weld track Production

The weld tracks were made on Al-Ce-Mn substrate coin samples. These substrates were previously additively manufactured using L-PBF method. The AM coins were used as a base because the fine dispersion of intermetallic particles could possibly mitigate some localized compositional differences. The Okuma machine used for creating the weld tracks, uses an argon cover gas. The weld tracks were performed on 15 mm diameter coins approximately 5 mm thick. The sample surface was ground with an 800-grit sandpaper before weld track experiments. The process parameters are shown in Table 4.1. There was no preheat used in the experiment.

4.1.2 Heat treatment

Post processing heat treatment was performed on weld track coins that were cross sectioned perpendicular to the weld track before heat treatment. The coins were heated to 400°C for 96 hours in air. This heat treatment was chosen for direct comparison with AM samples from Chapter 3. It is noteworthy that the AM samples after 96-hour heat treatment also allowed each region to be identified because of their incomplete decomposition state. Therefore, the 96-hour sample was used to ensure a large amount of the $Al_{20}Mn_2Ce$ would undergo decomposition and could be tracked back to the original microstructure. Then the samples were air cooled to room temperature and prepared for metallographic analysis. The heat treatment was performed by Andres Marques at Oak Ridge National Laboratory using a tube furnace at 400°C in air.

4.1.3 Scanning Electron Microscopy

Scanning electron microscopy (SEM) was performed using a Zeiss Gemini 450 Field Emission Microscope equipped with a backscattered electron (BSE) detector. The accelerating voltage was kept constant at 5 kV for all images. The spatial resolution varies for each image. All samples were mounted in epoxy using the XZ plane perpendicular to the build direction. The samples were ground to remove any surface effect from sectioning to a 4000 grit SiC. The samples were then polished to 3 μm and then finally to a 1 μm finish with a diamond slurry. Then the samples were ion milled using a Hitachi ArBlade at a voltage of 5 kV and a current of 2.5 nA for 15 minutes using the maximum eccentricity to ensure a clean surface for imaging.

Table 4.1 Weld track Experimental Parameters

Sample I.D.	Power (W)	Speed (mm/s)	Spot Size (mm)
1	200	1	1.5
2	500	10	1.5
3	500	15	1.5
4	500	23	1.5
5	500	35	1.5
6	500	54	1.5
7	500	83	1.5

4.1.4 Thermodynamic Driving Force Calculations

The driving force for nucleation of product phase was determined by computing the tangent plane between the two expected parent phases, FCC Al and $Al_{20}Mn_2Ce$ phases. The difference between the tangent plane and respective free energy of intermetallic compounds. For each calculation, the $Al_{20}Mn_2Ce$ is treated as a separate intermetallic compound with the stoichiometric composition $Al_{23-x-y}Mn_xCe_y$. Therefore, a unique tangent plane exists for each composition of FCC Al and $Al_{20}Mn_2Ce$.

4.2 Weld Tracks

In this section, the initial modeling of the solidification conditions will be explored. The goal of this section is to understand the change in phases as a function of solidification conditions, and the subsequent decomposition of phases during heat treatment.

4.2.1 Modeling of Thermal Conditions in Weld Tracks

The absorption efficiency of the laser was fit using the measured weld track depths for each weld track at the center. The width of the weld track is not considered. The thermophysical properties used in the current model were determined from an Al-Ce-Ni-Mn-Zr alloy data collected at Oak Ridge National Lab and are shown in Table 4.2. The specific heat was determined using differential scanning calorimetry. The thermal diffusivity was determined using laser flash diffusivity test. Thermal conductivity was determined using a combination of the previous values.

The absorption efficiencies for each model were calibrated by matching the predicted depth to the measured depth. The depth of each weld track is determined by measuring the SEM-BSE data from the top of the weld track to the base material. This measurement includes both the partially melted zone (PMZ) and the melt pool boundary (MPB). The width of the weld track is ignored. The PMZ and MPB are characterized using the predicted temperature distribution from Rosenthal equation [118]. An example of the of the separation of PMZ and MPB is observed in Figure 4.1.

Table 4.2 Thermophysical properties used in determining G and V from the two adopted Rosenthal models.

Thermophysical Properties	
Specific Heat (J/kg-K)	969.14
Thermal Conductivity (W/K-m)	134.17
Density (kg/m^3)	2920
$T_{isotherm}$ (K)	927, 1177

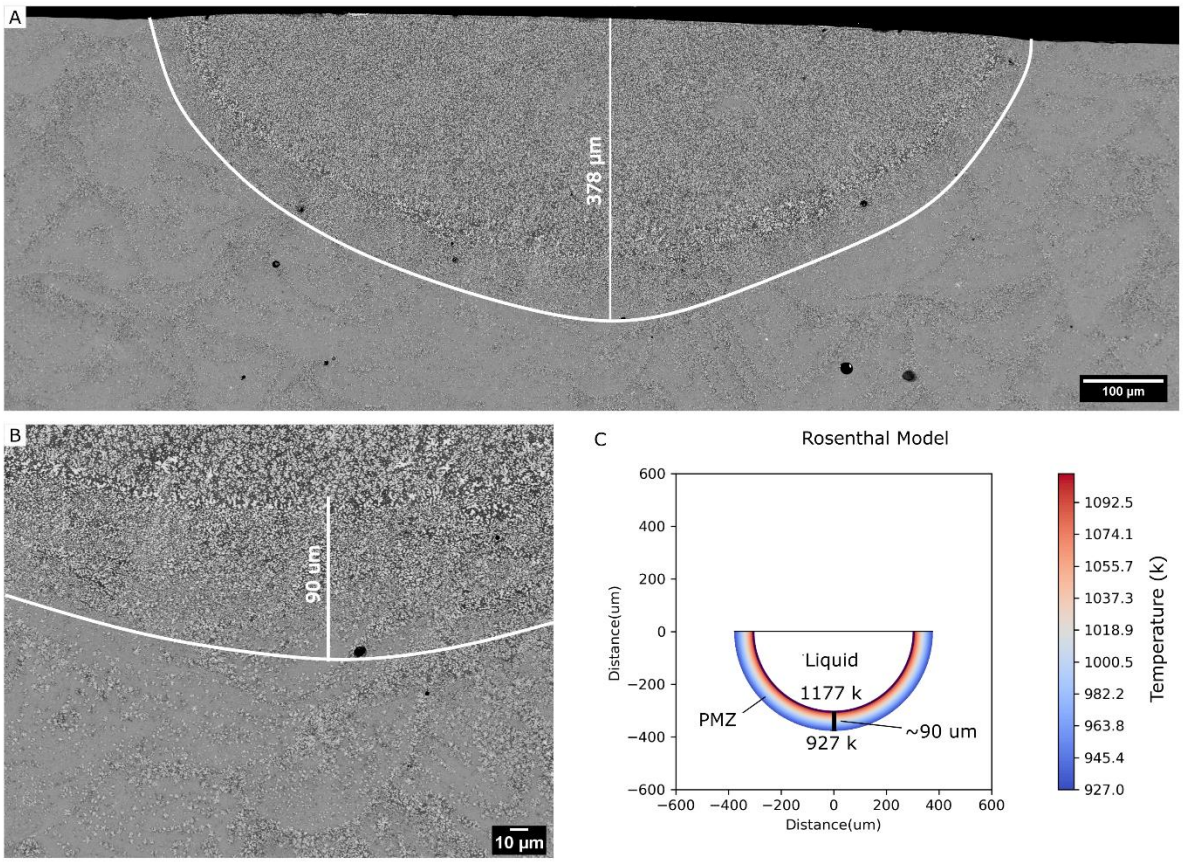

Figure 4.1 Demonstrates the used method for determining the weld track depth for the 54 mm/s weld track. Where (A) is the outline of the weld track including the PMZ, (B) is a zoomed in region near the MPB that demonstrates the expected 75µm width of the PMZ, and (C) is the temperature of the temperature distribution of the Rosenthal model plotted between the 927 and 1177 K, or the freezing range of the bulk composition.

To determine the PMZ, the parameters in Rosenthal equation are fitted to the 927 K isothermal across the measured depth. The depth measurements here are performed by visual observation. The PMZ width is defined by the distance between 927 and 1177 k isotherms in the weld track. The 1177 k isotherm is the expected liquidus temperature of the $Al_{20}Mn_2Ce$ phase at the bulk alloy composition. The 927-k temperature is the expected eutectic temperature between FCC Al and $Al_{20}Mn_2Ce$. The thermophysical properties are kept constant.

The depths of each weld track were measured in the center of the weld track to the MPB. The value for each depth is shown in Table 4.3. Using these depth values, the intersection of the Rosenthal model with the 927 K isothermal is fit by adjusting the absorption efficiency. All the fit absorption efficiencies are higher than the expected 0.33. The overestimated absorption efficiency may be related to the simplified Rosenthal model that is modeled as a point source and not a 3-dimensional gaussian distribution. The PMZ width is determined by finding the distance between the 927 and 1177 K isotherms.

The thermal gradients and solidification velocities of each weld track are extracted by determining the surface of the isotherm. The scipy least squares optimization method [173] was used to determine the liquidus iso-surface at the set temperature and bounded to only include negative numbers, below the surface of the weld. The thermal gradient of the Rosenthal model was determined by the derivative at each point on the surface of the weld track. A numerical derivative from the scipy package [173] is used to approximate the thermal gradient with a step size of $1x10^{-9}$ m.

The solidification velocity and thermal gradients are shown in Figure 4.2 for each parameter set. The isotherm is set to T = 927 K. The selected laser velocities were chosen to systematically understand the slower solidification rate of the Al-Ce-Mn system. In the first step, the 10-83 mm/s was chosen, but the microstructure did not show a clear transition to the $Al_{10}Mn_2Ce$ phase. Therefore, the additional 1 mm/s weld track was added to promote a larger primary region of $Al_{10}Mn_2Ce$. The phase selection will be discussed as a function of laser velocity in the next section. The transition to equilibrium $Al_{10}Mn_2Ce$ is targeted to understand the critical velocity for the formation of the $Al_{20}Mn_2Ce$ phase. Therefore, the full range of primary $Al_{20}Mn_2Ce$

Table 4.3 Measurement of the weld track depth for each laser velocity.

Laser Velocity (mm/s)	Weld Track Depth (μm)	Rosenthal Absp. Eff.	PMZ Width (μm)
1	271	0.721	60
10	540	0.605	147
15	518	0.595	138
23	461	0.545	120
35	425	0.51	108
54	378	0.495	90
83	326	0.46	75

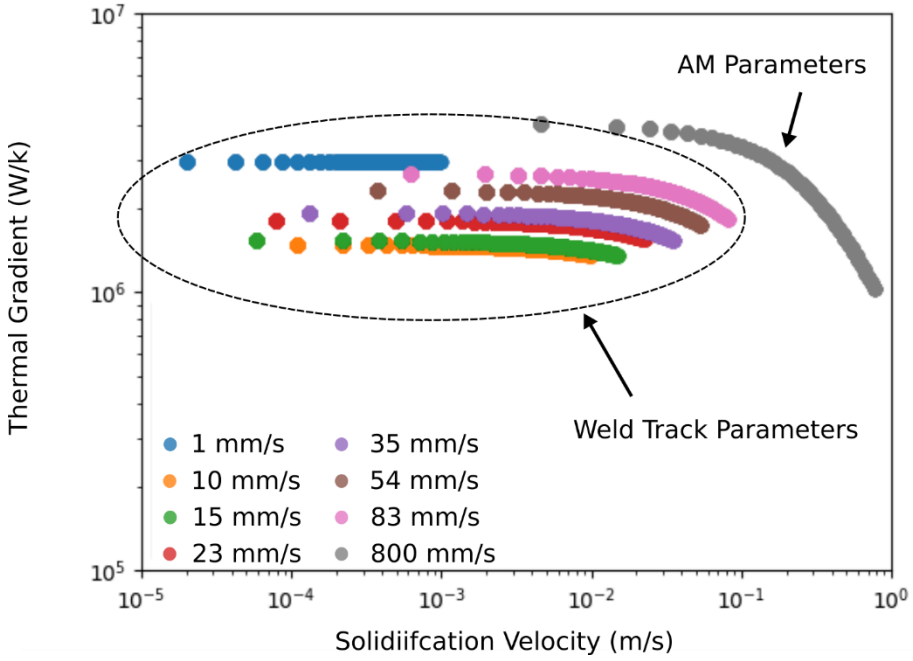

Figure 4.2 Plotting the Solidification Velocity and Thermal Gradient of the Rosenthal Model of each weld track and AM parameter. The liquidous isotherm is set to 927 k.

solidification can be captured to understand its decomposition pathways as a function of solidification condition.

The liquidus temperature is chosen at 927 K because it is the approximate solidification temperature of the eutectic between $Al_{20}Mn_2Ce$ and FCC Al in the current alloy. If the liquidus temperature is changed to 1177 K, the temperature for the formation of intermetallic, the magnitude of the thermal gradient and solidification velocity may also change. Therefore, the thermal gradient and solidification were calculated along the isotherms of 927 and 1177K for the weld track made with a welding velocity of 83 mm/s. The range of accessible the thermal gradient and solidification that is calculated for the 83 mm/s condition in Figure 4.3. It is noticeable that solidification velocity may change, and the thermal gradient increases (e.g.,$2x10^6$ to $6x10^6$ K/m) as the liquidus temperature increases. The reasoning for mentioning this is that there is not a clear distinction between the PMZ and the MPB, and it is only assumed to be the distance between the two isotherms.

4.2.2 As-Fabricated Weld tracks

Throughout literature, there are a variety of solidification conditions that are reported in Al-rich Al-Ce-Mn systems. These varied conditions, from casting to additive manufacturing, have led to large changes in solidified microstructure and are rationalized based on the cooling rates (cooling rate = G * V) that are relevant to each process. Therefore, a set of processing parameters were designed to modify the primary formation of each phase from the liquid. In the literature, there are different primary phases expected to form for the current alloy (Al-10Ce-8Mn wt.%) as we transition from slow to rapid cooling rates. At low cooling rates, the formation of $Al_{10}Mn_2Ce$, which is the equilibrium intermetallic phase, is expected based on computational thermodynamic calculations. With an increase in the cooling rates (i.e., an increase in the solidification velocity with similar thermal gradients), the formation of the $Al_{20}Mn_2Ce$ phase is expected from literature. The formation of $Al_{20}Mn_2Ce$ at high cooling rates is also observed in Chapter 3. Finally, when the cooling rate increases further, the primary intermetallic phase formation transitions to the formation of a eutectic microstructure which is a mixture of FCC Al and $Al_{20}Mn_2Ce$ phases.

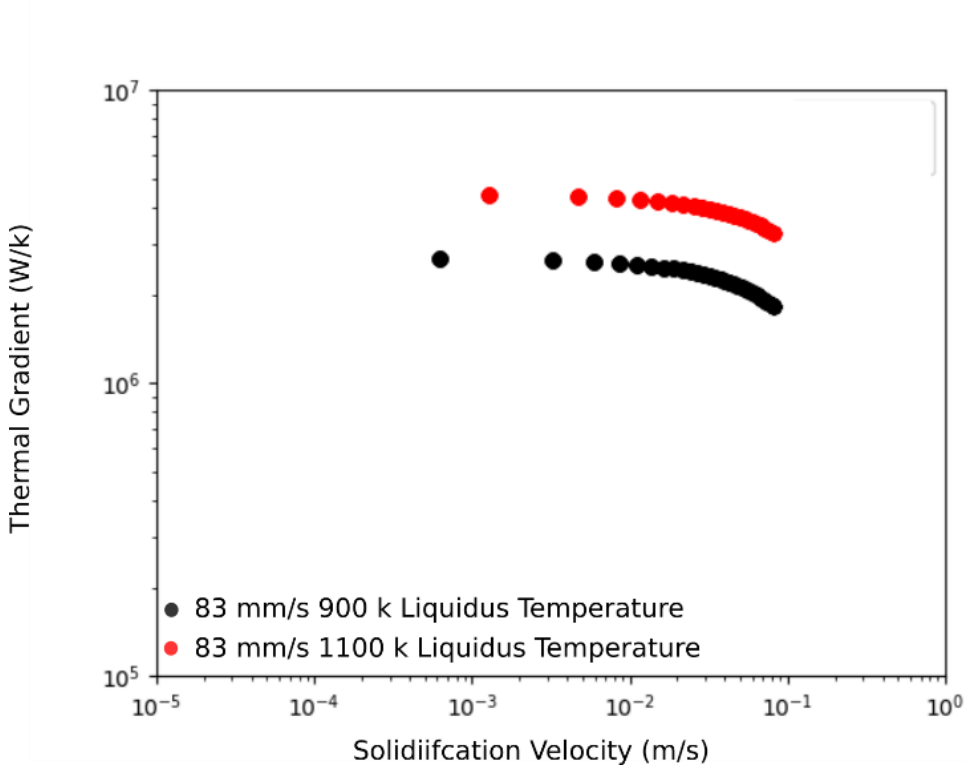

Figure 4.3 Plotting the G and V of the Rosenthal model using different liquidus temperatures.

With the above narrative, the microstructures in the weld track experiments are discussed. The general identification images in this section have the layout contained in schematic weld track in Figure 4.4. The layout in Figure 4.4 demonstrates an example of the A-D micrographs used for describing all the as-fabricated microstructure. The micrographs are not necessarily in the same exact locations but are used to indicate the ordering of the micrographs for the as-fabricated weld tracks. Three weld tracks are used to demonstrate the solidification conditions of the experiments. The goal is to identify the phases at each velocity to determine the phase presence in the system.

The slowest laser velocity of 1 mm/s is shown in Figure 4.5. The 1 mm/s weld track phase identification was originally performed using EBSD listed in the appendix. The identification of phases is performed using visual image contrast variations from SEM BSE. The order from brightest to darkest contrast in the as-fabricated samples is $Al_{11}Ce_3$ > $Al_{10}Mn_2Ce$ > $Al_{20}Mn_2Ce$ > FCC Al is based on the heavy element Ce concentration. This methodology has been proven to be a viable technique in Chapter 3 and allows for us to do large area phase characterization rapidly.

The solidified microstructure of the 1 mm/s weld track contains four phases, FCC Al, $Al_{10}Mn_2Ce$, $Al_{11}Ce_3$ and $Al_{20}Mn_2Ce$. In Figure 4.5A, at the bottom of the image is the base material (i.e., original AM material made by the L-PBF process). The region contains a dispersion of eutectic and primary microstructures as discussed in Chapter 3. Above the base material, the partially melted zone (PMZ) is observed. The PMZ is identified by being a sandwich between the fine microstructure of the base material and the coarsest microstructure at the edge of the weld track. In general, the PMZ is identified to be below the largest intermetallic particles in each weld track. The PMZ consists of a different microstructure morphology than the base material or the weld track. In Figure 4.5A, a more spherical $Al_{20}Mn_2Ce$ phase is surrounded by FCC Al and $Al_{11}Ce_3$ phases.

The spherical nature of $Al_{20}Mn_2Ce$ is likely related to thermal cycles that have different peak temperatures which may not dissolve the original phase mixtures created by the AM process. The PMZ contains the FCC Al, $Al_{11}Ce_3$, $Al_{20}Mn_2Ce$ and $Al_{10}Mn_2Ce$ phases in the 1 mm/s weld track. There is a notable gradient in size of the $Al_{20}Mn_2Ce$ phase across the PMZ, which is likely

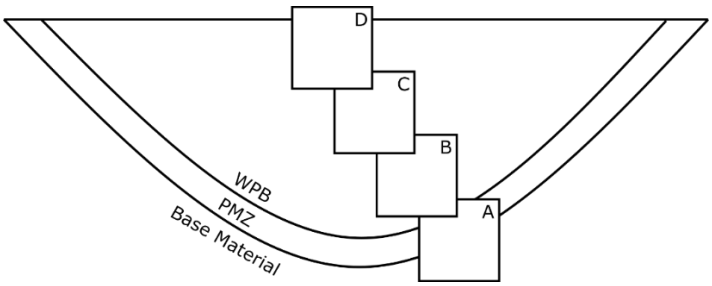

Figure 4.4 Schematic weld track demonstrating the location of images.

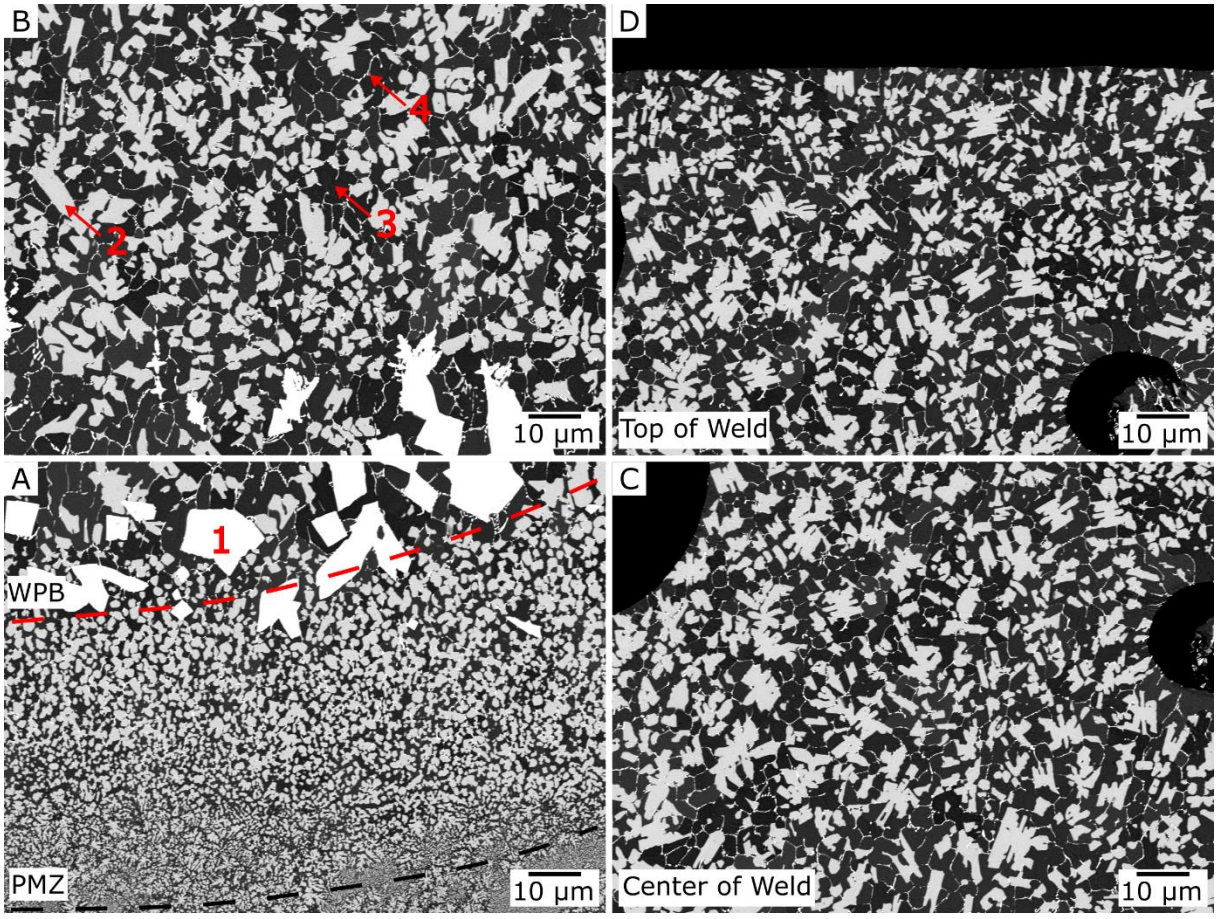

Figure 4.5 SEM of the 1 mm/s weld track. Where A) demonstrates the transition from the base metal to the PMZ region to the primary solidification of $Al_{10}Mn_2Ce$. B) demonstrates the transition from primary $Al_{10}Mn_2Ce$ solidification to primary $Al_{20}Mn_2Ce$ solidification. C) demonstrates the middle of the weld track where $Al_{10}Mn_2Ce$ is suppressed and $Al_{20}Mn_2Ce$ is the primary solidification phase. D) demonstrates the top of the weld track where $Al_{20}Mn_2Ce$ is the primary phase. The phases are denoted by number in the images where (1) is the $Al_{10}Mn_2Ce$ phase, (2) is the $Al_{20}Mn_2Ce$ phase, (3) is the FCC Al, and (4) is the $Al_{11}Ce_3$

due to the liquidus isotherm changing as a function of distance from the MPB. As the isotherm decreases away from the MPB, the amount of material melted will decrease. The FCC Al will also be preferentially melted because of its low liquidus temperature (933 k for pure Al), compared to the liquidus temperature of $Al_{20}Mn_2Ce$ (1177 k at the bulk alloy composition). At the MPB, denoted by the red 1 in Figure 4.5A, faceted $Al_{10}Mn_2Ce$ particles exist. The formation of the $Al_{10}Mn_2Ce$ phase must have been the result of nucleation, as no $Al_{10}Mn_2Ce$ exists within the base material. The result of faceted $Al_{10}Mn_2Ce$ is possibly because of preferential growth directions in the liquid, similar to what is observed in Al-Cu systems by Song *et al.* [174], where an Al_2Cu (θ) phase was observed to grow along preferential directions depending on thermal gradients.

The solidification conditions of the $Al_{10}Mn_2Ce$ phase can be bounded using the weld track modeling discussed in Section 4.2.1. To define the solidification bounds, the transition region from primary $Al_{10}Mn_2Ce$ to primary $Al_{20}Mn_2Ce$ can be used to determine the distance from the PMZ (isotherm of 927 k) and the distance from the MPB (1177 k). The transition between solidification modes can be related back to the spatial representation of the microstructure. The mapping of the microstructure is performed using the eutectic temperature (927 K) as a baseline to determine the solidification conditions based on the distance from the edge of the PMZ to the change in solidification microstructure from $Al_{10}Mn_2Ce$ to $Al_{20}Mn_2Ce$. To determine the distance, the weld track is assumed as a projection of the predicted weld surface onto a 2D plane. The distance from the edge of the weld track to the feature of interest is assumed to be the same as the depth of the weld track. The idea being that the cross section of the microstructure is a direct representation of the surface projection. The same is also done with the liquidus temperature (1177 K) to have a bounded comparison. The values calculated for the transition from primary $Al_{10}Mn_2Ce$ to primary $Al_{20}Mn_2Ce$ for the 1 mm/s weld track are given in Table 4.4.

In the next step, we evaluated the microstructures from 10 mm/s weld track. The phases ($Al_{10}Mn_2Ce$, $Al_{20}Mn_2Ce$, FCC Al, and $Al_{11}Ce_3$) are identified using the contrast from SEM BSE imaging. The individual phases are denoted using numbering in Figure 4.6.

Table 4.4 Measured distances in the 1mm/s weld track and corresponding solidification conditions predicted from the Rosenthal model from the transition of primary $Al_{10}Mn_2Ce$ to primary $Al_{20}Mn_2Ce$.

Isotherm	Distance from Isotherm (μm)	Solidification Velocity (m/s)	Thermal Gradient (K/m)
927 K	86	7.4×10^{-4}	2.45×10^{6}
1177 K	26	5.19×10^{-4}	4.78×10^{6}

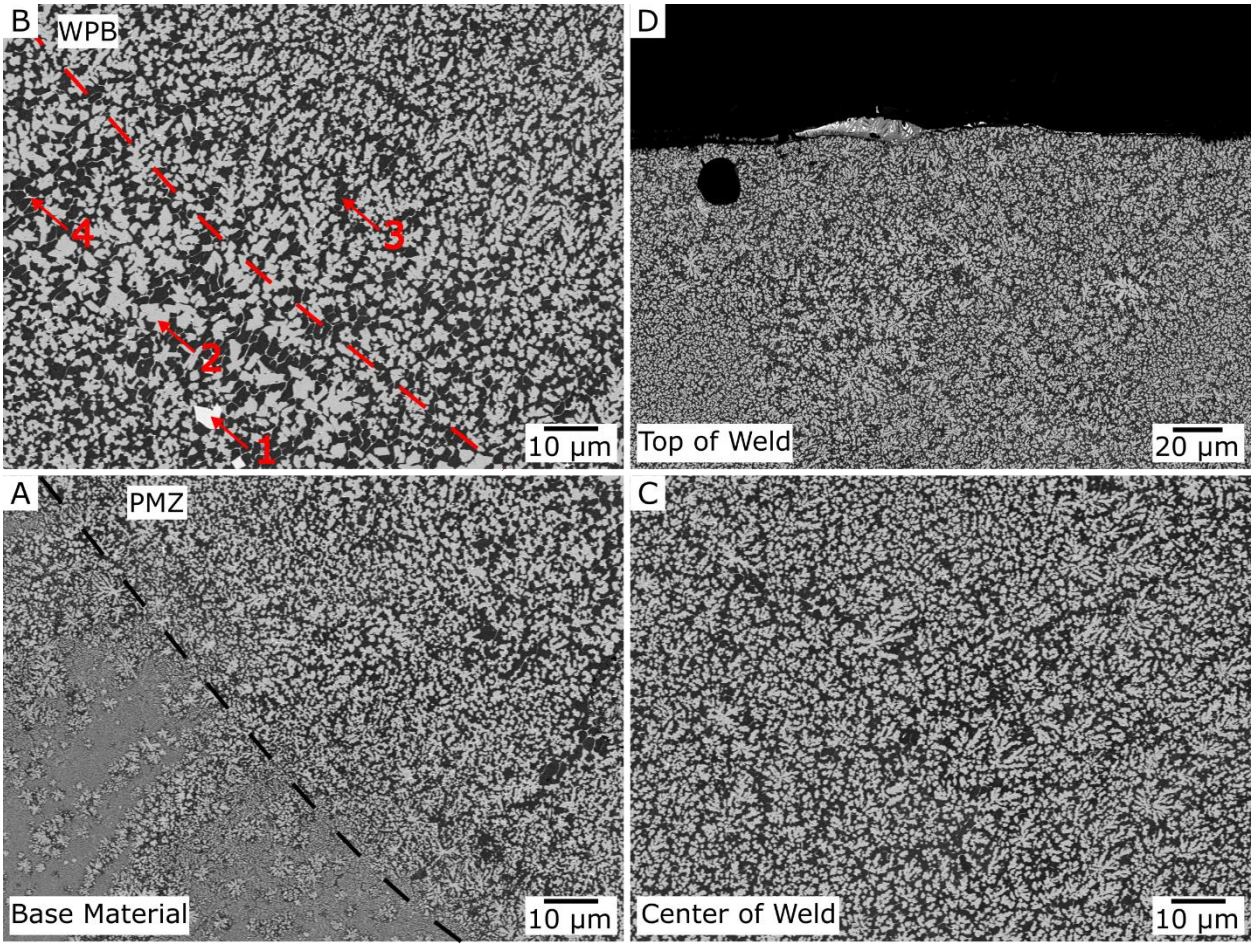

Figure 4.6 SEM of the 10 mm/s weld track. Where A) demonstrates the transition from the base metal to the weld track. B) represents the transition from the Partially Melted zone to the Weld track where the primary solidification of $Al_{10}Mn_2Ce$ is observed. C) demonstrates the middle of the weld track where $Al_{10}Mn_2Ce$ is suppressed and $Al_{20}Mn_2Ce$ is the primary solidification phase. D) demonstrates the top of the weld track where $Al_{20}Mn_2Ce$ is the primary phase. The phases are denoted by number in the images where (1) is the $Al_{10}Mn_2Ce$ phase, (2) is the $Al_{20}Mn_2Ce$ phase, (3) is the FCC Al, and (4) is the $Al_{11}Ce_3$.

The layout of the images in Figure 4.6 follow the schematic layout in Figure 4.4, but is mirrored across the centerline of the weld track. The image of the top of the weld track, Figure 4.6D, is at half the magnification of the other images to demonstrate a larger area at the top of the weld track. The red and black lines correspond to the MPB and PMZ boundary respectively. In Figure 4.6A, the transition from the base metal to the PMZ is shown. As expected, the base material microstructure is the same as that of sample made with 1 mm/s weld track.

In the PMZ the $Al_{10}Mn_2Ce$ phase can be observed in Figure 4.6B, below the MPB denoted by the red dotted line. At the MPB, as seen in Figure 4.6B, the formation of $Al_{10}Mn_2Ce$ particles is suppressed. As the solidification front moves away from the MPB, as observed in C and D, the $Al_{10}Mn_2Ce$ remains suppressed with an increase in liquid-solid interface velocity. The $Al_{20}Mn_2Ce$ phase is now the primary solidification phase throughout the remaining test conditions, excluding the PMZ of the 15 mm/s case. The phases in between the $Al_{20}Mn_2Ce$ are identified as FCC Al and $Al_{11}Ce_3$.

The as-fabricated weld track made with an 83 mm/s laser velocity is shown in Figure 4.7. The red and black lines corresponded to the MPB and PMZ boundaries respectively. There are three phases observed in the 83 mm/s weld track, $Al_{20}Mn_2Ce$, FCC Al, and $Al_{11}Ce_3$. The $Al_{20}Mn_2Ce$ and FCC Al are labeled in Figure 4.7, but the $Al_{11}Ce_3$ is not because of its small size.

The base material microstructure is the same as expected from the AM parts. In the PMZ and MPB in Figure 4.7A-B, the $Al_{10}Mn_2Ce$ is observed to be fully suppressed and the $Al_{20}Mn_2Ce$ is the primary solidified phase. Moving toward the center of the weld track in Figure 4.7C the primary solidified $Al_{20}Mn_2Ce$ eventually starts solidifying as a eutectic between FCC Al and $Al_{20}Mn_2Ce$. Above the eutectic region, in Figure 4.7D, the primary $Al_{20}Mn_2Ce$ reappears.

The eutectic solidification observed in Figure 4.8A, is a zoomed in region of Figure 4.7C inside the weld track. The eutectic $Al_{20}Mn_2Ce$ appears to emanate directly off the previous primary solidified $Al_{20}Mn_2Ce$. A schematic of the transition is demonstrated in Figure 4.8B. This geometric arrangement could be an indication that the orientation of $Al_{20}Mn_2Ce$ is maintained from primary to eutectic solidification.

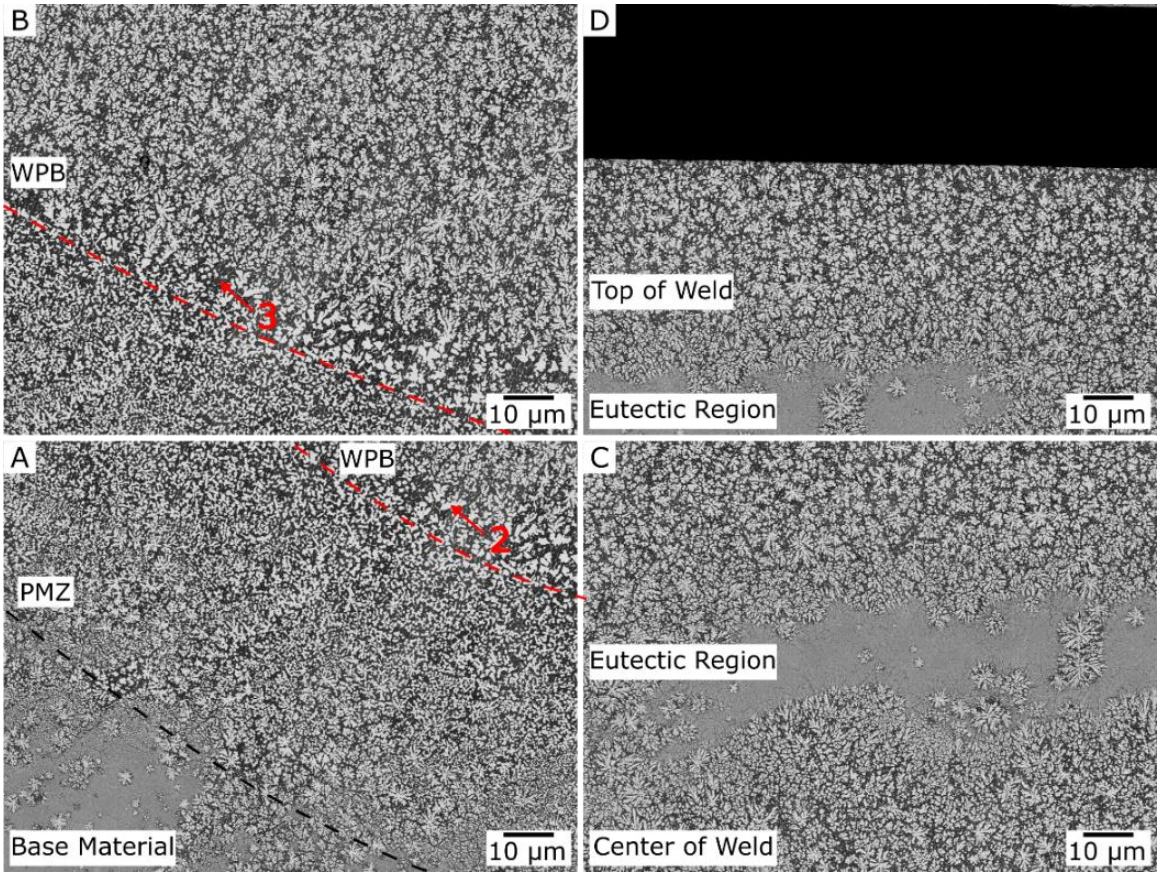

Figure 4.7 SEM of the 83 mm/s weld track where A) demonstrates the transition from the base metal to the PMZ. B) represents the transition from the PMZ to the MPB. C) represents the center of the weld track. D) represents the top of the weld track. The phases are denoted by number in the images where, (2) is the $Al_{20}Mn_2Ce$ phase and (3) is the FCC Al.

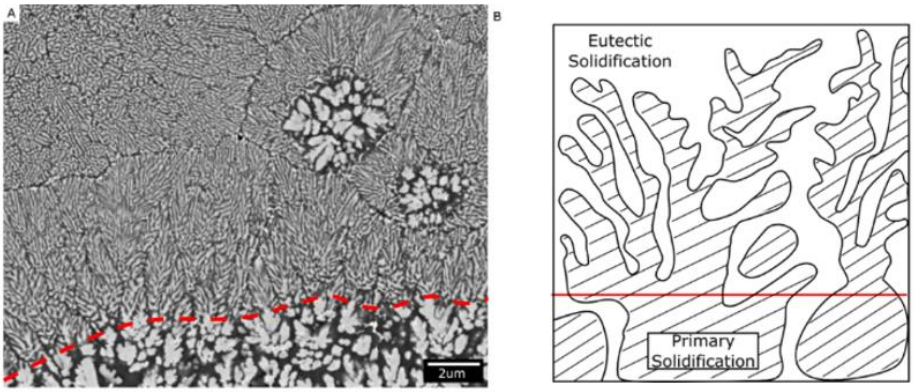

Figure 4.8 A) demonstrates SEM BSE of the transitions from primary to eutectic solidification approximated by the dotted red line. B) demonstrates a schematic at that interface demonstrating its interconnectedness

The image in Figure 4.8A is a higher resolution image of the eutectic region shown in Figure 4.7C. However, this hypothesis needs to be proven with site-specific transmission electron microscopy, which is beyond the scope of current research.

To approximate the transition between the primary $Al_{20}Mn_2Ce$ phase and the eutectic between $Al_{20}Mn_2Ce$, an analysis is performed for the 83 mm/s weld track like the 1 mm/s, as seen in Table 4.5. The distinction between the primary $Al_{20}Mn_2Ce$ and the eutectic is not as clear at the transition between $Al_{10}Mn_2Ce$ and primary $Al_{20}Mn_2Ce$. Therefore, an average of multiple distances from the weld track edge to the eutectic is used to determine where the solidification conditions should be calculated. An error bar is not shown, because it is expected that the isotherms bound the solidification conditions.

4.2.3 Summary of Microstructures in Weld Tracks

The solidification phase selection as a function of changing solidification conditions for an Al-10Ce-8Mn (wt.%) alloy has been explored. As the laser velocity increases from 1 to 23 mm/s, the primary $Al_{10}Mn_2Ce$ solidification transitions to primary $Al_{20}Mn_2Ce$ solidification. As the solidification velocity increases because of the laser velocity increasing from 23-83 mm/s, the primary $Al_{20}Mn_2Ce$ is suppressed in the center of the weld region, and a eutectic microstructure with FCC Al and $Al_{20}Mn_2Ce$ phases is promoted. The primary solidification modes for each weld track are outline in Table 4.6. The outline includes the PMZ and the weld track.

The transition from the $Al_{10}Mn_2Ce$ to $Al_{20}Mn_2Ce$ to a eutectic microstructure is shown in Figure 4.9 for the 927 K isotherm independent of thermal gradient. Figure 4.9 outlines visually the transition between phase selection as a function of solidification. Although the outline in Figure 4.9 is only for the 927K isotherm and independent of thermal gradient. Both solidification terms play a role in the transition to different phases. Using the 927K and 1177K isotherms as bounding conditions, the transition from the primary $Al_{10}Mn_2Ce$ to the primary $Al_{20}Mn_2Ce$ phase is expected to occur between a solidification of 5.19×10^{-4} to 7.4×10^{-4} (m/s) and a thermal gradient of 2.45×10^{6} to 4.78×10^{6} (K/m) determined from the 1 mm/s weld track. The transition from the primary $Al_{20}Mn_2Ce$ phase is expected to occur between a solidification velocity of 6.8×10^{-2} to 7.3×10^{-2} (m/s) and a thermal gradient of 1.49×10^{6} to 2.95×10^{6} (K/m), determined from the 1 mm/s weld track.

Table 4.5 Measured distances in the 83 mm/s and corresponding solidification conditions predicted from the Rosenthal model from the transition of primary $Al_{20}Mn_2Ce$ to eutectic FCC + $Al_{20}Mn_2Ce$.

Isotherm	Distance from Isotherm (μm)	Solidification Velocity (m/s)	Thermal Gradient (K/m)
927 K	189	$7.3x10^{-2}$	$1.49x10^{6}$
1177 K	114	$6.8x10^{-2}$	$2.95x10^{6}$

Table 4.6 Outline of solidification microstructures observed in each weld track.

Laser Velocity (mm/s)	Primary $Al_{10}Mn_2Ce$	Primary $Al_{20}Mn_2Ce$	FCC Al/$Al_{20}Mn_2Ce$ Eutectic
1	X	X	
10	X	X	
15	X	X	
23		X	
35		X	
54		X	X
83		X	X

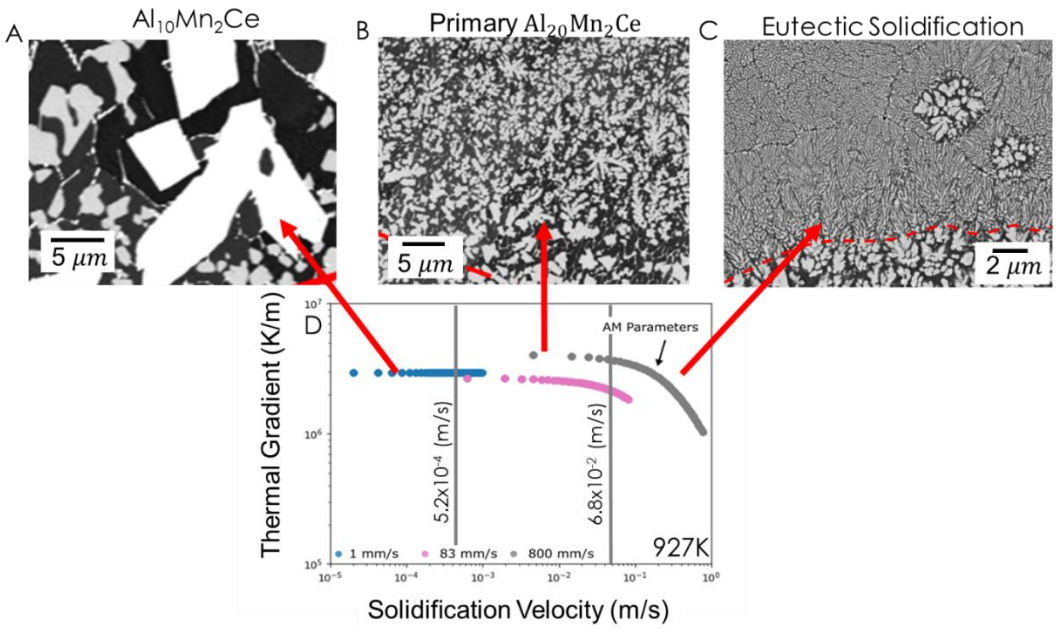

Figure 4.9 Demonstrates the transition of primary phase selection as a function of solidification velocity from the 927K isotherm. (A) demonstrates the primary solidification of $Al_{10}Mn_2Ce$ from the 1mm/s weld track below $5.2x10^{-4}$ (m/s) solidification velocity (B) demonstrates the primary solidification of $Al_{20}Mn_2Ce$ sthe eutectic solidification between FCC Al and $Al_{20}Mn_2Ce$ above $6.8x10^{-2}$ (m/s) solidification velocity. (D) demonstrates the solidification velocity and thermal gradient in the 1, 83, and 800 mm/s Rosenthal modeled weld tracks.

The thermal gradients in each laser velocity are not very different, and likely play less of a role than the solidification velocity. The effect of thermal gradient is explored in Chapter 5.

Overall, there appears to be the ability to control the primary solidification phase selection as a function of liquid-solid interface velocity. The observance of the primary $Al_{10}Mn_2Ce$ being suppressed with promotion of $Al_{20}Mn_2Ce$ at higher liquid-solid interface velocities agrees with literature in the Al-Ce-Mn system.

4.2.4 Heat Treated Weld Tracks

The as-fabricated weld tracks were heat treated at 400°C for 96 hours. The heat treatment was selected to understand the stability of the solidification microstructures. SEM BSE microscopy was performed on each weld track to determine the localized solid-state phase transformations in the system. The layout of the figures in this section are made to illustrate the site-specific changes to track individual phase transformation pathways. The first weld track investigated is 1 mm/s weld track after heat treatment for 400°C 96 hours, in Figure 4.10. The phases are identified for the reader through the contrast variation from the SEM BSE. In Figure 4.10A a schematic of each microstructure location within the weld track. The top of the weld track is not shown because it decomposes along the same pathway as observed in Figure 4.10E. An overview of the microstructure is shown in Figure 4.10B. The overview shows the PMZ (C), the MPB (D), and regions away from the MPB (E). The $Al_{20}Mn_2Ce$ in the PMZ decomposes into $Al_{11}Ce_3$ + Al-Mn binary phases. The Al-Mn binary phases could be $Al_{12}Mn$, Al_6Mn, or a mixture of both, but more evidence is needed to conclude that directly. As per thermodynamic calculations, the $Al_{12}Mn$ phase is the expected equilibrium phase at 400°C. $Al_{12}Mn$ and Al_6Mn have not been reported in literature to contain Ce. No exhaustive studies have been performed. In Figure 4.10D, right above the MPB, a large $Al_{10}Mn_2Ce$ particle is shown in the center of the image. This $Al_{10}Mn_2Ce$ particle does not appear to decompose around the edges of the phase. The $Al_{20}Mn_2Ce$ surrounding the $Al_{10}Mn_2Ce$ particle appears to decompose into $Al_{11}Ce_3$ + Al-Mn binary phases. In Figure 4.10E, the primary $Al_{20}Mn_2Ce$ phase appear to be decomposing into $Al_{11}Ce_3$+Al-Mn binary phases. In Figure 4.10F, a single $Al_{20}Mn_2Ce$ particle is shown that demonstrates a fine "Chinese script" microstructure of $Al_{11}Ce_3$ surrounded by an Al-Mn binary phase. The decomposition behavior of the 1 mm/s remains the same through the weld track.

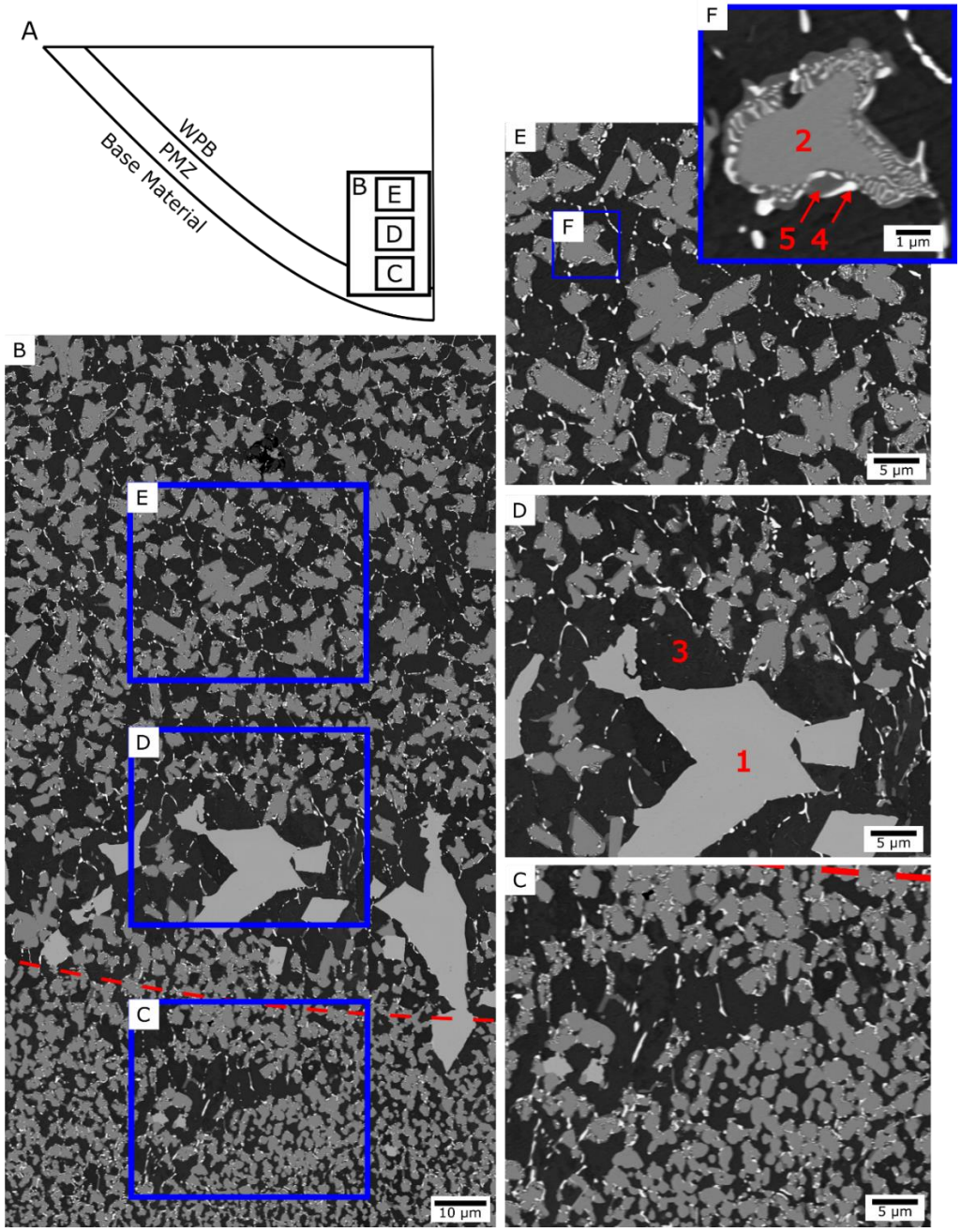

Figure 4.10 SEM BSE of the 1 mm/s weld track after 400°C 96 hour heat treatment, where (A) is a schematic that demonstrates where each image is taken in the weld track, (B) is an overview of the microstructure near the MPB, (C) represents the paritially melted zone (PMZ) of the micorstructure, (D) represents slightly above the MPB, (E) represents a region away from the MPB, and (F) is a cutout to demonstrate the localized decomposition around an $Al_{20}Mn_2Ce$ particle. The phases are denoted by number in the images where (1) is the $Al_{10}Mn_2Ce$ phase, (2) is the $Al_{20}Mn_2Ce$ phase, (3) is the FCC Al, (4) is the $Al_{11}Ce_3$, and (5) is the Al-Mn binary phases.

The 15 mm/s weld track is shown in Figure 4.11 after heat treatment of 400°C for 96 hours. The 10 mm/s weld track decomposition pathway is very similar. The only difference is related to the distance away from the MPB at which the phase decomposition pathways change. The decomposition of the $Al_{20}Mn_2Ce$ phase in the 15 mm/s weld track can be observed, in Figure 4.11. The phases are identified through morphology and contrast variation from the SEM BSE. In Figure 4.11A, a slightly different overview layout is shown. The microstructure shown in Figure 4.11E is taken from a region in the center of the weld track that demonstrates a pocket of decomposition.

An overview of the microstructure near the MPB is shown in Figure 4.11B. In Figure 4.11C, the PMZ and MPB regions are shown. In both regions, the decomposing phase is $Al_{20}Mn_2Ce$. The $Al_{20}Mn_2Ce$ appears to be decomposing into $Al_{11}Ce_3$+Al-Mn binary phases. Additionally, a small amount of $Al_{10}Mn_2Ce$ is present and does not appear to decompose. In Figure 4.11D slightly removed MPB, the decomposition of the $Al_{20}Mn_2Ce$ phase favors a different transformation pathway.

The $Al_{20}Mn_2Ce$ in Figure 4.11D region appears to be decomposition into a plate-like phase, denoted by the number 6 in the figure. Based on the results from previous chapters, this plate-like phase is identified as $Al_{51}Mn_7Ce_4$ based upon its morphology and contrast. The formation of the $Al_{51}Mn_7Ce_4$ phase was only observed to form in the ES region of the AM samples from Chapter 3. In the weld track experiments $Al_{51}Mn_7Ce_4$ appears from the decomposition of primarily solidified $Al_{20}Mn_2Ce$. Figure 4.11E shows pockets of complex decomposition microstructure that occurs randomly throughout the weld track away from the MPB. In the center of these pockets, $Al_{20}Mn_2Ce$ appears to decompose with the $Al_{11}Ce_3$ + Al-Mn pathway. At the edge of these pockets, the $Al_{20}Mn_2Ce$ appears to decompose into $Al_{51}Mn_7Ce_4$. Currently, it is very difficult to rationalize these changes and we hypothesize that such pockets are related to subtle changes in alloy compositions and solidification conditions forming near defects, such as porosity [175]. Finally, the microstructural change in the samples made with 83 mm/s after heat treatment at 400°C for 96 hours is evaluated. The decomposition of the primary $Al_{20}Mn_2Ce$ phase is shown in Figure 4.12. The microstructure observed in Figure 4.12 is focusing only on the regions with primary solidification of $Al_{20}Mn_2Ce$.

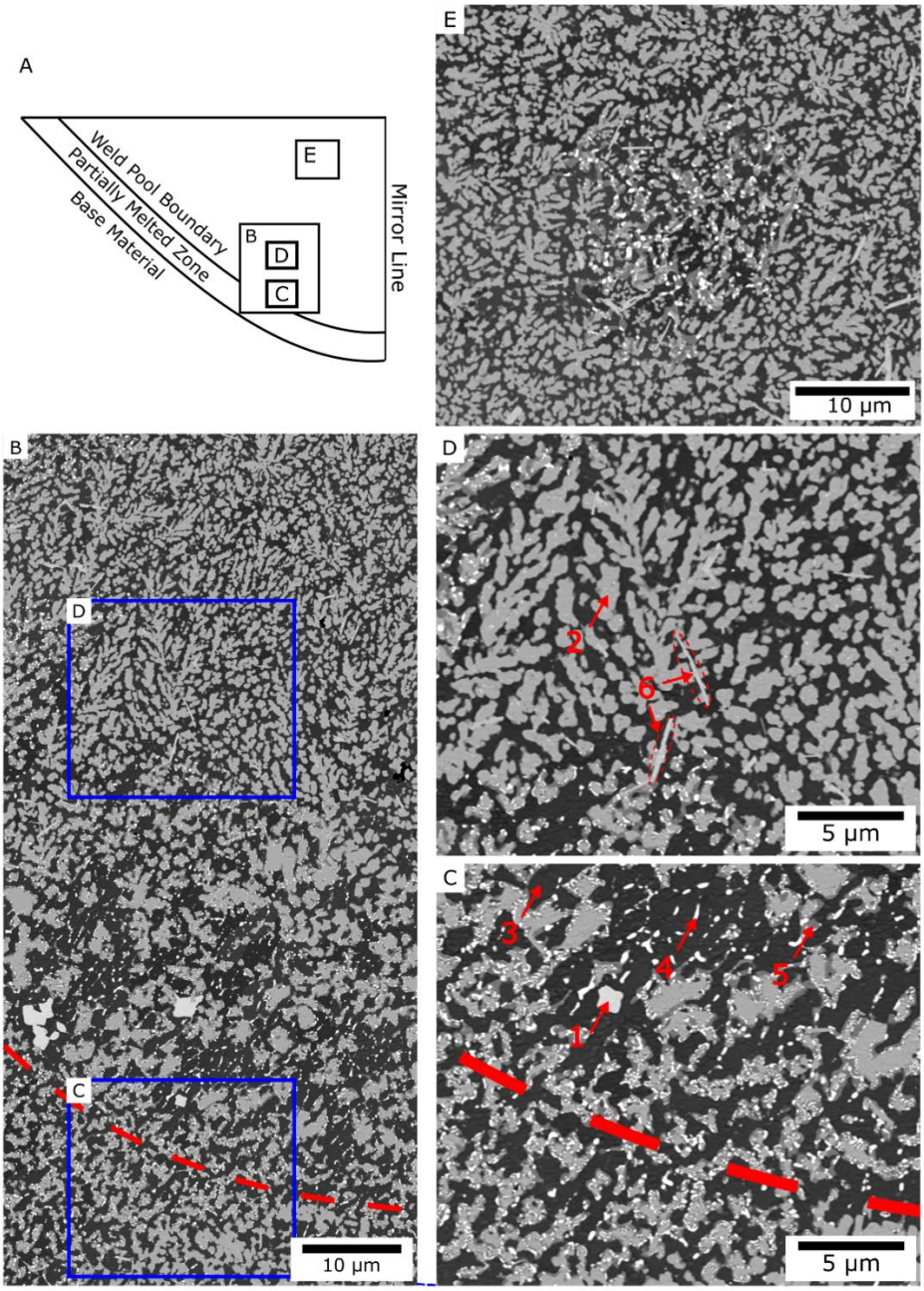

Figure 4.11 of the 15 mm/s weld track after 400°C 96 hour heat treatment, where (A) is a schematic that demonstrates where each image is taken in the weld track, (B) is an overview of the microstructure near the MPB, (C) represents the PMZ and MPB of the microstructure (D) represents above the MPB, (E) represents a region away from the MPB towards the center of the weld track. The phases are denoted by number in the images where (1) is the $Al_{10}Mn_2Ce$ phase, (2) is the $Al_{20}Mn_2Ce$ phase, (3) is the FCC Al, and (4) is the $Al_{11}Ce_3$, (5) is the Al-Mn binary phases, and (6) is the $Al_{51}Mn_7Ce_4$ phase.

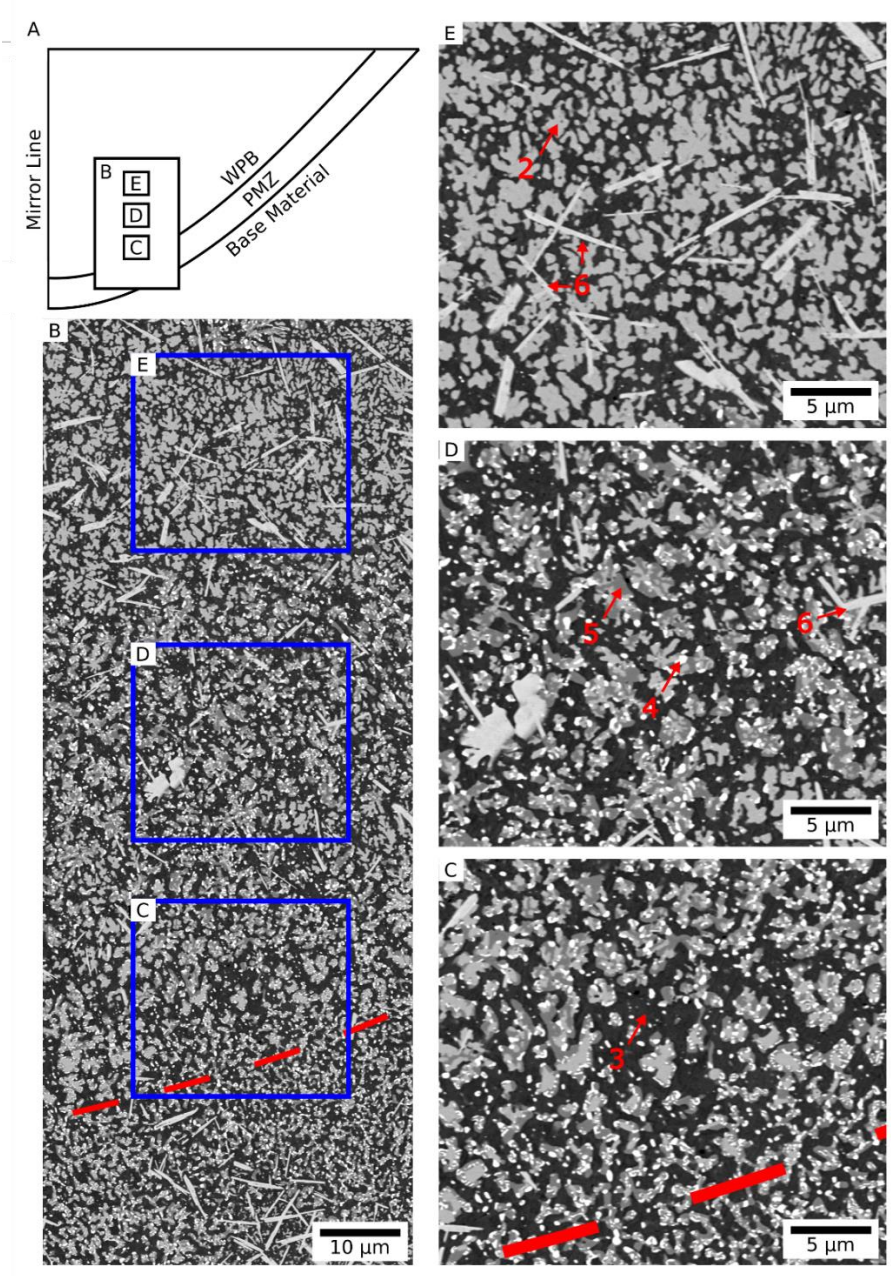

Figure 4.12 SEM BSE of the 83 mm/s weld track , where (A) is a schematic that demonstrates where each image is taken in the weld track, (B) is an overview of the microstructure near the MPB, (C) represents the MPB mcirostructure decomposing from $Al_{20}Mn_2Ce$ to $Al_{11}Ce_3$ + Al-Mn Binary phases, (D) represents a region above the MPB where $Al_{20}Mn_2Ce$ has mixed decomposition into $Al_{11}Ce_3$ + Al-Mn Binary phases and $Al_{51}Mn_7Ce_4$, and (E) represents a region above the mixed decomposition where $Al_{20}Mn_2Ce$ decomposes into $Al_{51}Mn_7Ce_4$. The phases are denoted by number in the images where (1) is the $Al_{10}Mn_2Ce$ phase, (2) is the $Al_{20}Mn_2Ce$ phase, (3) is the FCC A phase, (4) is the $Al_{11}Ce_3$ phase, (5) is the Al-Mn binary phases, and (6) is the $Al_{51}Mn_7Ce_4$ phase.

In Figure 4.12A, a schematic layout of the image location is shown. In Figure 4.12B, an overview of the microstructure is shown that demonstrates three different decomposition regions. In the PMZ the $Al_{20}Mn_2Ce$ phase appears to decompose into $Al_{11}Ce_3$, Al-Mn binary, and $Al_{51}Mn_7Ce_4$ phases. The decomposition region at the MPB is shown in Figure 4.12C. In the MPB region, the primary $Al_{20}Mn_2Ce$ decomposes into $Al_{11}Ce_3$+Al-Mn binary phases, which is indeed different from the PMZ decomposition pathway. Above the MPB in Figure 4.12D, mixed decomposition pathways are observed. Interestingly, this mixed decomposition region contains the other two decomposition pathways for $Al_{20}Mn_2Ce$ observed in different regions, i.e., $Al_{20}Mn_2Ce$ decomposes into $Al_{11}Ce_3$ + Al-Mn binary phases, as well as, into $Al_{51}Mn_7Ce_4$. In Figure 4.12E, the $Al_{20}Mn_2Ce$ phase appears to only decompose into the $Al_{51}Mn_7Ce_4$ phase. The decomposition of the eutectic solidification region is shown in Figure 4.13. Like other analyses, the phases are identified using SEM BSE contrast and morphology.

In Figure 4.13A, the overview of the microstructure confirms the decomposition of $Al_{20}Mn_2Ce$ into $Al_{51}Mn_7Ce_4$. Note that this $Al_{20}Mn_2Ce$ was originally present in the eutectic microstructure. In Figure 4.13B, the regions in the heat-treated samples that were originally at the transition from primary intermetallic to eutectic regions are summarized. In this condition, the primary $Al_{20}Mn_2Ce$ decomposed into $Al_{51}Mn_7Ce_4$. The approximate transition boundary to the original eutectic region is shown by a red line. In the eutectic region, the $Al_{20}Mn_2Ce$ appears to decompose into $Al_{51}Mn_7Ce_4$ at a rapid rate compared to the primary region. In Figure 4.13C, the red line again indicates the approximate transition out of the eutectic region what appear to be an additional primary region. Above the red line is a slim region where $Al_{20}Mn_2Ce$ appears to decompose into $Al_{51}Mn_7Ce_4$, but this is difficult to very as there is only a cross section of a 3-dimensional microstructure. At the top of Figure 4.13C, the decomposition of $Al_{20}Mn_2Ce$ is mixed with the above and $Al_{11}Ce_3$ and Al-Mn binary phase formation. The mixed decomposition is observed until the top of the weld track.

4.2.5 Heat Treated Weld Tracks Summary

The results of the decomposition of $Al_{20}Mn_2Ce$ are summarized in Table 4.7. Mixed decomposition implies that the weld tracks had a mixture of $Al_{11}Ce_3$ + Al-Mn decomposition surrounding $Al_{51}Mn_7Ce_4$, like what is observed in Figure 4.12D.

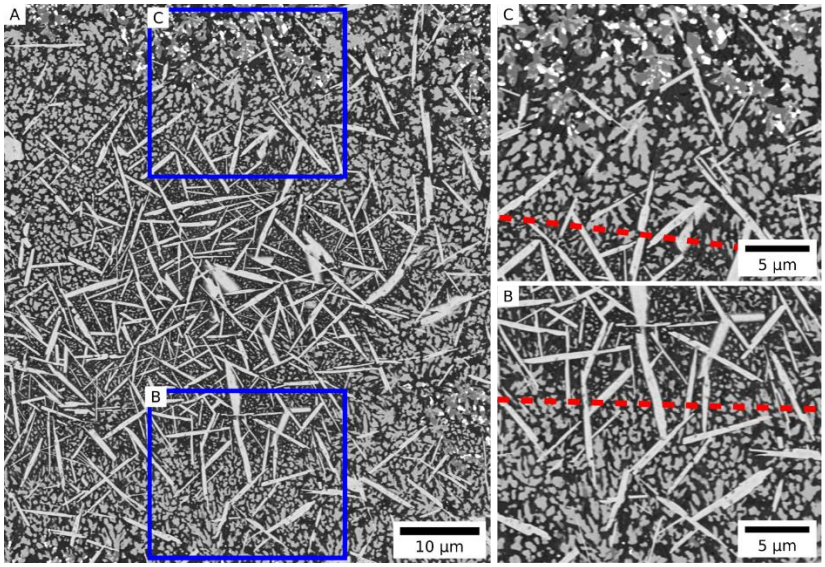

Figure 4.13 SEM BSE of the eutectic region observed in the 83 mm/s weld track after heat treatment for 400°C for 96 hours where (A) is an overview of the region showing three different decomposition pathways, (B) is an approach to the eutectic where the $Al_{20}Mn_2Ce$ is seen decomposing into $Al_{51}Mn_7Ce_4$ before the eutectic and the red line indicating approximately where the eutectic solidification region started, and (C) which demonstrates leaving the eutectic region, where the red line indicates where the eutectic region ends.

Table 4.7 Outline of solidification microstructures observed in each weld track.

Laser Velocity (mm/s)	$Al_{20}Mn_2Ce$ Decomposing to $Al_{11}Ce_3$+Al-Mn Binary	$Al_{20}Mn_2Ce$ Decomposing to $Al_{51}Mn_7Ce_4$	Mixed Decomposition
1	X		
10	X	X	
15	X	X	
23		X	X
35		X	X
54		X	X
83		X	X

It is to note that the eutectic between FCC Al and $Al_{20}Mn_2Ce$ is not listed on the table, has always been observed to decompose into $Al_{51}Mn_7Ce_4$. The overall conclusion leading to that as a function of laser velocity, the phase transformation in the Al-Ce-Mn system can be to some degree controlled. The primary $Al_{20}Mn_2Ce$ phase appears to have cascading phase transformations as a function of its solidification conditions, and not just its solidification mode. The observed solidification modes and their subsequent decomposition is outline in Figure 4.14.

4.3 Discussions on Phase Decomposition Pathways in Weld Tracks

In the discussion section, three key topics will be addressed.

- Why in the 83 mm/s sample does the solidification path into the weld pool transition from primary $Al_{20}Mn_2Ce$ to a eutectic between FCC Al and $Al_{20}Mn_2Ce$, back to primary $Al_{20}Mn_2Ce$.
- How does the partially melted zone decompose, and what that tells us about the solidification of the region?
- The decomposition pathways of the weld tracks, and how they are influenced by activation energy as a function of localized composition.

These topics are investigated to give insight into how the solidification of phases is affecting the subsequent phase decomposition.

4.3.1 Solidification Transitions in the 83 mm/s weld track

The 83 mm/s weld track was observed at the WPB to form primary $Al_{20}Mn_2Ce$. As the solidification front moves into the center of the weld track, the primary $Al_{20}Mn_2Ce$ phase is suppressed for a eutectic between FCC Al and $Al_{20}Mn_2Ce$. It would be suspected that the eutectic microstructure should continue until the top of the weld. However, the eutectic was observed to transition back into primary $Al_{20}Mn_2Ce$. The question now is what could cause this transition?

One of the subtleties of solidification that may be missed by the Rosenthal model is the inclusion of fluid flow and dissolution of $Al_{20}Mn_2Ce$ in the liquid. As mentioned previously, there is a significant change in the liquidus temperature of

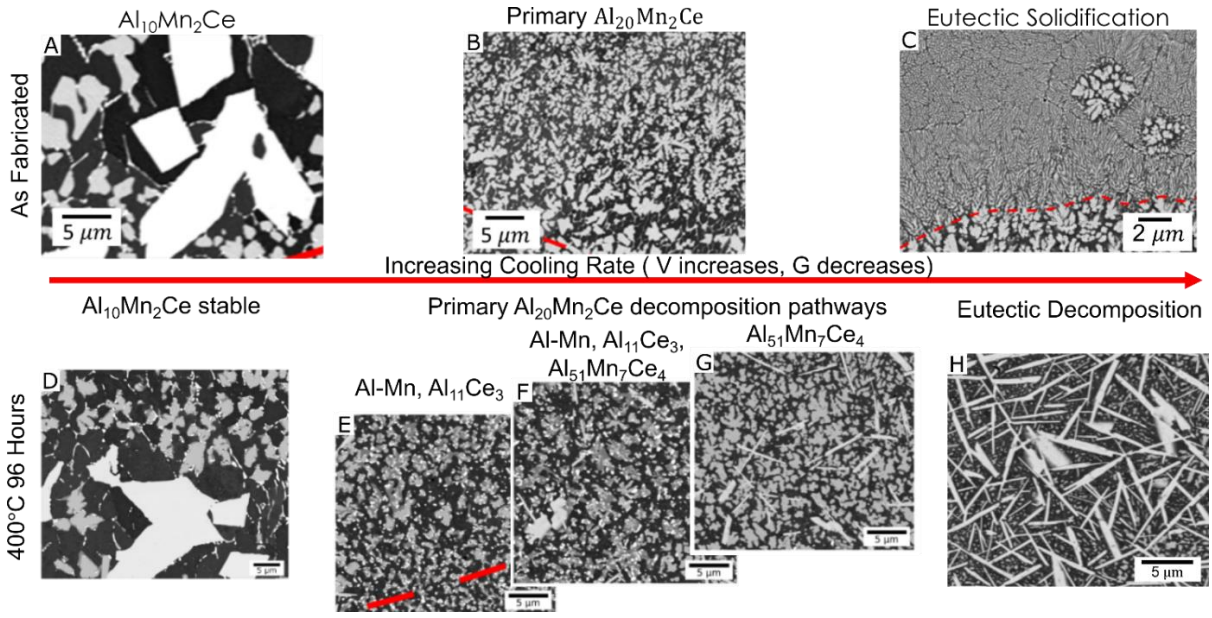

Figure 4.14 demonstrates the change in solidification microstructure and solid-state phase transformation as a function of increasing cooling rate. (A) shows the 1 mm/s weld track where the primary $Al_{10}Mn_2Ce$ is the prominent phase from solidification, (B) shows the 83 mm/s weld track near the MPB where the primary $Al_{20}Mn_2Ce$ phase is the prominent solidification phase, (C) shows the 83 mm/s weld track in the center of the weld track where a eutectic between FCC Al and $Al_{20}Mn_2Ce$ are observed, (D) shows the $Al_{10}Mn_2Ce$ phase appears to be stable, (E) shows the primary $Al_{20}Mn_2Ce$ decomposing into Al-Mn binary phases and $Al_{11}Ce_3$, (F) shows the primary $Al_{20}Mn_2Ce$ phase decomposing down the mixed decomposition pathway, (G) shows the primary $Al_{20}Mn_2Ce$ decomposing into $Al_{51}Mn_7Ce_4$, and (H) shows the decomposition of the eutectic microstructure to $Al_{51}Mn_7Ce_4$.

$Al_{20}Mn_2Ce$ (1177K) and FCC Al (~908K for the bulk composition). Therefore, it is possible that the $Al_{20}Mn_2Ce$ has not fully dissolved into the liquid and has particles floating with the fluid flow that act as nucleation sites for the $Al_{20}Mn_2Ce$ phase to regrow during solidification. A schematic of the possible solidification phenomenon is shown in Figure 4.15, where the partially melted $Al_{20}Mn_2Ce$ flows to the top of the weld track with the fluid flow present.

The partially melted particles can then act as a nucleation site for additional primary $Al_{20}Mn_2Ce$ to grow. Partial melting of secondary phases, specifically carbides has previously been observed in welding literature [176,177].

A second possibility to explain the transition in solidification velocity, is the mode of the weld pool. The Rosenthal model assumes that a conduction weld pool is occurring, although it is possible that the weld pool exists as a keyhole, which can change the solidification characteristics. Overall, it is unknown exactly why the transition from eutectic back to primary $Al_{20}Mn_2Ce$ is occurring, and more work needs to be done to understand the transition.

4.3.2 The Partially Melted Zone Decomposition

The PMZ region of microstructure generally consists of FCC Al, $Al_{11}Ce_3$, and primary $Al_{20}Mn_2Ce$ for the 23-83 m/s weld tracks. In the slower weld tracks (1-15 mm/s) the $Al_{10}Mn_2Ce$ is also observed but does not appear to decompose. Within the PMZ, the $Al_{20}Mn_2Ce$ phase has a variety of decomposition pathways. The different pathways mirror the weld tracks where the $Al_{20}Mn_2Ce$ picks either the $Al_{11}Ce_3$+Al-Mn phases or the $Al_{51}Mn_7Ce_4$ phase. The decomposition of $Al_{20}Mn_2Ce$ is always interacting with FCC Al. The different decomposition pathways of $Al_{20}Mn_2Ce$ can be observed in the 54 mm/s sample in the PMZ region in below Figure 4.16 the solid red line.

The question now is why the $Al_{20}Mn_2Ce$ in the PMZ is decomposing into different phases. One possible explanation is that the PMZ is experiencing a different solidification pathway than the bulk material. A different solidification pathway is possible because the two majority phases in the base material have varied melting points. What this means is that the base AM material contains 50 wt. % of each FCC Al, ~49 wt.% $Al_{20}Mn_2Ce$, and ~1 wt.% $Al_{11}Ce_3$. If we ignore the $Al_{11}Ce_3$ and say that the alloy is approximately 50/50 between FCC Al and $Al_{20}Mn_2Ce$, there are

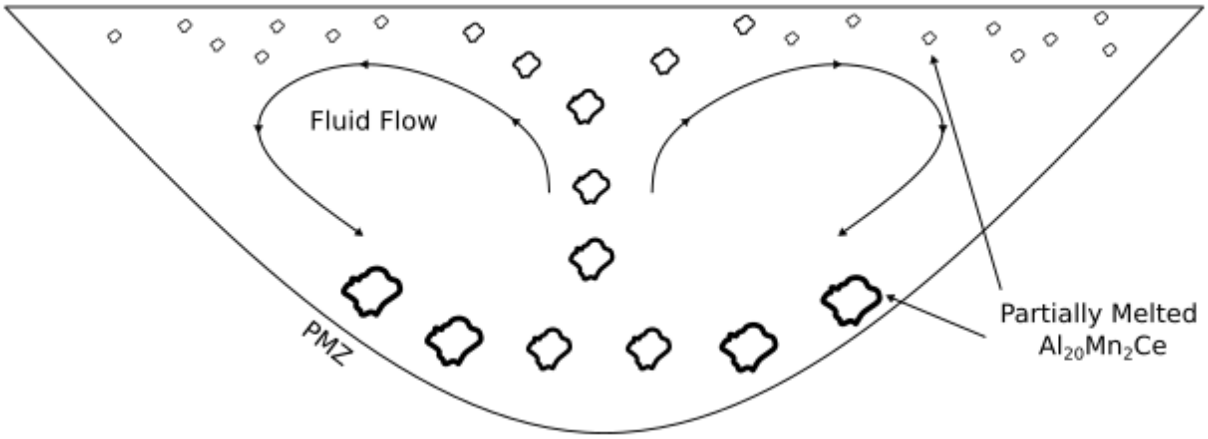

Figure 4.15 Demonstrates a schematic of partially melted $Al_{20}Mn_2Ce$ flows to the top of the weld track and acts as a nucleation site for primary $Al_{20}Mn_2Ce$.

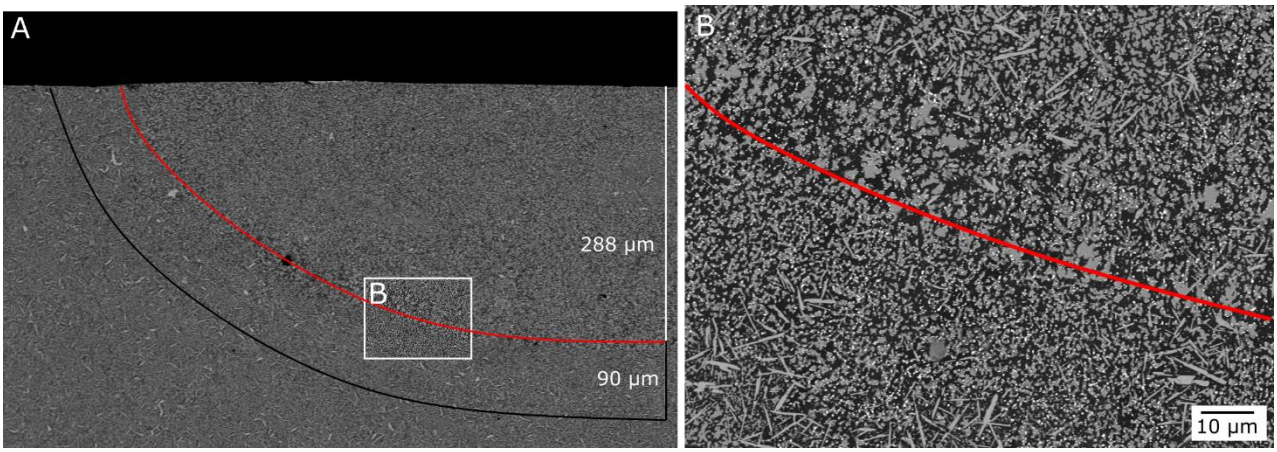

Figure 4.16 SEM BSE of (A) the 54 mm/s weld track after heat treatment of 400°C 96 hours. The MPB is approximated using the red line, and the PMZ is approximated using the black line (B) is an image of the MPB that demonstrates the decomposition of the PMZ.

two distinct liquidus points for each phase, 908K and 1177K respectively. As the isotherm away from the liquidus of $Al_{20}Mn_2Ce$, there will be a reduction in melting of the $Al_{20}Mn_2Ce$ phase. The reduction in melting of the $Al_{20}Mn_2Ce$ phase can cause a gradient in liquid composition. The gradient in liquid composition is caused because as the isotherm from the WPB moves into the PMZ, the local temperature decreases. As the local temperature decreases, the amount of $Al_{20}Mn_2Ce$ melting will also decrease.

Since the FCC Al in the system contains little to no Ce, as the isotherm moves away from the WPB, the Ce in the liquid will be depleted. If we have a depletion in Ce, the solidification pathway can change. It is additionally likely that Ce is not the only depleted element in the liquid. The base FCC Al in the AM sample is measured to have a maximum concentration of 1.651 at. % Mn, it is additionally likely the liquid away from the MPB in the PMZ is depleted of Mn as well, compared to the bulk material.

Since the PMZ is not fully $Al_{10}Mn_2Ce$ (the equilibrium phase), especially in the 1 mm/s weld track, it is possible to conclude that the partially melted $Al_{20}Mn_2Ce$ is regrowing into the liquid when heat is removed. The biggest clue as to how the $Al_{20}Mn_2Ce$ is regrowing is present in Figure 4.16B, where the resolidified $Al_{20}Mn_2Ce$ is decomposing down two pathways into $Al_{11}Ce_3$ + Al-Mn binary phases, and $Al_{51}Mn_7Ce_4$.

Inside the weld track experiments, it appears that solidification velocity is the primary variable that controls the decomposition pathway exception. Although, in the PMZ this is no longer true. The reasoning for this may be that the $Al_{20}Mn_2Ce$ is regrowing as its initial composition from the AM base material. As it was observed in Chapter 3, the composition of the $Al_{20}Mn_2Ce$ phase appears to play a large role in the decomposition pathways of the material. The idea being that in the PMZ, if the $Al_{20}Mn_2Ce$ is partially melted, and regrows as its original composition from the AM parts, it will also adopt the decomposition pathway from the original $Al_{20}Mn_2Ce$ composition. However, more work needs to be done to demonstrate that the composition of a partially melted $Al_{20}Mn_2Ce$ phase and its subsequent solidified cap will adopt the same composition.

4.3.3 Discussions on Decomposition Pathways in bulk of weld tracks

In the AM parts, the primary $Al_{20}Mn_2Ce$ was observed to work with FCC Al to decompose into $Al_{11}Ce_3$ and Al-Mn binary phases. The eutectic between FCC Al and $Al_{20}Mn_2Ce$ decomposed into $Al_{51}Mn_7Ce_4$. Initially it appeared that the solidification mode of the alloy was the primary influence on the decomposition pathway of the microstructure. However, in the 15 mm/s weld track, heat treated for 96 hours at 400°C, the primary $Al_{20}Mn_2Ce$ phase along with FCC Al appears to decompose into the $Al_{51}Mn_7Ce_4$ phase. The confidence that the primary $Al_{20}Mn_2Ce$ is playing a role in the formation of $Al_{51}Mn_7Ce_4$ is because a eutectic between FCC Al and $Al_{20}Mn_2Ce$ was not present in the as-fabricated state of the 15 mm/s sample. The question now becomes, what can allow the $Al_{51}Mn_7Ce_4$ to form from the decomposition of $Al_{20}Mn_2Ce$. If we recall Eq. (31), the three key components for a new phase to nucleate are the volumetric reduction in free energy for a new phase to form, ΔG_V, The interfacial energy between the phases associated with the formation and destruction of interfaces, γ, and the misfit strain energy ΔG_s, which is largely ignored for the current analysis.

Previously in Figure 3.10 a possible orientation relationship (OR) was observed between $Al_{20}Mn_2Ce$ and $Al_{51}Mn_7Ce_4$. An OR can indicate a reduced interfacial energy between the two phases. Additional OR have not been observed in the system, such as an OR between FCC Al and $Al_{51}Mn_7Ce_4$. The lack of observed OR does not imply that it does not exist. However, the interfacial energy is not the full piece of the puzzle, as without the reduction in chemical potential, the driving force, of the system it is impossible for a new phase to nucleate. Therefore, we can investigate how the driving force of the system will change as a function of local conditions, the same as what is performed in Chapter 3, to have a better understanding of when the $Al_{51}Mn_7Ce_4$ phase will be selected for decomposition.

For this analysis, we will assume the average composition measured in Chapter 3 are the bounding regions of possible composition of the $Al_{20}Mn_2Ce$ phase. This implies that the MPB composition measured as $Al_{19.92}Mn_{2.42}Ce_{0.67}$ and the eutectic composition measured as $Al_{19.92}Mn_{2.2}Ce_{1.18}$ will act as the boundaries of possible composition leaving us with the formula, $Al_{23-x-y}Mn_xCe_y$, where $2.2 < x < 2.42$ and $0.67 < y < 1.18$. Using this formula, two intermediate compositions, $Al_{19.85}Mn_{2.3}Ce_{0.85}$ and $Al_{19.7}Mn_{2.3}Ce_1$, are selected for further analysis to observe

the effect of Ce in the intermetallic phase on the driving force for other phases to form. The driving forces are calculated the same way as observed in Section 3.3. A second assumption will initially be made, which is that the FCC Al composition will contain 0.2 at.% Mn. The Mn content is like what is observed in the MPB region from the AM samples from Chapter 3. The resulting driving forces from this analysis are calculated in Table 4.8. Positive values indicate that there is a reduction in volumetric free energy for a phase to form.

The key take-away from Table 4.8, is that as a function of Ce content in the intermetallic phase, the $Al_{51}Mn_7Ce_4$ becomes more preferred as the Ce in the $Al_{20}Mn_2Ce$ increases. In contrast, the $Al_{12}Mn$ and Al_6Mn appear to maintain almost consistent driving force as the composition changes. As discussed in Chapter 3, it is likely a competition between the Al-Mn binary phases and the $Al_{51}Mn_7Ce_4$ phase to nucleate and growth to suppress the other present phase.

4.4 Conclusion

In this chapter, a series of weld tracks experiments were performed to determine the initial solidification microstructure as well as the subsequent solid-state decomposition of the same. The key conclusions are,

- As the laser velocity varied between 1-83 mm/s, the solidification conditions (G and V) changed. At low laser velocities, the $Al_{10}Mn_2Ce$ phase was observed at the edge of weld tracks. As the laser velocity increased, the $Al_{10}Mn_2Ce$ phase was suppressed, and the primary $Al_{20}Mn_2Ce$ phase formation was promoted. Eventually at the 54 and 83 mm/s laser velocities, a eutectic microstructure with FCC Al and $Al_{20}Mn_2Ce$ phases were observed at the center of the weld track.
- The decomposition pathway of the primary $Al_{20}Mn_2Ce$ phase is modified by the solidification conditions. In the 1 mm/s weld track, the primary $Al_{20}Mn_2Ce$ decomposed along the $Al_{11}Ce_3$ +Al-Mn decomposition pathway. In the 10 mm/s weld track, different regions of primary $Al_{20}Mn_2Ce$ phases were found to decompose along the $Al_{11}Ce_3$ +Al-Mn, as well as $Al_{51}Mn_7Ce_4$ pathways, which appeared to continue throughout the remaining weld tracks.

Table 4.8 Calculated Driving Forces for possible local equilibrium states assuming an FCC Al composition of (0.2 at.%) Mn.

	AM Primary	Transition 1	Transition 2	AM Eutectic
Phase Name	$Al_{19.92}Mn_{2.42}Ce_{0.67}$	$Al_{19.85}Mn_{2.3}Ce_{0.85}$	$Al_{19.7}Mn_{2.3}Ce$	$Al_{19.92}Mn_{2.2}Ce_{1.18}$
$Al_{11}Ce_3$ (j/mol)	-15718.54	-6128.1	74.41	5017.82
$Al_{12}Mn$ (j/mol)	943.8688	931.14	931.14	932.62
Al_6Mn (j/mol)	1723.46	1699.52	1699.53	1702.3
$Al_{51}Mn_7Ce_4$ (j/mol)	-3408.28	-539.98	1327.31	2817.74
$Al_{10}Mn_2Ce$ (j/mol)	-2603.2	813.36	3039.75	4817.2

- The decomposition of $Al_{20}Mn_2Ce$ appears to be sensitive to the solidification parameters. It is likely that the change in solidification conditions altered the composition of $Al_{20}Mn_2Ce$, which in turn changes the expected driving force for the nucleation of product phases such as $Al_{11}Ce_3$, Al-Mn and $Al_{51}Mn_7Ce_4$ phases. Additionally, the composition of the $Al_{20}Mn_2Ce$ phase appears to influence the rate of transformation observed in the alloy.
- The $Al_{51}Mn_7Ce_4$ phase appears to be one of many possible decomposition pathways for both eutectic and primary solidification of the $Al_{20}Mn_2Ce$ phase.

Chapter 5. Solidification Phase Selection using the Dendritic Interface Response Function

In Chapters 3 and 4, the solidification phase selection of the Al-Ce-Mn system appears to change as a function of solidification conditions (solidification velocity, thermal gradient, and composition). In Chapter 4, it was observed that primary solidification phase selection consisted of primary $Al_{10}Mn_2Ce$, primary $Al_{20}Mn_2Ce$, and a eutectic between FCC Al and $Al_{20}Mn_2Ce$. In this chapter, the changes in phase selection are rationalized based on different solidification conditions using the dendritic Interface Response Function (IRF). The goals of the chapter are as follows:

- Examine the linear phase diagram approximation IRF for the Al-Ce-Mn system and rationalize why it may not apply to the $Al_{10}Mn_2Ce$ and $Al_{20}Mn_2Ce$ intermetallic phases.
- Implement a new methodology to directly calculate the undercooling of a phase from CALPHAD phase descriptions for the IRF, specifically for fixed composition phases, such as intermetallic compounds.
- Implement a new methodology to directly calculate the undercooling of a phase from CALPHAD phase descriptions for the IRF, specifically for solid solution phases, such as FCC Al.
- Apply the direct calculation methods to Al-Zr and Al-Si alloys as a test case to understand the differences in undercooling predicted by the linear approximation method and the direct calculation method.
- Using the direct calculation method IRF to model the Al-Ce-Mn system to predict the transitions of phase selection between the $Al_{10}Mn_2Ce$, $Al_{20}Mn_2Ce$, and eutectic solidification regions observed in the weld track experiments.
- Investigate the sensitivity of alloy composition and solidification conditions on phase selection in the Al-Ce-Mn system.

5.1 Dendritic Interface Response Function for the Al-Ce-Mn system using a Linearly Approximated Phase Diagram

In Section 2.2.2, the undercooling at a dendrite tip was approximated using a simplified linear phase diagram. In this section, the methodology from Section 2.2.2 will be applied to the Al-Ce-Mn system. The example here is to evaluate if new methods need to be explored for the dendritic IRF. The input to the model is the solidification conditions (thermal gradient and liquid/solid interface velocity) and alloy composition and the output is the dendrite tip temperature. The calculation of the dendrite tip temperature will tell which phase will come from the liquid first.

In the experiments from AM and Laser Tracks, the primary phase selection changes based on local thermal gradient and solidification velocity. At high thermal gradient and low solidification velocity, the primary $Al_{10}Mn_2Ce$ is the observed solidification phase. At high thermal gradient and high solidification velocity, the eutectic is observed. The goal here is to predict what phase will come out of the liquid using the IRF so that in the future, the phase selection during solidification can be predicted a-priori.

5.1.1 The IRF linear solution applied to an Al-Ce-Mn alloy.

The goal of this modeling is to rationalize the results seen in Chapter 4 by predicting the dendrite tip temperature of primary solidification regions of $Al_{10}Mn_2Ce$, $Al_{20}Mn_2Ce$, and FCC Al. The values are compared to equilibrium eutectic temperature between $Al_{20}Mn_2Ce$ and FCC Al predicted by Schiel simulations.

The needed input conditions for the dendritic IRF are outline in Table 5.1 for the $Al_{20}Mn_2Ce$ and $Al_{10}Mn_2Ce$ phases. The input conditions for FCC Al are outlined in

Table 5.2. The eutectic IRF is not calculated because of limitations in the eutectic solution. The eutectic IRF does not have a solution for higher order systems past binary. Instead, the eutectic temperature (927K) for the eutectic containing $Al_{20}Mn_2Ce$ and FCC Al, is predicted by a Scheil solidification simulation using PANDAT. The predicted temperature will be used to have a reference point to determine the transition between primary $Al_{20}Mn_2Ce$ and the observed eutectic microstructure. Using the linear IRF, two cases will be calculated to show the results from the linear approximation of a phase diagram for the intermetallic components.

Table 5.1 Parameter used in the IRF Calculations for $Al_{10}Mn_2Ce$ and $Al_{20}Mn_2Ce$

Parameters	$Al_{20}Mn_2Ce$	$Al_{10}Mn_2Ce$	Sources
Initial Ce Composition, $C_{0,Ce}$ (at. %)	2.18	2.18	Given
Initial Mn Composition, $C_{0,Mn}$ (at. %)	4.48	4.48	Given
Gibbs-Thomson Coefficient (m-k)	1.35×10^{-7}	1.47×10^{-7}	Yang *et al.* [150]
Liquid Diffusivity of Mn, D_L^{Mn} (m^2/s)	3.34×10^{-9}	3.34×10^{-9}	Du *et al.* [171]
Liquid Diffusivity of Ce, D_L^{Ce} (m^2/s)	2.5×10^{-9}	2.5×10^{-9}	Assumed
Liquidus Slope Ce, m_{Ce} (K/at. %)	-51.28	-81.30	Calculated
Liquidus Slope, m_{Mn} (K/at. %)	-26.24	-40.98	Calculated
Partition Coefficient, $k_{0,Mn}$	1.93	3.42	Calculated
Partition Coefficient, $k_{0,Ce}$	1.98	3.49	Calculated
Dendrite Tip Selection Parameter σ	0.025	0.025	Mohammadpour *et al.* [130].
Thermal Gradient (K/m)	$1x10^6$	$1x10^6$	Assumed
Speed of Sound in FCC Al, V_0 (m/s)*	5100	5100	Assumed as FCC
Diffuse interface thickness, a_0 (m)	1×10^{-9}	$1x10^{-9}$	Assumed

Table 5.2 Parameters used in the IRF for determining the undercooling of FCC Al in the Al-Ce-Mn System

Parameter (Unit)	FCC Al	Sources
Initial Ce Composition, $C_{0,Ce}$ (at. %)	2.18	Given
Initial Mn Composition, $C_{0,Mn}$ (at. %)	4.48	Given
Eq. Melting Temperature, T_0 (K)	908.525	Calculated
Liquidus Slope Ce, m_{Ce} (K/at. %)	-12.20	Calculated
Liquidus Slope, m_{Mn} (K/at. %)	10.06	Calculated
Partition Coefficient, $k_{0,Ce}$	$1.72x10^{-5}$	Calculated
Partition Coefficient, $k_{0,Mn}$	1.593	Calculated
Gibbs-Thomson Coefficient, Γ (mk)	1.96×10^{-7}	Hunt *et al.* [178]
Liquid Diffusivity of Mn, D_L^{Mn} (m^2/s)	3.34×10^{-9}	Du *et al.* [171]
Liquid Diffusivity of Ce, D_L^{Ce} (m^2/s)	2.5×10^{-9}	Assumed
Diffuse interface thickness, a_0 (m)	1×10^{-9}	Assumed
Speed of Sound in FCC Al, V_0 (m/s)	5100	Dantzig *et al.* [125]
Dendrite Tip Selection Parameter σ	0.025	Mohammadpour *et al.* [130].
Thermal Gradient (K/m)	$1x10^6$	Assumed

The first case will be where all values are sourced from literature or assumed relative to available data. The second will attempt to fit the dendritic IRF to the observed transition points in Chapter 4, by manipulating the Gibbs-Thomson coefficient which impacts the selection of dendrite tip radius and the undercooling from the curvature of a dendrite. In both cases, the $Al_{20}Mn_2Ce$ composition will be manipulated to the measured values in Chapter 3 to ensure that possible composition changes are accounted for. The liquid diffusivity is not used as a fit value and is taken at the eutectic temperature.

To calculate the IRF the first thing to do is to define key input values. The most important values are the diffusivity in the liquid and the Gibbs-Thomson Coefficient of each phase. The diffusivity in the liquid is taken at the eutectic temperature (927K) for Mn. The Ce liquid diffusivity is assumed to be near Mn, however the diffusivity of Ce in liquid Al has not been determined in literature and is set at a value of $2.5x10^{-9}$ (m^2/s). The Gibbs-Thomson coefficient is adopted from Yang *et al.* [150], shown in Table 5.1. The FCC Al adopts the Gibbs-Thomson coefficient taken from the Al-Si system from Mohammadpour *et al.* [130]. The speed of sound, V_0, in a material is used to approximate the kinetic undercooling, and is assumed as pure FCC Al. The kinetic undercooling only contributes at most 2K of undercooling at the investigated velocities.

The first calculation is shown in Figure 5.1. The calculation in Figure 5.1 uses the values from Table 5.1 and Table 5.2 It is observed in Figure 5.1A that the trend of phase selection does not match the experimental observations in Chapter 4. In the calculation, initially $Al_{10}Mn_2Ce$ is the expected growth phase at low solidification velocity. As the velocity increases, a transition is observed from the primary $Al_{10}Mn_2Ce$ to a primary $Al_{20}Mn_2Ce$, which agrees with the experimental results. However, the primary $Al_{20}Mn_2Ce$ undercooling does not reach the eutectic temperature (927K) denoted by the horizontal black line, deviating from the experimental results. In Figure 5.1B and C, the composition in the liquid at the dendrite tip for Mn and Ce are shown respectively. In the $Al_{20}Mn_2Ce$ alloy, it is observed that as the undercooling of the system increased the composition in front of the dendrite tip decreases. This observation is caused by the solid phase, $Al_{10}Mn_2Ce$ and $Al_{20}Mn_2Ce$ having a partitioning coefficient greater than one, which means solute in front of the dendrite tip is depleted at the solid/liquid interface.

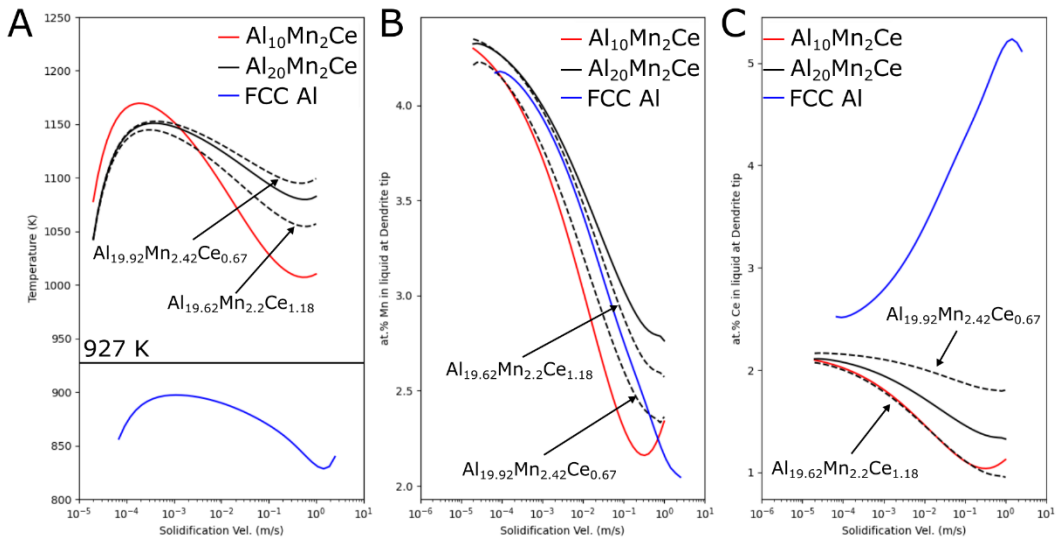

Figure 5.1 (A) shows the undercooling calculated by the dendritic IRF for the $Al_{10}Mn_2Ce$, $Al_{20}Mn_2Ce$, and FCC Al phases. The eutectic temperature for FCC Al and $Al_{20}Mn_2Ce$ is shown as a straight black line at 927 K. (B) shows the at.% Mn in the liquid at the dendrite tip for each condition, (C) shows the at.% Ce in the liquid at the dendrite tip.

To attempt to better represent the experimental results, the composition of $Al_{20}Mn_2Ce$ is manipulated. It is known, from Chapter 3, that the $Al_{20}Mn_2Ce$ phase exists as a solid solution. For this comparison, two discrete compositions, $Al_{19.92}Mn_{2.42}Ce_{0.67}$ (the primary composition measured in Chapter 3) and $Al_{19.62}Mn_{2.2}Ce_{1.18}$ (the eutectic composition measured in Chapter 3), are used to manipulate the partition coefficient to the $Al_{20}Mn_2Ce$ phase. The only change in the modeling procedure is the change in the C_s term. The C_s term is the composition of the solid phase. For the $Al_{20}Mn_2Ce$ compound, C_s is fixed because it is modeled as a line compound. Therefore, the C_S of Ce and Mn are directly changed to each composition to manipulate the diffusion profile to the dendrite tip. The C_S term is used in the calculation of the partition coefficient, which is defined by $k_0 = \frac{C_l}{C_s}$, where C_l is the liquid composition at the dendrite tip, and C_s is the solid composition at the dendrite tip. The addition of the measured compositions from Chapter 3 are observed to change the amount of undercooling as a function of solidification velocity, but in the current case the changes do not account for the discrepancy in undercooling.

In Figure 5.2, the Gibbs-Thomson Coefficient of $Al_{10}Mn_2Ce$ and $Al_{20}Mn_2Ce$ are manipulated to $1x10^{-6}$ (m-K), an order of magnitude greater than what was determined by Yang *et al.* [150]. The change increase in the Gibbs-Thomson coefficient increases the undercooling predicted by the IRF, but the system still does not represent the experimental data. The primary issue is that the transition from $Al_{20}Mn_2Ce$ to eutectic solidification is not predicted. A wide range of Gibbs-Thomson coefficients ($1x10^{-5}$ to $1x10^{-8}$ m-k) were used to calculate the dendrite tip temperature but were unable to represent the observed experimental transition from $Al_{20}Mn_2Ce$ to the eutectic solidification. The result increasing the Gibbs-Thomson coefficient will eventually cause the solution to be unstable, meaning that especially at high velocities (>0.01 m/s), the IRF will fail to converge. Since the current model does not describe the experimental results observed in Chapter 4, the linear IRF solution is reinvestigated.

5.2 Using Non-linear phase boundaries in the Dendritic Interface Response Function.

In this section, the dendritic IRF will be reexamined to determine the undercooling of a phase directly from the CALPHAD phase description.

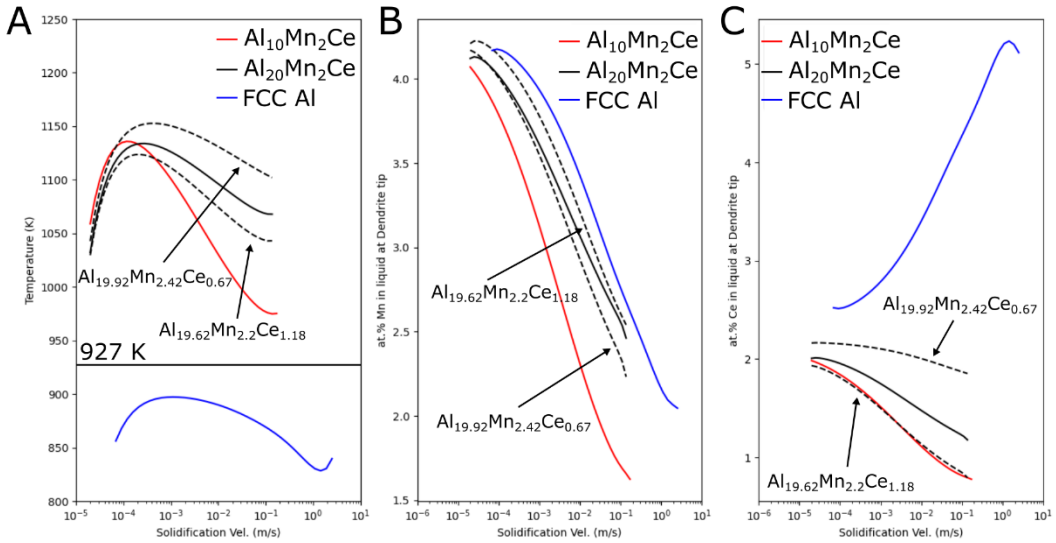

Figure 5.2(A) shows the undercooling calculated by the dendritic IRF for the $Al_{10}Mn_2Ce$, $Al_{20}Mn_2Ce$, and FCC Al phases after modifying the Gibbs-Thomson coefficient of $Al_{10}Mn_2Ce$ and $Al_{20}Mn_2Ce$ to $1x10^{-6}$ (m-k).The eutectic temperature for FCC Al and $Al_{20}Mn_2Ce$ is shown as a straight black line at 927 K. (B) shows the at.% Mn in the liquid at the dendrite tip for each condition, (C) shows the at.% Ce in the liquid at the dendrite tip.

The goal is to evaluate if the removal of the linear approximation can predict the transition from primary $Al_{20}Mn_2Ce$ to a eutectic, which is assumed to form at 927K[wording]. To demonstrate new calculation methodologies for the dendritic IRF, Al-Si and Al-Zr alloys are used as two cases to demonstrate the validity of the linear phase diagram approximation.

5.2.1 The Al-Zr System: Implementation of Direct Calculation and Comparison with the Linear Approximation.

The Al-Zr was chosen to evaluate this methodology since it has a non-linear liquidus slope for the formation of Al_3Zr intermetallic. Therefore, the hypothesis is that the dendrite tip temperature of Al_3Zr should have large variance depending on which of the calculation methods are used, direct or linear. In Figure 5.3, the phase diagram was calculated between liquid and Al_3Zr, using the COST 507 [179] database. Figure 5.3 demonstrates two compositions of Zr that have different liquidus slopes. The two initial starting conditions (approximately 0.25, and 1.25 at.% Zr), have drastically different linear slopes necessary to reasonably approximate each starting condition.

The issue with this different slope adoption based on starting location is the propensity to have underapproximations of undercoolings. The two different slopes in Figure 5.3 predict an approximate 200 K difference in predicted undercooling at ~0.0 at. % Zr, based on composition alone. To show the effect of this under approximation, the undercooling of the Al_3Zr phase, which is the phase described in Figure 5.3, is calculated using both the linear approximation method and a direct liquid calculation method. The linear approximation is the same method described in Eq. (20), but the kinetic term is ignored because it will contribute less than 1 K of undercooling. The undercooling of the system is directly calculated from the CALPHAD descriptions using the equation,

$$\Delta T = f(C_0) - f(C_t) + \frac{2\Gamma}{R} + \frac{GD}{V} \qquad (38)$$

where $f(C_0)$ is the temperature described by the phase diagram for the bulk liquid, and $f(C_t)$ is the temperature described by the phase diagram at the dendrite tip composition. To calculate the liquidus temperature at each of these compositions,

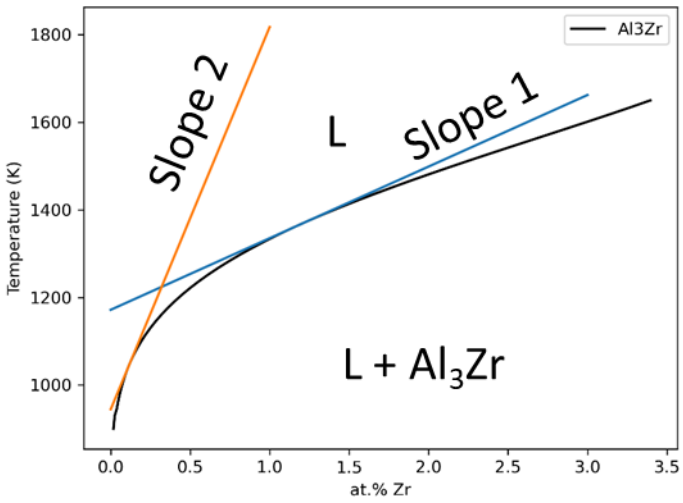

Figure 5.3 Demonstrates the Al_3Zr liquidus line in black, and two fit linear slopes in blue and orange. The idea here is that the selection of a liquidus slope can drastically manipulate the projected undercooling when a phase diagram is reduced to a linear fit.

the chemical potentials of each phase are determined to be equal $\mu_{Zr}^{Liquid} = \mu_{Zr}^{Al_3Zr}$ and $\mu_{Al}^{Liquid} = \mu_{Al}^{Al_3Zr}$, which is iteratively solved using the fsolve function in Scipy [173].

The solution described in Section 2.2.2 is adopted to determine the dendrite tip radius and composition at the dendrite tip. However, the non-equilibrium liquidus slope approximation and non-equilibrium partition coefficients are ignored, because the Al_3Zr is considered a stoichiometric intermetallic compound. Additionally, the liquidus slope is updated to the slope at the dendrite tip temperature with every iteration.

The dendritic IRF parameters for Al_3Zr are described in Table 5.3. Using these values, the dendritic IRF can be calculated for the Al_3Zr phase using the linear and direct calculation methods. The difference between the two methods is shown in Figure 5.4. The key difference observed in the figure is that the direct liquidus calculation has a significantly increased undercooling. FCC Al is included, but it is calculated using the linear approximation as described in Section 2.2.2. The parameters used to calculate the IRF For FCC Al are listed in Table 5.4.

It is notable that the linear approximation IRF for Al_3Zr does not meet an undercooling for FCC Al to be the primary growth phase, while the direct calculation IRF for Al_3Zr does. The calculation for the Al_3Zr intermetallic clearly shows that you need to calculate the non-linear phase diagram. Additionally, it is observed, in Figure 5.4B and C that the composition at the dendrite tip and the dendrite tip radius are manipulated by changing how the phase diagram is investigated, respectively. These values are important for understanding the localized compositions after solidification, which can in turn be used in solid state modeling.

The direct calculation of the liquidus temperature from the Gibbs Free energy descriptions is not the first approach to correct the linear approximation problem. Trivedi *et al.* [181] demonstrated the effect of linearization in an Ag-Cu system. In the calculation of the system, the solution to remove the linearization effect was by fitting curves to both the liquidus temperature as a function of composition and the partition coefficient as a function of temperature. The methodology presented here disregards the additional fitting step and directly calculates it from the CALPHAD descriptions.

Table 5.3 Initial Parameters for the Calculation of the IRF for the Al_3Zr phase in the Al-Zr system

Parameter (Unit)	Linear Approximation	Direct Liquidus Temperature Calculation	Sources
Initial Composition of Zr, C_0 (at. %)	2.5	2.5	Given
Eq. Melting Temperature, T_0 (K)	1541.89	1541.89	Cost 507 [179]
Liquidus Slope, m_0 (K/at. %)	144.76	Dependent	Cost 507 [179]
Partition Coefficient, k_0	10	Dependent	Cost 507 [179]
Gibbs-Thomson Coefficient, Γ (m-k)	3.51×10^{-6}	3.51×10^{-6}	Thermo-Calc® [180]
Liquid Diffusivity, D_L (m^2s^{-1})	3×10^{-9}	3×10^{-9}	Approximate at 933 K
Thermal Gradient (K/m)	1×10^5	1×10^5	Given

Table 5.4 Initial Parameters for the Calculation of the IRF for the FCC Al phase in the Al-Zr system

Parameter (Unit)	FCC Al	Sources
Initial Ce Composition, $C_{0,Zr}$ (at. %)	2.5	Given
Eq. Melting Temperature, T_0 (K)	938.5	Calculated from PANDAT[167]
Liquidus Slope Ce, m_{Zr} (K/at. %)	76.95	Calculated from PANDAT[167]
Partition Coefficient, $k_{0,Zr}$	0.8836	Calculated from PANDAT[167]
Gibbs-Thomson Coefficient, Γ (mk)	1.96×10^{-7}	Taken from FCC in Al-Si
Liquid Diffusivity of Mn, D_L^{Zr} (m^2/s)	3×10^{-9}	Approximate at 933 K
Diffuse interface thickness, a_0 (m)	1×10^{-9}	Assumed
Dendrite Tip Selection Parameter σ	0.025	Mohammadpour *et al.* [130].
Thermal Gradient (K/m)	1×10^6	Assumed

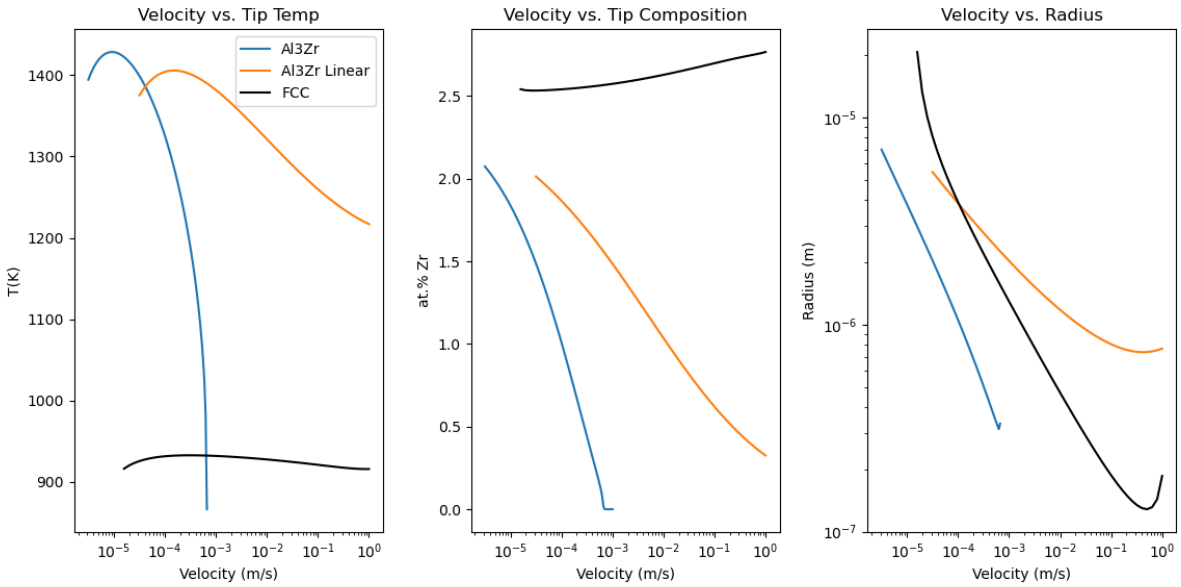

Figure 5.4 Demonstrates the difference between the linear approximation and the direct liquid computation using the IRF. The calculation includes the undercooling related to ΔT_R(curvature) ,ΔT_C (solute) and ΔT_{cell} (cellular). The kinetic undercooling, ΔT_K, is ignored because it has a minimal contribution.

5.2.2 Implementation of non-linear calculation for binary solid solution

The previous section discussed intermetallic compounds. This section discusses the removal of the linear phase diagram assumption for solid solution phases. Solid solution phases are well known to show non-equilibrium partitioning, also known as solute trapping as the liquid/solid interface velocity increases. In this section, for a generic liquid and solid solution system, the dendrite tip temperature will be determined directly from the Gibbs free energy curves.

The improvements to the original model are targeted by changing two things,

1. Direct calculation of phase diagram.
2. Calculation of a Non-equilibrium phase diagram based on k_v values.

To incorporate these two improvements, a methodology is shown in Figure 5.5. The remainder of the model is left unchanged and will be used in the same manor described in Section 2.2.2.

Step 1: Compute Thermodynamic Equilibrium and Non-Equilibrium Partitioning

To start the calculation, thermodynamic equilibrium, and non-equilibrium partition coefficients must be calculated. To solve thermodynamic equilibrium, the chemical potential tangent line between the solid and liquid must be defined. To determine the chemical potential tangent lines between phases, the free energy of each phase must be defined as a function of composition and temperature. The free energy of the liquid is defined by

$$G^{Liquid} = X_A G_A^{Liquid} + X_B G_B^{Liquid} + \Omega^{Liquid} X_A X_B + RT(X_A \ln(X_A) + X_B \ln(X_B)) \qquad (39)$$

where G_A, and G_B are the molar free energies of the pure components defined by Dinsdale *et al.* [182] and are a function of temperature. Ω are the binary interaction parameters defined in a CALPHAD database. X_A defines fraction of solute, and X_B defines the fraction of solvent, $X_A = 1 - X_B$. The description for the free energy curves for each system investigated is given in the appendix. The chemical potential of the solute is defined by

$$\mu_A = G_A + \Omega^{Liquid}(1 - X_A)^2 + RTln(X_A) \qquad (40)$$

Ω is a function of temperature. The chemical potential of the solvent is defined by

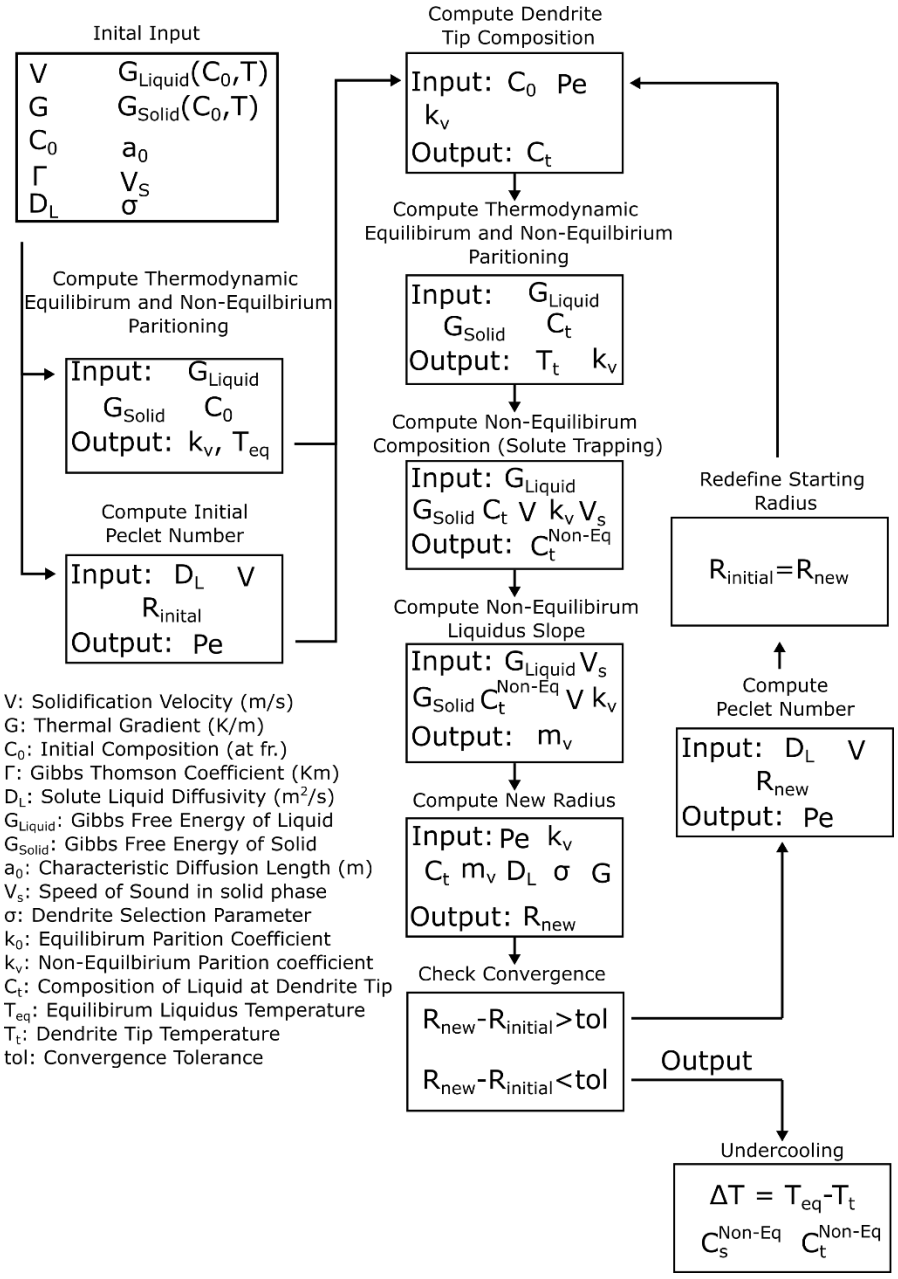

Figure 5.5 Schematic Algorithm the describes how the IRF is solved for a binary solid solution system at a set solidification velocity and thermal gradient.

$$\mu_B = G_B + \Omega^{Liquid}(1 - X_B)^2 + RTln(X_B) \quad (41)$$

The tangent line to the liquid free energy curve is defined by

$$\mu^{Liq} = \left(\mu_B^{Liq} - \mu_A^{Liq}\right)X_A + \mu_A^{Liq} \quad (42)$$

Now that the Gibbs free energy of the liquid is understood, the Gibbs free energy of the solid is defined by.

$$G^{Solid} = X_A G_A^{Solid} + X_B G_B^{Solid} + \Omega^{Solid} X_A X_B + RT(X_A \ln(X_A) + X_B \ln(X_B)) \quad (43)$$

where each term, $G_A, G_B,$ and Ω are defined with respect to the phase it represents. The chemical potentials for the solid phase are defined similarly to the liquid phase, using the parameters for a solid phase. To determine equilibrium at a particular temperature and composition, the chemical potentials of the phases must be equal.

$$\begin{aligned} \mu_A^{Liquid} &= \mu_A^{Solid} \\ \mu_B^{Liquid} &= \mu_B^{Solid} \end{aligned} \quad (44)$$

The solution to equilibrium requires one of three variables to be known. The three variables are the composition of the liquid C_L, the composition of the solid C_S, and the temperature T.

In the current solution, the series of equations is solved by starting with an initial liquidus temperature, based on bulk composition. The equilibrium tangent line can be solved between the two free energy curves to get the C_s (initial solid composition). In the current implementation, equilibrium is solved using the fsolve function from Scipy [173], which is a root finding algorithm for multivariable functions.

Once equilibrium ($\mu_A^i = \mu_B^i$) is found, the composition of the solid and the liquidus temperature is known. The equilibrium partitioning coefficient can be determined using the relationship $k_0 = C_s/C_L$. The equilibrium partitioning coefficient can now be used to determine the non-equilibrium partition coefficient, using the Aziz relationship in Eq. (25).

Step 2: Compute Initial Peclet Number

The Peclet number is now calculated from Eq. (15) using the input solidification velocity (V) and liquid diffusivity of the solute element, along with an assumed initial radius, generally taken as $1x10^{-8}$ m for the current implementation. For subsequent iterations, the initial radius is calculated from the previous iteration.

Step 3: Compute Dendrite Tip Composition

The composition at the dendrite tip can be calculated using the Ivantsov relationship in Eq. (14). After the composition of the dendrite tip is known for a Peclet number, the new thermodynamic equilibrium can be calculated for the composition at the dendrite tip.

Step 4: Compute Thermodynamic and Non-Equilibrium Partitioning

The new equilibrium allows for the calculation of a new dendrite tip temperature and partition coefficient. The non-equilibrium partitioning is solved with the Aziz relationship in Eq. (25). Step 4 follows exactly Step 1, reusing Eq. (44), with the new liquidus composition determined by the Ivantsov solution in Step 3.

Step 5: Compute Non-equilibrium Partitioning Composition (Solute Trapping)

Now that equilibrium is determined at the dendrite tip, non-equilibrium effects can be included. The non-equilibrium effects are solved using a similar approach to equilibrium, but different starting values. Once the new dendrite tip temperature is known, the equilibrium partitioning is calculated for that temperature. Since the temperature of the system is defined, this leaves two unknowns to solve for, the composition of the solid C_S and liquid C_L. An additional constraint on the system is that the ratio of C_S and C_L are defined by the Aziz's non-equilibrium partition coefficient. Since there is a fixed ratio of solute in the liquid and solid, the Gibbs-Free energy of the solid is increased by following the reaction rate theory of atomic jumps is discussed by Kurz and Trivedi [76]. The reaction rate theory for atomic jumps has historically been called kinetic undercooling and assumed as a separate term approximated for dilute solutions.

$$\Delta G_m = R_g T_i ln\left(1 - \left(\frac{V}{V_0}\right)\right) \quad (45)$$

Where ΔG_m is the increased Gibbs free energy in the solid, R_g is the universal gas constant, T_i is the equilibrium interface temperature, V is the solidification velocity, and V_0 on the order of the speed of sound in a material. The determined driving force from the reaction rate theory of atomic jumps is used to allow non-equilibrium compositions to form by allowing a driving force for the solid phase from the liquid. The driving force can be incorporated if free energy of the solid phase is defined as a function of the solute in the solid,

$$G^{Solid} = (1 - X_B)G_A + X_B G_B + \Omega^{Solid}(1 - X_B)X_B + RT((1 - X_B)\ln(1 - X_B) + X_B \ln(X_B)) \quad (46)$$

Using the previous equation, we can determine the liquid and solid compositions from the two equations in terms of the liquid composition, where $X_B = k_v C_L$. The previous relationships allow for the definition of the two following equations.

$$\mu^{Liq}(C_L) = \left(\mu_B^{Liq} - \mu_A^{Liq}\right)C_L + \mu_A^{Liq} \quad (47)$$

$$G^{Solid}(C_L k_v) = (1 - C_L k_v)G_A + C_L k_v G_B + \Omega^{Solid}(1 - C_L k_v)C_L k_v + RT((1 - C_L k_v)\ln(1 - C_L k_v) + X_B \ln(C_L k_v)) \quad (48)$$

Then Eq. (47) and (48) are iteratively solved using the fsolve method from Scipy along with the additional attachment kinetic driving force at the equilibrium temperature at the dendrite tip composition.

$$\mu^{Liq}(C_L k_V) - \left(G^{Solid}(C_L k_V) + \Delta G_m\right) = 0 \quad (49)$$

This step is solving for a liquid composition that has a particular driving force for a solid composition based on the fixed interval defined by Aziz's solute trapping. The goal of this

section is still to solve for chemical potential equality similar to equilibrium calculation, although the free energy in the solid is increased.

Step 6: Compute Non-equilibrium Liquidus Slope

The non-equilibrium liquidus slope is approximated using numerical methods, where the derivative is approximated by the Scipy derivative function. The equilibrium liquidus composition is varied to determine the approximate slope.

Step 7: Compute a new Radius.

The radius is solved by using Eq. (17)-(19), and the previous calculated values.

Step 8: Check Radius Convergence

The radius is then checked against a selected tolerance criterion. If the tolerance criterion is met, the undercooling of the system will be output. If the tolerance criterion is not met, the system will be iterated upon using Step 9.

Step 9: Re-evaluate based on a Peclet Number.

Using the newly determined radius, recalculate the Peclet number and set the initial radius to the new radius to recalculate all steps 3-9 based upon the updated Peclet number. The processes will be repeated until the system converges. It is not possible for all systems to converge. If a system diverges, the radius will typically be calculated as an imaginary number.

N^{th} systems

This methodology has not been extended for multicomponent systems.

5.2.3 A verification of the above approach for FCC Al in the Al-Si system.

The verification here is relevant for the direct calculation of chemical potentials during the iterative dendritic IRF. The Al-Si alloy is an appropriate test case for the dendritic IRF because its phase diagram is close to linear. The thermodynamic descriptions for Al-Si are adopted from the COST 507 database [179]. The thermodynamic descriptions of each phase are listed in the appendix. Examining the Al-Si phase diagram as shown in Figure 5.6 by solving

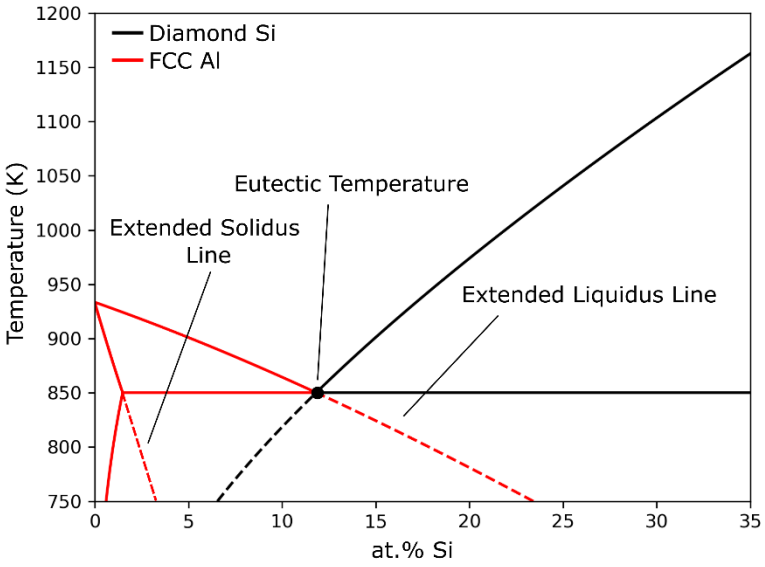

Figure 5.6 Al-Si Phase Diagram with extended liquidus lines

for $\mu_{Al}^{FCC\ Al} - \mu_{Si}^{FCC\ Al} = \mu_{Al}^{Liquid} - \mu_{Si}^{Liquid}$ at each temperature using the thermodynamic descriptions. In the case of a binary substitutional phase models, μ_{Al} and μ_{Si} are described by Eq. (40) and (41).

Each calculation is performed between the liquid and respective solid phase. Therefore, the only consideration is the tangent line between the two input phases. In the current case i and j are the respective phases in the system (for Al-Si these phases are liquid, FCC Al, and diamond Si). The FCC Al and Liquid (being $\mu_{Al}^{Liquid} = \mu_{Al}^{FCC\ Al}$ and $\mu_{Si}^{Liquid} = \mu_{Si}^{FCC\ Al}$) are shown in red, where the liquidus and solidus compositions are solved from temperature (933 k to 750 k). The solid red line denoted by the T_L^{FCC} decreases until the eutectic point at 850.1 K. Then, a dotted red line denoting the extended liquidus line is calculated.

The extended liquidus line is the continued equilibrium between FCC Al and Liquid assuming the absence of the Diamond Si phase in the system. The extended solidus of FCC Al line is also computed at the same time. The liquidus temperature of FCC Al is continually depressed as the Si content in the alloy is increased. The same effect is observed in the Diamond Si phase with decreasing Si. The liquidus line of diamond Si continues to decrease as the Si in the alloy decreases. The Diamond Si phases are calculated using the same method for FCC and Liquid, but the FCC phase is suppressed instead of the Diamond Si phase.

The liquidus and solidus lines are solved using Scipy fsolve package [173]. A key feature of the phase diagram is that the liquidus and solidus compositions can be determined using an input temperature. This, while trivial, can now be used to compute the non-equilibrium phase diagrams that are dependent on the solidification velocity of the dendrite tip.

Now that the equilibrium phase diagram is defined, the non-equilibrium phase diagram described by Eq. (49) needs to be defined as a function of solidification velocity. In Figure 5.7, three phase diagrams between FCC Al and liquid are shown as a function of velocity. The first denoted in red is the equilibrium liquids and solidus line assuming only FCC Al and liquid exists in the system. The two blue lines are the non-equilibrium liquidus and solidus lines assuming solidification velocities of 1 and 3 m/s. The phase diagrams demonstrate the combination of solute trapping and attachment kinetics.

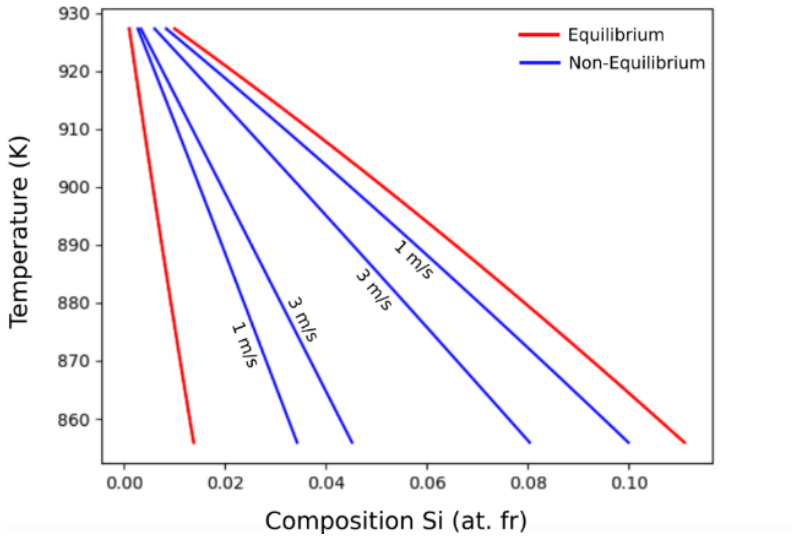

Figure 5.7 Al-Si Phase Diagram Computed from COST 507 Database using only FCC Al and Liquid that demonstrates the equilibrium phase diagram in red and the non-equilibrium phase diagrams as a function of velocity in blue.

The non-equilibrium phase diagram is solved by inputting a temperature, and then determining the solidus and liquidus composition from Eq. (49). As the solidification velocity approaches zero the equilibrium phase diagram is recovered.

After determining the non-equilibrium phase diagram, the undercooling of the Al-Si system can be determined and compared between the direct liquidus computation and the linear approximation methods. The non-equilibrium phase diagrams are used to determine the non-equilibrium liquidus slopes which can increase the undercooling in the system. The parameters to calculate the dendritic IRF are listed in Table 5.5.The remaining parameters are determined from the phase diagram.

The IRF is now calculated using the two methodologies (linear phase diagram and direct calculation of liquidus temperature) to evaluate the differences in the models, as seen in Figure 5.8. The IRF was calculated at a thermal gradient of $1x10^5$ (K/m). The calculation in this section is specifically for undercooling caused by compositional effects and capillary effects are ignored. Cellular undercooling, which is prevalent at low solidification velocities, is ignored.

Figure 5.8 shows good agreement between the linear approximation and direct liquidus calculation methods, especially at low solidification velocities. It is notable that the (at. %) Si in the liquid at the dendrite tip and the dendrite tip radius of each method are similar the same. The slight differences are accounted for in the change in partitioning and liquidus slopes that in turn change the composition at the dendrite tip, effecting the constitutional undercooling.

The comparison between the two methodologies demonstrates that it is reasonable to approximate a phase diagram by using linearization when the liquidus slope is near constant for the domain of interest. However, in Figure 5.4, using the Al-Zr system, it is also demonstrated that the linearization of a phase diagram may not always reasonably apply.

It is notable that in the current state, this discussed solution for the dendritic IRF is only valid for solid solutions. The application of this solution to intermetallic compounds, modeled as individual points in CALPHAD cannot be performed because of the limitation of a fixed phase composition description. The reasoning is that the driving force from attachment kinetics and the velocity dependent partition coefficient will only change the composition of the liquid, as the

Table 5.5 Parameters used in the IRF for determining the undercooling of FCC Al in the Al-Si System

Parameter (Unit)	Linear Approximation	Direct Calculation	Source
Initial Composition of Si, C_0 (at. %)	6.5	6.5	Given
Eq. Melting Temperature, T_0 (K)	883.17	883.17	Calculated
Liquidus Slope, m (K/at. %)	7.31	Dependent	Calculated
Partition Coefficient, k_0	0.1161	Dependent	Calculated
Gibbs-Thomson Coefficient, Γ (mk)	1.96×10^{-7}	1.96×10^{-7}	Hunt *et al.* [178]
Liquid Diffusivity, D_L (m^2s^{-1})	2.5×10^{-9}	2.5×10^{-9}	Mohammadpour *et al.* [92].
Diffuse interface thickness, a_0 (m)	1×10^{-9}	1×10^{-9}	Aziz *et al.* [132]
Speed of Sound in FCC Al (m/s)*	5100	5100	Dantzig *et al.* [125]

*The speed of sound in FCC Al is used in Eq. (45)

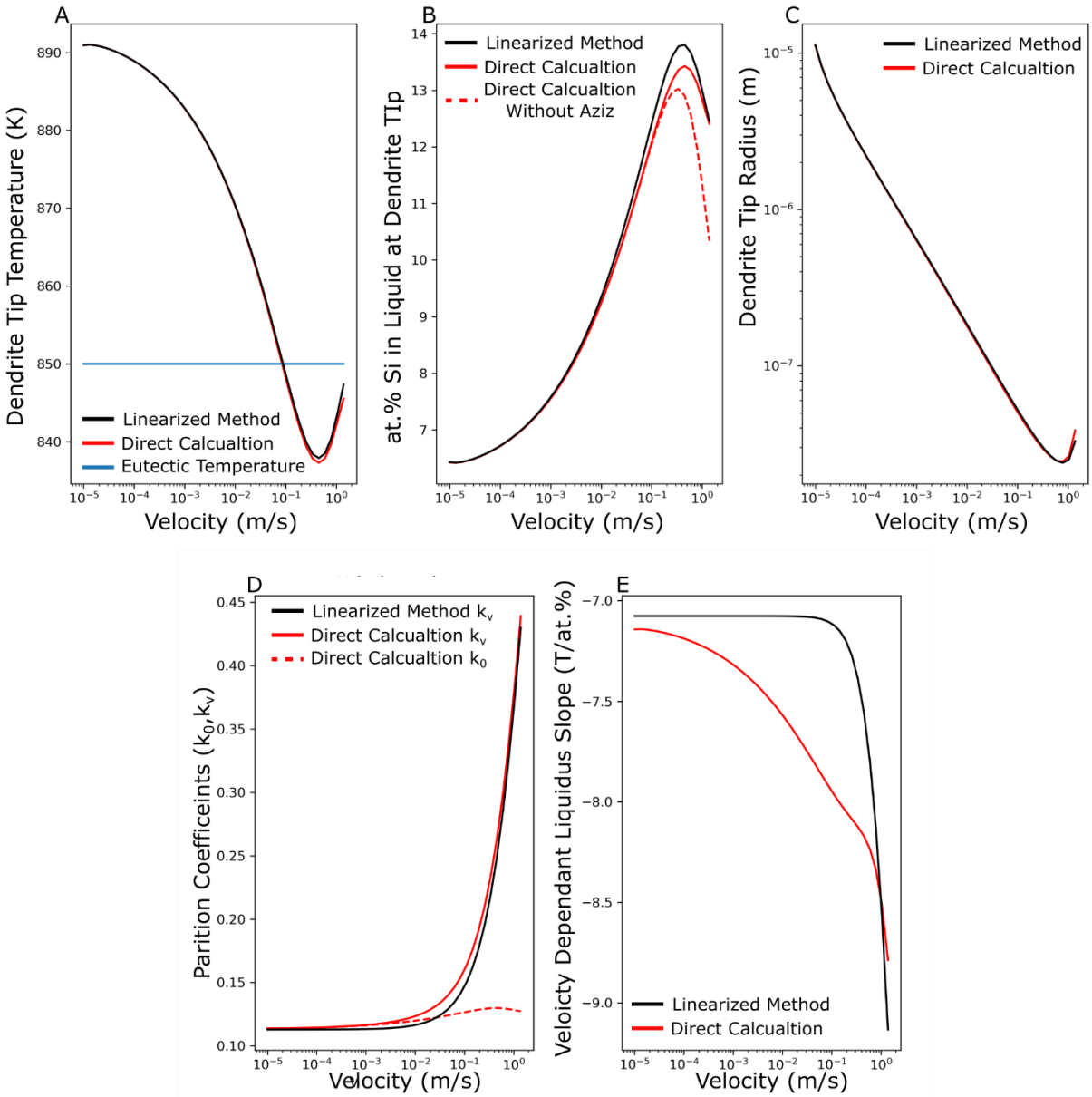

Figure 5.8 Demonstrates the IRF of an Al-6Si (at. %) alloy. The IRF was calculated at a thermal gradient of 10 K/m. where A) is the Dendrite tip temperature as a function of solidification velocity that demonstrates the undercooling of the Direct calculation is initially much quicker than the Traditional method, B) demonstrates the (at. %) Si in the liquid at the dendrite tip as a function of solidification velocity, C) demonstrates the dendrite tip radius as a function of solidification velocity, D) demonstrates the non-equilibrium partition coefficients (k_v) for each method and the equilibrium partition coefficient using the Direct Calculation method (k_0), and E) represents the liquidus slope as a function of solidification velocity.

composition of the solid is fixed, over defining the system. Although, in intermetallic compounds defined as a fixed composition, the undercooling based on the CALPHAD approach is still possible to perform ignoring the non-equilibrium affects, which will be discussed in the next section.

5.3 Using the Non-Linear Dendritic Interface Response Function to determine undercooling in the Al-Ce-Mn System.

In this section, the dendritic IRF will be calculated for the $Al_{10}Mn_2Ce$ and $Al_{20}Mn_2Ce$ phases using the methodology outlined in Section 5.2.1. The solid solution cannot be used because the CALPHAD descriptions are line compounds, meaning they have a fixed composition. The goal is to apply the new non-linear IRF to calibrate to the experimental observations in Chapter 4.

5.3.1 Fitting the Interface Response function Using the Results from Chapter 4

The IRF allows for an understanding of what is the preferred stable growth phase as a function of solidification conditions. However, in the current linear model used for the Al-Ce-Mn system, the undercooling calculations did not match the transition from intermetallic to eutectic. To address this limitation, the direct calculation of the dendrite tip temperature will be adopted as described in section 5.2.1. The CALPHAD models for $Al_{10}Mn_2Ce$ and $Al_{20}Mn_2Ce$ are taken from Yang et al [150]. The values used in the calculation are summarized in Table 5.6.

The approach is using the PANDAT CALPHAD description to calculate the non-linearized liquid slope and temperature. Since the thermodynamic parameters are restricted, CALPHAD is used to do the direct calculation.

The Gibbs-Thomson Coefficient will be the primary input value used to fit the system. The initial values are taken from Yang *et al.* [150], where the Gibbs-Thomson Coefficients were determined as $1.35x10^{-7}$ (m-K) for $Al_{20}Mn_2Ce$, and $1.47x10^{-7}$ (m-K) for $Al_{10}Mn_2Ce$. The values were approximated by Yang were determined using Turnbull's First-order approximation of interfacial energy [183]. Then the interfacial energy of the phases is used to calculate the Gibbs-Thomson coefficient. To fit the system, the Gibbs-Thomson coefficient is increased until the phase selection from the dendritic IRF matches the experimental data. The changing of the Gibbs-Thomson coefficient is simply to make the data match experimental results.

Table 5.6 Parameter used in the IRF Calculations for $Al_{10}Mn_2Ce$ and $Al_{20}Mn_2Ce$

Parameters	$Al_{20}Mn_2Ce$	$Al_{10}Mn_2Ce$	Source
Initial Ce Composition, $C_{0,Ce}$ (at. %)	2.18	2.18	Given
Initial Mn Composition, $C_{0,Mn}$ (at. %)	4.48	4.48	Given
Gibbs-Thomson Coefficient (m-k)	8.5×10^{-7}	8.85×10^{-7}	Yang *et al.* [150]
Liquid Diffusivity of Mn, D_L^{Mn} (m^2/s)	3.34×10^{-9}	3.34×10^{-9}	Du *et al.* [171]
Liquid Diffusivity of Ce, D_L^{Ce} (m^2/s)	2.5×10^{-9}	2.5×10^{-9}	Assumed
Dendrite Tip Selection Parameter σ	0.025	0.025	Mohammadpour *et al.* [92].
Thermal Gradient (K/m)	$1x10^6$	$1x10^6$	Assumed

To fit the experimental results with the dendritic IRF modeling, the Gibbs Thomson coefficient for each phase were increased to $8.85x10^{-7}$ (m-K) and $8.5x10^{-7}$ (m-K) for $Al_{10}Mn_2Ce$ and $Al_{20}Mn_2Ce$ respectively. The recalculation of the dendritic IRF with these new values is shown in Figure 5.9.

Although additional experimentation may be necessary to calibrate the system, the current fitting of data gives a starting point in which process modeling can be used to predict the fraction of microstructures. In Figure 5.9, the vertical pink lines indicate the measured transitions for phase selection from Chapter 4. These values initially ignore thermal gradient, and only discuss the transition between phases with respect to solidification velocities. The transition from $Al_{10}Mn_2Ce$ to $Al_{19.92}Mn_{2.42}Ce_{0.67}$ is calculated from Chapter 4 between $5.19x10^{-4}$ and $7.4x10^{-4}$ (m/s). The transition between these two phases is denoted by Transition 1 in Figure 5.9, which represent $7.4x10^{-4}$ (m/s). The transition from the $Al_{19.62}Mn_{2.2}Ce_{1.18}$ to the eutectic solidification is calculated from Chapter 4 between $6.8x10^{-2}$ and $7.3x10^{-2}$ (m/s). The transition between from the intermetallic to the eutectic is denoted by Transition 2 in Figure 5.9, represent $7.3x10^{-2}$ (m/s).

A key assumption that influences the fitting of the system is each transition region is represented by different compositions. The first transition is assumed to occur between the primary $Al_{10}Mn_2Ce$ to the primary $Al_{19.92}Mn_{2.42}Ce_{0.67}$. The second transition is assumed to occur between the primary $Al_{19.62}Mn_{2.2}Ce_{1.18}$ to the eutectic microstructure. The downside of this assumption is that the transition between compositions of $Al_{19.92}Mn_{2.42}Ce_{0.67}$ and $Al_{19.62}Mn_{2.2}Ce_{1.18}$ is not modeled.

5.4 Discussion

There three key points in the discussion that are focused on

- How does the thermal gradient play a role in a phase selection map for the dendritic IRF.
- What other considerations may need to be evaluated in the future to better model the Al-Ce-Mn system.
- What is the effect of localized composition on the solidification phase selection, and how does it relate to the PMZ.

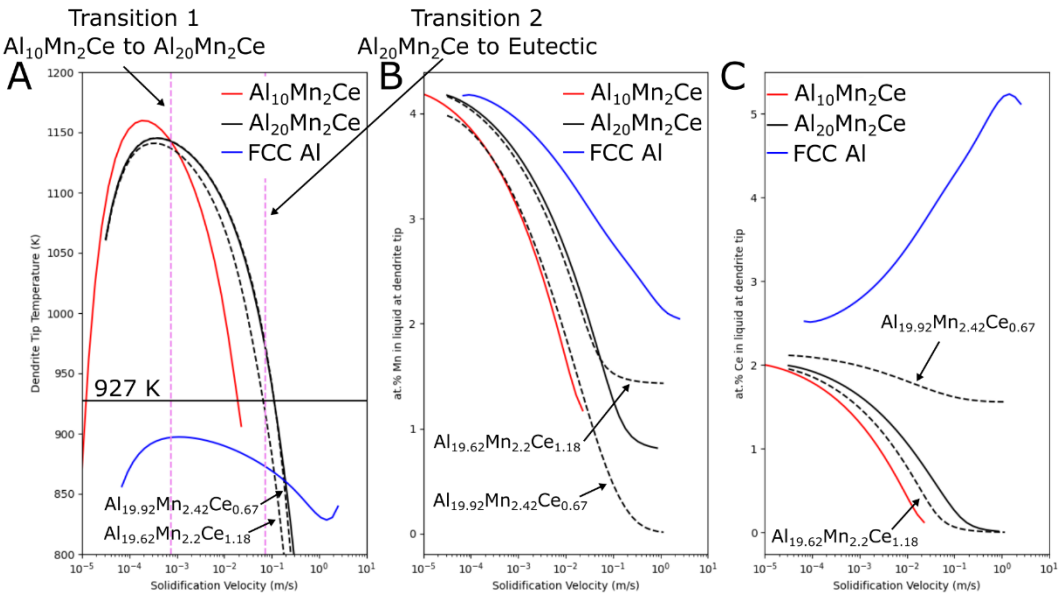

Figure 5.9 (A) Demonstrates the IRF calculated with Fitted Gibb-Thomson Coefficient values for the bulk alloy composition, (B-C) demonstrate the Ce and Mn solute in the liquid at the dendrite tip respectively. The vertical pink bands indicate the transition points calculated by the Rosenthal model.

5.4.1 Solidification Phase Selection Maps using the IRF for the Al-Ce-Mn System

After the Al-Ce-Mn system has been fitted by manipulating the Gibbs-Thomson coefficient, a phase selection map can be calculated. The phase selection map is for the three solidification modes of primary $Al_{10}Mn_2Ce$, primary $Al_{20}Mn_2Ce$, and eutectic (between FCC Al and $Al_{20}Mn_2Ce$). The map is calculated for a range of G and V values shown in Figure 5.10. The No Solution region in the figure is typically attributed to planar growth states, although planar growth is not calculated for the current modeling. The phase selection maps can now be used in future efforts to attempt to control the selected microstructure as a function of processing parameters, as well as complex scan strategies. The G and V prediction from the Rosenthal model does demonstrate that in the 83 mm/s weld track the primary $Al_{10}Mn_2Ce$ phase is not predicted to be in a stable growth state. The caveat to all the modeling is that the eutectic selection is taken at the eutectic temperature (927 K) and not actively modeled.

5.4.2 Additional Considerations for the IRF

One of the key assumptions of the dendritic IRF is the chosen dendrite tip radius solution used by Kurz and Trivedi, shown in Eq. (17). Hartmann *et al.* [184] discusses the solidification of a $Ti_{45}Al_{55}$ alloy, where the solution for a radius is fit using values for anisotropic surface energies and kinetic parameters. The adoption of a more complex radius solution may provide additional insight into the solidification of these compounds. The methodology by Hartmann is not adopted because it adds additional fit terms to the system, as well as additional unknown parameters.

While it may not be practical to adopt a different radius solution, it is possible to investigate the radius solution adopted by Kurz and Trivedi [76]. The first question someone might ask is do each of the phases solidify as a parabolic dendrite. If the phases are not solidifying as a parabolic dendrite, a different solution needs to be adopted. The second question is, does the dendrite tip selection parameter, σ^*, represent the system well. Kurz and Trivedi use a predicted maximum for the dendrite tip selection parameter σ^*, which is taken as a 0.025. By reducing the σ^* term, there is a similar effect to increasing the Gibbs Thomson coefficient. The reason for increasing the Gibbs-Thomson coefficient is because the work is not focused on reexamining the radius solution, but to explain the experimental results by manipulating input values. The manipulation of either of these parameters has a similar effect on the overall solution.

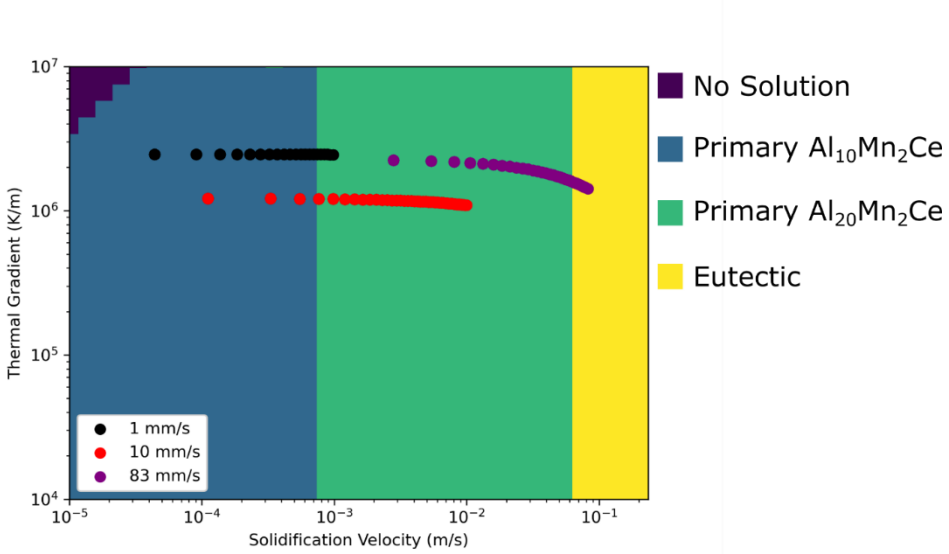

Figure 5.10 Demonstrates a phase selection map for primary $Al_{10}Mn_2Ce$, primary $Al_{20}Mn_2Ce$, and eutectic solidification between FCC Al and $Al_{20}Mn_2Ce$. On top of the processing map, the thermal gradient and solidification velocities from the three weld tracks (1, 10, and 83 mm/s) are shown.

It may also be important to frame the solidification of the $Al_{20}Mn_2Ce$ phase with the Ni_3Al intermetallic. There has been a significant amount of work on understanding the Ni_3Al that may provide insight into the current case [185]. The first interesting observation that is possible is that the Ni_3Al phase has an order to disorder transformation. In experiments by Cahn *et al.* [186,187] it was shown that the ordering temperature varied from 1360°C to 1450°C which is above and below the solidus temperature of 1385°C as a function of intermetallic composition. It may be possible that an order-disorder transformation in $Al_{20}Mn_2Ce$ is influencing the composition of the phase. It has been previously observed in the Ni_3Al intermetallic phase interstitial solute as well as substitutional elements occur on both Ni and Al sites [188]. However, the mechanism for composition change in the $Al_{20}Mn_2Ce$ phase is largely unknown and requires additional information.

5.4.3 The Effect of Composition

The initial composition of the liquid assumed by the dendritic IRF will have an impact on the predicted undercooling of each phase. In the PMZ region of microstructure, the selective melting of FCC Al over the $Al_{20}Mn_2Ce$ phase allows the liquid composition to differ from the bulk. If the dendritic IRF is used in a scenario where the bulk liquid composition is reduced in Ce and Mn because of localized melting, the primary $Al_{10}Mn_2Ce$ phase is no longer selected at solidification velocities $<7.4x10^{-4}$ (m/s). Assuming all other parameters are equal, the initial composition of the system is changed to 0.5 at. % Ce and 2 at. % Mn. The result of the change in composition, as seen in Figure 5.11, is that the $Al_{10}Mn_2Ce$ phase is never predicted as the stable growth phase.

In the weld track observed in Chapter 4, the $Al_{10}Mn_2Ce$ phase was suppressed after the $7.4x10^{-4}$ (m/s) solidification velocity using the 927 K isotherm. In Figure 5.9, the dendritic IRF function is fit to approximately this value. However, if the composition of the liquid is not the bulk measured composition from the AM part, the fitting of the transition from primary $Al_{10}Mn_2Ce$ to primary $Al_{20}Mn_2Ce$ may be invalid. It is possible that a similar effect is happening at the edge of the weld track, in the 23-54 mm/s weld tracks, where the $Al_{10}Mn_2Ce$ is observed to be suppressed, even though the weld track is solidifying at a slow enough rate for it to be predicted to grow.

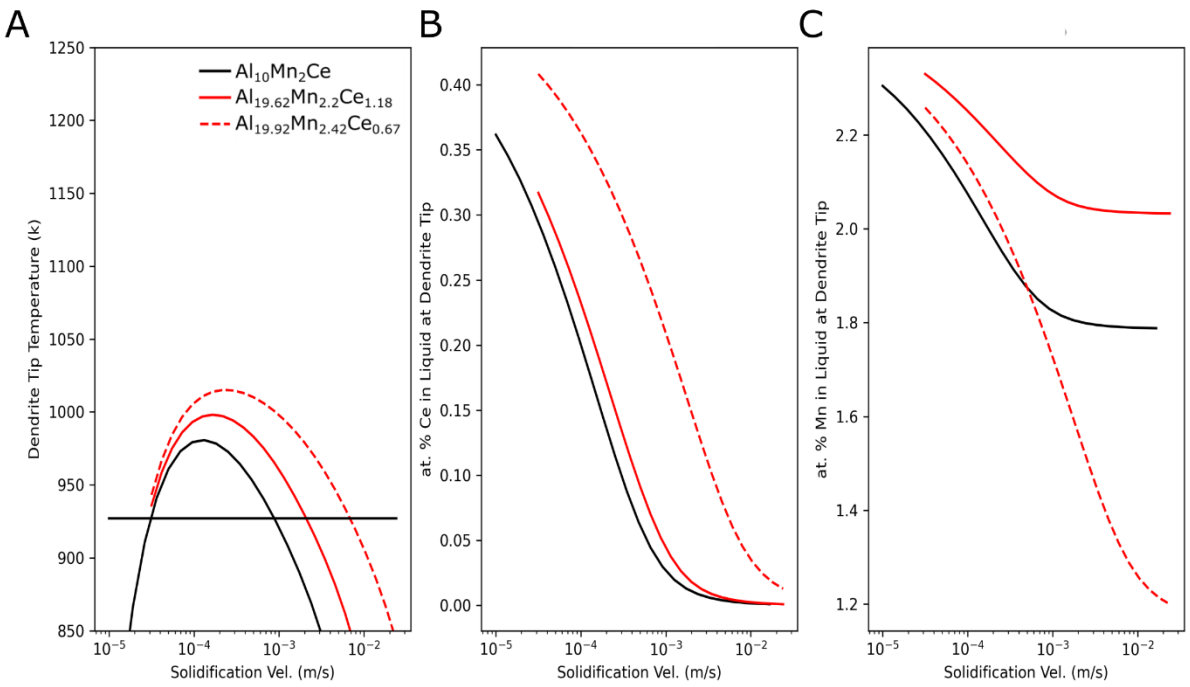

Figure 5.11 (A) Demonstrates the IRF calculated with Fitted Gibb-Thomson Coefficient values for a 0.5 at. % Ce and 2 at. % Mn alloy composition, (B-C) demonstrates the Ce and Mn solute in the liquid at the dendrite tip respectively.

5.5 Conclusions

The models discussed in Chapter 5 allow for the modeling of solidification phase selection using a at a particular solidification condition. They key takeaways from the modeling in chapter 5 are listed below:

- The linear phase diagram approximation of the IRF was evaluated for the Al-Ce-Mn system. The results showed an inability to predict the transition from primary $Al_{20}Mn_2Ce$ to a eutectic between FCC Al and $Al_{20}Mn_2Ce$.
- A new implementation of the IRF, deemed the direct calculation method, was explored for intermetallic compounds with the Al-Zr system. The result is a dramatic increase of undercooling as a function of solidification velocity. In a comparison between the linear and direct calculation methods the Al_3Zr was observed to have a change in undercooling > than 200K between the two methods.
- A new implementation of the IRF was developed for solid solution phases. The direct calculation of the phase diagram was combined with Aziz's solute trapping to approximate non-equilibrium phase diagram.
- The direct calculation IRF for intermetallic compounds was applied to the Al-Ce-Mn system. The system was fit to experimental results by manipulating the Gibbs-Thomson coefficient of the $Al_{10}Mn_2Ce$ and $Al_{20}Mn_2Ce$ phases.

Chapter 6. Conclusions and Future Work

6.1 Conclusions

6.1.1 Additively Manufacturing Al-10Ce-8Mn (wt.%) Alloy and Solid-State Phase Transformations

An additive manufactured alloy of Al-10Ce-8Mn (wt. %) was observed to produce two distinct solidification regions. The first region indicated by the primary solidification $Al_{20}Mn_2Ce$ surrounded by FCC Al and $Al_{11}Ce_3$ in the MPB typically is observed at low solidification velocities. The second is a eutectic solidification region between $Al_{20}Mn_2Ce$ + FCC Al near the center of a weld pool at higher solidification velocities. The MPB region started with three phases $Al_{20}Mn_2Ce$, FCC Al, and $Al_{11}Ce_3$. After heat treatment at 400°C the primary $Al_{20}Mn_2Ce$ decays and results in an increase in Al_6Mn, $Al_{12}Mn$, and $Al_{11}Ce_3$. The eutectic region started with $Al_{20}Mn_2Ce$ and FCC Al phases. After heat treatment at 400°C the eutectic region largely transformed into the $Al_{51}Mn_7Ce_4$ phase.

It was demonstrated through the usage of APT that the $Al_{20}Mn_2Ce$ phase is acting as a solid solution as a function of its solidification mode: primary or eutectic. It appears that the decomposition of the $Al_{20}Mn_2Ce$ phase is dependent on the localized composition of itself, and the FCC Al surrounding it.

The identification of the $Al_{51}Mn_7Ce_4$ phase was done through a combination of STEM atomic resolution imaging and synchrotron diffraction experiments from APS. The synchrotron x-ray diffraction data was used to determine that the $Al_{51}Mn_7Ce_4$ phase is present in the material.

The phase transformations of each region were rationalized based upon the solid solution nature of the $Al_{20}Mn_2Ce$ phase and solidification mode. The $Al_{20}Mn_2Ce$ phase was found using APT that there is variability in the Mn and Ce from different solidification modes.

6.1.2 Weld Track Experimentation: Experimental Phase Selection

Using laser remelting experiments, it was found as a function of laser velocity, the $Al_{10}Mn_2Ce$ phase could be suppressed to form the $Al_{20}Mn_2Ce$ phase. If the laser velocity continued to increase, the primary $Al_{20}Mn_2Ce$ can be suppressed to form the eutectic $Al_{20}Mn_2Ce$ + FCC Al.

The weld tracks were thermally exposed at 400°C for 96 hours. It was observed that the primary $Al_{10}Mn_2Ce$ phase does not appear to decompose at 400°C. The primary $Al_{20}Mn_2Ce$ phase was largely observed to decompose in two different pathways. The first, into $Al_{11}Ce_3$ and Al-Mn binary phases, and the second into $Al_{51}Mn_7Ce_4$. It is rationalized that the change in composition of the $Al_{20}Mn_2Ce$ phase is controlling the phase transformation pathway.

The eutectic region is observed to transform in the $Al_{51}Mn_7Ce_4$ phase. The combination of these three solidification modes and different solid state decomposition pathways gives the ability to have a highly manipulatable microstructure that could be investigated to target properties.

6.1.3 IRF: Modeling Phase Selection

A new methodology was introduced for the IRF wherein the free energy equations for each phase are used to determine the undercooling of that phase by combining the solute trapping and interface attachment kinetics to directly solve for the composition in the liquid and solid as a function of solidification conditions. The previously mentioned methodology removes the linear phase diagram assumption, and the undercooling of the system is directly calculated from the CALPHAD descriptions of phases in for solid solution compounds such as FCC Al. For intermetallic compounds, a similar calculation was used, except the non-equilibrium effects were not included in the solution. The adoption of the direct calculation method from CALPHAD descriptions is because of the significant under approximation of undercooling using a linearized phase diagram. The linearized phase diagram causes under approximation because of a highly variable liquidus slope that was not accounted for.

Then, the dendritic IRF model was investigated and fit to the measured solidification conditions determined in Chapter 4. The CALPHAD model of $Al_{10}Mn_2Ce$ and $Al_{20}Mn_2Ce$ was provided by Yang *et al.* [150]. The dendritic IRF was used to calculate the undercooling of phases of interest and compared to the experimental results indicating, after fitting, agreement between the predicted primary phases being $Al_{10}Mn_2Ce$, $Al_{20}Mn_2Ce$, and equilibrium eutectic $Al_{20}Mn_2Ce$ + FCC Al. It is to note that the eutectic formation was assumed to occur at the eutectic temperature.

The IRF can now be used as a tool to understand the phase selection of the $Al_{10}Mn_2Ce$, $Al_{20}Mn_2Ce$ and eutectic microstructures as a function of solidification conditions, which can in the future allow for a tailoring of microstructure selection.

6.2 Future Work

A determination of the interfacial energy between the solid-solid interfaces of phases can give valuable insight into how the phase transformations in the systems occur. It is possible that the interfacial energy plays a very significant role in the nucleation of $Al_{51}Mn_7Ce_4$. The quantification of the interfacial energy would allow for a more direct comparison of interfacial energy vs. driving force. To determine an interfacial energy between phases, there are two readily studied methods. The first is an *ab initio* method for determining the interfacial energies between OR as described by Zhang *et al.* [189]. The *ab initio* method will need additional characterization to determine if OR do exists between phases before calculations can be performed. A second possibility is to modify Lifshitz-Slyozov-Wagner (LSW) coarsening theory that can be used to evaluate the solid/solid interfacial energy from experimentally measured coarsening rates. One solution to the LSW model is described in Eq. (3) Additionally, determining a more robust CALPHAD model for the $Al_{51}Mn_7Ce_4$ phase would give insight into the role the changes in composition of the $Al_{20}Mn_2Ce$ play.

A second possibility for investigation is to determine the composition of $Al_{20}Mn_2Ce$ as a function of location in a weld track. A key question that remains is what the equilibrium composition of $Al_{23-x-y}Mn_xCe_y$ is. It has been shown in this work that the $Al_{20}Mn_2Ce$ is simply shorthand for a more complex solid solution phase. The determination of the composition of the phase as a function of solidification velocity, can be compared to Aziz's solute trapping model to investigate if the behavior for the $Al_{20}Mn_2Ce$ intermetallic compound is the same to that of a solid solution. The difficulty with this investigation is directly linking the solidification conditions to the $Al_{20}Mn_2Ce$ composition. It may be possible by using weld track location linked with the solidification conditions to determine the solidification-composition relationship. Although, in the current state, as observed in the 83 mm/s weld track, it may not be as simple because of the transition back from a eutectic microstructure to primary $Al_{20}Mn_2Ce$. More work

needs to be done to understand the fundamental solidification of the intermetallic phase to understand how it is affected by solidification conditions.

A third possibility is to investigate the ability to stabilize the $Al_{20}Mn_2Ce$ phase with the addition of different solutes. Since the $Al_{23-x-y}Mn_xCe_y$ appears to be represented as a solid solution, it may be possible to stabilize the phase using additional elements. An example of an additional element would be titanium because of the observed $Al_{20}Ti_2Ce$ phase by Niemann and Jeitschko [190]. The ability to stabilize the phase could offer decreased degradation of the microstructure with temperature and time.

A final possible future work is a targeted solidification condition design in AM to take advantage of the observations in the dissertation. The goals of this study would be to attempt to make different regions of a single part have a different quantity of starting microstructure and subsequent decomposition. The reasoning for controlling the microstructure and decomposition is to provide site specific properties that can be leveraged to create a desired mechanical response, such as failure along a certain region of a part.

References

[1] Metal AM parts in series production for BMW's new i8 Roadster, (2017).

[2] D. Scimeca, General Motors Builds Happier Employees with Additive Manufacturing, Ind. Week. (2022). https://www.industryweek.com/technology-and-iiot/article/21253942/general-motors-builds-happier-employees-with-additive-manufacturing.

[3] GM, General Motors Increases Agility and Speed by Opening All-New Additive Industrialization Center Dedicated to 3D Printing, (n.d.). https://news.gm.com/newsroom.detail.html/Pages/news/us/en/2020/dec/1214-additive.html.

[4] D. Scimeca, General Motors Builds Happier Employees with Additive Manufacturing, Ind. Week. (2022).

[5] D. Fitzgerald, NASA's New Material Built to Withstand Extreme Conditions, Nasa. (2022).

[6] A. Broda, Additive manufacturing insight, Innov. Q. (2019).

[7] M. Molitch-Hou, Ford to Mass Produce Metal 3D Printed Part for Popular Car, 3D Print. (2021). https://3dprint.com/284045/ford-to-mass-produce-metal-3d-printed-part-for-popular-car/.

[8] E. Wakefield, Liebherr to supply first complex 3D printed component for Airbus A350, 3D Print. Media Netw. (2022).

[9] R.A. Michi, A. Plotkowski, A. Shyam, R.R. Dehoff, S.S. Babu, Towards high-temperature applications of aluminium alloys enabled by additive manufacturing, Int. Mater. Rev. 67 (2022) 298–345. https://doi.org/10.1080/09506608.2021.1951580.

[10] A. Mauduit, Study of the suitability of aluminum alloys for additive manufacturing by laser powder bed fusion., (2017).

[11] S.C. Alt, V.A. Yardley, Z. Shi, J. Lin, Challenges in additive manufacturing of high-strength aluminium alloys and current developments in hybrid additive manufacturing, 4 (2021). https://doi.org/10.1016/j.ijlmm.2020.12.004.

[12] R.A. Michi, A. Plotkowski, A. Shyam, R.R. Dehoff, S.S. Babu, Towards high-temperature applications of aluminium alloys enabled by additive manufacturing, Int. Mater. Rev. (2021). https://doi.org/10.1080/09506608.2021.1951580.

[13] S. Thapliyal, S. Shukla, L. Zhou, H. Hyer, P. Agrawal, P. Agrawal, M. Komarasamy, Y. Sohn, R.S. Mishra, Design of heterogeneous structured Al alloys with wide processing window for laser-powder bed fusion additive manufacturing, Addit. Manuf. 42 (2021) 102002. https://doi.org/10.1016/j.addma.2021.102002.

[14] R. Li, M. Wang, Z. Li, P. Cao, T. Yuan, H. Zhu, Developing a high-strength Al-Mg-Si-Sc-Zr alloy for selective laser melting: Crack-inhibiting and multiple strengthening mechanisms, Acta Mater. 193 (2020) 83–98. https://doi.org/10.1016/j.actamat.2020.03.060.

[15] G. Langelandsvik, O.M. Akselsen, T. Furu, H.J. Roven, Review of aluminum alloy development for wire arc additive manufacturing, Materials (Basel). 14 (2021) 1–26. https://doi.org/10.3390/ma14185370.

[16] S. Kou, A criterion for cracking during solidification, 88 (2015) 366–374.

[17] E. Spinelli, R. Kakitani, R. V Reyes, A. Garcia, Relationship between spacing of eutectic colonies and tensile properties of transient directionally solidi fi ed Al-Ni eutectic alloy, 733 (2018) 59–68. https://doi.org/10.1016/j.jallcom.2017.10.288.

[18] P.W. Voorhees, The Theory of Ostwald Ripening, 38 (1985).

[19] P.W. Voorhees, Ostwald Ripening of Two-Phase Mixtures, Annu. Rev. Mater. Sci. 22 (1992) 197–215.

[20] A. Plotkowski, O. Rios, N. Sridharan, Z. Sims, K. Unocic, R.T. Ott, R.R. Dehoff, S.S. Babu, Evaluation of an Al-Ce alloy for laser additive manufacturing, Acta Mater. 126 (2017) 507–519. https://doi.org/10.1016/j.actamat.2016.12.065.

[21] K. Sisco, A. Plotkowski, Y. Yang, D. Leonard, B. Stump, P. Nandwana, R.R. Dehoff, S.S. Babu, Microstructure and properties of additively manufactured Al–Ce–Mg alloys, Sci. Rep. 11 (2021) 1–14. https://doi.org/10.1038/s41598-021-86370-4.

[22] D.R. Eyers, A.T. Potter, Industrial Additive Manufacturing: A manufacturing systems perspective, Comput. Ind. 92–93 (2017) 208–218. https://doi.org/10.1016/j.compind.2017.08.002.

[23] A. Bhatia, A.K. Sehgal, Additive manufacturing materials, methods and applications: A review, Mater. Today Proc. (2021). https://doi.org/10.1016/j.matpr.2021.04.379.

[24] W.J. Sames, F.A. List, S. Pannala, R.R. Dehoff, S.S. Babu, The metallurgy and processing science of metal additive manufacturing, Int. Mater. Rev. 61 (2016) 315–360. https://doi.org/10.1080/09506608.2015.1116649.

[25] A. Plotkowski, R. Dinwiddie, S.S. Babu, Thermal design of hybrid materials produced via ultrasonic additive manufacturing, Mater. Eval. 76 (2018).

[26] A. Levy, A. Miriyev, N. Sridharan, T. Han, E. Tuval, S.S. Babu, M.J. Dapino, N. Frage, Ultrasonic additive manufacturing of steel: Method, post-processing treatments and properties, J. Mater. Process. Technol. 256 (2018) 183–189. https://doi.org/10.1016/j.jmatprotec.2018.02.001.

[27] R.S. Mishra, R.S. Haridas, P. Agrawal, Friction stir-based additive manufacturing, Sci. Technol. Weld. Join. 27 (2022) 141–165. https://doi.org/10.1080/13621718.2022.2027663.

[28] M. Srivastava, S. Rathee, S. Maheshwari, A. Noor Siddiquee, T.K. Kundra, A Review on Recent Progress in Solid State Friction Based Metal Additive Manufacturing: Friction Stir Additive Techniques, Crit. Rev. Solid State Mater. Sci. 44 (2019) 345–377. https://doi.org/10.1080/10408436.2018.1490250.

[29] ISO/ASTM Internacional, Additive Manufacturing - General Principles Terminology (ASTM52900), Rapid Manuf. Assoc. 2021 (2013) 10–12. http://www.ciri.org.nz/nzrma/technologies.html.

[30] M. Rauch, J.-Y. Hascoët, M. Mallaiah, Repairing Ti-6Al-4V aeronautical components with DED additive manufacturing, MATEC Web Conf. 321 (2020) 03017. https://doi.org/10.1051/matecconf/202032103017.

[31] N.E. Gorji, P. Saxena, M. Corfield, A. Clare, J.P. Rueff, J. Bogan, P.G.M. González, M. Snelgrove, G. Hughes, R. O'Connor, R. Raghavendra, D. Brabazon, A new method for assessing the recyclability of powders within Powder Bed Fusion process, Mater. Charact. 161 (2020) 110167. https://doi.org/10.1016/j.matchar.2020.110167.

[32] D. Galicki, F. List, S.S. Babu, A. Plotkowski, H.M. Meyer, R. Seals, C. Hayes, Localized Changes of Stainless Steel Powder Characteristics During Selective Laser Melting Additive Manufacturing, Metall. Mater. Trans. A Phys. Metall. Mater. Sci. 50 (2019) 1582–1605. https://doi.org/10.1007/s11661-018-5072-7.

[33] A.T. Sutton, C.S. Kriewall, S. Karnati, M.C. Leu, J.W. Newkirk, Characterization of AISI 304L stainless steel powder recycled in the laser powder-bed fusion process, Addit. Manuf. 32 (2020) 100981. https://doi.org/10.1016/j.addma.2019.100981.

[34] C.L.A. Leung, R. Tosi, E. Muzangaza, S. Nonni, P.J. Withers, P.D. Lee, Effect of preheating on the thermal, microstructural and mechanical properties of selective electron beam melted Ti-6Al-4V components, Mater. Des. 174 (2019) 107792. https://doi.org/10.1016/j.matdes.2019.107792.

[35] M. Haines, A. Plotkowski, C.L. Frederick, E.J. Schwalbach, S.S. Babu, A sensitivity analysis of the columnar-to-equiaxed transition for Ni-based superalloys in electron beam additive manufacturing, Comput. Mater. Sci. 155 (2018) 340–349. https://doi.org/10.1016/j.commatsci.2018.08.064.

[36] GE Additive, Concept Laser X Line 2000R, (n.d.). https://www.ge.com/additive/additive-manufacturing/machines/dmlm-machines/x-line-2000r.

[37] Direct Metal Laser Sintering, 2008. (n.d.).

[38] Arcam-AB, EBM hardware, Arcam-AB. (2015).

[39] A. GE, Concept Laser Concept Laser M2 Series 5 Enabling repeatability at scale, (n.d.) 1–5.

[40] J. Metelkova, L. Vanmunster, H. Haitjema, D. Ordnung, J. Kruth, B. Van Hooreweder, Hybrid dual laser processing for improved quality of inclined up-facing surfaces in laser powder bed fusion of metals, 298 (2021) 1–10.

[41] GE Additive, Concept Laser X Line 2000R, (n.d.).

[42] A. Shyam, A. Plotkowski, S. Bahl, K. Sisco, L.F. Allard, Y. Yang, J.A. Haynes, R.R. Dehoff, An additively manufactured AlCuMnZr alloy microstructure and tensile mechanical properties, Materialia. 12 (2020). https://doi.org/10.1016/j.mtla.2020.100758.

[43] D. Svetlizky, B. Zheng, T. Buta, Y. Zhou, O. Golan, U. Breiman, R. Haj-Ali, J.M. Schoenung, E.J. Lavernia, N. Eliaz, Directed energy deposition of Al 5xxx alloy using Laser Engineered Net Shaping (LENS®), Mater. Des. 192 (2020) 108763. https://doi.org/10.1016/j.matdes.2020.108763.

[44] N.R. Wald, Engineered Net Shaping Advances Additive Manufacturing and Repair, (2007).

[45] P.J.J. Withers, H.K.D.H.K.D.H. Bhadeshia, Residual stress. Part 1– Measurement techniques, Mater. Sci. Technol. 17 (2001) 366–375. https://doi.org/10.1179/026708301101510087.

[46] R. Landgraf, Ronald W; Chernenkoff, Residual Stress Effects on Fatigue of Surface Processed Steels, Anal. Exp. Methods Residual Stress Eff. Fatigue, ASTM STP. 1004 (1988) 1–12. https://doi.org/10.1520/STP17167S.

[47] S. Chen, H. Gao, Y. Zhang, Q. Wu, Review on residual stresses in metal additive manufacturing : formation mechanisms , parameter dependencies , prediction and control approaches, J. Mater. Res. Technol. 17 (2022) 2950–2974. https://doi.org/10.1016/j.jmrt.2022.02.054.

[48] Z. Fang, Z. Wu, C. Huang, C. Wu, Review on residual stress in selective laser melting additive manufacturing of alloy parts, Opt. Laser Technol. 129 (2020) 106283. https://doi.org/10.1016/j.optlastec.2020.106283.

[49] Z. Fang, Z. Wu, C. Huang, C. Wu, Review on residual stress in selective laser melting additive manufacturing of alloy parts, Opt. Laser Technol. 129 (2020) 106283. https://doi.org/10.1016/j.optlastec.2020.106283.

[50] D. Buchbinder, W. Meiners, N. Pirch, Investigation on reducing distortion by preheating during manufacture of aluminum components using selective laser melting of aluminum components using selective laser melting, J. Laser Appl. 26 (2014). https://doi.org/10.2351/1.4828755.

[51] H. Ali, H. Ghadbeigi, K. Mumtaz, Processing Parameter Effects on Residual Stress and Mechanical Properties of Selective Laser Melted Ti6Al4V, J. Mater. Eng. Perform. 27 (2018) 4059–4068. https://doi.org/10.1007/s11665-018-3477-5.

[52] K. Kempen, L. Thijs, B. Vrancken, S. Buls, J. Van Humbeeck, J.-P. Kruth, PRODUCING CRACK-FREE, HIGH DENSITY M2 HSS PARTS BY SELECTIVE LASER MELTING: PRE-HEATING THE BASEPLATE, (2013) 131–139.

[53] M. Rappaz, J.M. Drezet, M. Gremaud, A new hot-tearing criterion, Metall. Mater. Trans. A Phys. Metall. Mater. Sci. 30 (1999) 449–455. https://doi.org/10.1007/s11661-999-0334-z.

[54] B.Y.C.E. Cross, Applying Solidification Theory to Aluminum Weldability and Consumable Development growth, (2022) 209–223.

[55] S. Kou, A criterion for cracking during solidification, Acta Mater. 88 (2015) 366–374. https://doi.org/10.1016/j.actamat.2015.01.034.

[56] U. Gratzke, P.D. Kapadia, J. Dowden, J. Kroos, G. Simon, Theoretical Approach to The Humping Phenomenon in Welding Processes, J. Phys. D. Appl. Phys. 25 (1992) 1640–1647. https://doi.org/10.1088/0022-3727/25/11/012.

[57] L. Scime, J. Beuth, Anomaly detection and classification in a laser powder bed additive manufacturing process using a trained computer vision algorithm, Addit. Manuf. 19 (2018) 114–126. https://doi.org/10.1016/J.ADDMA.2017.11.009.

[58] L. Scime, D. Siddel, S. Baird, V. Paquit, Layer-wise anomaly detection and classification for powder bed additive manufacturing processes: A machine-agnostic algorithm for real-time pixel-wise semantic segmentation, Addit. Manuf. 36 (2020) 101453. https://doi.org/10.1016/j.addma.2020.101453.

[59] A. Matsunawa, J.-D. Kim, N. Seto, M. Mizutani, S. Katayama, Dynamics of keyhole and molten pool in laser welding, J. Laser Appl. 10 (1998) 247–254. https://doi.org/10.2351/1.521858.

[60] A. Matsunawa, J. Kim, S. Katayama, Porosity formation in laser welding - Mechanisms and suppression methods, 73 (1997). https://doi.org/10.2351/1.5059740.

[61] A. Matsunawa, N. Seto, J. Kim, S. Katayama, Dynamics of keyhole and molten pool in high-power CO2 laser welding, (2000). https://doi.org/10.1117/12.377006.

[62] Y. Huang, T.G. Fleming, S.J. Clark, S. Marussi, K. Fezzaa, J. Thiyagalingam, C. Lun, A. Leung, P.D. Lee, Keyhole fluctuation and pore formation mechanisms during laser powder bed fusion additive manufacturing, (n.d.) 1–11. https://doi.org/10.1038/s41467-022-28694-x.

[63] M. Bayat, A. Thanki, S. Mohanty, A. Witvrouw, S. Yang, J. Thorborg, N. Skat, J. Henri, Keyhole-induced porosities in Laser-based Powder Bed Fusion (L-PBF) of Ti6Al4V : High-fidelity modelling and experimental validation, Addit. Manuf. 30 (2019) 100835. https://doi.org/10.1016/j.addma.2019.100835.

[64] S.J. Foster, K. Carver, R.B. Dinwiddie, F.L. Iii, K.A. Unocic, A. Chaudhary, S.S. Babu, Process-Defect-Structure-Property Correlations During Laser Powder Bed Fusion of Alloy 718: Role of In Situ and Ex Situ Characterizations, (n.d.). https://doi.org/10.1007/s11661-018-4870-2.

[65] S.K. Everton, M. Hirsch, P. Stravroulakis, R.K. Leach, A.T. Clare, Review of in-situ process monitoring and in-situ metrology for metal additive manufacturing, JMADE. 95 (2016) 431–445. https://doi.org/10.1016/j.matdes.2016.01.099.

[66] S.K. Everton, M. Hirsch, P. Stravroulakis, R.K. Leach, A.T. Clare, Review of in-situ process monitoring and in-situ metrology for metal additive manufacturing, JMADE. 95 (2016) 431–445. https://doi.org/10.1016/j.matdes.2016.01.099.

[67] M. Rappaz, S.A. David, J.M. Vitek, L.A. Boatner, Analysis of solidification microstructures in Fe-Ni-Cr single-crystal welds, Metall. Trans. A. 21 (1990) 1767–1782. https://doi.org/10.1007/BF02672593.

[68] R.R. Dehoff, M.M. Kirka, F.A. List, K.A. Unocic, W.J. Sames, Crystallographic texture engineering through novel melt strategies via electron beam melting: Inconel 718, Mater. Sci. Technol. (United Kingdom). 31 (2015) 939–944. https://doi.org/10.1179/1743284714Y.0000000697.

[69] W.J. Sames, K.A. Unocic, G.W. Helmreich, M.M. Kirka, F. Medina, R.R. Dehoff, S.S. Babu, Feasibility of in situ controlled heat treatment (ISHT) of Inconel 718 during electron beam melting additive manufacturing, Addit. Manuf. 13 (2017). https://doi.org/10.1016/j.addma.2016.09.001.

[70] Carolin Korner, H. Helmer, A. Bauerei, R.F. Singer, Tailoring the grain structure of IN718 during selective electron beam melting, 08001 (2014). https://doi.org/10.1051/matecconf/20141408001.

[71] R.R. Dehoff, M. Kirka, W.J. Sames, H. Bilheux, A.S. Tremsin, L.E. Lowe, S.S. Babu, Site specific control of crystallographic grain orientation through electron beam additive manufacturing, Mater. Sci. Technol. (United Kingdom). 31 (2015) 931–938. https://doi.org/10.1179/1743284714Y.0000000734.

[72] P. Fernandez-Zelaia, M.M. Kirka, A.M. Rossy, Y. Lee, S.N. Dryepondt, Nickel-based superalloy single crystals fabricated via electron beam melting, Acta Mater. 216 (2021) 117133. https://doi.org/10.1016/j.actamat.2021.117133.

[73] S.C. Gill, W. Kurz, Rapidly solidified AlCu alloys-I. experimental determination of the microstructure selection map, Acta Metall. Mater. 41 (1993) 3563–3573. https://doi.org/10.1016/0956-7151(93)90237-M.

[74] S.C. Gill, W. Kurz, Rapidly solidified AlCu alloys-II. Calculation of the microstructure selection map, Acta Metall. Mater. 43 (1995) 139–151. https://doi.org/10.1016/0956-7151(95)90269-4.

[75] S. Fukumoto, W. Kurz, Solidification phase and microstructure selection maps for Fe-Cr-Ni alloys, ISIJ Int. 39 (1999) 1270–1279. https://doi.org/10.2355/isijinternational.39.1270.

[76] R. Trivedi, W. Kurz, Dendritic Growth, Int. Mater. Rev. 39 (1994) 49–74.

[77] R. Trivedi, Interdendritic Spacing: Part Ii. a Comparison of Theory and Experiment., Metall. Trans. A, Phys. Metall. Mater. Sci. 15 A (1984) 977–982. https://doi.org/10.1007/bf02644689.

[78] W. Kurz, D.J. Fisher, Dendrite growth at the limit of stability: tip radius and spacing, Acta Metall. 29 (1981) 11–20. https://doi.org/10.1016/0001-6160(81)90082-1.

[79] D.J. Fisher, W. Kurz, A theory of branching limited growth of irregular eutectics, Acta Metall. 28 (1980) 777–794. https://doi.org/10.1016/0001-6160(80)90155-8.

[80] R. Trivedi, P. Magnin, W. Kurz, Theory of eutectic growth under rapid solidification conditions, Acta Metall. 35 (1987) 971–980. https://doi.org/10.1016/0001-6160(87)90176-3.

[81] A.M.Y.J. Godfrey, J. Simpson, D. Leonard, K. Sisco, R.R. Dehoff, S.S. Babu, Heterogeneity and Solidification Pathways in Additively Manufactured 316L Stainless Steels, Metall. Mater. Trans. A. (2022). https://doi.org/10.1007/s11661-022-06747-6.

[82] F. Czerwinski, Current Trends in Automotive Lightweighting Strategies and Materials, (2021).

[83] F. Czerwinski, W. Kasprzak, D. Sediako, D. Emadi, S. Shaha, J. Friedman, D. Chen, High-Temperature Aluminum Alloys for Automotive Powertrains, (n.d.).

[84] E.E. and R.E.V.T. Program, Advanced Combustion Engine Research and Development, DOE-ACE-2011AR. (2011).

[85] W.E. Frazier, Metal additive manufacturing: A review, J. Mater. Eng. Perform. 23 (2014) 1917–1928. https://doi.org/10.1007/s11665-014-0958-z.

[86] J.J. Lewandowski, M. Seifi, Metal Additive Manufacturing: A Review of Mechanical Properties, Annu. Rev. Mater. Res. 46 (2016) 151–186. https://doi.org/10.1146/annurev-matsci-070115-032024.

[87] E. Atzeni, A. Salmi, Study on unsupported overhangs of AlSi10Mg parts processed by Direct Metal Laser Sintering (DMLS), J. Manuf. Process. 20 (2015) 500–506. https://doi.org/10.1016/j.jmapro.2015.04.004.

[88] S. Romano, A. Brückner-Foit, A. Brandão, J. Gumpinger, T. Ghidini, S. Beretta, Fatigue properties of AlSi10Mg obtained by additive manufacturing: Defect-based modelling and prediction of fatigue strength, Eng. Fract. Mech. 187 (2018) 165–189. https://doi.org/10.1016/j.engfracmech.2017.11.002.

[89] N.T. Aboulkhair, N.M. Everitt, I. Ashcroft, C. Tuck, Reducing porosity in AlSi10Mg parts processed by selective laser melting, Addit. Manuf. 1 (2014) 77–86. https://doi.org/10.1016/j.addma.2014.08.001.

[90] E. Brandl, U. Heckenberger, V. Holzinger, D. Buchbinder, Additive manufactured AlSi10Mg samples using Selective Laser Melting (SLM): Microstructure, high cycle fatigue, and fracture behavior, Mater. Des. 34 (2012) 159–169. https://doi.org/10.1016/j.matdes.2011.07.067.

[91] K. Kempen, L. Thijs, J. Van Humbeeck, J.P. Kruth, Mechanical Properties of AlSi10Mg Produced by Selective Laser Melting, Phys. Procedia. 39 (2012) 439–446. https://doi.org/10.1016/j.phpro.2012.10.059.

[92] N.E. Uzan, R. Shneck, O. Yeheskel, N. Frage, High-temperature mechanical properties of AlSi10Mg specimens fabricated by additive manufacturing using selective laser melting technologies (AM-SLM), Addit. Manuf. 24 (2018) 257–263. https://doi.org/10.1016/j.addma.2018.09.033.

[93] N. Read, W. Wang, K. Essa, M.M. Attallah, Selective laser melting of AlSi10Mg alloy: Process optimisation and mechanical properties development, Mater. Des. 65 (2015) 417–424. https://doi.org/10.1016/j.matdes.2014.09.044.

[94] N. Takata, H. Kodaira, K. Sekizawa, A. Suzuki, M. Kobashi, Change in microstructure of selectively laser melted AlSi10Mg alloy with heat treatments, Mater. Sci. Eng. A. 704 (2017) 218–228. https://doi.org/10.1016/j.msea.2017.08.029.

[95] N. Takata, H. Kodaira, K. Sekizawa, A. Suzuki, M. Kobashi, Change in microstructure of selectively laser melted AlSi10Mg alloy with heat treatments, Mater. Sci. Eng. A. 704 (2017) 218–228. https://doi.org/10.1016/j.msea.2017.08.029.

[96] J. Zhang, Y. Gao, C. Yang, P. Zhang, J. Kuang, Microalloying Al alloys with Sc : a review, Rare Met. 39 (2020) 636–650. https://doi.org/10.1007/s12598-020-01433-1.

[97] A.B. Spierings, K. Dawson, T. Heeling, P.J. Uggowitzer, R. Schäublin, F. Palm, K. Wegener, Microstructural features of Sc- and Zr-modified Al-Mg alloys processed by selective laser melting, Mater. Des. 115 (2017) 52–63. https://doi.org/10.1016/j.matdes.2016.11.040.

[98] A.B. Spierings, K. Dawson, P. Dumitraschkewitz, S. Pogatscher, K. Wegener, Microstructure characterization of SLM-processed Al-Mg-Sc-Zr alloy in the heat treated and HIPed condition, Addit. Manuf. 20 (2018) 173–181. https://doi.org/10.1016/j.addma.2017.12.011.

[99] Q. Jia, F. Zhang, P. Rometsch, J. Li, J. Mata, M. Weyland, L. Bourgeois, M. Sui, X. Wu, Precipitation kinetics, microstructure evolution and mechanical behavior of a developed Al–Mn–Sc alloy fabricated by selective laser melting, Acta Mater. 193 (2020) 239–251. https://doi.org/10.1016/j.actamat.2020.04.015.

[100] Q. Jia, P. Rometsch, P. Kürnsteiner, Q. Chao, A. Huang, M. Weyland, L. Bourgeois, X. Wu, Selective laser melting of a high strength Al-Mn-Sc alloy: Alloy design and strengthening mechanisms, Acta Mater. 171 (2019) 108–118. https://doi.org/10.1016/j.actamat.2019.04.014.

[101] J.A. Glerum, C. Kenel, T. Sun, D.C. Dunand, Synthesis of precipitation-strengthened Al-Sc, Al-Zr and Al-Sc-Zr alloys via selective laser melting of elemental powder blends, Addit. Manuf. 36 (2020) 101461. https://doi.org/10.1016/j.addma.2020.101461.

[102] F. Czerwinski, Cerium in aluminum alloys, J. Mater. Sci. 55 (2020) 24–72. https://doi.org/10.1007/s10853-019-03892-z.

[103] Z.C. Sims, O.R. Rios, D. Weiss, P.E.A. Turchi, A. Perron, J.R.I. Lee, T.T. Li, J.A. Hammons, M. Bagge-Hansen, T.M. Willey, K. An, Y. Chen, A.H. King, S.K. McCall, High performance aluminum–cerium alloys for high-temperature applications, Mater. Horizons. 4 (2017) 1070–1078. https://doi.org/10.1039/C7MH00391A.

[104] Z.C. Sims, D. Weiss, S.K. McCall, M.A. McGuire, R.T. Ott, T. Geer, O. Rios, P.A.E. Turchi, Cerium-Based, Intermetallic-Strengthened Aluminum Casting Alloy: High-Volume Co-product Development, JOM. 68 (2016) 1940–1947. https://doi.org/10.1007/s11837-016-1943-9.

[105] D. Porter A., K. Easterling E., M. Sherif Y., Phase Transformations in Metals and Alloys, 2009.

[106] I.M. Lifshitz, V. V. Slyozov, The Kinetics of Precipitation from Supersaturated Solid Solutions, 19 (1961) 35–50. https://doi.org/10.1016/0022-3697(61)90054-3.

[107] L. Zhou, T. Huynh, S. Park, H. Hyer, A. Mehta, S. Song, Y. Bai, B. McWilliams, K. Cho, Y. Sohn, Laser powder bed fusion of Al–10 wt% Ce alloys: microstructure and tensile property, J. Mater. Sci. 55 (2020) 14611–14625. https://doi.org/10.1007/s10853-020-05037-z.

[108] H.B. Henderson, J.A. Hammons, A.A. Baker, S.K. McCall, T.T. Li, A. Perron, Z.C. Sims, R.T. Ott, F. Meng, M.J. Thompson, D. Weiss, O. Rios, Enhanced thermal coarsening resistance in a nanostructured aluminum-cerium alloy produced by additive manufacturing, Mater. Des. 209 (2021) 109988. https://doi.org/10.1016/j.matdes.2021.109988.

[109] S. Bahl, K. Sisco, Y. Yang, F. Theska, S. Primig, L.F. Allard, R.A. Michi, C. Fancher, B. Stump, R. Dehoff, A. Shyam, A. Plotkowski, Al-Cu-Ce(-Zr) alloys with an exceptional combination of additive processability and mechanical properties, Addit. Manuf. 48 (2021) 102404. https://doi.org/10.1016/j.addma.2021.102404.

[110] S. Bahl, A. Plotkowski, K. Sisco, D.N. Leonard, L.F. Allard, R.A. Michi, J.D. Poplawsky, R. Dehoff, A. Shyam, Elevated temperature ductility dip in an additively manufactured Al-Cu-Ce alloy, Acta Mater. 220 (2021) 117285. https://doi.org/10.1016/j.actamat.2021.117285.

[111] F. Theska, Y. Yang, K.D. Sisco, A. Plotkowski, S. Primig, On the high-temperature stability of the Al8Cu3Ce intermetallic in an additively manufactured Al-Cu-Ce-Zr alloy, Mater. Charact. 191 (2022) 112109. https://doi.org/10.1016/j.matchar.2022.112109.

[112] T. Wu, A. Plotkowski, A. Shyam, D.C. Dunand, Microstructure and creep properties of cast near-eutectic Al–Ce–Ni alloys, Mater. Sci. Eng. A. 833 (2022) 142551. https://doi.org/10.1016/j.msea.2021.142551.

[113] R.A. Michi, K. Sisco, S. Bahl, Y. Yang, J.D. Poplawsky, L.F. Allard, R.R. Dehoff, A. Plotkowski, A. Shyam, A creep-resistant additively manufactured Al-Ce-Ni-Mn alloy, Acta Mater. 227 (2022) 117699. https://doi.org/10.1016/j.actamat.2022.117699.

[114] J. Bi, Z. Lei, Y. Chen, X. Chen, Z. Tian, N. Lu, X. Qin, J. Liang, Microstructure, tensile properties and thermal stability of AlMgSiScZr alloy printed by laser powder bed fusion, J. Mater. Sci. Technol. 69 (2021) 200–211. https://doi.org/10.1016/j.jmst.2020.08.033.

[115] R.A. Michi, K. Sisco, S. Bahl, L.F. Allard, K.B. Wagner, J.D. Poplawsky, D.N. Leonard, R.R. Dehoff, A. Plotkowski, A. Shyam, Microstructural evolution and strengthening mechanisms in a heat-treated additively manufactured Al–Cu–Mn–Zr alloy, Mater. Sci. Eng. A. 840 (2022) 142928. https://doi.org/10.1016/j.msea.2022.142928.

[116] X. Hu, S. Bahl, A. Shyam, A. Plotkowski, B. Milligan, L. Allard, J.A. Haynes, Y. Ren, A. Chuang, Repurposing the θ (Al2Cu) phase to simultaneously increase the strength and ductility of an additively manufactured Al–Cu alloy, Mater. Sci. Eng. A. 850 (2022) 143511. https://doi.org/10.1016/j.msea.2022.143511.

[117] T.C. Lin, C. Cao, M. Sokoluk, L. Jiang, X. Wang, J.M. Schoenung, E.J. Lavernia, X. Li, Aluminum with dispersed nanoparticles by laser additive manufacturing, Nat. Commun. 10 (2019) 1–9. https://doi.org/10.1038/s41467-019-12047-2.

[118] D. Rosenthal, Mathematical Theory of Heat Distribution During Welding and Cutting, Weld. J. 20 (1941) 220–234.

[119] A. Plotkowski, M.M. Kirka, S.S. Babu, Verification and validation of a rapid heat transfer calculation methodology for transient melt pool solidification conditions in powder bed metal additive manufacturing, Addit. Manuf. 18 (2017) 256–268. https://doi.org/10.1016/j.addma.2017.10.017.

[120] O. Grong, Metallurgical modelling of welding, 34 (1995) 289. https://doi.org/10.1016/1044-5803(95)80084-0.

[121] M.F.A. J. C. Ion, K. E. Easterling, A Second Report on Diagrams of Microstructure and Hardness for heat-affected zones, Acta Met. 32 (1984) 1949–1962.

[122] H.L. Wei, T. Mukherjee, W. Zhang, J.S. Zuback, G.L. Knapp, A. De, T. DebRoy, Mechanistic models for additive manufacturing of metallic components, Prog. Mater. Sci. 116 (2021) 100703. https://doi.org/10.1016/j.pmatsci.2020.100703.

[123] N. Raghavan, R. Dehoff, S. Pannala, S. Simunovic, M. Kirka, J. Turner, N. Carlson, S.S. Babu, Numerical modeling of heat-transfer and the influence of process parameters on tailoring the grain morphology of IN718 in electron beam additive manufacturing, Acta Mater. 112 (2016). https://doi.org/10.1016/j.actamat.2016.03.063.

[124] T. Mukherjee, H.L. Wei, A. De, T. DebRoy, N. Raghavan, R. Dehoff, S. Pannala, S. Simunovic, M. Kirka, J. Turner, N. Carlson, S.S. Babu, Heat and fluid flow in additive manufacturing – Part II: Powder bed fusion of stainless steel, and titanium, nickel and aluminum base alloys, Acta Mater. 112 (2018) 303–314. https://doi.org/10.1016/j.commatsci.2018.04.027.

[125] J.A. Dantzig, M. Rappaz, Solidification, 2nd Editio, EPFL Press, 2016.

[126] B. Stump, A. Plotkowski, An adaptive integration scheme for heat conduction in additive manufacturing, Appl. Math. Model. 75 (2019) 787–805. https://doi.org/10.1016/j.apm.2019.07.008.

[127] B. Stump, A. Plotkowski, Spatiotemporal parallelization of an analytical heat conduction model for additive manufacturing via a hybrid OpenMP + MPI approach, Comput. Mater. Sci. 184 (2020) 109861. https://doi.org/10.1016/j.commatsci.2020.109861.

[128] T. Mukherjee, H.L. Wei, A. De, T. DebRoy, Heat and fluid flow in additive manufacturing – Part II: Powder bed fusion of stainless steel, and titanium, nickel and aluminum base alloys, Comput. Mater. Sci. 150 (2018) 369–380. https://doi.org/10.1016/j.commatsci.2018.04.027.

[129] L. Parietti, K. Lam, L. Parietti, K. Lam, Los Alamos Validation of a Multi-Physics Software Package for Simulations of Pulsed Laser Welding at Los Alamos National Laboratory Validation of a Multi-Physics Software Package for Simulations of Pulsed Laser Welding at Los Alamos National Laboratory, 836 (n.d.). http://lucie.ericandlucie.com/Resume/Reports/Valid of Multi-Physics Software for Simulations of Pulsed Laser Welding at LANL (LA-UR-06-7622).pdf.

[130] P. Mohammadpour, A. Plotkowski, A.B. Phillion, Revisiting Solidification Microstructure Selection Maps in the Frame of Additive Manufacturing, Addit. Manuf. 31 (2020) 100936. https://doi.org/10.1016/j.addma.2019.100936.

[131] D.M. Herlach, Non-equilibrium solidification of undercooled metallic melts, Metals (Basel). 4 (2014) 196–234. https://doi.org/10.3390/met4020196.

[132] M.J. Aziz, Model for solute redistribution during rapid solidification, J. Appl. Phys. 53 (1982) 1158–1168. https://doi.org/10.1063/1.329867.

[133] A. Suzuki, H. Kimura, Nucleation of Theta' Precipitates in an Al-4% Cu Alloy, Mater. Sci. Eng. A. 6 (1970) 384–390.

[134] B. Noble, Theta-prime precipitation alloys* in aluminium-copper-cadmium, (1968).

[135] M.E. Fine, Precipitation hardening of aluminum alloys, Metall. Trans. A. 6 (1975) 625–630. https://doi.org/10.1007/BF02672283.

[136] V.D. Scott, S. Kerry, R.L. Trumper, S. Kerry, R.L.T. Nucleation, R.L. Trumper, Nucleation and growth of precipitates in Al – Cu – Mg – Ag alloys Nucleation and grovvth of precipitates in, Mater. Sci. Technol. 0836 (2013) 827–835. https://doi.org/10.1179/mst.1987.3.10.827.

[137] F. Liu, F. Sommer, C. Bos, E.J. Mittemeijer, Analysis of solid state phase transformation kinetics: Models and recipes, Int. Mater. Rev. 52 (2007) 193–212. https://doi.org/10.1179/174328007X160308.

[138] J.W. Christian, S.L. Chan, The Theory of Transformations in Metals and Alloys : an Advanced Textbook in Physical Metallurgy. , 3rd ed., lsevier Science & Technology, 2002.

[139] K.C. Russel, NUCLEATION IN SOLIDS : THE INDUCTION AND STEADY STATE EFFECTS, Adv. Colloid Interface Sci. 13 (1980) 205–318.

[140] W.E. Lange, M. Enomoto, H.I. Aaronson, The Kinetics of Ferrite Nucleation at Austenite Grain Boundaries in Fe-C Alloys, I (1988).

[141] H.I. Aaronson, H.I. Aaronson, M. Tech-, Generalization of the Nucleus Shape- Dependent Parameters in the Nucleation Rate Equation, (1978) 9–10.

[142] C. Zener, Theory of growth of spherical precipitates from solid solution, J. Appl. Phys. 20 (1949) 950–953. https://doi.org/10.1063/1.1698258.

[143] H.B.. Aaron, A.D. Brailsford, Growth of Grain-Boundary Precipitates, J. Appl. Phys. 40 (1969).

[144] B. Aaron, H.I. Aaronson, Growth of Grain Boundary Precipitates in Al-4% Cu by Interfacial Diffusion, 16 (1968).

[145] S. Nagakura, T. Suzuki, K. Michiko, Structure of Precipitated Particles at the Third Stage of Tempering of Matensitic Iron-Carbon Steel Studied by High Resolution Electron Microscopy, 22 (1981).

[146] M. Avrami, Kinetics of phase change. I: General theory, J. Chem. Phys. 7 (1939) 1103–1112. https://doi.org/10.1063/1.1750380.

[147] M. Avrami, Kinetics of phase change. II Transformation-time relations for random distribution of nuclei, J. Chem. Phys. 8 (1940) 212–224. https://doi.org/10.1063/1.1750631.

[148] M. Avrami, Granulation, phase change, and microstructure kinetics of phase change. III, J. Chem. Phys. 9 (1941) 177–184. https://doi.org/10.1063/1.1750872.

[149] J.D. Robson, H.K.D.H. Bhadeshia, Kinetics of Precipitatin in Power Plant Steels, 20 (1997).

[150] Y. Yang, S. Bahl, K. Sisco, M. Lance, D. Shin, A. Shyam, A. Plotkowski, R.R. Dehoff, Primary solidification of ternary compounds in Al-rich Al–Ce–Mn alloys, J. Alloys Compd. 844 (2020) 156048. https://doi.org/10.1016/j.jallcom.2020.156048.

[151] A. Plotkowski, K. Sisco, S. Bahl, A. Shyam, Y. Yang, L. Allard, P. Nandwana, A.M. Rossy, R.R. Dehoff, Microstructure and properties of a high temperature Al–Ce–Mn alloy produced by additive manufacturing, Acta Mater. 196 (2020). https://doi.org/10.1016/j.actamat.2020.07.014.

[152] F.G. Coury, C.S. Kiminami, W.J. Botta, C. Bolfarini, M.J. Kaufman, Design and production of Al-Mn-Ce alloys with tailored properties, Mater. Des. 110 (2016) 436–448. https://doi.org/10.1016/j.matdes.2016.08.008.

[153] F.G. Coury, W.J. Botta, C. Bolfarini, C.S. Kiminami, M.J. Kaufman, Reassessment of the effects of Ce on quasicrystal formation and microstructural evolution in rapidly solidified Al–Mn alloys, Acta Mater. 98 (2015) 221–228. https://doi.org/10.1016/J.ACTAMAT.2015.07.046.

[154] F.G. Coury, E.L. Pires, W. Wolf, F.H. Paes de Almeida, A.L. Costa e Silva, W.J. Botta, C.S. Kiminami, M.J. Kaufman, Insight into the complex ternary phase behavior in Al-Mn-Ce alloys, J. Alloys Compd. 727 (2017) 460–468. https://doi.org/10.1016/j.jallcom.2017.08.136.

[155] A.. Inoue, M.. Watanabe, H.M.. Kimura, F.. Takahaski, A.. Nagata, T.. Masumoto, High Mechanical Strength of Quasicrystalline Phase Surrounded by fcc-Al Phase in Rapidly Solidified Al–Mn–Ce Alloys, Met Trans. 33 (1992) 723–729. https://doi.org/https://doi.org/10.2320/matertrans1989.33.723.

[156] A. Inoue, H. Kimura, High-strength aluminum alloys containing nanoquasicrystalline particles, Mater. Sci. Eng. A. 286 (2000) 1–10. https://doi.org/10.1016/S0921-5093(00)00656-0.

[157] M.A. Gordillo, I. Cernatescu, T.T. Aindow, T.J. Watson, M. Aindow, Phase stability in a powder-processed Al–Mn–Ce alloy, J. Mater. Sci. 49 (2014) 3742–3754. https://doi.org/10.1007/s10853-014-8086-6.

[158] P.M. Smith, M.J. Aziz, Solute trapping in aluminum alloys, Acta Metall. Mater. 42 (1994) 3515–3525. https://doi.org/10.1016/0956-7151(94)90483-9.

[159] J. Wang, B.H. Toby, P.L. Lee, L. Ribaud, S.M. Antao, C. Kurtz, M. Ramanathan, R.B. Von Dreele, M.A. Beno, A dedicated powder diffraction beamline at the Advanced Photon Source: Commissioning and early operational results, Rev. Sci. Instrum. 79 (2008) 1–7. https://doi.org/10.1063/1.2969260.

[160] B.H. Toby, R.B. Von Dreele, GSAS-II: The genesis of a modern open-source all purpose crystallography software package, J. Appl. Crystallogr. 46 (2013) 544–549. https://doi.org/10.1107/S0021889813003531.

[161] V.M.T. Thiede, W. Jeitschko, Preparation and Crystal Structure of the Intermetallics La4Mo7Al51and La4W7Al51, J. Solid State Chem. 143 (1999) 198–201. https://doi.org/10.1006/jssc.1999.8076.

[162] M. Hellenbrandt, The inorganic crystal structure database (ICSD) - Present and future, Crystallogr. Rev. 10 (2004) 17–22. https://doi.org/10.1080/08893110410001664882.

[163] N. Ünlü, Preparation of high quality Al TEM specimens via a double-jet electropolishing technique, Mater. Charact. 59 (2008) 547–553. https://doi.org/10.1016/j.matchar.2007.04.003.

[164] S. Roy, L.F. Allard, A. Rodriguez, T.R. Watkins, A. Shyam, Comparative Evaluation of Cast Aluminum Alloys for Automotive Cylinder Heads: Part I—Microstructure Evolution, Metall. Mater. Trans. A Phys. Metall. Mater. Sci. 48 (2017) 2529–2542. https://doi.org/10.1007/s11661-017-3985-1.

[165] K. Thompson, D. Lawrence, D.J. Larson, J.D. Olson, T.F. Kelly, B. Gorman, In situ site-specific specimen preparation for atom probe tomography, Ultramicroscopy. 107 (2007) 131–139. https://doi.org/10.1016/j.ultramic.2006.06.008.

[166] M.K. Miller, Atom probe tomography: analysis at the atomic level, 2000. http://books.google.fr/books?id=uxgx5hRGXywC.

[167] W. Cao, S.L. Chen, F. Zhang, K. Wu, Y. Yang, Y.A. Chang, R. Schmid-Fetzer, W.A. Oates, PANDAT software with PanEngine, PanOptimizer and PanPrecipitation for multi-component phase diagram calculation and materials property simulation, Calphad Comput. Coupling Phase Diagrams Thermochem. 33 (2009) 328–342. https://doi.org/10.1016/j.calphad.2008.08.004.

[168] H.I. Aaronson, K.R. Kinsman, K.C. Russell, The volume free energy change associated with precipitate nucleation, Scr. Metall. 4 (1970) 101–106. https://doi.org/10.1016/0036-9748(70)90172-9.

[169] V.A. Lubarda, On the effective lattice parameter of binary alloys, Mech. Mater. 35 (2003) 53–68. https://doi.org/10.1016/S0167-6636(02)00196-5.

[170] R. Kilaas, MacTempas a Program for Simulating High Resolution TEM Images and Diffraction Patterns., (n.d.). http://www.totalresolution.com.

[171] Y. Du, Y.A. Chang, B. Huang, W. Gong, Z. Jin, H. Xu, Z. Yuan, Y. Liu, Y. He, F.Y. Xie, Diffusion coefficients of some solutes in fcc and liquid Al: Critical evaluation and correlation, Mater. Sci. Eng. A. 363 (2003) 140–151. https://doi.org/10.1016/S0921-5093(03)00624-5.

[172] C. Weiping, Diffusion of cerium in the aluminium lattice, J. Mater. Sci. Lett. 16 (1997) 1824–1826. https://doi.org/10.1023/A:1018572803223.

[173] P. Virtanen, R. Gommers, T.E. Oliphant, M. Haberland, T. Reddy, D. Cournapeau, E. Burovski, P. Peterson, W. Weckesser, J. Bright, S.J. van der Walt, M. Brett, J. Wilson, K.J. Millman, N. Mayorov, A.R.J. Nelson, E. Jones, R. Kern, E. Larson, C.J. Carey, İ. Polat, Y. Feng, E.W. Moore, J. VanderPlas, D. Laxalde, J. Perktold, R. Cimrman, I. Henriksen, E.A. Quintero, C.R. Harris, A.M. Archibald, A.H. Ribeiro, F. Pedregosa, P. van Mulbregt, A. Vijaykumar, A. Pietro Bardelli, A. Rothberg, A. Hilboll, A. Kloeckner, A. Scopatz, A. Lee, A. Rokem, C.N. Woods, C. Fulton, C. Masson, C. Häggström, C. Fitzgerald, D.A. Nicholson, D.R. Hagen, D. V. Pasechnik, E. Olivetti, E. Martin, E. Wieser, F. Silva, F. Lenders, F. Wilhelm, G. Young, G.A. Price, G.L. Ingold, G.E. Allen, G.R. Lee, H. Audren, I. Probst, J.P. Dietrich, J. Silterra, J.T. Webber, J. Slavič, J. Nothman, J. Buchner, J. Kulick, J.L. Schönberger, J.V. de Miranda Cardoso, J. Reimer, J. Harrington, J.L.C. Rodríguez, J. Nunez-Iglesias, J. Kuczynski, K. Tritz, M. Thoma, M. Newville, M. Kümmerer, M. Bolingbroke, M. Tartre, M. Pak, N.J. Smith, N. Nowaczyk, N. Shebanov, O. Pavlyk, P.A. Brodtkorb, P. Lee, R.T. McGibbon, R. Feldbauer, S. Lewis, S. Tygier, S. Sievert, S. Vigna, S. Peterson, S. More, T. Pudlik, T. Oshima, T.J. Pingel, T.P. Robitaille, T. Spura, T.R. Jones, T. Cera, T. Leslie, T. Zito, T. Krauss, U. Upadhyay, Y.O. Halchenko, Y. Vázquez-Baeza, SciPy 1.0: fundamental algorithms for scientific computing in Python, Nat. Methods. 17 (2020) 261–272. https://doi.org/10.1038/s41592-019-0686-2.

[174] Z. Song, O. V Magdysyuk, T. Sparks, Y. Chiu, B. Cai, Revealing growth mechanisms of faceted Al 2 Cu intermetallic compounds via high-speed Synchrotron X-ray tomography, Acta Mater. 231 (2022) 117903. https://doi.org/10.1016/j.actamat.2022.117903.

[175] T.M. Pollock, A.J. Clarke, S.S. Babu, Design and Tailoring of Alloys for Additive Manufacturing, Metall. Mater. Trans. A. 51 (n.d.) 6000–6019. https://doi.org/10.1007/s11661-020-06009-3.

[176] S. Liu, Y. Zhou, X. Xing, J. Wang, X. Ren, Q. Yang, Growth characteristics of primary M7C3 carbide in hypereutectic Fe-Cr-C alloy, Sci. Rep. 6 (2016) 1–8. https://doi.org/10.1038/srep32941.

[177] D.W. Deng, H.F. Xia, Y.L. Ge, Influence of welding currents on microstructure and microhardness of Ni45 alloy reinforced with spherical tungsten carbides (40 mass%) by plasma transferred arc welding, Mater. Trans. 54 (2013) 2144–2150. https://doi.org/10.2320/matertrans.M2013263.

[178] J.D. Hunt, P. Road, THE MEASUREMENT OF SOLID-LIQUID SURFACE ENERGIES IN THE Al-Cu, Al-Si AND Pb-Sn SYSTEMS, Acta Metall. 33 (1985) 1651–1672.

[179] I. Ansara, A.T. Dinsdale, M.H. Rand, Thermochemical database for light metal alloys, 1998.

[180] J.O. Andersson, T. Helander, L. Höglund, P. Shi, B. Sundman, Thermo-Calc & DICTRA, computational tools for materials science, Calphad Comput. Coupling Phase Diagrams Thermochem. 26 (2002) 273–312. https://doi.org/10.1016/S0364-5916(02)00037-8.

[181] R. Trivedi, W. Kurz, Theory of Microstructural Development During Rapid Solidification., Acta Metall. 34 (1986) 260–267. https://doi.org/10.1007/978-94-009-4456-5_24.

[182] A.T. Dinsdale, SGTE data for elements, Calphad. 15 (1991) 317–425.

[183] D. Turnbull, Formation of crystal nuclei in liquid metals, J. Appl. Phys. 21 (1950) 1022–1028. https://doi.org/10.1063/1.1699435.

[184] H. Hartmann, P.K. Galenko, D. Holland-Moritz, Nonequilibrium solidification in undercooled Ti45Al55 melts, 073509 (2007). https://doi.org/10.1063/1.2903920.

[185] N.S. Stoloff, V.K. Sikka, Physical Metallurgy and Processing of Intermetallic Compounds, Chapman and Hall, 1996.

[186] R.W. Cahn, P.A. Siemers, J.E. Geiger, P. Bardhan, The order-disorder transformation in Ni3Al and Ni3AlFe alloys-I. Determination of the transition temperatures and their relation to ductility, Acta Metall. 35 (1987) 2737–2751. https://doi.org/10.1016/0001-6160(87)90273-2.

[187] R.W. Cahn, P.A. Siemers, E.L. Hall, The Order-Disorder Transformation in Ni3Al and Ni3Al-Fe Alloys-II. Phase transfromations and microstructures, Acta Metall. 35 (1987).

[188] T. Suzuki, Y. Oya, S. Ochiai, MECHANICAL BEHAVIOR OF NONSTOICHIOMETRIC COMPOUNDS Ni3Si, Ni3Ge, AND Fe3Ga., Metall. Trans. A, Phys. Metall. Mater. Sci. 15 A (1984) 173–181. https://doi.org/10.1007/BF02644399.

[189] C. Zhang, P. Peng, H. Lv, H. Gao, Y. Wang, J. Wang, B. Sun, Orientation relationships and interface structure between Al11Ce3 and Al in Al–Ce eutectic, J. Mater. Res. Technol. 18 (2022) 693–704. https://doi.org/10.1016/j.jmrt.2022.02.132.

[190] S. Niemann, W. Jeitschko, Ternary Aluminides AT2Al20 (A = Rare Earth Elements and Uranium; T = Ti, Nb, Ta, Mo, and W) with CeCr2Al20-Type Structure, J. Solid State Chem. 114 (1995) 337–341. https://doi.org/10.1006/JSSC.1995.1052.

[191] J. Schindelin, I. Arganda-Carreras, E. Frise, V. Kaynig, M. Longair, T. Pietzsch, S. Preibisch, C. Rueden, S. Saalfeld, B. Schmid, J.Y. Tinevez, D.J. White, V. Hartenstein, K. Eliceiri, P. Tomancak, A. Cardona, Fiji: An open-source platform for biological-image analysis, Nat. Methods. 9 (2012) 676–682. https://doi.org/10.1038/nmeth.2019.

Appendix

Appendix A Atom Probe Peak Identification for AM Al-Ce-Mn Samples

The atom probe data observed in Figure 3.4, can be viewed as mass/charge spectrum. In Figure A.1, the mass/charge spectrum is shown, demonstrating the individual peaks for each element.

The spectrum shows that the Al, Mn, and Ce peaks are well distinguishable. Additionally, contamination from an imperfect vacuum is shown in the form of O, HO, H_2O, AlH_2, CO_2, and HCO_2. There is additional contamination from the Ga used to make the atom probe tip.

Appendix B AM Al-10Ce-8Mn (wt.%) X-ray Diffraction Additional Analysis

Figure A.2 shows the prominent (>15% normalized intensity) XRD reflections for the FCC Al, $Al_{20}Mn_2Ce$, and $Al_{11}Ce_3$ phases identified in the as fabricated sample.

In Figure A.3 shows the prominent XRD reflections (>15% normalized intensity for each phase) for the FCC Al, $Al_{11}Ce_3$, $Al_{20}Mn_2Ce$, Al_6Mn, $Al_{12}Mn$, $Al_{51}Mn_7Ce_4$ phases identified in the sample heat treated at 400 °C 1000 h.

Appendix C The Nucleation of $Al_{11}Ce_3$ in the AM Al-Ce-Mn Samples

There may be questioning as to if additional $Al_{11}Ce_3$ nucleates as a function of heat treatment in the AM Al-Ce-Mn samples. In Figure A4, it demonstrates that the number density of the $Al_{11}Ce_3$ is increasing as a function of thermal exposure at 400°C in the material.

Appendix D Quantification of Phases Using SEM in AM Al-10Ce-8Mn (wt.%)

The limitations of SEM BSE imaging force were considered while responding to this comment. First, the $Al_{12}Mn$ and Al_6Mn phases are treated as a similar Al-Mn binary because of the similarity in contrast observed through SEM imaging. Second, this analysis was used to understand the initial and final heat treatment states. The intermediate states usually contain six different phases that are largely intermixed. As a result, it is difficult to distinguish each one of them due to their fine size and similar BSE contrast gradients. The lack of distinguishable BSE contrast is attributed to the interaction volume of electron beam interaction with materials.

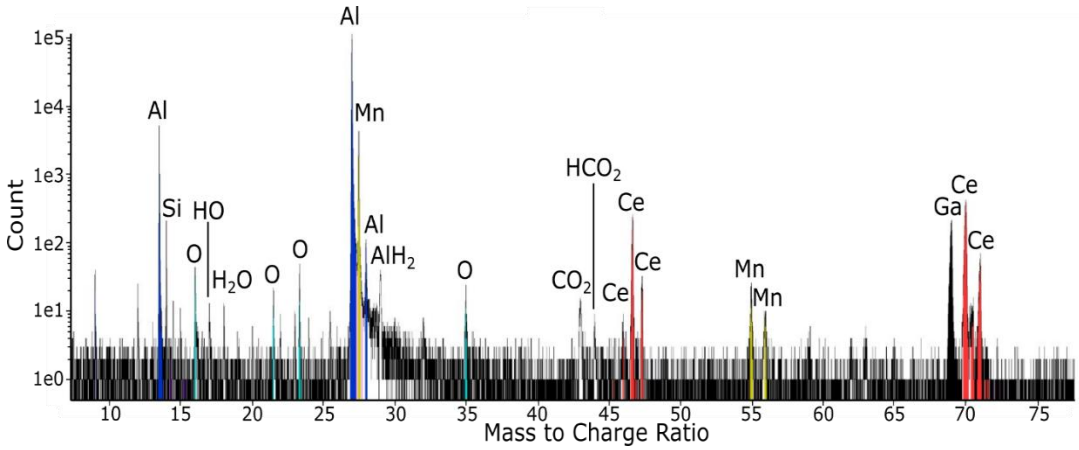

Figure A.1 Appendix Figure Mass to Charge Ratio observed in APT data.

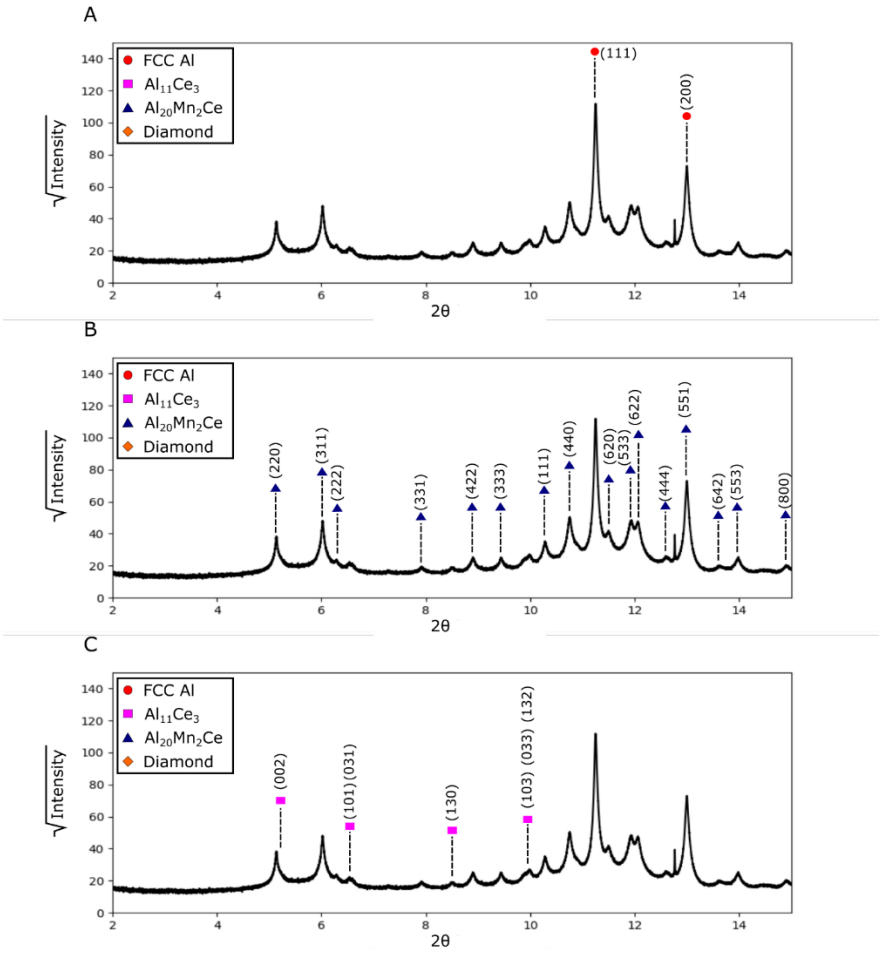

Figure A.2 Prominent reflections of each phase identified in the Al-Ce-Mn system A) FCC Al reflections, B) $Al_{20}Mn_2Ce$ reflections and C) $Al_{11}Ce_3$ reflections.

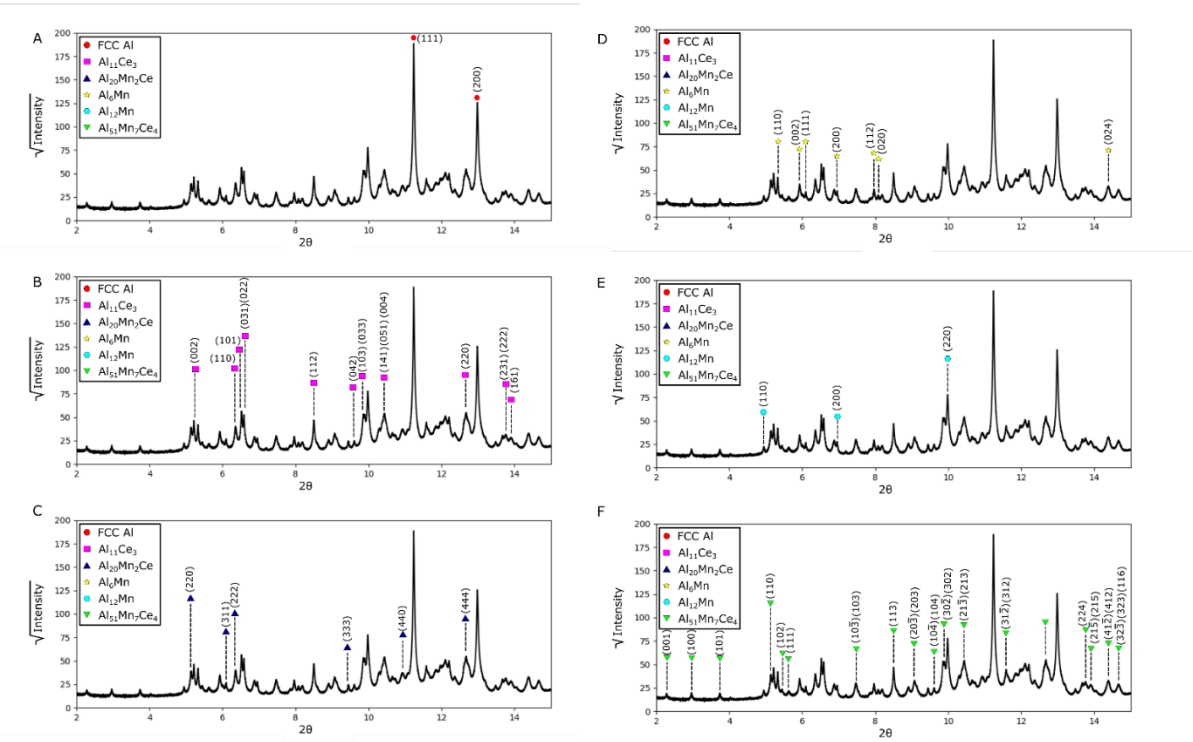

Figure A.3 Prominent reflections of each phase identified in the produced alloy after heat treatment at 400 °C for 1000 h. A) FCC Al reflections, B) $Al_{11}Ce_3$ reflections, C) $Al_{20}Mn_2Ce$ reflections D) Al_6Mn reflections, E) $Al_{12}Mn$ reflections, and F) $Al_{51}Mn_7Ce_4$ reflections.

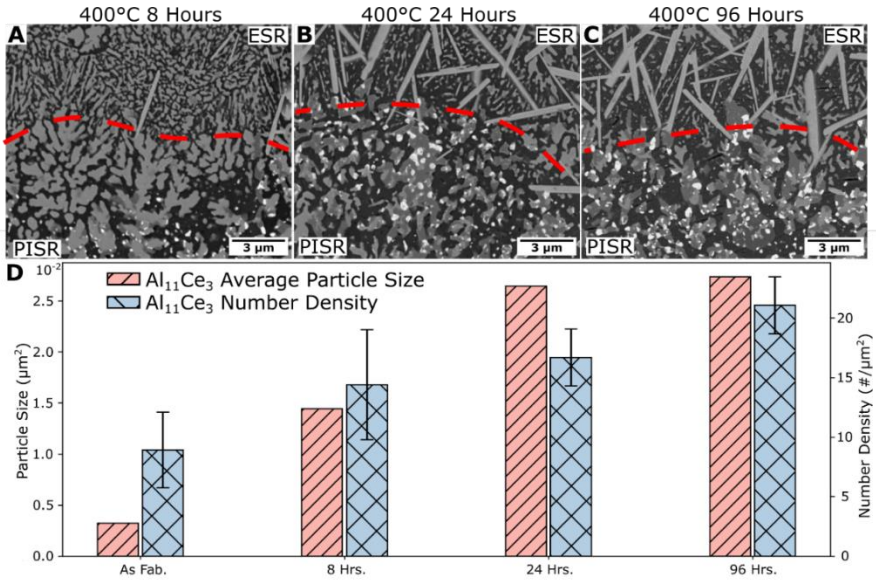

Figure A.4 Prominent reflections of each phase identified in the produced alloy after heat treatment at 400 °C for 1000 h. A) FCC Al reflections, B) $Al_{11}Ce_3$ reflections, C) $Al_{20}Mn_2Ce$ reflections D) Al_6Mn reflections, E) $Al_{12}Mn$ reflections, and F) $Al_{51}Mn_7Ce_4$ reflections.

While the above issues cannot not be eliminated by just looking at the initial and final states, the accuracy of analysis is increased by ignoring the more complex areas in the image analysis routine as described below. All of the image processing steps were performed with the FIJI software [191].

Initially looking at the as-fabricated case, there are two ways to determine phases. First, simple step binarization. The step binarization is taken in order to approximate the fraction of three phases, FCC Al, $Al_{11}Ce_3$ and $Al_{20}Mn_2Ce$. The "step" binarization is basically binning the as-fabricated case into three samples: FCC Al from 0 to 110, $Al_{20}Mn_2Ce$ from 125 to 150, and $Al_{11}Ce_3$ from 150 to 255.

Second, we investigated the 400°C 1000-hour sample. If we use a simple step binarization, we noticed a problem in delineating the phases. The problem is largely because of the number of phases identified have overlap in contrast because of the limitations of the BSE detectors used (see below)

The overlap, specifically seen in Figure A5B raises the question related to validity of the binarization methodology.

The results of processing A8, and a comparable image (being the magnification and pixel size are the same) in the as fabricated state are shown in Table A1.

Therefore, two different approaches are utilized to remove false positives. Initially a step binarization is applied in order to separate the bulk of each phase. In the 400°C 1000-hour sample, four distinguishable contrasts are present, which are attributed to FCC Al, Al-Mn Binaries, $Al_{51}Mn_7Ce_4$, and $Al_{11}Ce_3$. These phases are separated using the intensity value 0-80, 80-150, 150-225, and 225-255 respectively. These values were determined manually in order to achieve the least amount of ghosting, while maintaining the bulk of each phase.

Additional processing is performed on the Al-Mn binary phases and $Al_{51}Mn_7Ce_4$ phase. The Al-Mn binary phases had an additional distance map filter implemented to remove "thin" lines. A distance map measures the distance of a white pixel to a black pixel. Then, a threshold is set for distance to remove the thin lines, in this case 6 pixels.

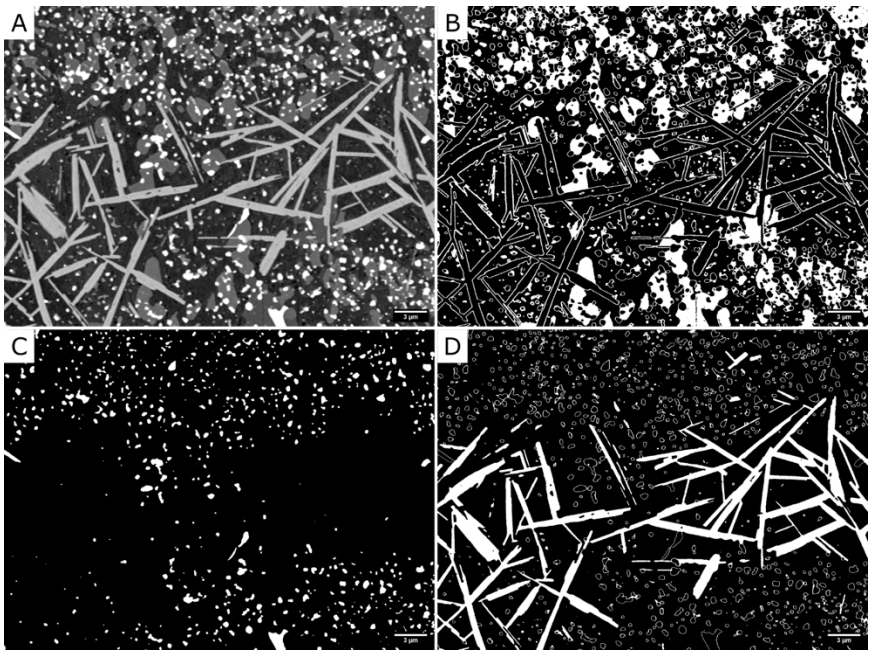

Figure A5 A) Demonstrates two microstructure regions of the MPB and ES. B) is a binarized image focused on extracting the Al-Mn binaries. C) is a binarized image focused on extracting the $Al_{11}Ce_3$, and D) is a binary image focused on extracting $Al_{51}Mn_7Ce_4$.

Table A1 Quantified Phase Fraction from SEM.

Phase	As Fabricated	400 C 1000 Hours (Lower Bound)	400 C 1000 Hours (Upper Bound)
FCC Al	53.7	48.54	58.87
$Al_{11}Ce_3$	1.54	5.39	6.54
$Al_{20}Mn_2Ce$	44.74	N/a	N/a
Al-Mn Binary	N/a	15.60	18.92
$Al_{51}Mn_7Ce_4$	N/a	12.91	15.67

The image has a pixel size of 13.96 nm. The distance filter eliminates most falsely measured data, and some of the accurate data. The data is then dilated to “put back” the pixels eliminated on the edges of the determined phases.

A dilation adds pixels around the edge of white pixels in a binarized image. The dilation method is done with FIJI software. The results of this process can be observed in Figure A6.

For the $Al_{51}Mn_7Ce_4$ a simpler methodology was used because the overestimated pixels are generally detached from the $Al_{51}Mn_7Ce_4$ plates. The image is initially binarized for intensities between 150 and 225. Then, the shape of each particle is analyzed by the circularity and size. The circularity of a particle must be less than 0.25 and the size of a particle must be greater than 0.1 μm^2, which mean the particle needs to be larger than 18 connected pixels. The results of this process can be seen in Figure A7. The processing of each image from Figures A5-A7 were initially processed using A8, and then cropped down to make a more viewable example.

The as-fabricated state is processed without significant difficulty because it is largely composed of two phases, FCC Al and $Al_{20}Mn_2Ce$. It is to note that the $Al_{11}Ce_3$ is small, and has the same issues observed in Figure A5 C, but the overall phase fraction of $Al_{11}Ce_3$ can increase up to a percent depending on what the cutoff is chosen to be. The 400 C 1000 Hour sample has considerably more complexity. By processing the images to remove the unwanted pixels in each segmentation, the result is that about 18 % of the pixels do not have an attributed phase. Therefore, a lower and upper bound is demonstrated from this process. The upper bound is calculated from all possible pixels, and the lower bound is calculated from all identified pixels.

Overall, the image analysis results show reasonable agreement between the X-ray diffraction results. It is to note that FCC is likely overestimated in all cases because it has the highest uncertainty in delineation. In the 400C 1000 Hour sample, the upper bound is very likely the excess observed FCC Al is contributing to the Al-Mn binary phases.

Appendix E Al-Ce-Mn Weld Track 1 mm/s EBSD

The phases were confirmed observed in Figure 4.5 using EBSD as seen in Figure A9. While the existence of FCC Al and $Al_{10}Mn_2Ce$ are very clear, the $Al_{20}Mn_2Ce$ and $Al_{11}Ce_3$ phases are not. The $Al_{11}Ce_3$ difficulty in precise identification is likely because the $Al_{11}Ce_3$ is small.

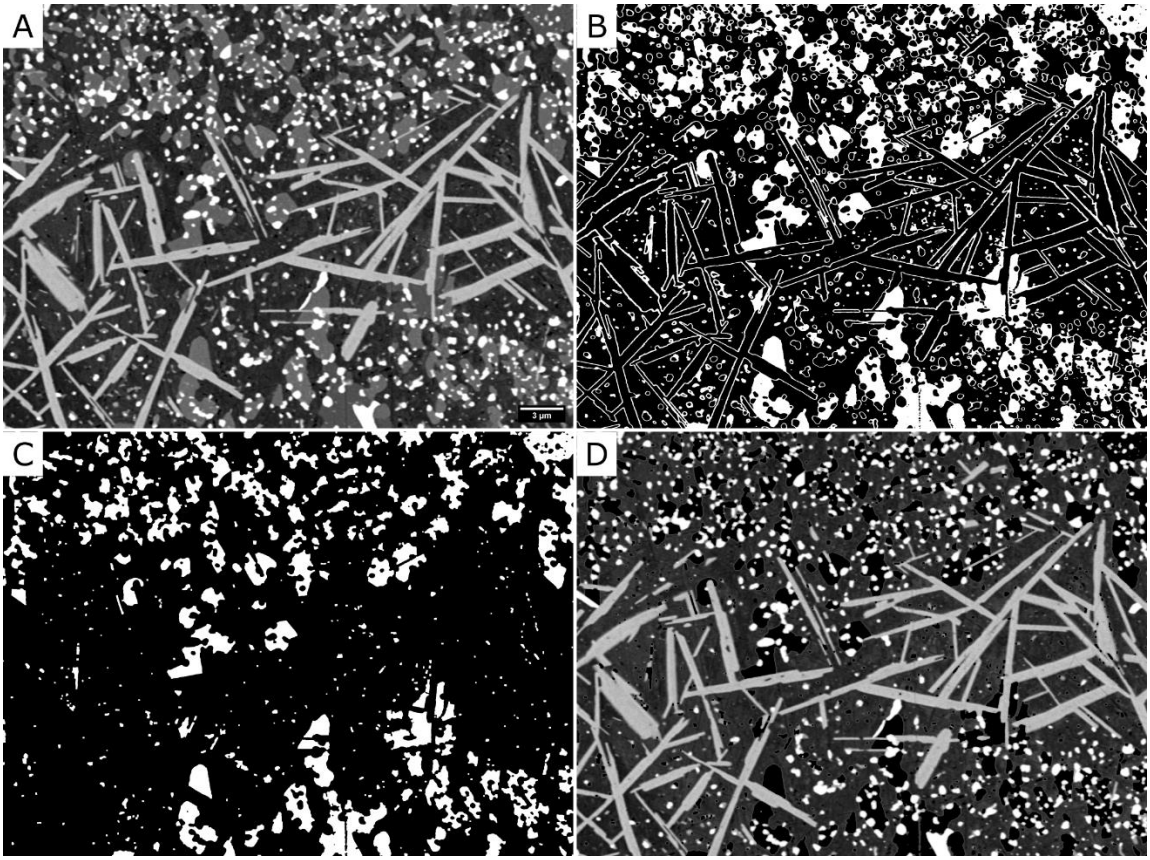

Figure A6 A) demonstrates SEM of the Al-Ce-Mn 400C 1000 Hour microstructure. B) demonstrates a binarized microstructure for the Al-Mn binary that is incorrect because of a halo effect caused by SEM interaction volume. C) is a processed image attempting to remove the edge effects. D) is the initial image minus the Al-Mn phases to demonstrate good matching between the methods.

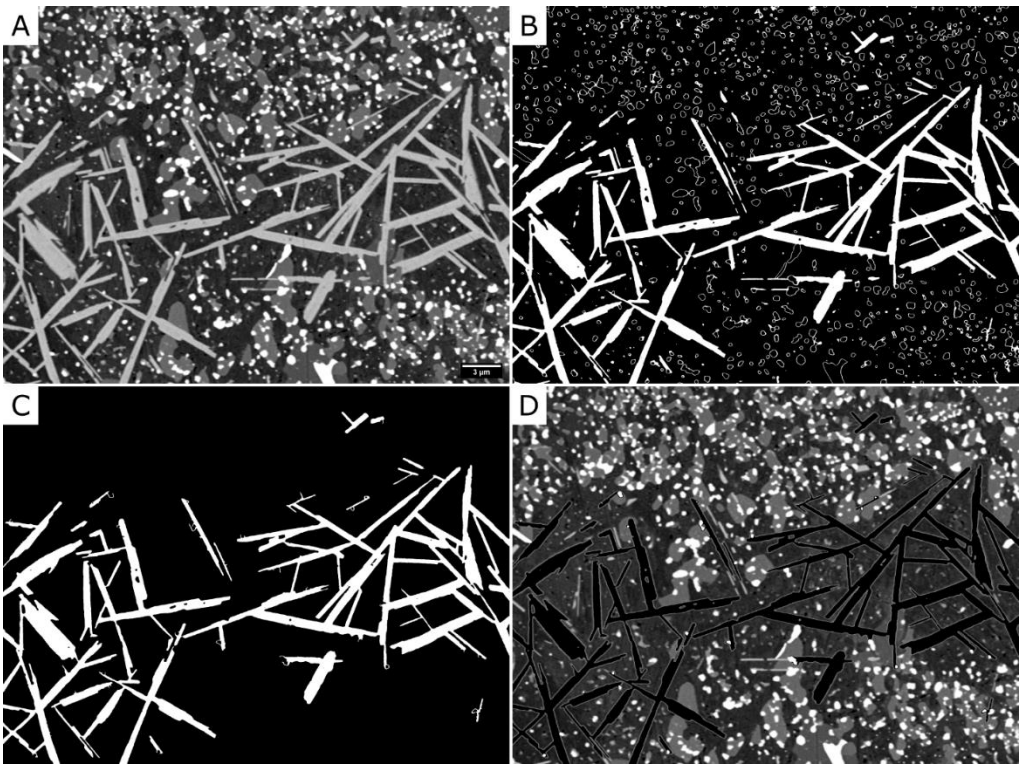

Figure A7 A) demonstrates SEM of the Al-Ce-Mn 400C 1000 Hour microstructure. B) demonstrates the binarization of the $Al_{51}Mn_7Ce_4$ phase. C) demonstrates the image cleaned using the circularity (<0.25) and minimum size (>0.25 um^2) to pull out the $Al_{51}Mn_7Ce_4$ phase. D) is the initial image minus the $Al_{51}Mn_7Ce_4$ phase to show good matching between the methodology.

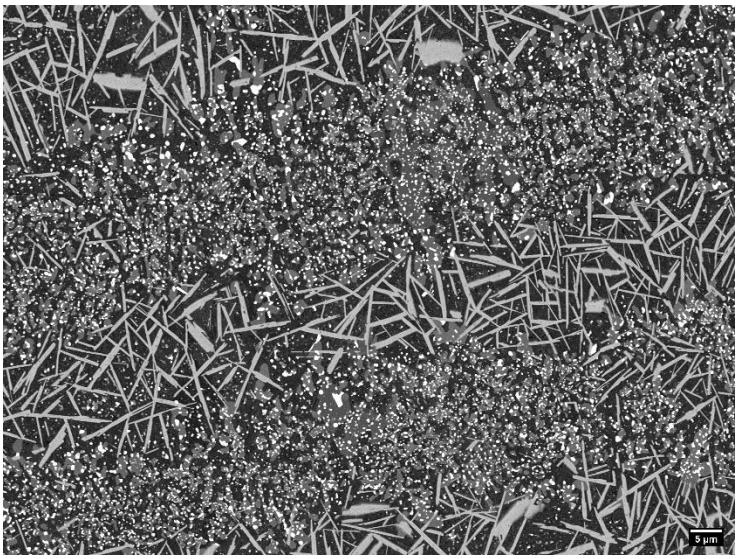

Figure A8 Large Area SEM Image of the Al-10Ce-8Mn system.

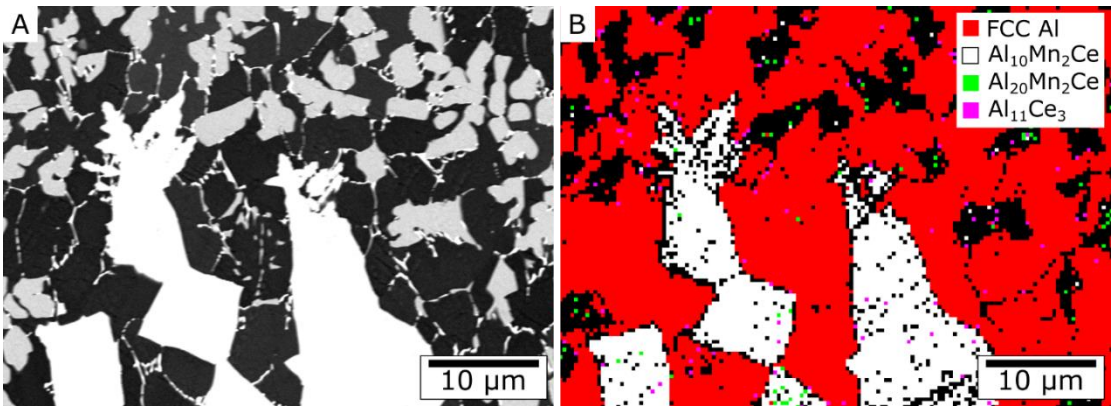

Figure A9 (A) SEM BSE of the MPB region of the 1 mm/s weld track. (B) EBSD Phase Map of the same region showing the phases identified

Table A2 Demonstrates the Normalized Perimeter and Average Particle spacing across multiple weld tracks.

Laser Velocity (mm/s)	Normalized Perimeter $\left(\frac{\mu m}{\mu m^2}\right)$	Average Particle Spacing (μm)
1	2.348	0.993
10	4.158	1.1533
15	4.563	0.9679
23	5.129	0.9516
35	5.141	0.8705
54	5.295	0.7359
83 Primary	6.381	0.5841
83 Eutectic	36.287	0.1448

The $Al_{20}Mn_2Ce$ also has difficulty in detection, although it is unknown why. It does have a small size which likely contributes, but in general it does not give a good enough EBSD pattern to index, excluding unreasonable scan length, such as 5-6 hours for a similar sized region.

Therefore, a smaller region was indexed to confirm $Al_{20}Mn_2Ce$ as seen in Figure A10.

Interestingly as seen in Figure A10B there is a 60-degree misorientation angle across the center of the particle, likely influencing the shape observed.

Appendix F Thermodynamic Descriptions

The thermodynamic descriptions of the phases examined in the current work are listed here. The governing equations adopted from Yang *et al.* [150] used for the current work only assumes binary interaction parameters. The Gibbs energy function for Al, Si, Mn, and Ce were adopted from the STGE Database [182] by Dinsdale *et al.* The Gibbs Free energy for a ternary phase in the Al-Ce-Mn system is described by [179].

$$
\begin{aligned}
G = {} & x_{Al}G_{Al}^{Phase} + x_{Mn}G_{Mn}^{Phase} + x_{Ce}G_{Ce}^{Phase} \\
& + RT(x_{Al}\ln(x_{Al}) + x_{Mn}\ln(x_{Mn}) + x_{Ce}\ln(x_{Ce})) \\
& + x_{Al}x_{Mn}\sum_{i=0} L_{Al,Mn}^{v}\,(x_{Al} - x_{Mn})^{v} + x_{Al}x_{Ce}\sum_{i=0} L_{Al,Ce}^{v}\,(x_{Al} - x_{Ce})^{v} \\
& + x_{Ce}x_{Mn}\sum_{i=0} L_{Ce,Mn}^{v}\,(x_{Ce} - x_{Mn})^{v}
\end{aligned}
\tag{50}
$$

Where the $G_{Al}^{Liq}, G_{Mn}^{Liq}, G_{Ce}^{Liq}$ is described by where T is temperatures described in kelvin:

$$
G_{Al}^{Liq} = \begin{cases} T < 933.6 : 11005.553 - 11.840873T + 7.9401e-20T^{7} + GHSERAL(T) \\ T \geq 933.6 : 10481.974 - 11.252014T + 1.234264e28(\frac{1}{T^{9}}) + GHSERAL(T) \end{cases}
\tag{51}
$$

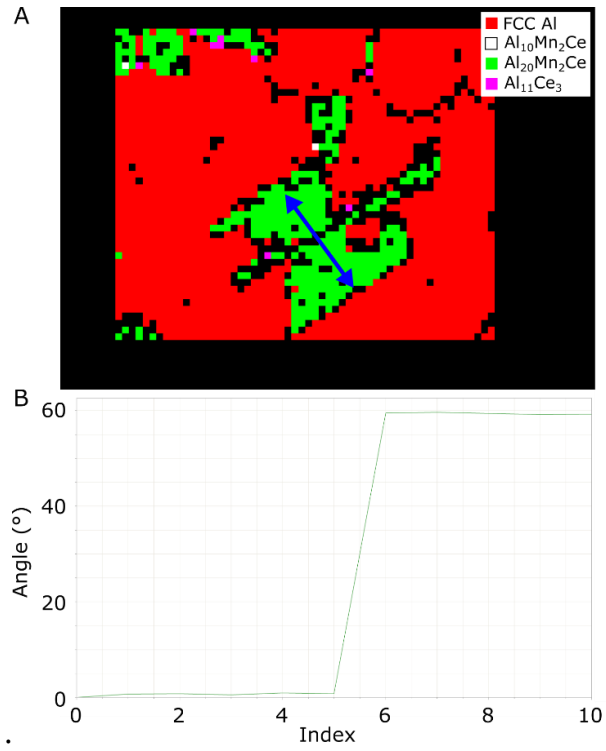

Figure A10 (A) EBSD Phase ID for $Al_{20}Mn_2Ce$, (B) Misorientation angle across $Al_{20}Mn_2Ce$ particle marked by blue arrow in (A)

$$G_{Mn}^{Liq} \quad (52)$$
$$= \begin{cases} T < 1519 : 17859.91 - 12.6208T - 4.41929e-21T^7 + GHSERMN(T) \\ T \geq 1519 : 18739.51 - 13.2288T - 1.656847e30(\frac{1}{T^9}) + GHSERMN(T) \end{cases}$$

$$G_{Ce}^{Liq} \quad (53)$$
$$= \begin{cases} T < 1000 : 4117.865 - 11.423898T - 7.5383948T * LN(T) - .02936407T^2 + \\ 4.827734e-6T^3 - 198834 * (1/T) \\ T \geq 1000 : -6730.605 + 183.023193 * T - 37.6978 * T * LN(T) \end{cases}$$

Where the GHSERAL, GHSERMN, and GHSERCE are defined by Dinsdale et al [182].

$$GHSERAL(T) \quad (54)$$
$$= \begin{cases} T < 700: -7976.15 + 137.071542T - 24.3671976T * LN(T) - .001884662 * T^2 \\ - 8.77664e-7 * T^3 + 74092 * (\frac{1}{T}) \\ T \geq 700 \; and \; T < 933.6 : -11276.24 + 223.02695 * T - 38.5844296 * T * LN(T) \\ + .018531982 * T^2 - 5.764227e-06 * T^3 + 74092 * (\frac{1}{T}) \\ T \geq 933.6 : -11277.683 + 188.661987T - 31.748192T * LN(T) \\ - 1.234264e28 * (\frac{1}{T^9}) \end{cases}$$

$$GHSERMN(T) \quad (55)$$
$$= \begin{cases} T < 1519 : -8115.28 + 130.059T - 23.4582T * LN(T) \\ -.00734768T^2 + 69827(\frac{1}{T}) \\ T \geq 1519 : -28733.41 + 312.2648T - 48T * LN(T) + 1.656847e30(\frac{1}{T^9}) \end{cases}$$

$$GHSERCE(T) \quad (56)$$

$$= \begin{cases} T < 1000: \ -7160.519 + 84.23022T \ - 22.3664T * LN(T) - .0067103T^2 \\ \qquad -3.20773e-7T^3 - 18117(\frac{1}{T}) \\ T \geq 1000 \ and \ T < 2000: \ -79678.506 + 659.4604T - 101.32248T * LN(T) \\ \qquad +.026046487 * T^2 - 1.930297E-06 * T^3 + 11531707(\frac{1}{T}) \\ \qquad T \geq 2000: \ -14198.639 + 190.370192 * T - 37.6978 * T * LN(T) \end{cases}$$

The interaction parameters between each element are defined by $x_i x_j \sum_{k=0} L_{i,j}^k \left(x_i - x_j\right)^k$. The liquid binary interaction parameters are listed below

$$\sum_{k=0} L_{Al,Mn}^k \left(x_{Al} - x_{Mn}\right)^k \quad (57)$$

$$= \left((-66174 \ + \ 27.0988 * T) + \ (-7509 \ + \ 5.4836 * T) * (x_{Al} - x_{Mn}) \right.$$

$$\left. + \ (-2639) * (x_{Al} - x_{Mn})^2 \right)$$

$$\sum_{k=0} L_{Al,Ce}^k \left(x_{Al} - x_{Ce}\right)^k \quad (58)$$

$$= \left((-130371 \ + \ 38.523 * T) + \ (-36330 \ + \ 6.362 * T) * (x_{Al} - x_{Ce}) \right.$$

$$\left. + \ (-9208 \ + \ 4.065 * T) * (x_{Al} - x_{Ce})^2 \right)$$

$$\sum_{k=0} L_{Ce,Mn}^k \left(x_{Ce} - x_{Mn}\right)^k \quad (59)$$

$$= \left((15584.7 \ - \ 5.30258 * T) + \ (-2736.1) * (x_{Ce} - x_{Mn}) + \ (-1532.3) \right.$$

$$\left. * (x_{Ce} - x_{Mn})^2 \right)$$

The $Al_{20}Mn_2Ce$ and $Al_{10}Mn_2Ce$ phases are described as an intermetallic compound which is more simply described by Yang et al [150]

$$G_{Al_{20}Mn_2Ce} = 20 * GHSERAL(T) + 2 * GHSERMN(T) + GHSERCE(T) - 353610 + 20T \quad (60)$$

$$G_{Al_{10}Mn_2Ce} = 10 * GHSERAL(T) + 2 * GHSERMN(T) + GHSERCE(T) - 410158 + 40T \quad (61)$$

The Al-Si system is described in a similar manner, except it is binary which results in the Gibbs free energy being defined by

$$G = x_{Al}G_{Al}^{Liq} + x_{Si}G_{Si}^{Liq} + RT(x_{Al}\ln(x_{Al}) + x_{Si}\ln(x_{Si})) + x_{Al}x_{Si}\sum_{i=0} L_{Al,Si}^{v}(x_{Al} - x_{Si})^{v} \quad (62)$$

Where,

$$G_{Al}^{Liq} = \begin{cases} T < 933.6: \ 11005.029 - 11.841867 * T + 7.934e - 20T^7 + GHSERAL(T) \\ T \geq 933.6: \ 10482.382 - 11.841867T + 7.934e - 20T^7 + GHSERAL(T) \end{cases} \quad (63)$$

$$GHSERSI(T) = -8162.609 + 137.236859 * T - 22.8317533 * T * LN(T) - 1.912904e - 3 * T^2 - 0.003552e - 6 * T^3 + 176667(\frac{1}{T}) \quad (64)$$

The FCC Phase is defined by the following equations

$$G = x_{Al}GHSERAl(T) + x_{Mn}GHSERSI(T) + RT(x_{Al}\ln(x_{Al}) + x_{Si}\ln(x_{Si})) + x_{Al}x_{Si}\sum_{i=0} L_{Al,Si}^{v}(x_{Al} - x_{Si})^{v} \quad (65)$$

$$\sum_{i=0} L_{Al,Si}^{v}(x_{Al} - x_{Si})^{v} = -3143.78 + 0.39297 * T \quad (66)$$

Vita

Kevin Dean Sisco obtained a bachelor's degree from the University of Tennessee (UTK) in Mechanical engineering. He then attended UTK for a Ph.D. in Materials sciences in Engineering.